Lode gold mineralization in the Paleoproterozoic (Birimian) volcano-sedimentary sequence of Afema gold district, southeastern Côte d'Ivoire

Doctoral Thesis

(Dissertation)

to be awarded the agree of
Doctor rerum naturalium (Dr. rer. nat.)

submitted by

KOUADIO ETIENNE ASSIE

from Abengourou, Côte d'Ivoire

approved by the Faculty of
Energy and Economic Sciences
Technical University of Clausthal

Date of oral examination
19 February 2008

Gold-Mineralisation in der paläoproterozoischen (Birimian) vulkano-sedimentären Sequenz des Afema-Goldbezirks, südöstliches Côte d'Ivoire

Dissertation

zur Erlangung des Doktorgrades
der Naturwissenschaften

vorgelegt von

KOUADIO ETIENNE ASSIE

aus Abengourou, Côte d'Ivoire

genehmigt von der Fakultät für
Energie und Wirtschaftswissenschaften
der Technischen Universität Clausthal

Tag der mündlichen Prüfung
19. Februar 2008

Chairperson of the Board of Examinations: Prof. Dr. Heike Y. Schenk-Mathes
Chief Reviewer: Prof. Dr. Bernd Lehmann
Reviewer: Prof. Dr. Kurt Mengel

This dissertation was undertaken at the Economic Geology Department of the Institute of Mineralogy and Mineral Resources of the Technical University of Clausthal.

This thesis is dedicated to Régina, Olive and Eliane in appreciation of their patience and encouragement.

"The more one knows about a given process of ore deposition, the better one knows where (or where not) to look for more ore."

Edwin Roedder

CONTENTS

ACKNOWLEDGEMENTS

I would like to thank through these lines all those people who in different ways have made this work possible and have contributed to its success.

First, I gratefully acknowledge my supervisors Prof. Bernd Lehmann, Prof. Kabran Pothin, and Dr. Wolfgang Hirdes for their support, friendship and interest in this project. To Prof. Lehmann in particular, I would like to say once again: thank you professor, for your kindness, your simplicity, your clarity, and your rigor. In other words, thank you for all…

I am grateful to Prof. Kurt Mengel for his help and availability.

I am grateful to Fred Türck and Dr. Eike Gierth for their regular help in the field of informatics and ore microscopy, respectively.

I wish to thank Helga Vollbrecht, our secretary, for her permanent assistance.

Ulf Hemmerling is thanked for the professional elaboration of thin sections, polished sections and doubly polished sections. Thanks to Klaus Herrmann for measurement operations and constructive suggestions during microprobe investigations.

Special thanks go to Dr. Jens Wittenbrink and Daniel Hennig for their assistance during my first days in Clausthal, and also for their permanent availability.

I thank Mohammed Nekouvaght, Victor Akwinga, Farhad Torab, Lingang Xu, Stephanie Lohmeier, Alex Wasmus, Dr. Karl Strauß, Ingo Böttcher, Ines Harms, Charlotte Redler, Guy-Alain Youmbi, Brice Ipo, Bernard Husson, Dr. Alain Kouamelan, Dr. Coulibaly Yacouba, Dr. Adama Ouattara, Dr. Fernand Kouamé, Dr. N'Guesan Aghui, Prof. Cherubin Djro, Dr. Benjamin Allou, Dr. Keita Moussa, Serge Sonna, Barthelemy Kramo, Emmanuel Essan, Ghislaine

Pkan, Dr. Moussa Koné, Dr. Salia Diaby, Flora Manzan, Frédéric Tanoh for their friendliness, interest, help and fruitful discussions.

I would like to thank all the staff of the Institute of Mineralogy and Mineral Resources at the Technical University of Clausthal for friendliness and assistance. I will also not forget the department of Earth Sciences and Mineral Resources at the University of Cocody (Abidjan) for permanent encouragement.

I think Dr. Thomas Oberthür and Dr. Wilfried Ließmann for offer of important geological documents.

I also wish to thank Marie Ama Manouan, who encouraged me to apply for the DAAD scholarship.

I wish to thank Dr. Robert Yobou and SODEMI (Société pour le Développement Minier de la Côte d'Ivoire) for permission to work on the Afema district gold deposits.

Sincere gratitude is due to Dr. Bertin Yao, Yaridjima Koné, Gilbert Konan, Appolos Ahimon and all the staff of the "Direction de la Géologie" (Abidjan) for their generous assistance during my field work.

This project has been financially and logistically supported by the German Academic Exchange Service (DAAD: Deutscher Akademischer Austausch Dienst) and the Institute of Mineralogy and Mineral Resources of the Technical University of Clausthal. Additional support was received by Newmont Mining Corporation from the Society of Economic Geologists (SEG) through a research grant for Ph.D. students. They are gratefully acknowledged.

I am grateful to all my family and friends for their encouragement. Finally, I thank all those who directly or indirectly contributed to the success of this project.

ABSTRACT

The Afema gold district is located in southeastern Côte d'Ivoire, in Paleoproterozoic formations, locally termed Birimian. This region contains numerous epigenetic gold deposits hosted in deformed greenschist metamorphosed terranes, in a tectonic corridor striking NNE and dipping subvertically. This tectonic zone constitutes the contact between a metasedimentary assemblage (Kumasi basin) and a metavolcanic assemblage (Sefwi belt).

At the studied deposits (Aniuri and Jonction), gold mineralization occurs in metasedimentary rocks (e.g. metaarenite). It appears post-peak metamorphism and structurally controlled. The geochemical signature is characterized by Au-As-S-Sb-W-Cu-Zn-Te-Bi, where Au-As-S represents the main association. Two primary ore types are recognized: (1) sulfide ore (refractory ore), which corresponds to the principal ore, and where pyrite, arsenian pyrite and arsenopyrite represent the main sulfides, and (2) quartz-carbonate veins characterized by the presence of "free gold" and absence of As-rich Fe sulfide minerals. The two types of ore occur together.

In the main ore type (e.g. sulfide ore), two types of pyrite have been identified: (1) fine-grained pyrite, which is generally arsenic-rich (arsenian pyrite) and gold-bearing; (2) coarse-grained pyrite, which is arsenic-poor and barren. In this main ore type, gold occurs as micrometric inclusions and interstitial fillings in fine-grained arsenian pyrite crystals, and also as "invisible" (submicroscopic) gold in both arsenian pyrite and arsenopyrite.

The mineralogical assemblage in the main ore zones suggests reducing mineralizing fluids, enriched in CO_2 and H_2S. Gold was transported as bisulfide complexes and precipitated at intermediate temperatures (~205 - 410°C) in contact with arsenian pyrite and arsenopyrite crystals. This process was electrochemically mediated by arsenic through semiconductor effects.

The geotectonic setting recognized is oceanic island arc, and isotopic evidence indicates that the basement overlain by supracrustal rocks is mainly juvenile: $\varepsilon_{Nd(2190\ Ma)}$ values are between +1.0 and +3.9.

Ar-Ar ages for hydrothermal muscovite from metasediment-hosted ores give 1833 ± 16 Ma and 1840 ± 17 Ma. Re-Os dating on gold-bearing arsenopyrite and pyrite yields an errorchron age of 1943 ± 100 Ma, and Re-Os model ages on Re-rich sulfides are up to 2.1 Ga. The younger ages obtained from the Ar-Ar method are likely due to argon diffusion during thermal overprint.

Considering the combined temporal and spatial association of gold mineralization with highly deformed zones, and age data from the mineralization system and host-rocks, we conclude that gold mineralization in the Afema gold district is synkinematic, post-metamorphic and belongs to the family of orogenic gold deposits.

ZUSAMMENFASSUNG

Der Afema-Goldbezirk im Paläoproterozoikum (Birimian) des südöstlichen Côte d'Ivoire umfasst mehrere Scherzonen-kontrollierte epigenetische Goldlagerstätten in einem NNE-streichenden Korridor in foliierten steil stehenden Grünschiefer-faziellen vulkanosedimentären Gesteinen. Diese tektonische Zone stellt den Kontakt zwischen einer metasedimentären Sequenz (Kumasi Becken) und einer metavolkanischen Sequenz (Sefwi Gürtel) dar.

In den untersuchten Lagerstätten (Aniuri und Jonction) tritt die Goldmineralisation in den metasedimentären Gesteinen auf (vorwiegend Meta-Sandstein) und ist post-metamorph (in Bezug auf das Maximum der Metamorphose) und strukturell kontrolliert. Die geochemische Signatur zeichnet sich durch die Assoziation Au-As-S-Sb-W-Cu-Zn-Te-Bi aus, wobei Au-As-S dominant sind. Zwei primäre Erz-Typen können unterschieden werden: (1) Sulfiderz (refraktäres Erz), welches das Haupterz darstellt, und in dem Pyrit, arsenhaltiger Pyrit und Arsenkies die Hauptsulfide sind, und (2) Quarz-Karbonat-Gange mit "freiem" Gold bei Fehlen von As-reichen Fe Sulfidmineralen. Die beiden Erztypen treten zusammen auf.

Im Sulfiderz wurden zwei Pyrit-Typen identifiziert: (1) feinkörniger Pyrit, der Arsen-reich (arsenhaltiger Pyrit) und Gold-reich ist; (2) grobkörniger Pyrit, der Arsen-arm und steril ist. Gold tritt als mikrometrische Einschlüsse und interstitielle Füllung in feinkörnigen arsenhaltigen Pyritkristallen und auch als "unsichtbares" (submikroskopisch) Gold im arsenhaltigen Pyrit und im Arsenkies auf.

Die Mineral-Assoziation in den Haupterzzonen zeigt ein reduzierendes CO_2- und H_2S-führendes Fluidsystem an. Gold wurde wahrscheinlich als Bisulfid-Komplex transportiert und bei Temperaturen von ~205-410°C in Verbindung mit arsenhaltigem Pyrit- und Arsenkies ausgefällt. Die Gold-Fixierung wurde elektrochemisch durch Halbleitereffekte in Verbindung mit As-S-Substitution ausgelöst.

Das geotektonische Milieu ist das eines ozeanischen Inselbogens, und Nd-Isotopendaten zeigen, daß das kristalline Basement und die suprakrustale Sequenz hauptsächlich juvenil sind, mit $\varepsilon_{Nd(2190\ Ma)}$-Werten von +1,0 bis +3,9.

Ar-Ar Plateau-Alter für hydrothermalen Muscovit aus der Erzzone geben 1833 ± 16 Ma und 1840 ± 17 Ma. Re-Os-Isotopendaten von Arsenkies und Pyrit definieren ein Errorchron-Alter von 1943 ± 100 Ma, und Re-Os-Modell-Alter von Re-reichen Sulfiden reichen bis zu 2,1 Ga. Die jüngeren Alter aus der Ar-Ar-Methode gehen wahrscheinlich auf Argon-Verlust während der thermischen Überprägung zurück.

Die zeitliche und räumliche Assoziation der Goldmineralisation mit Zonen starker Deformation, sowie die Altersdaten der Alteration/Mineralisation zeigen

die synkinematische und post-metamorphe Stellung der Gold-Mineralisation und deren Affinität zur Familie der orogenen Gold-Lagerstätten.

RÉSUMÉ

Le district aurifère d'Aféma est situé dans le Sud-Est de la Côte d'Ivoire, dans des formations paléoprotérozoïques, localement appelées Birimien. Cette région contient plusieurs gisements d'or épigénétiques situés dans des terrains déformés, affectés par un métamorphisme de faciès schiste vert. Ces gisements se trouvent par ailleurs, dans un corridor tectonique orienté NNE et plongeant de façon subverticale. Cette zone tectonique constitue le contact entre un ensemble métasédimentaire (bassin de Kumasi) et un ensemble métavolcanique (ceinture de Sefwi).

Au niveau des gisements étudiés, (Aniuri et Jonction), la minéralisation aurifère se trouve dans des roches métasédimentaires (métaarénite essentiellement). Elle apparaît post-métamorphique et est marquée par un contrôle structural. La signature géochimique est caractérisée par Au-As-S-Sb-W-Cu-Zn-Te-Bi, où Au-As-S représente la principale association. Deux types de minerai primaire sont identifiés : (1) minerai de sulfures (minerai réfractaire), correspondant au principal type, et où pyrite, pyrite arsenifère et arsénopyrite représentent les principaux sulfures ; et (2) veines de quartz-carbonate caractérisées par la présence « d'or libre » et l'absence de sulfures de Fe riches en As. Les deux types de minerai apparaissent ensemble.

Dans le principal type de minerai (minerai de sulfures), deux sortes de pyrite ont été identifiés : (1) pyrite à grain fin, généralement riche en arsenic (pyrite arsenifère) et aurifère ; (2) pyrite à grain grossier, pauvre en arsenic et stérile. Dans ce type de minerai, l'or s'observe sous forme d'inclusions micrométriques et de remplissages interstitiels dans des cristaux de pyrite arsenifère à grain fin. Il se trouve en outre sous forme « invisible » (submicroscopique) à la fois dans la pyrite arsenifère et dans l'arsénopyrite.

L'assemblage minéralogique du principal type de minerai suggère un caractère réducteur des fluides minéralisateurs, enrichis en CO_2 et H_2S. Le transport de l'or s'est fait sous forme de complexes bisulfures, suivi de sa précipitation à des températures intermédiaires (~205 – 410°C) au contact avec des cristaux de pyrite arsenifère et d'arsénopyrite. Ce processus aurait été électrochimiquement favorisé par l'arsenic à travers des effets de sémiconducteur.

Le contexte géotectonique identifié est de type arc insulaire océanique, et des évidences isotopiques indiquent un caractère juvénile du socle recouvert par les roches supracrustales : les valeurs de $\varepsilon_{Nd(2190\ Ma)}$ sont comprises entre +1,0 et +3,9.

Des âges Ar-Ar sur muscovite hydrothermale des métasédiments encaissant la minéralisation sont de 1833 ± 16 Ma et de 1840 ± 17 Ma. La datation Re-Os sur arsénopyrite et pyrite aurifères rapporte un âge errorchrone de 1943 ± 100 Ma et des âges modèles jusqu'à 2,1 Ga obtenus sur des sulfures riches en Re.

Les âges les plus jeunes obtenus par la méthode Ar-Ar sont vraisemblablement dus à la perte d'argon au cours d'évènements thermaux postérieurs.

En considerant l'association temporelle et spatiale de la minéralisation aurifère avec des zones fortement déformées, ainsi que des données d'âge du système de minéralisation et des rocks hôtes, nous concluons que la minéralisation aurifère dans le district aurifère d'Aféma est syncinématique, post-métamorphique et appartient à la famille des gisements d'or orogéniques.

LIST OF ABBREVIATIONS

a.p.f.u.:	atoms per formula unit
AI:	Alteration Index
ASP:	Arsenopyrite
at.%:	Atomic percent
ATZ:	Afema Tectonic Zone
Au:	Gold
CCPI:	Chlorite-Carbonate-Pyrite Index
CHUR:	Chondritic Uniform Reservoir
CP:	Chalcopyrite
cp	Critical point
cps:	Count per second
C-PY:	Coarse-grained pyrite
DDH:	Diamond Drill Hole
EMPA:	Electron Microprobe Analysis
F-PY:	Fine-grained pyrite
FW:	Footwall
Ga:	Billion year
g/t:	Gram per tonne
GP:	Graphite
HW:	Hanging Wall
LA-ICP-MS:	Laser Ablation – Inductively Coupled Plasma – Mass Spectrometry
Ma:	Million year
MSWD:	Mean Square of Weighted Deviates
MZ:	Monazite
pg:	Picogram
PO:	Pyrrhotite
ppt:	parts per trillion
P_t	Trapping pressure
PY:	Pyrite

REE:	Rare Earth Element
RL:	Reference line
RT:	Rutile
Somiaf:	Société des Mines d'Aféma
SP:	Sphalerite
TH:	Tetrahedrite
T_h	Homogenization temperature
$T_{h(L)}$	Homogenization temperature into liquid
TT:	Tennantite
T_t	Trapping temperature
UUC:	Upper Continental Crust
VHMS:	Volcanic-Hosted Massive Sulfide
wt.%:	Weight percent

LIST OF FIGURES

LIST OF TABLES

INTRODUCTION

The Afema gold district, in the southeastern part of Côte d'Ivoire, was known since the 19th century. It contains several lode gold deposits. From February 1992 to August 1998, about 4 tonnes of gold were recovered from a series of open pits (oxidized ore) by heap leaching technique.

Geologically, the Afema gold district is located in metamorphosed and deformed Paleoproterozoic Birimian formations, and constitutes a prolongation of the Kumasi Basin (metasedimentary assemblage) and the Sefwi Belt (metavolcanic assemblage) in neighboring Ghana. Ghana is currently the second gold producing country in Africa, and hosts several large lode gold deposits (e.g. Ashanti, Prestea, Chirano, Bibiani, etc.). Note that a lode deposit is a mineral deposit consisting of a zone of veins, veinlets, disseminations, or planar breccias; in other words, it is a mineral deposit in consolidated rock as opposed to placer deposits (Neuendorf *et al.*, 2005). The Birimian tectonometamorphic terranes and the structural pattern of Ghana can be followed into southeastern Côte d'Ivoire, but the state of geological knowledge in the Ivorian part is relatively poor.

The major aim of this work is to improve the understanding of the metallogeny of gold in this area, and attempt to correlate it with similar terranes in Ghana. On the basis of this main objective, the present work intends to answer the following questions:

- What is the geological and structural setting of the gold mineralization?
- What is the timing relation between deformation, peak-metamorphism, and gold mineralization?
- What are the mineralogical and physico-chemical characteristics of the gold mineralization?
- What are the geochronological characteristics of the gold mineralization system?
- How can the gold mineralization in the Afema district be correlated to the gold mineralization in neighboring Ghana?

To achieve these objectives, first, the geographical and the geological settings of the Afema gold district are described relative to the regional context. The analytical methods used in this study are also briefly described. Then, the results and their interpretations are treated in detail to finally arrive at conclusions, where a genetic model for gold mineralization in the Afema gold district is proposed as well as some recommendations for exploration.

1. GENERAL ASPECTS

1-1. Geographical setting

1-1-1. Location and accessibility of the study area

The Afema gold district (study area) is located in the southeastern part of Côte d'Ivoire, in West Africa (Figure 1). With geographical coordinates of 3° W to 8° W longitude and 5° N to 10° N latitude, the territory of Côte d'Ivoire covers 322,462 km^2. Bordering the Atlantic Ocean, it neighbors to the west Guinea and Liberia, to the north Burkina Faso and Mali, and to the east Ghana. The Afema district belongs to the administrative area of "Région du Sud-Comoé" which is located in the southeastern part of the country between the Comoé River and Ghana, with Aboisso as capital.

The study area is a part of the concession area of the former mining company Somiaf ("Société des Mines d'Aféma"), subsidiary of Eden Roc Mineral Corporation. Its geographical limits are about 2°40' W to 3°15' W longitude and 5°15' N to 5°45' N latitude. The study area is approximately 42 km to the east of the town of Aboisso, and 160 km from Abidjan the economic capital of Côte d'Ivoire. It is easily accessible by tarred road until Maféré (town located at 28 km to the east of Aboisso) and beyond, by dirt road for approximately 14 km.

1-1-2. Topography and hydrography

The topography of the Afema district is characterized by an alternation of small valleys and hills which show in places steep slopes. The altitudes vary between less than 20 m and about 200 m. The topographically highest zones are located north of the mining claim, particularly in the area of the villages of Kotoka and Diby (Figure 1). The hydrographic network of the region is of dendritic type with one major river (e.g. Bia) and three relatively smaller ones (e.g. Eholié, Ehania and Noé) with many small affluents each. Ehania and Noé are tributaries of the Tanoé River which marks the border between Côte d'Ivoire and Ghana. All these rivers have a flow direction from North to South and

empty either in the Aby lagoon (e.g. Bia and Ehohié) or in the Ehy lagoon (e.g. Tanoé). Two hydroelectric dams (Ayamé 1 and Ayamé 2) are built on the Bia River near the town of Ayamé.

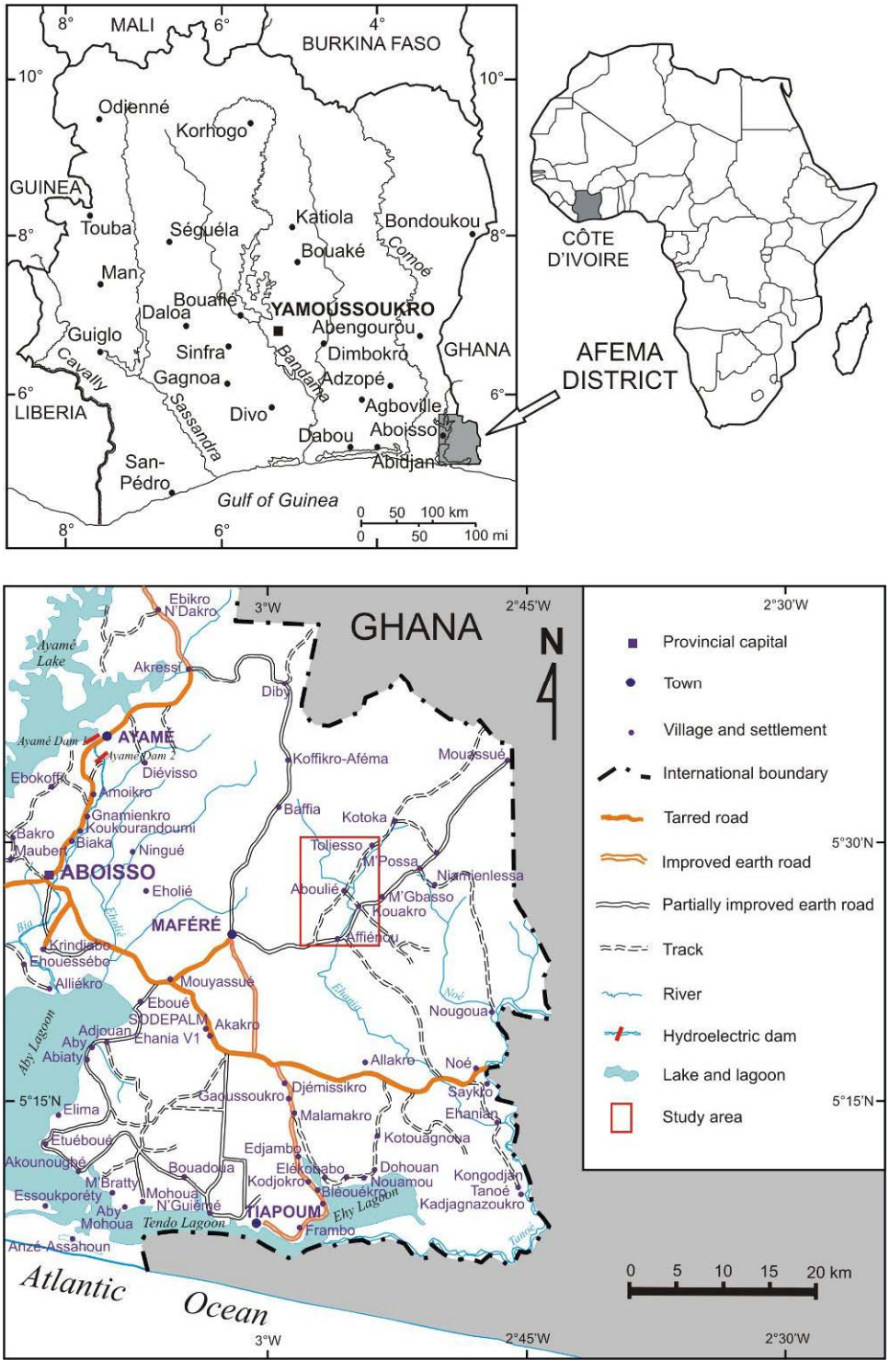

Figure 1. Location of the study area in the Afema district.

1-1-3. Climate and vegetation

The climate prevailing in the Afema district is of sub-equatorial type, like the whole southern part of the country. The temperatures oscillate between 21°C and 33°C with 26°C as annual average. Hot and wet, the region is distinguished by a succession of four seasons of unequal duration: a great dry season from December to March, a great rainy season from April to July, a small dry season from August to September, and a small rainy season from October to November. For this part of the country, the annual pluviometry varies between 1400 and 2500 mm. The great rainy season corresponds to the period of river floods.

The vegetation is also of sub-equatorial type with a dense forest distinguished by trees with persistent leaves. This forest gives more and more way to plantations of cocoa tree, coffee tree, palm tree and rubber tree, which cover in places very important areas.

1-2. Geological setting and gold mineralization

1-2-1. Geological overview of West African craton

The West African craton (Figure 2) presents two principal zones of outcrop: the Reguibat shield in the north and the Man shield (also called Leo shield or Guinea Rise) in the south. Between these two segments are two small windows, namely the Kedougou-Kenieba and Kayes inliers. The West African craton is bounded to the north by the Anti-Atlas, to the west by the mobile zone of West Africa, and to the east by the mobile zone of central Africa. It is largely covered by sedimentary formations of Neoproterozoic and Paleozoic age, namely the Tindouf basin in the north and the Taoudeni basin in the central part (Bessoles, 1977).

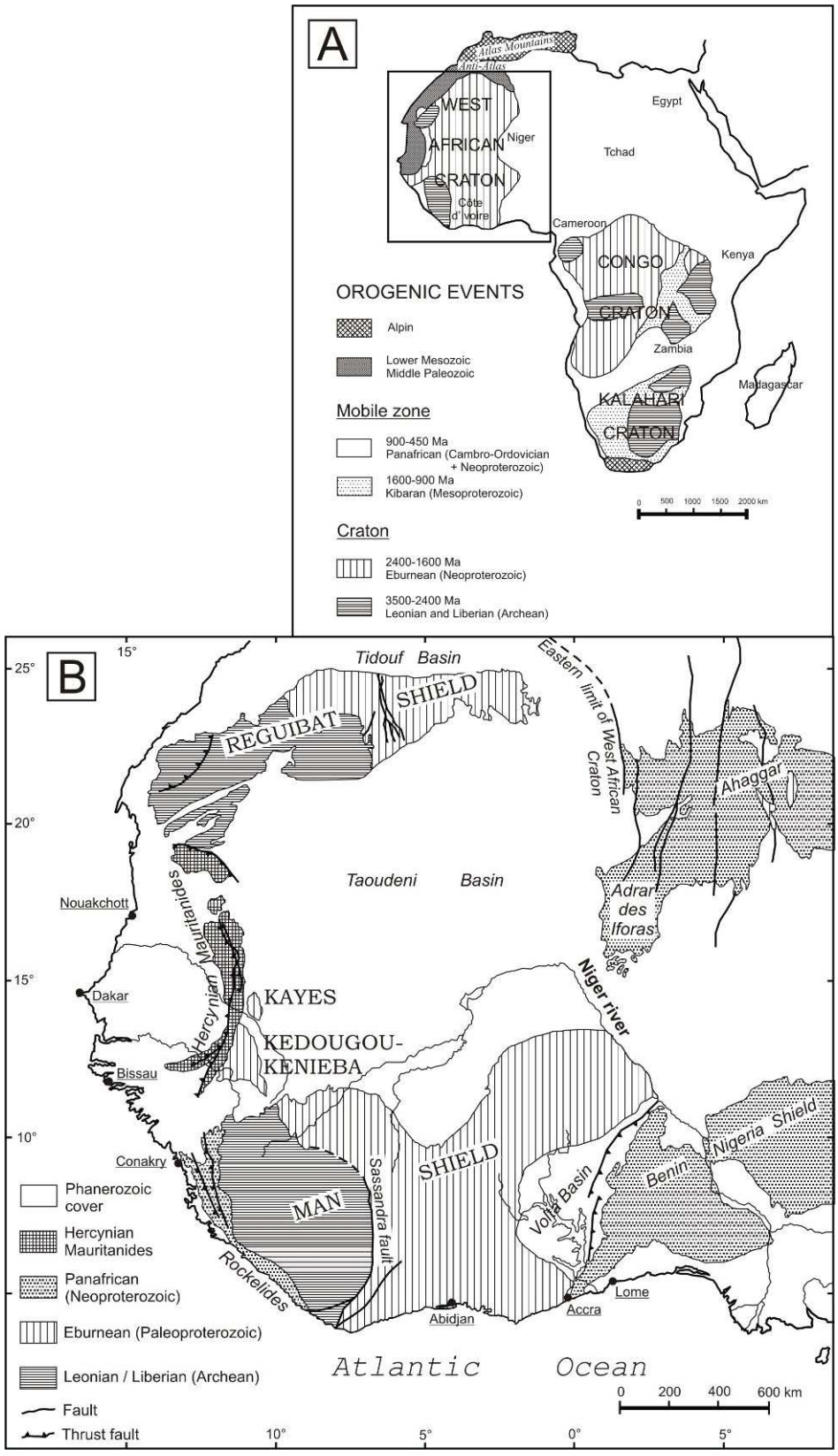

Figure 2. A) Cratons and mobile belts in Africa (modified after Clifford, 1970); B) Geological outline map of West Africa showing basement outcrops and basins (modified after Boher *et al.*, 1992).

The Precambrian crustal evolution in West Africa is characterized by five orogenic cycles which are superimposed in space and time (Yacé, 1984): Leonean, Liberian, Eburnean, Kibaran and Panafrican orogenic cycles. The Leonian, the oldest orogenic cycle, extends from 3500 to 2900 Ma, which corresponds to the Paleo- and Mesoarchean. The age of the Liberian orogenic cycle ranges between 2900 and 2400 Ma, corresponding roughly to the Neoarchean. The Eburnean orogeny, called Eburnean megacycle for its long duration, extends from 2500 or 2400 Ma to 1600 or 1500 Ma, which is equivalent to 800-1000 Ma of duration (Yacé, 2002). It corresponds to the Paleoproterozoic. The manifestation of the Kibaran orogeny (suspected in Nigeria, but not formally recognized) takes place between 1600 and 900 Ma, i.e. during the Mesoproterozoic. The last orogenic cycle having affected West Africa is the Panafrican cycle. It ranges between 900 and 450 Ma, and corresponds to the Neoproterozoic. The Leonean, Liberian and Eburnean orogenies relate to major crustal growth and cratonization of West Africa. According to Yacé (1984), the West African craton stabilized at about 1600 Ma, with the Kibaran and Panafrican orogenies present in peripheral mobile zones.

The southern part of the West African craton, i.e. the Man Shield, stretches over several countries, namely: Côte d'Ivoire, Ghana, Mali, Burkina Faso, Guinea, Liberia, Sierra Leone, west Niger, and north Togo (Figure 3). This cratonic domain is bounded to the west by the Panafrican mobile zone of the Mauritanides-Rokellides, to the north and the east by the transgressive cover of the Phanerozoic Taoudeni and Volta basins (Figure 2).

The Man shield is made up of two domains: (1) an Archean nucleus, called Kenema-Man domain, which is composed of geological formations structured during the Leonian and the Liberian orogenies and thus known as Leonian and Liberian formations; (2) a Paleoproterozoic domain or Baoulé-Mossi domain, with relics of Archean basement. In this domain occur Birimian and Tarkwaian rocks.

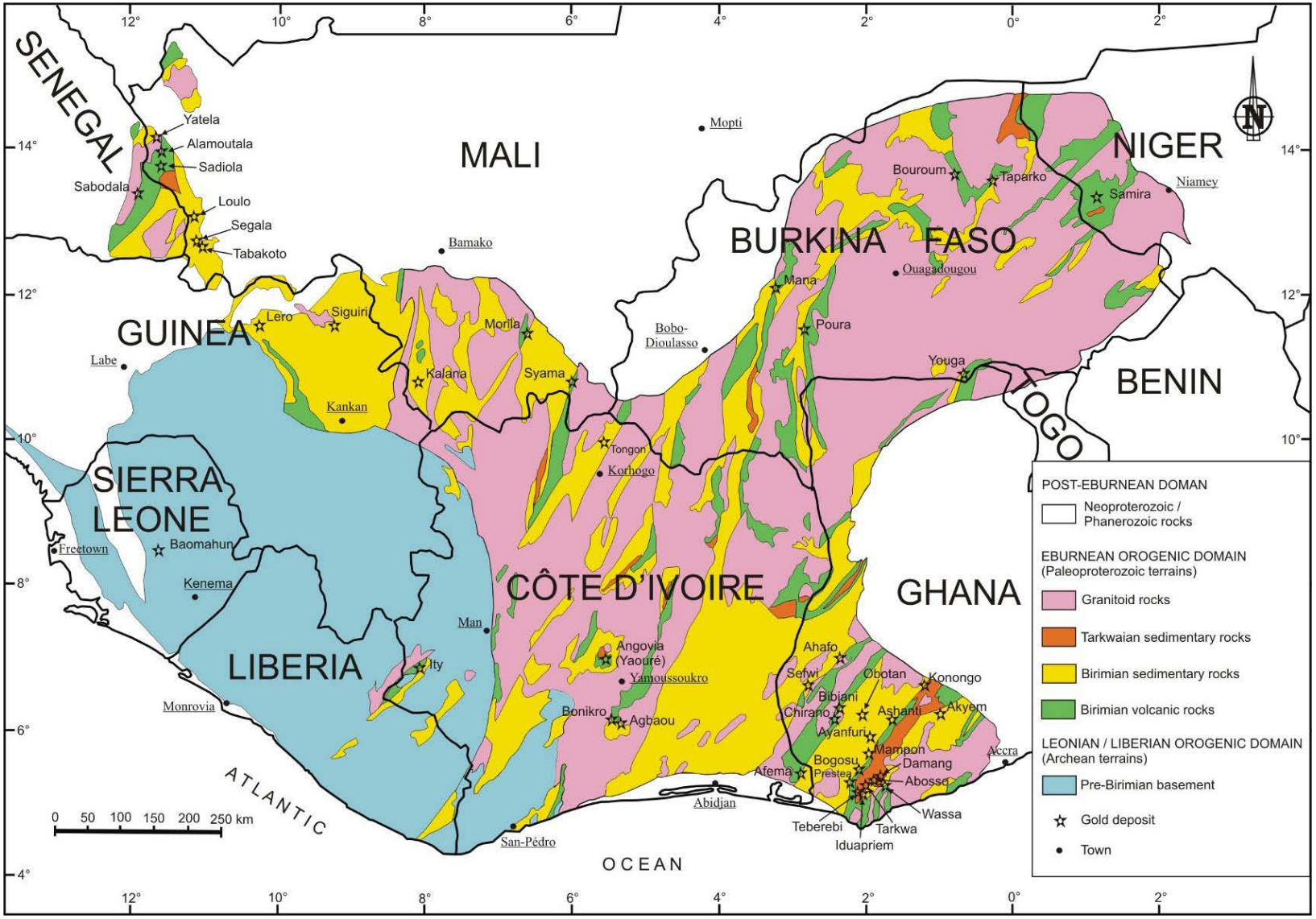

Figure 3. Regional geology of Man Shield and location of major known gold deposits (modified after Milési *et al.*, 1992).

The Birimian (also termed Birimian Supergroup) represents geological formations deposited during the Eburnean orogeny over a maximum time interval of ca. 2.27 Ga to 2.05 Ga (Abouchami *et al.*, 1990; Boher *et al.*, 1992; Hirdes *et al.*, 1992; Hirdes *et al.*, 1996; Oberthür *et al.*, 1998; Hirdes and Davis, 2002; Pigois *et al.*, 2003). The term Tarkwaian (or Tarkwaian Group) refers to clastic sedimentary rocks representing erosional products of Birimian provenance. The Tarkwaian consists of a subordinate arenaceous and conglomeratic sequence occurring among the Birimian Supergroup (Wright *et al.*, 1985; Milési *et al.*, 1992). Davis *et al.* (1994) indicated that the maximum age of Tarkwaian sedimentation is 2132 ± 3 Ma.

1-2-2. Geological overview of Côte d'Ivoire

The territory of Côte d'Ivoire can be divided into two principal geological zones: a Mesozoic-Cenozoic sedimentary basin covering the southern part of the country (with an extension into the Atlantic Ocean), and a Precambrian basement complex appearing in the remainder of the country (Figure 4).

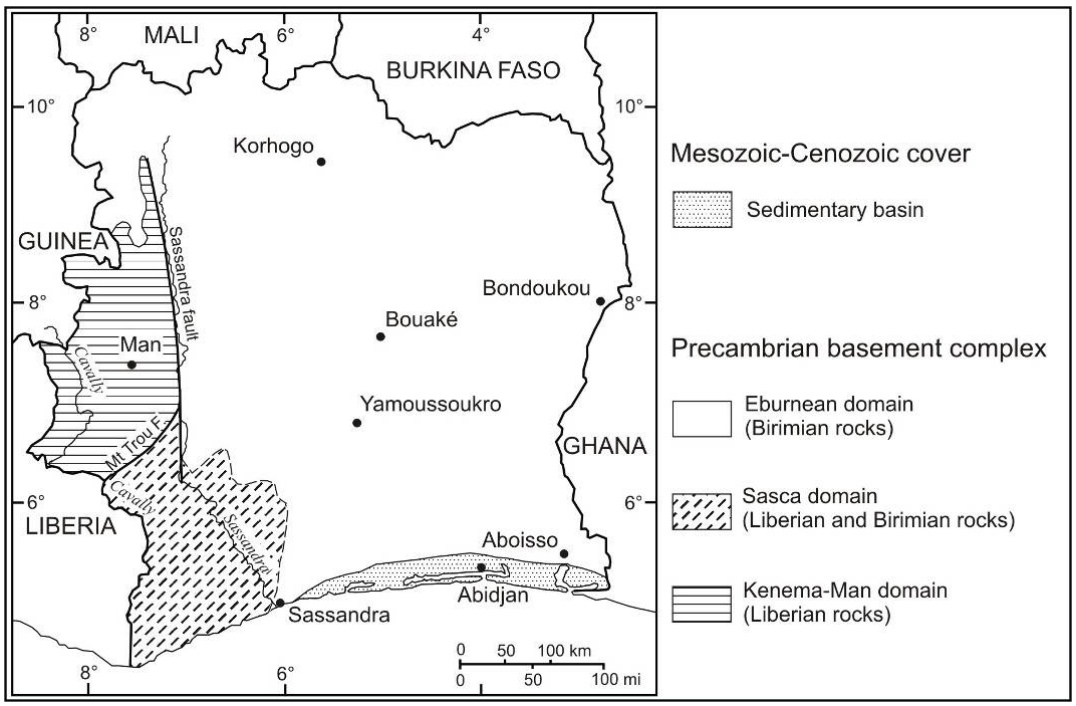

Figure 4. Geological domains of Côte d'Ivoire.

The emerged part of the sedimentary basin of Côte d'Ivoire extends in a crescent shape along the coast, from the region of Sassandra-Fresco to the town of Axim in Ghana. In Côte d'Ivoire, it covers a surface of less than 3% of the territory. According to Yacé (2002), the oldest events of the sedimentary basin of Côte d'Ivoire are allotted to Middle Cretaceous; however, some authors think that as in Ghana, this limit should be prolonged to Lower Cretaceous and even to Jurassic. The uppermost part of the stratigraphic sequence of the sedimentary basin of Côte d'Ivoire consists of a set of reddened continental formations (colored in red by iron oxides) called “Continental terminal” which extends from Miocene to Holocene.

The Precambrian basement complex of Côte d'Ivoire can be subdivided into three domains (Figure 4): Liberian domain, Sasca domain, and Eburnean domain.

The Liberian domain (also called Kenema-Man domain) is mainly made up of Liberian formations. This domain is bounded to the east by the Sassandra fault and to the south by the Mont Trou fault (also called Guiglo fault). It mainly consists of hypersthene-bearing rocks called charnockitic suite (or granulitic suite by some authors). In addition, ferruginous quartzites, basic and ultrabasic rocks transfomed to pyroxenites and amphibolo-pyroxenites, gneisses, migmatites, and granites occur in this area (Yacé, 2002). The metamorphism varies from catazonal to mesozonal, i.e. from granulite facies to amphibolite facies.

The Sasca domain is represented by the zone located in the southwestern part of the country, between the Sassandra and the Cavally rivers. In fact, the term Sasca comes from the contraction of the words Sassandra and Cavally (Papon, 1973). This domain consists of rocks formed during the Eburnean orogeny with relics of Liberian rocks. Contrary to the Man domain where the effect of Eburnean orogeny on the Liberian formations is expressed by the isotopic rejuvenation of biotite and sometimes of microcline, here the Liberian formations were intensely overprinted by the Eburnean orogeny. They are

characterized by amphibolite facies to granulite facies metamorphism (Bessoles, 1977). The Liberian formations of this domain are represented by gneiss (rarely with hypersthene), migmatite, leptynite, micaschist, amphibolo-pyroxenite, quarzite and granite (Yacé, 2002). The Eburnean formations of the Sasca domain are predominantly composed of schist, sandstone, quarzite and conglomerate. The metamorphism varies from epizonal to mesozonal, with a predominance of the greenschist facies. The southwestern part of Côte d'Ivoire hosts Eburnean plutonic rocks represented by granite, granodiorite and syenite.

The essentially Eburnean domain (the remainder of the national territory) is mainly made up of Birimian formations which cover more than two thirds of the country. These Birimian formations are represented by an alternation of granitic zones and volcano-sedimentary units (composed of metamorphic rocks of sedimentary and igneous origin). These volcano-sedimentary units mainly consist of metagabbro, metadolerite, metabasalt, metaandesite, metarhyolite, metarhyodacite, metadacite, amphibolite, volcaniclastite, various schists and quarzite. The granitoids are represented by granite, granodiorite and tonalite (Yacé, 1984, 2002). The metamorphic rocks are more or less folded and strike NNE-SSW with a sub-vertical dip. The regional metamorphism is mostly of greenschist facies.

1-2-3. Present state of knowledge of the Birimian Supergroup of West Africa

The term “Birimian” was introduced by Kitson (1928) to describe rocks from the valley of the River Birim in Ghana. The stratigraphic subdivision of the Birimian (or Birimian Supergroup) has been a matter of considerable debate since the middle of the last century.

The stratigraphy established by early authors (Junner, 1935, 1940; Bates, 1956) who studied the Birimian Supergroup was characterized by a lower unit

with prevalence of sedimentary rocks (Lower Birimian), and an upper unit with prevalence of volcanic rocks (Upper Birimian).

Arnould (1959) and then Tagini (1971), proposed a different stratigraphy with Lower Birimian predominantly volcanic and Upper Birimian predominantly sedimentary rocks (with flysch-type character). In fact, Tagini explained the stratigraphy of the Eburnean orogenic cycle while referring to the Alpine geosyncline model defined by Aubouin (1961). According to the conception of Aubouin, in the Alpine basins (eugeosyncline), one observed at the base volcanic formations (ophiolitic nature), surmounted by a unit known as “filling unit” made up of flysch and molasse.

Bessoles (1977), refusing the concept of geosyncline and ophiolite proposed by Tagini (1971), thought that the Birimian formations were assemblages of rocks of volcanic, sub-volcanic and sedimentary origin, which were deposited within many parallel rifted basins. He called these assemblages Birimian units. Based on an unpublished work of André Papon, he subdivided the Birimian units into two categories: type I units composed of various volcanic rocks and flysch-type formations attesting the existence of deep basins, and type II units composed of subcontinental sedimentary formations with lack of basic volcanic rocks of ophiolitic character. The type I units were distinguished by their relatively narrow width compared to their length, whereas the type II units corresponded to shallow basins and present more elongated forms than those of type I.

Lemoine *et al.* (1985) and Tempier (1986) defined Birimian as the stratigraphic sequence of the Eburnean orogenic cycle *sensu stricto*. In fact, these authors divided the Eburnean megacycle into two distinct orogenic cycles: (1) the Burkinian orogenic cycle from 2400 Ma to 2100 Ma (later changed to 2400 - 2150 Ma) with a stratigraphic sequence termed Dabakalian, and (2) the Eburnean orogenic cycle (*s.s.*) from 2150 Ma to 1800 Ma.

Using structural and geochronological arguments, Milési *et al.* (1989) defined a Lower Birimian or Birimian 1 (B1) characterized by a flysch-type unit and an

Upper Birimian or Birimian 2 (B2) made up of a predominantly volcanic unit. They defined a first collisional tectonic phase D1 (dated at about 2100 Ma) which is regarded as one of the essential criteria to distinguish B1 from B2, since it affects only the B1 unit. The B2 unit is on the other hand only affected by two late phases of deformation: D2 and D3.

The works of Junner (1940) and Arnould (1961) allowed to distinguish two main types of Paleoproterozoic granitoids that intrude the Birimian sequences, i.e. concordant and discordant granitoids. The concordant granitoids were known as “Baoulé-type” granites in Côte d'Ivoire and as “Cape Coast-type” granites in Ghana. This type of granitoids has important size and is associated spatially to the metasedimentary Birimian rocks. The discordant granitoids, called “Bondoukou-type” granites in Côte d'Ivoire and “Dixcove-type” granites in Ghana are characterized by small dimensions, and they intrude the metavolcanic Birimian rocks. Arnould (1961) regarded the Baoulé/Cape Coast-type granites as older than the Bonkoukou/Dixcove-type granites. Tempier (1969) was against this chronology on the basis of radiometric data and the presence of pebbles similar to the discordant granites (Bondoukou/Dixcove-type) in the conglomerates intruded by concordant granites. The results of the works from Hirdes *et al.* (1992) and from Davis *et al.* (1994) corroborated the point of view of Tempier. These authors obtained U-Pb ages (zircon) of 2179 ± 2 Ma and 2172 ± 2 Ma on discordant granites ("belt-type granitoids" in Leube *et al.*, 1990) in Ghana. Furthermore, they obtained ages of 2116 ± 2 Ma (U-Pb on zircon), 2090 ± 1 Ma (U-Pb on zircon and monazite), and 2088 ± 1 Ma (U-Pb on monazite) on concordant (“basin-type”) granitoids. These authors thought that the discordant granitoids and the volcanic belts were contemporaneous and comagmatic; whereas the concordant granitoids were interpreted as formed towards the end of the deformation, i.e. late kinematic.

Using isotope and structural data of geological formations of Ghana, Hirdes *et al.* (1987), Leube *et al.* (1990), Hirdes *et al.* (1992), Taylor *et al.* (1992), Hirdes *et al.* (1993) estimated that the predominantly volcanic unit (“volcanic belts”) and the predominantly sedimentary unit (“sedimentary basins”) of the Birimian

Supergroup formed quasi-contemporaneously as laterally equivalent facies. The authors explained this concept by proposing a model for the evolution of the Birimian. In this model, tholeiitic lava was initially deposited in marine conditions after rifting of the Archean sialic crust. This lava accumulated to form ridges emerging from the sea. During this period of accumulation occurred intrusions of granitoids (discordant or "belt-type granitoids") within these volcanic belts and the deposition of volcanogenic sediments in subsiding basins. At the end of the volcanic activity, an erosional phase took place which allowed the deposition of clastic sediments. The accretion and collision of relatively competent volcanic belt terrains and intense deformation (isoclinal folds, shearing and overlapping) of incompetent terrains from the basins produced crustal shortening oriented NW-SE. Partial melting of the basinal sediments, towards the end of the deformation, produced late kinematic concordant granitoids called "basin-type granitoids".

Hirdes *et al.* (1996) suggested the subdivision of the Birimian zone into two subprovinces (eastern and western) separated by an important regional N-S trending lineament named "Ouango-Fitini lineament". The eastern subprovince covering the eastern part of Côte d'Ivoire, Ghana and the eastern part of Burkina Faso, has volcanic belts and synvolcanic plutonism from approximately 2190 Ma to 2150 Ma (U-Pb on zircon and monazite). This subprovince almost lacks younger volcanism. The western subprovince covers the center and western part of Côte d'Ivoire, Guinea, Mali and Senegal. It is characterized by slightly younger volcanic belts with coeval belt-type granitoids of around 2105 Ma age. According to this temporal subdivision, Hirdes *et al.* (1996) proposed the term of "Bandamian" for the younger Birimian formations (western subprovince), and the term of Birimian *sensu stricto* for the older formations, i.e. those of the eastern subprovince.

1-2-4. Gold deposits in West Africa

The major gold deposits in West Africa are located in Precambrian terranes, essentially in Paleoproterozoic formations, i.e. Birimian Supergroup and Tarkwaian Group (Figure 3). Milési *et al.* (1989; 1992), using criteria such as type of host rock, host structure, and geometry of the ore body and its paragenesis, distinguished five major types of primary gold deposits and two types of secondary gold mineralization in West Africa. The main characteristics of these different types of gold deposits are summarized in Table 1.

Table 1. Main types of gold deposits in West Africa after Milési *et al.* (1989; 1992)

Gold deposit types	**Host rocks**	**Features of the mineralization**	**Examples**
Type 1: Tourmalinized-turbidite hosted gold deposits	Tourmalinized turbidite formations: fine to coarse-grained tourmalinized black sandstones, in places conglomeratic	- Highest gold grades in highly tourmalinized sulfide zone. - Sulfides are essentially pyrite, pyrrhotite, pentlandite, gersdorffite and arsenopyrite. - Gold as fine particles (10-40 μm) in fissures or at the surfaces of pyrite crystals with which it is generally associated; it is however coarser in quartz and carbonates of the stockworks and in the oxide ore.	- Loulo (Mali)
Type 2: Disseminated Au-sulfide deposits	Mafic tholeiitic volcanites	- Disseminated sulfides with absence of Pb, Sb and As minerals. - Main sulfides: pyrite (abundant), chalcopyrite (common) and rare pyrrhotite, pentlandite and magnetite. - Gold as inclusions (1-150 μm) in gangue minerals (white mica, quartz or carbonate), and as fine inclusions (1-50 μm) in pyrite (exceptionally chalcopyrite) or at the edges of pyrite crystals.	- Yaouré (Côte d'Ivoire) - Syama (Mali)
Type 3: Gold-bearing conglomerate deposits	Quartz-pebble conglomerate (Banket formations of Tarkwaian Group)	- Highest gold grades in the lower part of the main conglomerate horizon ("main reef"). - Gold as free gold and apparently associated with iron enriched conglomeratic horizons.	- Paleoplacers of the Tarkwa district in Ghana (e.g. Tarkwa, Teberebie, Iduaprem)

Gold deposit types	Host rocks	Features of the mineralization	Examples
Type 4: Mesothermal auriferous arsenopyrite and gold-bearing quartz vein deposits	Commonly metasediments (mainly argillite, greywacke or epiclastic rocks), but may also be mafic to intermediate or (rarely) acid intrusions	- Gold mineralization within tectonic corridors several tens of kilometers long with a general NE-SE strike, and commonly several kilometers wide. - Two common associations of ore in the mineralized column: (a) disseminated gold-bearing arsenopyrite which provides about 60% of Ashanti production, and (b) quartz vein and stockworks with free gold and polymetallic sulfides (pyrite, chalcopyrite, tetrahedrite, pyrrhotite), which truncate the disseminated mineralization. N.B.: The second paragenesis is comparable to that of the type 5 described below.	- Ashanti (Obuasi), Prestea, Konongo in Ghana. - Aniuri and Asupiri (Afema district) in Côte d'Ivoire
Type 5: Mesothermal gold-quartz vein deposits with polymetallic sulfides	- Metasedimentary rocks - Volcanic and sandstone-conglomeratic sequences - Granite	Mineralized bodies consist of quartz ± carbonate veins, lenses or stockworks with disseminations of polymetallic (Pb, Cu, Zn) sulfides, cupro-argentiferous sulfosalts, and native gold.	- Poura (Burkina Faso) - Sabodala (Senegal)
Type 6: Alluvial and eluvial placers	-	-	-
Type 7: Lateritic gold ore deposits	Ferralitic weathered rocks	- Gold mineralization located in a lateritic profile. - Gold ore consists of argillized rocks with iron oxide minerals. - Native gold appears as zoned nuggets (up to 10 mm).	Ity (Côte d'Ivoire)

The lode gold deposits, which correspond to the types 4 and 5 occur in metamorphic terranes and constitute a coherent class of epigenetic precious-metal deposits. They are associated in space and time with accretionary tectonics (McCuaig and Kerrich, 1998). This class of gold deposits is the most important in terms of production in West Africa (Partington and Williams,

2000). The lode gold deposits are variously termed by different authors with respect to:

- hydrothermal process (e.g. mesothermal gold deposit);
- metamorphic process (e.g. mesozonal gold deposit: Gebre-Mariam *et al.*, 1995);
- host-rock type (e.g. greenstone-hosted gold deposit: Hutchinson, 1987; or greenstone gold deposit: Robert and Poulsen, 2001);
- host-rock age (e.g. Proterozoic lode gold deposit: Partington and Williams, 2000);
- type location (e.g. Homestake and Mother Lode gold deposits);
- orogenic belts related (e.g. orogenic gold deposit: Goldfarb *et al.*, 2001).

1-2-5. Geological and structural setting of the study area

The geology of Afema district is characterized by NE-SW striking lithologies of Birimian formations which can be followed up to the adjacent Ghanaian territory (Figure 5). These formations represent supracrustal rocks consisting of a metavolcanic and a metasedimentary rock assemblage (termed Sefwi belt and Kumasi basin, respectively in Ghana), both intruded by batholiths and/or sills of acid to basic composition. Sedimentary rocks of Cenozoic age ("Continental terminal") discordantly cover the Birimian terranes in the southern part of the region.

The Sefwi volcano-plutonic belt is predominantly composed of low-grade metamorphic tholeiitic basalts with intercalated volcaniclastics and felsic flow rocks, and associated synvolcanic granitoid intrusions. The Kumasi sedimentary basin, however, consists of volcaniclastics, wackes and argillites. Radiometric dating was carried out on these geological formations in Côte d'Ivoire (Afema district) as well as in Ghana (Figure 5 and Table 2).

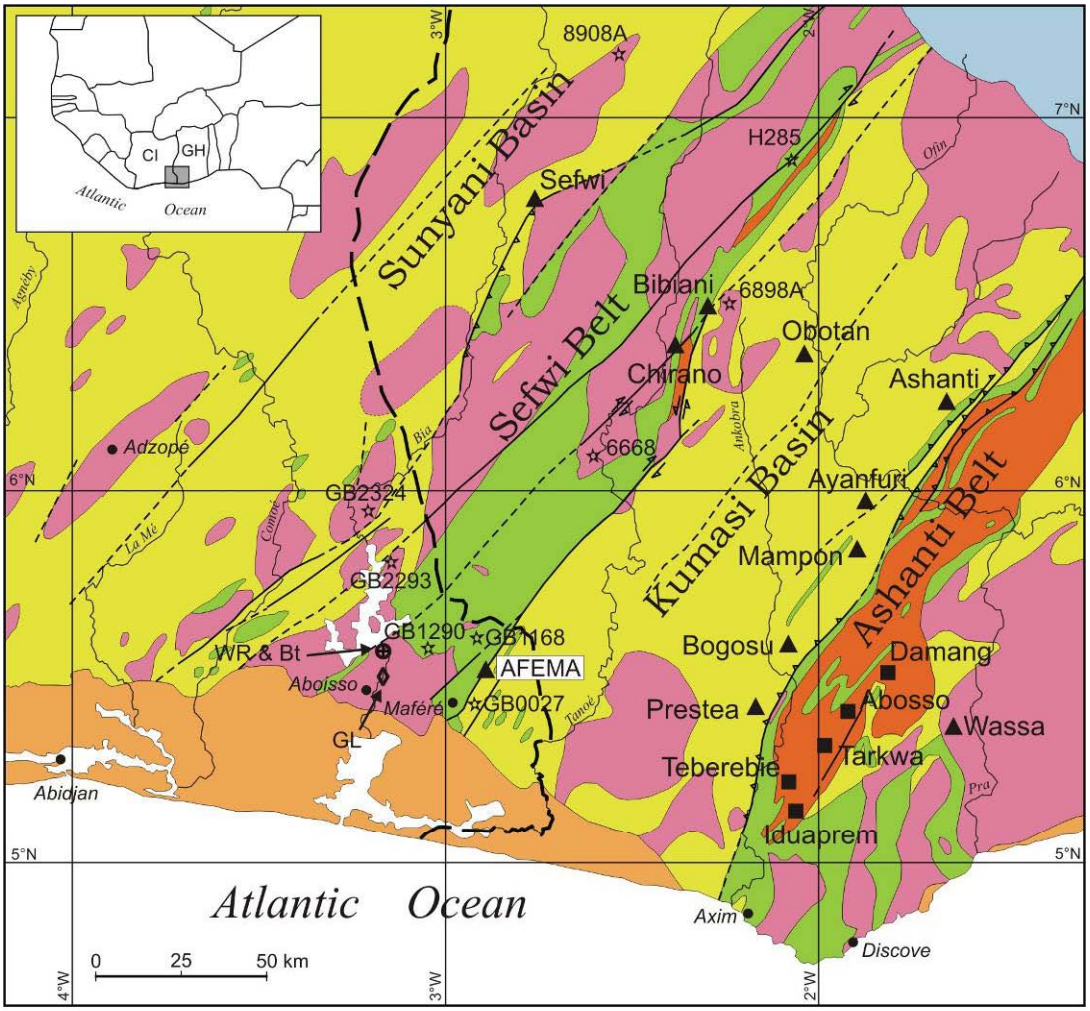

POST-EBURNEAN ANOROGENIC DOMAIN

- Phanerozoic rocks (Cretaceous to recent)
- Neproterozoic to Paleozoic rocks

EBURNEAN OROGENIC DOMAIN
Paleoproterozoic terrains (2.4-1.6 Ga)

- Granitoid rocks
- Tarkwaian sedimentary rocks
- Birimian sedimentary rocks
- Birimian volcanic rocks

- Lode gold deposit
- Paleoplacer gold deposit
- Town
- River
- Country boundary
- Fault certain, presumed
- Strike-slipe fault with diriction of mouvement
- Thrust fault

Sample locality (dating)

- U-Pb zircon
- Pb-Pb galena
- Rb-Sr whole rock and Rb-Sr biotite

Figure 5. Simplified geological map of southeast Côte d'Ivoire and southwest Ghana (modified after Milési *et al.*, 1989). See Table 2 for age data.

A rhyolite flow from the Sefwi volcanic belt yielded a U-Pb zircon age of 2166 ± 2 Ma in the Afema district (Hirdes *et al.*, 2007), and 2189 ± 1 Ma in neighboring Ghana (Hirdes and Davis, 1998). The Sefwi volcanic belt was therefore interpreted as a tectonically stacked sequence of several volcanic chains which formed between 2189 Ma and 2166 Ma. The U-Pb zircon age of discordant granitoid intrusions gave 2163 ± 1 Ma in the Afema district and 2179 ± 2 Ma in Ghana (Hirdes *et al.*, 1992).

Table 2. Age data for southeast Côte d'Ivoire and southwest Ghana. Location of the samples is shown on Figure 5.

Sample	Locality	Rock type	Age	Method	Reference
GB2324	Sunyani Basin (Côte d'Ivoire)	Concordant granitoid (Basin granitoid)	2081 ± 1 Ma	U-Pb zircon	Hirdes *et al.* (2007)
8909A	Sunyani Basin (Ghana)	Concordant granitoid (Basin granitoid)	2088 ± 1 Ma	U-Pb zircon	Hirdes *et al.* (1992)
6898	Kumasi Basin (Ghana)	Concordant granitoid (Basin granitoid)	2116 ± 2 Ma	U-Pb zircon	Hirdes *et al.* (1992)
GB2293	Sefwi Belt (Côte d'Ivoire)	Discordant granitoid (Belt granitoid)	2162 ± 1 Ma	U-Pb zircon	Hirdes *et al.* (2007)
GL	Sefwi Belt (Côte d'Ivoire)	Discordant granitoid (Belt granitoid)	2220 ± 70 Ma	Pb-Pb galena	Delor *et al.* (1992)
WR	Sefwi Belt (Côte d'Ivoire)	Discordant granitoid (Belt granitoid)	2169 ± 38 Ma	Rb-Sr whole rock	Delor *et al.* (1992)
Bt	Sefwi Belt (Côte d'Ivoire)	Discordant granitoid (Belt granitoid)	1869 ± 32 Ma	Rb-Sr biotite	Delor *et al.* (1992)
6668	Sefwi Belt (Ghana)	Discordant granitoid	2179 ± 2 Ma	U-Pb zircon	Hirdes *et al.* (1992)
GB1290	Sefwi Belt (Côte d'Ivoire)	Rhyolite	2166 ± 2 Ma	U-Pb zircon	Hirdes *et al.* (2007)
GB1168	Sefwi Belt (Côte d'Ivoire)	Andesitic volcaniclastic rock	2180 ± 2 Ma	U-Pb zircon	Hirdes *et al.* (2007)
H285	Sefwi Belt (Ghana)	Rhyolite	2189 ± 1 Ma	U-Pb zircon	Hirdes and Davis (1998)
GB0027	Kumasi Basin (Côte d'Ivoire)	Basal conglomerate	2156 ± 1 Ma	U-Pb zircon	Hirdes *et al.* (2007)

The U-Pb ages obtained from zircon grains of the Kumasi basin range from ca. 2190 Ma to 2129 Ma (Hirdes *et al.*, 2007). Based on these radiometric data, Hirdes *et al.* (2007) argue that the granitoid intrusions were coeval to the volcanic rocks of the Sefwi belt. Furthermore, they suggest that the volcanic rocks of the Sefwi belt and the adjacent Kumasi basin sediments represent at least partly contemporaneous lateral facies equivalents, with sedimentation

outlasting volcanism (by up to 37 Ma). Thus, the Kumasi basin sediments are considered to probably be derived from the Sefwi volcano-plutonic belt.

The supracrustal sequence was folded and metamorphosed under greenschist facies conditions. However, higher metamorphic grades of upper greenschist to amphibolite facies have been reported to the northwest of the Sefwi belt (Delor *et al.*, 1992; Hirdes *et al.*, 2007).

The contact between the metavolcanic assemblage (Sefwi belt) and the metasedimentary assemblage (Kumasi basin) is made by a tectonic corridor, commonly called “Afema shear-zone”, or “Afema tectonic zone” (Tourigny, 1998), or “Afema high-strain zone” (Hirdes *et al.*, 2007). The Afema gold mines (all are open pits) are located in this zone (Figures 6 and 7). The Afema tectonic zone (ATZ) is a major fault zone 700 m to 3 km wide and several tens of kilometers long from the Afema district up to Ghana. This major structure strikes NNE and dips approximately 70-80° to the SE, and it shows steeply plunging folds, crenulation cleavage, S/C textures, tension gashes, boudinage quartz veins, as well as cataclasites and mylonites (Figure 8).

The structural analysis of the study area (formerly mining concession) is mainly based on the unpublished work of Tourigny (1998). Because of the scarcity of outcrops caused by deep weathering, the general geology of the study area was largely elucidated by data from drill cores made by the ex mining company Somiaf. These data were supplemented by the cartography of some rare outcrops and exposures in the open cast mines. The structural measurements are almost completely from the different open pit mines.

According to their stratigraphic and structural characteristics, the volcano-sedimentary assemblages of the study area can be subdivided in three parallel lithotectonic domains, e.g. Northwest domain, Central domain, and Southeast domain (Figure 7).

The NW domain represents the footwall of the ATZ. It is little deformed, monoclinal and facing toward the southeast. The rocks of this domain mainly consist of intermediate to basic lavas with interlayering of sills of gabbro (± diorite) and some rare horizons of acid volcanic rocks. These lithologies have a general strike direction of NE-SW and dip more than 70° SE.

The Central domain is represented by a zone of intense ductile deformation with approximately 100 m to more than 500 m width. It is separated from the NW and SE domains by two large inverse shear zones. This domain is mainly composed of sedimentary rock sequences represented by polymictic metaconglomerates and metaarenite (in places conglomeratic). The latter constitutes the principal host rock of the Aniuri and Jonction gold deposits. The principal structural characteristic of the Central domain corresponds to an intense mylonitic foliation whose general attitude is 030-035° with a steep dip towards SE or NW.

The SE domain is contiguous with the Central domain along an important inverse shear zone. This domain consists of metagraywacke interstratified with more or less graphitic metaargillite. In the SE domain, the primary structures observed are normal grading, parallel laminations and seldom oblique laminations.

In the Afema Tectonic Zone, the volcano-sedimentary rocks that host the gold mineralization exhibit discrete strain features resulting from three generations of structures (e.g. D_1, D_2 and D_3) that affected the stratification S_0 (Figure 7). The S_0 planes have a very variable attitude. In the area of the Jonction mine for instance, S_0 is subparallel to S_2 schistosty and presents a general NNE-SSW strike with steep dips towards the NW or the SE. The D_1 deformation is essentially represented by NW-SE folds observed in the metagraywacke and metaargillite. However, the structural elements assigned to this deformation phase are rarely identifiable in the field. They are almost entirely obliterated by the intensity of the D_2 deformation.

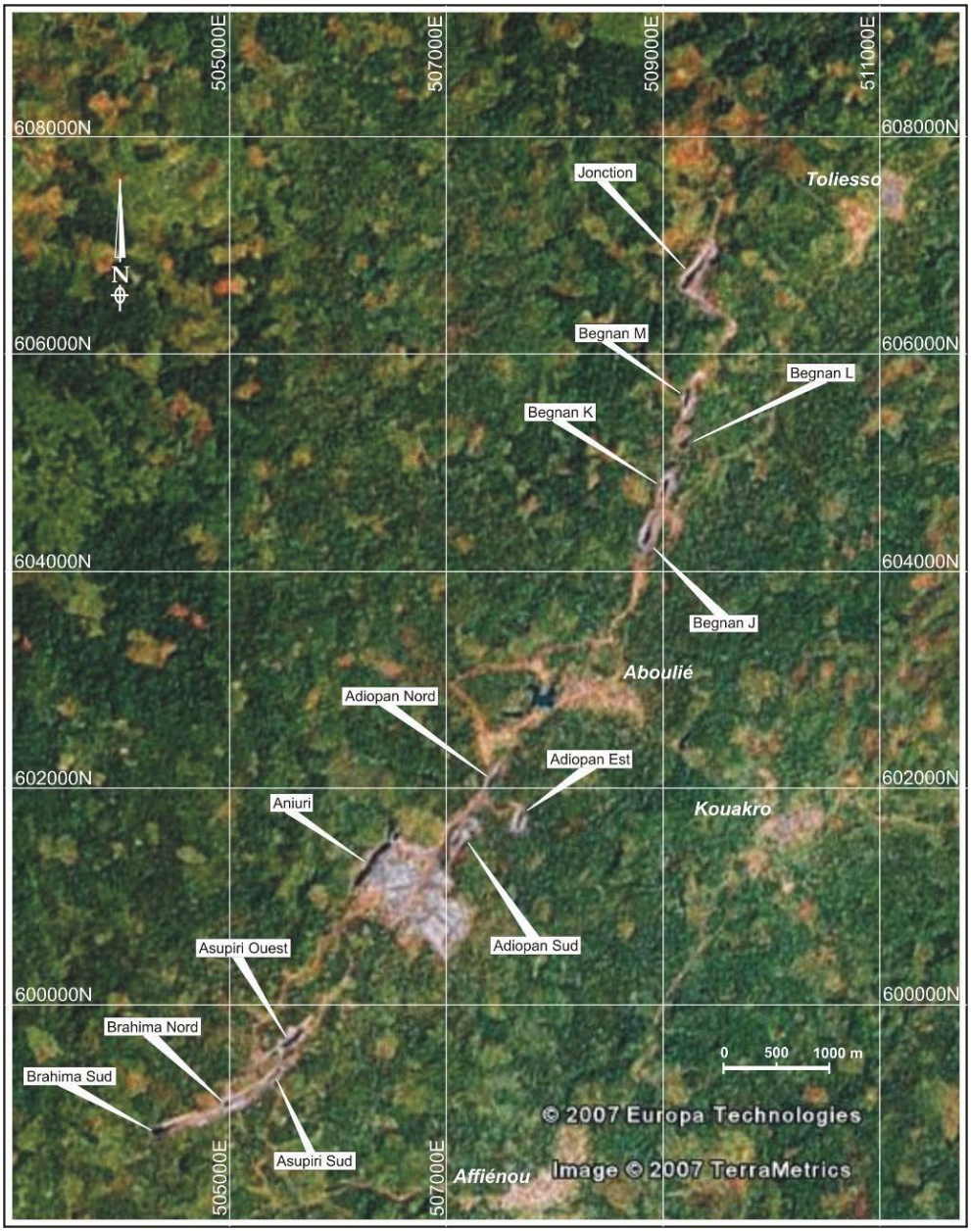

Figure 6. The Afema gold trend as outlined by a series of now abandoned open pits (image from Google Earth, 2007).

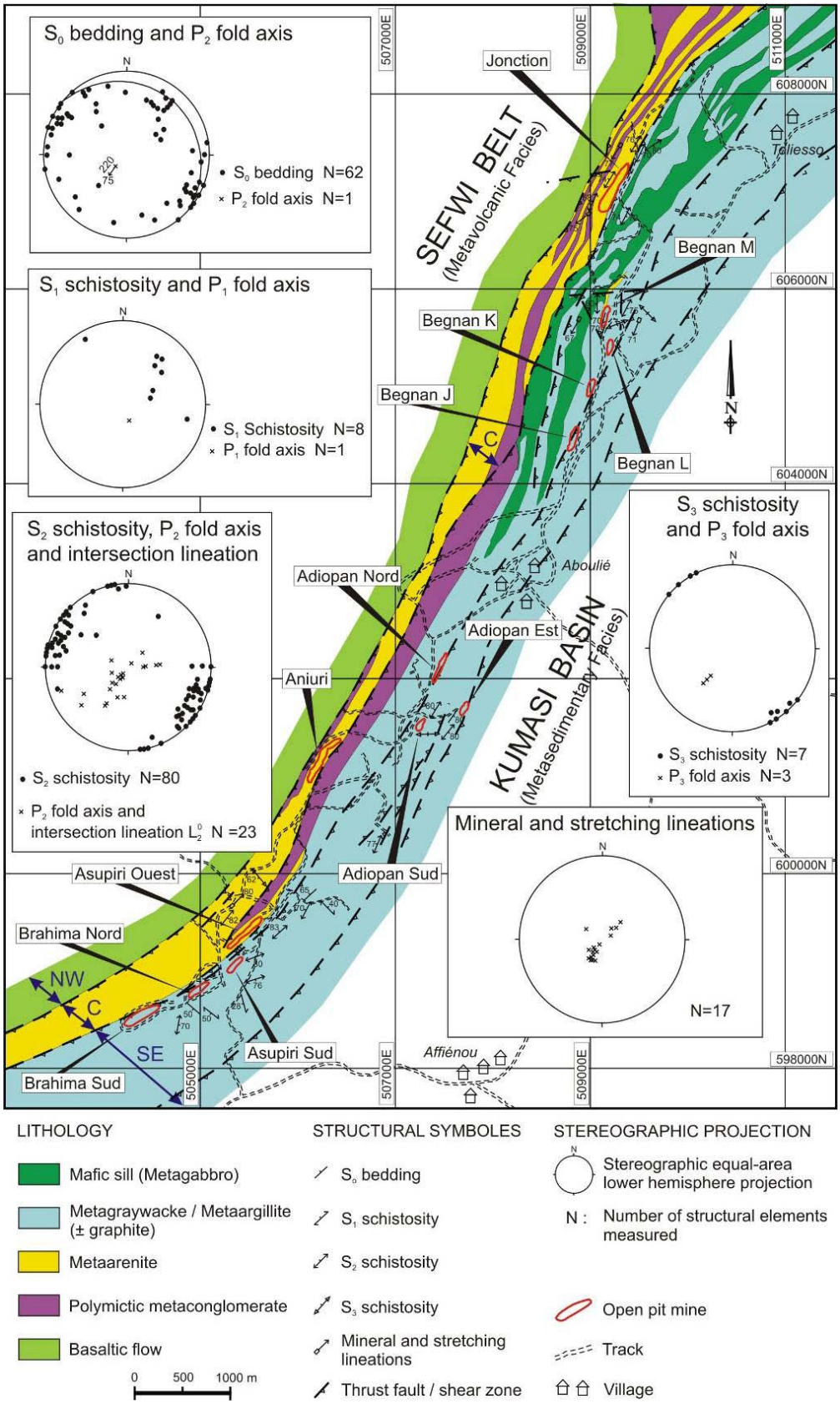

Figure 7. Structural geology of the Afema tectonic zone (modified after Tourigny, 1998). This area corresponds to that of Figure 6. SE: Southeast domain; C: Central domain; NW: Northwest domain.

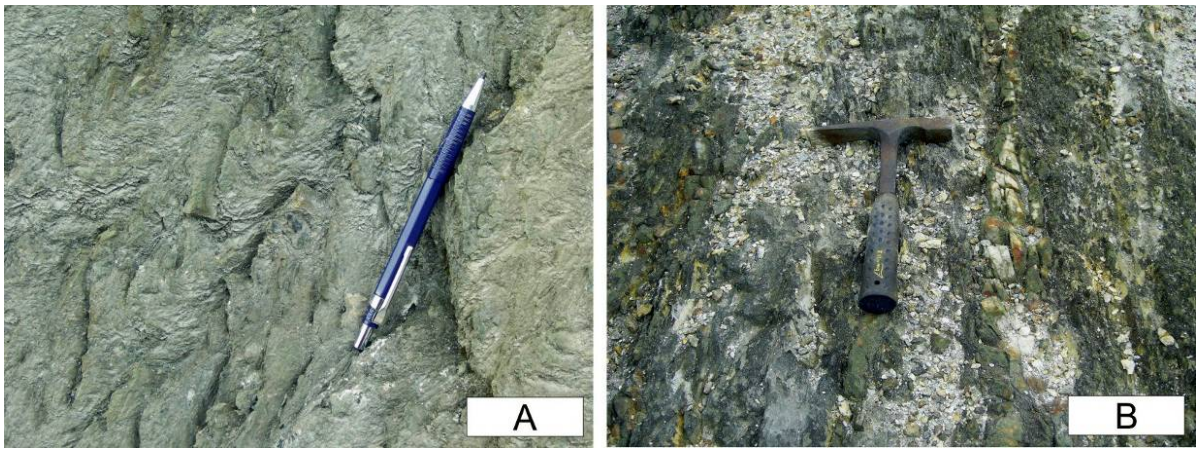

Figure 8. Photographs of high-strain structures observed near the "Brahima Nord" pit. A) S/C structure in a metasedimentary rock; B) Boudinaged and sheared quartz veins wrapped by mylonitic foliation (S_2).

D_2 represents the bulk of the penetrative strain and is characterized by a steeply inclined NNE-trending S_2 foliation, tight to isoclinal F_2 folds as well as a complex network of gold-bearing shear zones. The S_2 foliation contains well-developed mineral and stretching lineations plunging steeply southwestward. D_3 structures have produced an ENE striking extensional crenulation and minor asymmetric sinistral folds developed in the most anisotropic rocks of the shear zones. The D_3 mesoscopic structures distorted earlier-formed structures to a minor extent and have no geometrical controls on the location and internal morphology of the ore zones.

Hirdes *et al.* (2007) described four generations of deformation in the northwest of the study area, i.e. in the Aboisso North area. Their first two generations of deformation (D_1 and D_2) correspond roughly to those defined by Tourigny (1998). They described also a D_3 deformation phase, but that phase is represented by NW-, NE- and rarely E-trending transcurrent faulting expressed as crenulation cleavage or jointing/fracturing (S/C). The last phase D_4 reactivated all above planar structures and is mainly expressed as slickensides or as striae on the latest quartz veins.

2. SAMPLING AND ANALYTICAL METHODS

2-1. Field sampling, petrographic and metallographic studies

The quasi totality of rock samples collected was limited to drill cores from deep level in order to avoid the effects of tropical weathering. Only a few were samples taken from rock exposures in the open pits and from outcrops. For petrographic and metallographic studies, thin sections and polished sections prepared at the Technical University of Clausthal were examined using a Zeiss metallographic microscope.

2-2. Whole rock geochemical analysis

Major elements and some trace elements (e.g. Ba, Bi, Cr, Cu, Ga, Mo, Nb, Ni, Pb, Rb, Sn, Sr, V, Zn, Zr, and Y) were analyzed by X-ray fluorescence spectrometry on lithium metaborate fused disks at BGR (Bundesanstalt für Geowissenschaften und Rohstoffe) in Germany. Other trace elements (e.g. As, Au, Br, Co, Cs, Hf, Hg, Ir, Sb, Sc, Se, Ta, Th, U, W, La, Ce, Nd, Sm, Eu, Tb, Yb, and Lu) were measured by INAA (Instrumental Neutron Activation Analysis) at Actlabs Activation Laboratories Ltd in Canada. A few data are included from previous work performed on the study area (Assie, 1998). For these additional data, both major and trace elements were analyzed by ICP (Inductively Coupled Plasma); major element analysis was after digested by lithium borate fusion, whereas the trace elements (e.g. As, Cd, Co, Cr, Cu, Li, Nb, Ni, Pb, Te, Zn, and La) were analyzed after Aqua Regia digestion ($HCl:HNO_3$). In a few samples Nb, Rb, Zr and Y were measured by X-ray fluorescence on pressed pellets. All these older analyses were conducted at ITS (Intertek Testing Services) in Canada. Gold from the additional data was however analyzed by fire-assay at Somiaf (Société des Mines d'Aféma) analytical laboratories. All data are summarized in APPENDICES 1 and 2.

2-3. Electron microprobe analysis

The chemical composition of selected sulfides, silicates (particularly muscovite and chlorite), carbonate, and gold of about forty polished sections from the Aniuri and Jonction deposits were determined with a CAMECA SX100 electron microprobe at the Technical University of Clausthal.

Sulfides and gold analyses were performed first, with 20 kV accelerating voltage, 100 nA beam current, and usually 1 µm beam diameter. The standards used were: $CuFeS_2$ for S K_α, Cu K_α and Fe K_α; ZnS for Zn K_α; PbS for Pb L_β; GaAs for As L_α; Sb for Sb L_α; Ag for Ag L_α; Au for Au L_α; Ni for Ni K_α, and Co for Co K_α. The detection limits (in wt.%) were approximately: 0.02 for Ni; 0.03 for S, Co and As; 0.04 for Fe and Sb; 0.05 for Ag and Cu; 0.06 for Zn and Au; 0.4 for Pb. This setting was thereafter changed to 30 kV for accelerating voltage, 300 nA for current beam, 10 µm for beam diameter, and 600 seconds as peak counting time for Au (against 36 seconds in the first setting) in order to decrease the detection limit of gold in sulfides to about 40 ppm Au. In this later case, some standards have been changed: FeS_2 for S K_α and Fe K_α; InAs for As L_α.

Carbonate, mica and chlorite analysis settings were characterized by 15 kV accelerating voltage, 20 nA beam current, and 5-10 µm beam diameter. Standards used for carbonate analysis were: kaersutite for Na K_α, K K_α, Ti K_α and Fe K_α; K-feldspar for Al K_α and Ba L_α; dolomite for Ca K_α, pyrope for Mg K_α, almandine for Mn K_α; and $SrSO_4$ for Sr L_α. Standards for chlorite analysis were: kaersutite for Na K_α, Al K_α, K K_α, Ca K_α, and Ti K_α; pyrope for Mg K_α, Fe K_α, and Si K_α; almandine for Mn K_α; Cr_2O_3 for Cr K_α. In the case of mica, the standards were: kaersutite for Na K_α, Mg K_α, Al K_α, Ca K_α, Ti K_α, Fe K_α, and Si K_α; K-feldspar for K K_α; and almandine for Mn K_α.

2.4. Laser ablation - inductively coupled plasma - mass spectrometry

In addition to electron microprobe analysis, the content of Au in pyrite and in arsenopyrite was measured by laser ablation – inductively coupled plasma – mass spectrometry (LA-ICP-MS) at the University of Würzburg, Germany (analyst: Helen Bätz). This later investigation was performed with a single collector quadrupole AGILENT 7500i ICP-MS equipped with a 266 nm Merchantek LUV 266x laser. Argon was used as carrier gas. The reference material Po724 B2 SRM (Sulfide standard, Memorial University Newfoundland) was used for external calibration, and on line data reduction was done by GLITTER Version 3.0 for LA-ICP-MS by Macquarie Research Ltd (2000). The laser beam was fired at 10 Hz repetition rate with energy ranging from 0.15 to 0.28 mJ/pulse. The error for a single measurement was with 1σ = <10%. The spot size was 30 μm, and the acquisition time for S and Au was respectively 10 ms and 50 ms. The detection limit for gold was 0.01 – 0.02 ppm. Cu, As, Te and Bi were measured as relative concentrations in counts, as there is no standard available for these elements.

2-5. Isotope geochemistry

2-5-1. Rb-Sr and Sm-Nd isotope analysis

Rb-Sr and Sm-Nd isotope analyses were done at the Institute of Precambrian Geology and Geochronology, St Petersturg, Russia (analyst: Boris Belyatsky). The measurements were performed on a Finnigan MAT-261 mass spectrometer equipped with eight collectors under static mode. The $^{143}Nd/^{144}Nd$ ratio was normalized within-run to $^{148}Nd/^{144}Nd$ = 0.241570 and adjusted to a $^{143}Nd/^{144}Nd$ value of 0.511680 for La Jolla. Repeat measurements of $^{143}Nd/^{144}Nd$ ratio of the La Jolla standard varied from 0.511875 to 0.511912 with a mean value of 0.511894 ± 10 (n = 57). Sr isotope composition was normalized within-run to $^{88}Sr/^{86}Sr$ = 8.37521. The value of Sr isotope standard SRM-987 during this work was $^{87}Sr/^{86}Sr$ = 0.710248 ± 15 (2σ, 16 runs).

Assigned errors (2σ) for $^{147}Sm/^{144}Nd$ and $^{143}Nd/^{144}Nd$ were ± 0.3 and ± 0.000015%, $^{87}Rb/^{86}Sr$ ± 0.5, $^{87}Sr/^{86}Sr$ ± 0.000025% according to results of multiple standard analyses (external reproducibility). The 2σ errors cited in Table 9 for $^{143}Nd/^{144}Nd$ and $^{87}Sr/^{86}Sr$ reflect in-run precision. The blank level was 0.01 ng for Sm and 0.5 ng for Nd, 0.05 ng for Rb and 0.2 for Sr. The data obtained for the BCR-1 standard are: [Sr] = 335.8 ppm, [Rb] = 47.16 ppm, [Sm] = 6.487 ppm, [Nd] = 28.45 ppm, $^{87}Sr/^{86}Sr$ = 0.705053 ± 11, $^{87}Rb/^{86}Sr$ = 0.40615, $^{143}Nd/^{144}Nd$ = 0.512663 ± 9, $^{147}Sm/^{144}Nd$ = 0.13829.

2-5-2. Ar-Ar isotope analysis of muscovite

The $^{40}Ar/^{39}Ar$ analysis was conducted at the School of Earth, Atmospheric and Environmental Sciences of the University of Manchester, United Kingdom (analyst: Ray Burgess).

The $^{40}Ar/^{39}Ar$ geochronological technique is a variant of the conventional K-Ar geochronology, which is based on the decay of ^{40}K to ^{40}Ar. The Ar-Ar method, however, is based on the formation of ^{39}Ar by irradiation of potassium-bearing samples in a nuclear reactor. The sample to be dated and a standard of known age are irradiated together to produce ^{39}Ar from ^{39}K by fast-neutron bombardment. During irradiation of K-bearing samples with neutrons in the nuclear reactor, isotopes of argon are formed by several reactions involving potassium, calcium, and chlorine (Faure, 1986). There are interferences of other elements (e.g. Ca and Cl), and a series of corrections must be made.

As far as we are concerned, Ar-Ar analysis was performed on two muscovite samples, which were cleaned in acetone followed by deionized water in an ultrasonic bath and then dried using an infra-red heating lamp. Samples were weighed, wrapped in Al foil and sealed in quartz ampoules together with the flux monitor Hb3gr (t = 1073.6 +/- 5.3 Ma; Jourdan and Renne, 2007). Neutron irradiation was carried out in position B2W of the SAFARI-1 reactor at Pelindaba in South Africa. Error-weighted average irradiation parameters (J, α,

and β) were determined from Hb3gr and are defined and listed in Table 10 (see section 3-5-2). Argon was extracted from the samples using a Ta resistance furnace over the temperature interval 400-1400°C using heating steps of 30 minutes duration. The Ar was purified using a SEAES NP10 getter at 250°C and transferred to the custom-built MS1 mass spectrometer for isotopic analysis. The MS1 is a 90° sector noble gas mass spectrometer with a Baur-Signer source and Faraday detector. Blank levels determined at three temperatures during the course of the experiments, in units of 10^{-15} moles ^{40}Ar, were: 22 ± 4 (600°C); 40 ± 9 (1000°C) and 97 ± 19 (1400°C). All blanks had an approximately atmospheric Ar isotope composition. Raw data were corrected for mass discrimination (calibrated using atmospheric argon), radioactive decay and neutron interference corrections. The latter were determined from pure CaF_2 and K_2SO_4 salts included in the ampoule with the following values: $(^{40}Ar/^{39}Ar)K$ = 0.044 ± 0.023; $(^{38}Ar/^{39}Ar)K$ = 0.01243 ± 0.00002; $(^{39}Ar/^{37}Ar)Ca$ = 0.000745 ± 0.000003; and $^{36}Ar/^{37}Ar)Ca$ = 0.000269 ± 0.000007. Irradiation parameters and Ar-Ar stepped heating data are given in Table 10. All ages are reported at the 2σ level of uncertainty. More details on the analytical technique of the Ar-Ar method can be found in standard texts, e.g. Faure (1986), Dickin (1997).

2-5-3. Re-Os isotope analysis

Re-Os isotope analysis was conducted at the National Research Center of Geoanalysis, a service of the Chinese Academy of Geological Sciences. The separation of pyrite and arsenopyrite from rock samples was performed by this laboratory in China (analyst: Andao Du). The enriched ^{190}Os and enriched ^{185}Re were however obtained from Oak Ridge National Laboratory (USA). The small size and the very close association of arsenopyrite and pyrite did not permit the separation of these sulfides. Consequently, pyrite and arsenopyrite were concentrated and analyzed together. The detailed methodology used for the Re-Os analysis of pyrite and arsenopyrite is summarized in Du *et al.* (2004). In brief, a Carius tube (a thick-walled borosilicate glass ampoule)

digestion was used for sample preparation. The weighed sample is loaded in a Carius tube through a long thin-necked funnel. The mixed ^{190}Os and ^{185}Re spike solutions, 5 ml of 10 M HCl, 15 ml of 15 M HNO_3 and 3 ml 30% H_2O_2 were loaded while the bottom part of the tube was frozen at -50°C to -80°C in ethanol-liquid nitrogen slush. The top was sealed using an oxygen-propane torch. The tube was then placed in a stainless-steel jacket and heated for 24 h at 200°C. After cooling, the bottom part of the tube was again frozen and the neck of the tube was broken. The contents of the tube were poured into a distillation flask and the residue washed out with 40 ml of water. The OsO_4 was distilled at 105 to 110°C for 50 min and was trapped in 5 ml of water that was used for ICP-MS (TJA X-series) determination of the Os isotope ratio. The residual Re-bearing solution was saved in 50 ml beaker for Re separation. The Re-bearing solution was evaporated to dryness; 1 ml of water was added and the sample was heated to near-dryness twice. 10 ml of 25% NaOH were added to the residue followed by Re extraction with 10 ml of acetone in a 120 ml Teflon separation funnel. The water phase was then discarded and the acetone phase washed with 2 ml of 20% NaOH. The acetone phase was transferred to 100 ml beaker that contained 2 ml of water. After evaporation to dryness, the Re was picked up in 2% HNO_3 that was used for the ICP-MS determination of the Re isotope ratio. The average blanks for the total procedure were ca. 15 pg Re and ca. 0.1 pg Os.

The evaluation of Rb-Sr, Sm-Nd and Re-Os data was done using the Isoplot/Ex program (Ludwig, 2001).

2-6. Fluid inclusion microthermometry

The fluid inclusion study was conducted on doubly polished thick (~220 μm) sections of quartz. Microthermometric measurements were performed at the Technical University of Clausthal using a Linkam THMS 600 heating-freezing stage with an operation range from -196°C to +600°C. This stage was fitted to a petrographic Zeiss microscope and the temperature was controlled with the

Linksys software. Freezing and heating experiments were conducted on the same inclusions in order to be able to correlate final melting and homogenization temperatures (T_h). During the freezing experiments, inclusions were cooled to -150°C and then slowly heated up.

3. RESULTS AND INTERPRETATIONS

The Afema district contains about fifteen “small” gold deposits mined with the open-cast mining method and heap leaching. The different gold mines of the Afema district are shown on Figures 6 and 7. The present study focuses on the Aniuri and Jonction mines (Figure 9). This choice is supported by two main motivations: first, Aniuri and Jonction have been the object of several deep drillings (which allows sampling bellow the thick weathered horizon), and, secondly, we were personally implied in the realization of many of the drill holes of both deposits as exploration geologist from 1996 to 1998.

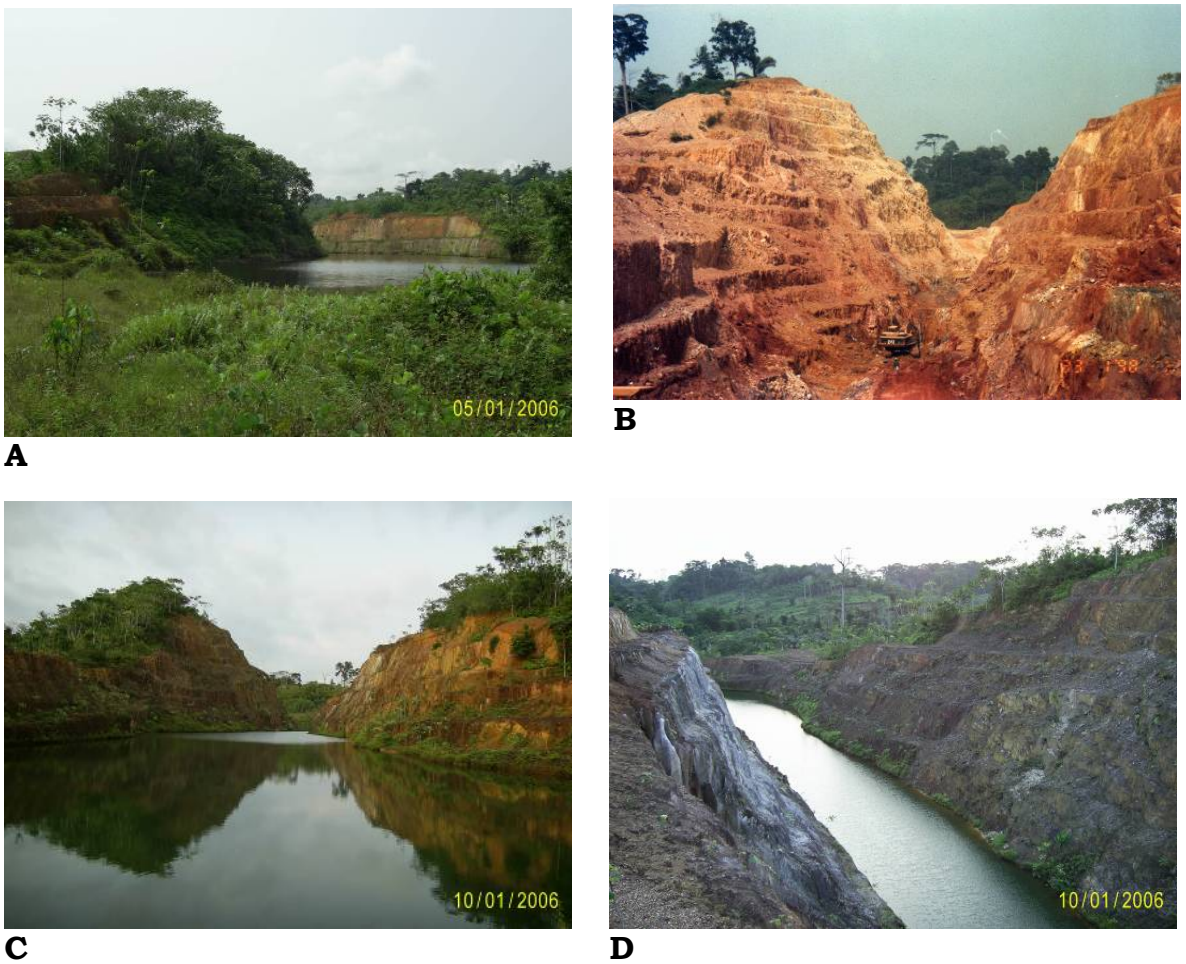

Figure 9. Overviews of Aniuri and Jonction mines. A) Aniuri mine, several years after the end of mining operations. B) Jonction mine, at the end of mining operations in 1998. C) and D) Jonction mine in 2006, eight years after its closure.

The Aniuri gold deposit is located 16 km to the east of the town of Maféré and at about 3 km to the southwest of the village of Aboulié (Figures 1, 6 and 7). This deposit was found in 1935 by the Major Lumb, who did not consider it as economic at that time (Sonnendrucker, 1967). However, in 1992, Aniuri became the first gold deposit mined by the ex company Somiaf, and that mining operation worked only the oxidized cover of the deposit.

The Jonction deposit is located about 2 km southwest from the village of Toliesso and 7 km in the northeastern prolongation from Aniuri (Figures 6 and 7). It has been discovered in 1997 by the company Somiaf, and its oxidized part has been mined for about one year. Jonction represents the last gold deposit mined by the ex company Somiaf in the Afema district.

3-1. Lithological and petrographical studies of Aniuri and Jonction deposits

The geological formations of the Afema district are NE trending, with a dip varying between the vertical position and about 60° toward the southeast. The thickness of the weathered horizon reaches several tenths of meters (up to 40 m at Aniuri and 70 m at Jonction). At Aniuri, the lithological sequence defined by drill core information is from southeast to northwest: coarse-pebble metaconglomerate, metaarenite, small-pebble metaconglomerate and metabasalt (Figure 10). At Jonction, however, the major lithology from southeast to northwest is characterized by an alternation of metagraywacke-metaargillite (generally graphitic) with interlayering sills of metagabbro, and metaarenite (Figure 11). Some outcrops of metabasalt occur to the northwest of the metaarenite. Gold mineralization occurs in metaarenite facies at Aniuri as well as at Jonction. The main regional schistosity (S_2) is subparallel to the bedding of the metasedimentary rocks.

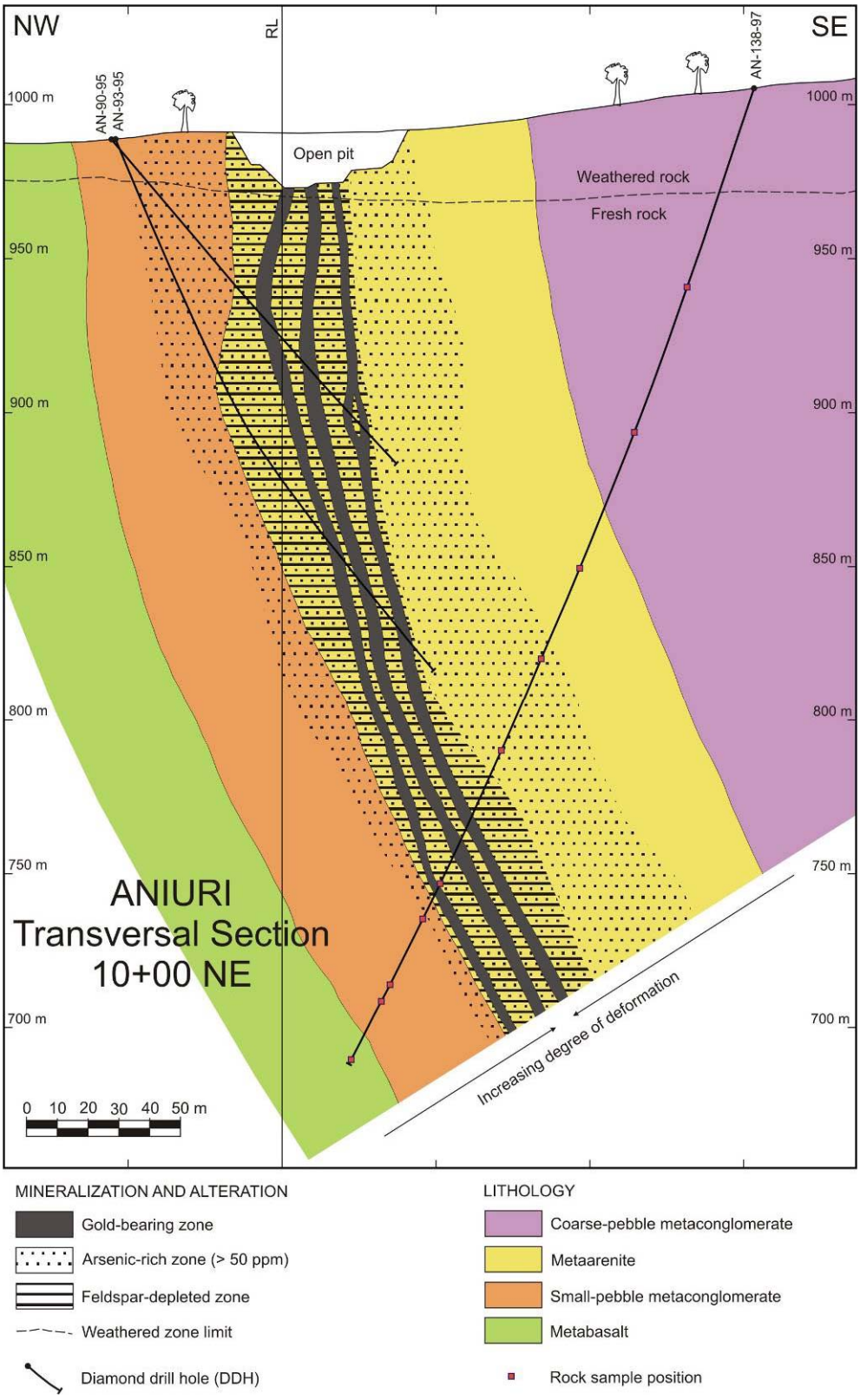

Figure 10. Representative transversal section of the Aniuri deposit showing geology, mineralization and alteration. The marked altitudes correspond to relative levels obtained by adding a constant to true values of altitude. RL: Reference Line

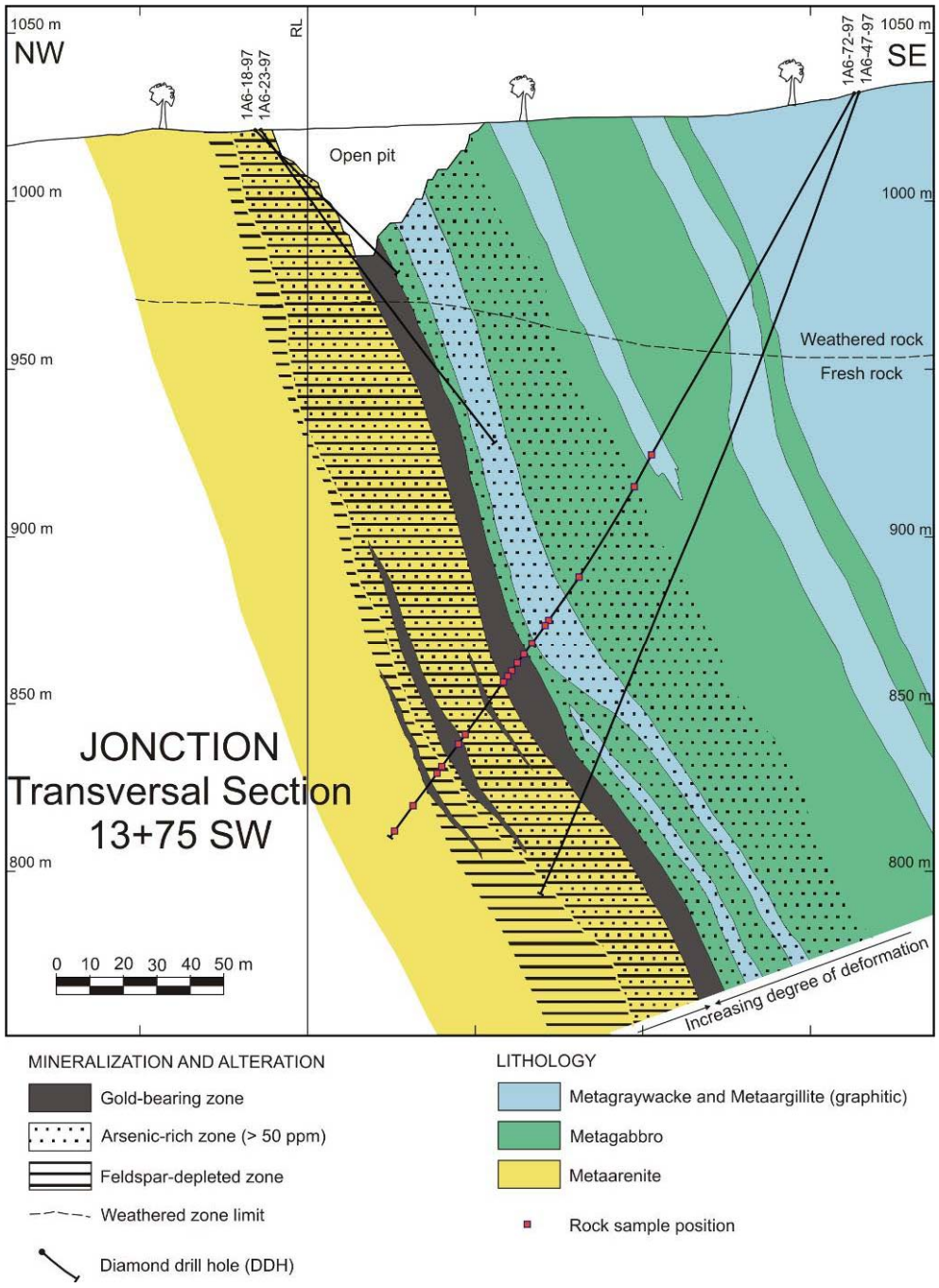

Figure 11. Representative transversal section of the Jonction deposit showing geology, mineralization and alteration. The marked altitudes correspond to relative levels obtained by adding a constant to true values of altitude. RL: Reference Line

The metamorphism which affected the study area is of greenschist facies type. This metamorphic imprint is marked by the development of chlorite, calcite, albite, sericite and epidote. The rocks of the study area have been regionally

deformed, to some degree cataclastically and partly by ductile deformation, producing undulose extinction and subgrains of some minerals like quartz.

The nomenclature here adopted for the sandstones (Figure 12) is based on the classification of Dott (1964) modified by Pettijohn *et al.* (1987). In that classification, sandstones are termed arenites, when they have less than 15 percent matrix (<30 microns), and wackes, with matrix proportion between 15 and 75 percent. For each group, some subdivisions are then applied on the grounds of various mineral and rock particles present.

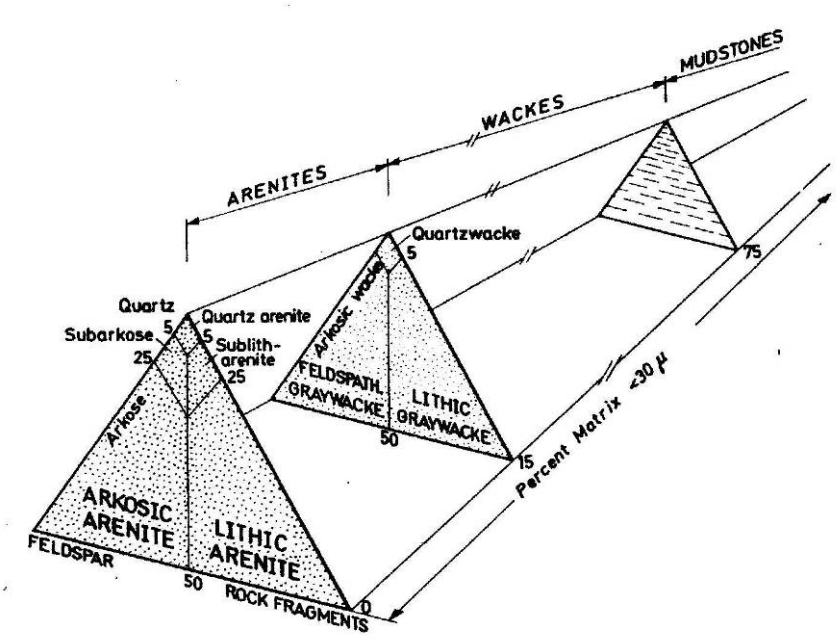

Figure 12. Classification of siliciclastic arenaceous sedimentary rocks (Dott, 1964; Pettijohn *et al.*, 1987).

** Metagraywacke / Metaargillite*

Metagraywacke and metaargillite constitute a sequence characterized by pronounced bedding expressed by an alternation of black (metaargilite) and grey levels (metagraywacke). This sequence represents the hanging wall of the Jonction deposit (Figure 13). The main regional schistosity is parallel to the stratification of the sequence. The various structural deformations are well preserved. In places, the rock is highly graphitic, and some coarse idiomorphic

pyrite crystals (up to 1 cm in size) can be observed along quartz-carbonate veinlets parallel to the schistosity.

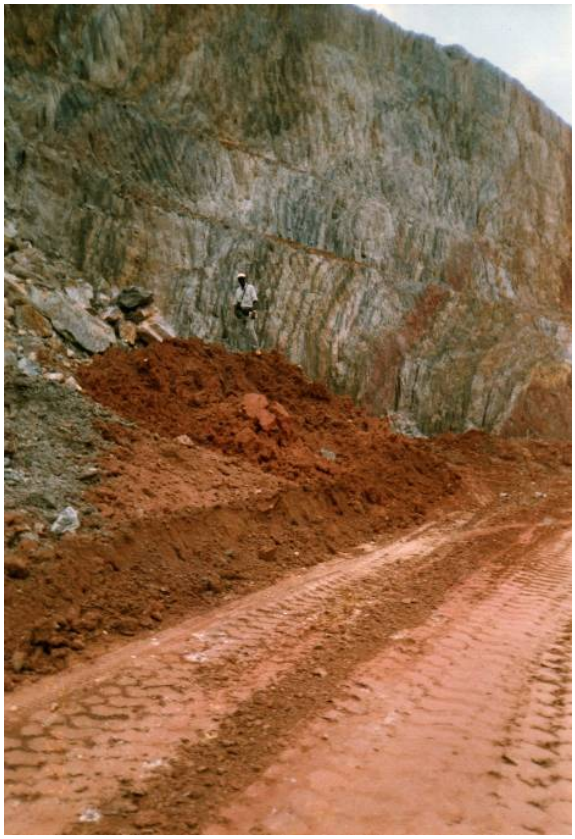

A

B – Sample 1A6-72-97/184.40m

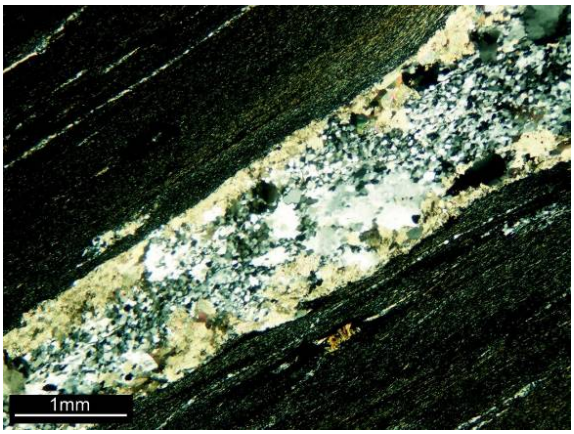

D – Sample 1A6-72-97/183.10m

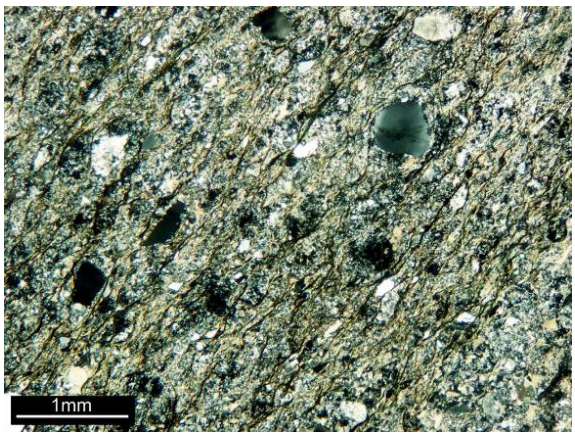

C – Sample 1A6-72-97/124.80m

Figure 13. Metagraywacke-metaargillite sequence of the Jonction deposit at mesoscopic, hand specimen and microscopic scales. A) Southeastern side of Jonction mine, consisting of metagraywacke-metargillite sequence and representing the hanging wall. B) Drill core of metagraywacke with carbonate grains made brown by oxidation. C) Metagraywacke consisting of quartz and feldspar clasts with a matrix made up of feldspar, quartz, chlorite, sericite, carbonate and graphite (transmitted light, crossed nicols). D) Metaargillite crossed by veinlets of quartz-carbonate (transmitted light, crossed nicols).

The metagraywacke is represented by poorly sorted sandstone, with a high proportion of matrix (more than 50%), which consists of feldspar, quartz, graphite (in places), chlorite, sericite and some clay minerals. The clasts are principally composed of feldspar with some quartz crystals. Carbonate is also present as secondary mineral and comes probably from the alteration of feldspar with which it is generally associated. It also fills fractures. The alignment of sheet minerals highlights the regional schistosity. The high content of feldspar minerals of this rock points to its immature character.

The metaargilite is represented by fine-grained rocks, with oriented texture. It is practically impossible to identify the rock-forming minerals, even at high magnification. This rock is generally crossed by several quartz-carbonate veinlets oriented parallel to the schistosity.

** Metaarenite*

The metaarenite shows several sub-facies according to its position relative to the mineralization zone (Figures 10, 11 and 14). The appearance of different varieties of this facies is mainly due to hydrothermal alteration which variably affected the rocks of the study area. At Jonction, for instance, in the ore zone, the metaarenite is sulfide-bearing, sericitic, dolomitic, silicified and in places graphitic. In the adjacent footwall of the ore zone occurs a chloritic metaarenite which changes to arkosic metaarenite at the northwestern extremity of the drilled zone. At Aniuri, the metaarenite presents the same character in the mineralization zone as that of Jonction. However, away from the ore zone it becomes feldspathic and chloritic. The different types of metaarenite are easily recognized from microscopic observations. These types of metaarenite are mainly, defined by the presence or absence of feldspar (Figure 15). The metaarenite, is in general, moderately well sorted and consists of a medium-grained fraction of quartz, feldspars (absent in inner and proximal ore zones) and some rare lithic fragments. The matrix is made up of fine-grained quartz and feldspar associated with sericite, chlorite and carbonate. Some rare crystals of apatite, tourmaline and zircon are observed. The cleavage is defined

by the preferred dimensional orientation of quartz and feldspar clasts, but mainly by the preferred orientation of sheet silicates (chlorite and sericite). The clasts show undulose extinction due to ductile deformation and are flattened in the plane of foliation.

A

B – Sample 1A6-67/134.80m

C – Sample 1A6-51-97/129.10m

D – Sample AN-122-96/av154.23m

Figure 14. Metaarenite at mesoscopic and hand specimen (drill core) scale. A) Northeastern side of Jonction mine, consisting of metaarenite and representing the footwall. B) Feldspar-depleted metaarenite from Jonction. C) Arkosic metaarenite from Jonction. D) Feldspar-depleted metaarenite from Aniuri.

As mentioned above, the metaarenite represents the host-rock of gold mineralization at both the Jonction and Aniuri deposits. The ore zones in metaarenite will be described in detail in a separate section.

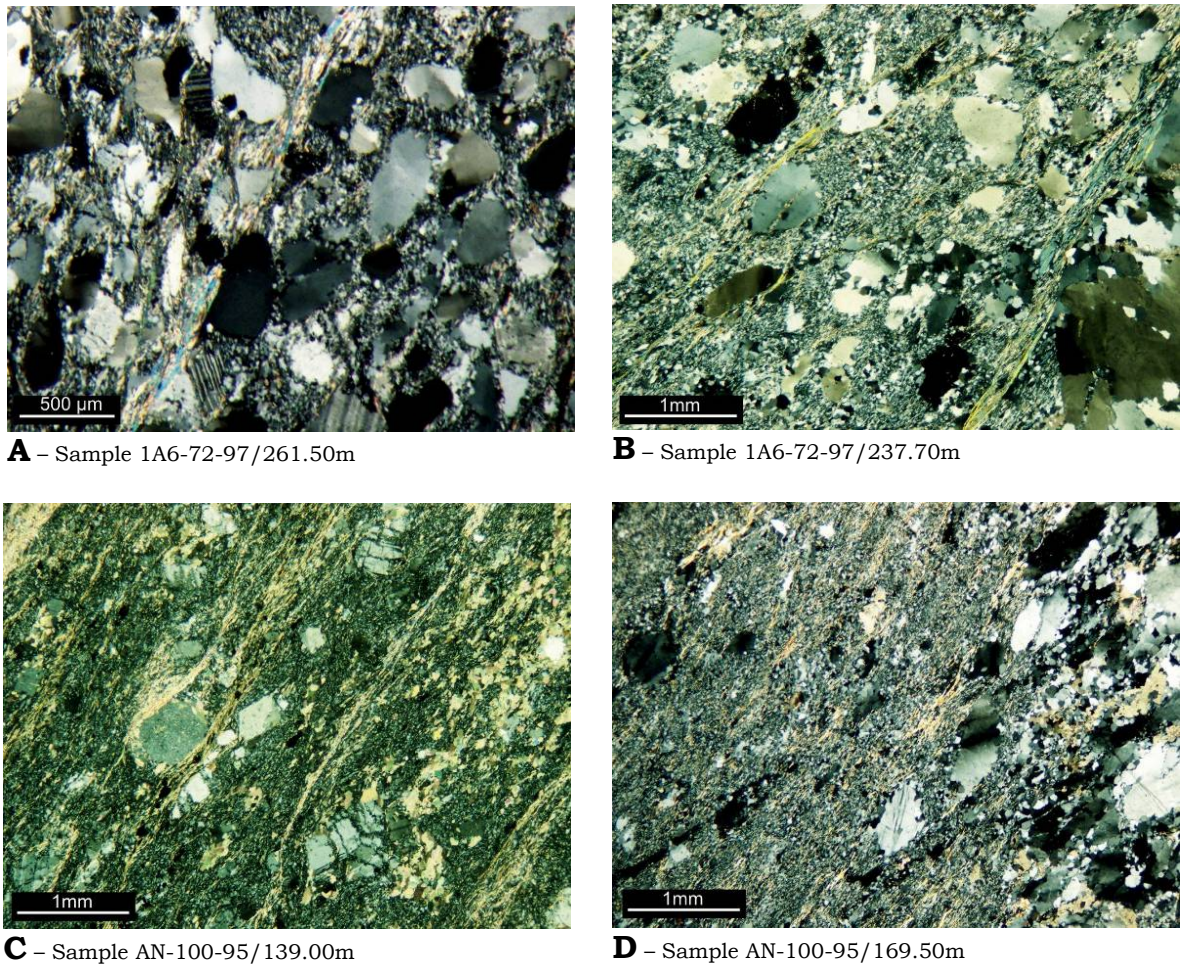

A – Sample 1A6-72-97/261.50m

B – Sample 1A6-72-97/237.70m

C – Sample AN-100-95/139.00m

D – Sample AN-100-95/169.50m

Figure 15. Microscopic view of various types of metaarenite (transmitted light, crossed nicols). A) Arkosic metaarenite from Jonction. B) Feldspar-depleted metaarenite from Jonction. C) Arkosic metaarenite from Aniuri deposit. D) Feldspar-depleted metaarenite from Aniuri. Note that in both cases, feldspar-depleted metaarenite was sampled proximal to the main mineralization zones, whereas arkosic metaarenite (e.g. feldspar-rich metaarenite) samples were taken distal to those zones.

** Metaconglomerate*

There are two types of metaconglomerate occurring at Aniuri (Figure 10). One is located in the hanging wall (SE of the mineralization zone), and the second in the footwall (NW of the mineralization zone).

The hanging-wall metaconglomerate is distinguished by its rounded and lenticular coarse pebbles (up to more than 5 cm in diameter) of different nature namely volcanic rocks, quartz, granitoids, etc., and large bands of chlorite (Figure 16). We term this type of polymictic metaconglomerate “coarse-pebble

metaconglomerate". This rock is in places crossed by carbonate (calcite) veinlets with irregular orientation. It is barren and shows a net contact with the metaarenite. The matrix consists of sandstone characterized by quartz and feldspar crystals, chlorite, sericite, epidote, carbonate, argillaceous minerals and iron or titanium oxides. The quartz crystals show undulose extinction. Chlorite is probably rich in magnesium considering its anomalous brown interference colors (Deer *et al.*, 1992). The pebbles and the fibrous minerals of the matrix are stretched by the deformation following the main regional schistosity direction.

A – Sample AN-124-96/av135.64m

B – Sample AN-146-97/78.10m

C – Sample AF-01.6_30

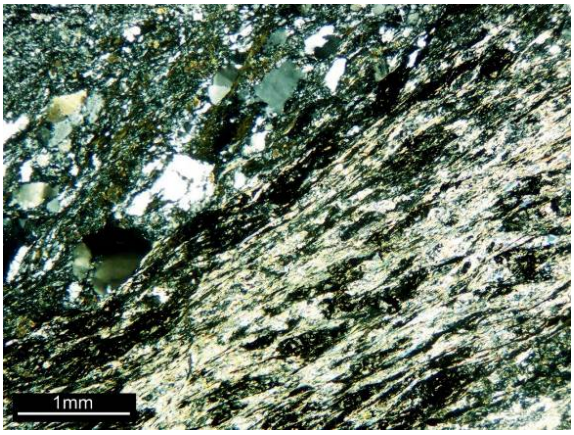

D – Sample AN-138-97/68.30m

Figure 16. Coarse-pebble metaconglomerate in the hanging wall of Aniuri. A) Quartz pebble and chlorite "bands". Note the centimeter size of this pebble. B) Sub-rounded pebble of granitoid (brown) and quartz. C) Lenticular pebble of volcanic rock (light green) oriented according to the direction defined by chloritic bands. D) Matrix made up of quartz crystals (with undulose extinction), feldspar, sericite, carbonate, Ti and Fe oxides, argillaceous minerals and chlorite with brown interference color (transmitted light, crossed nicols).

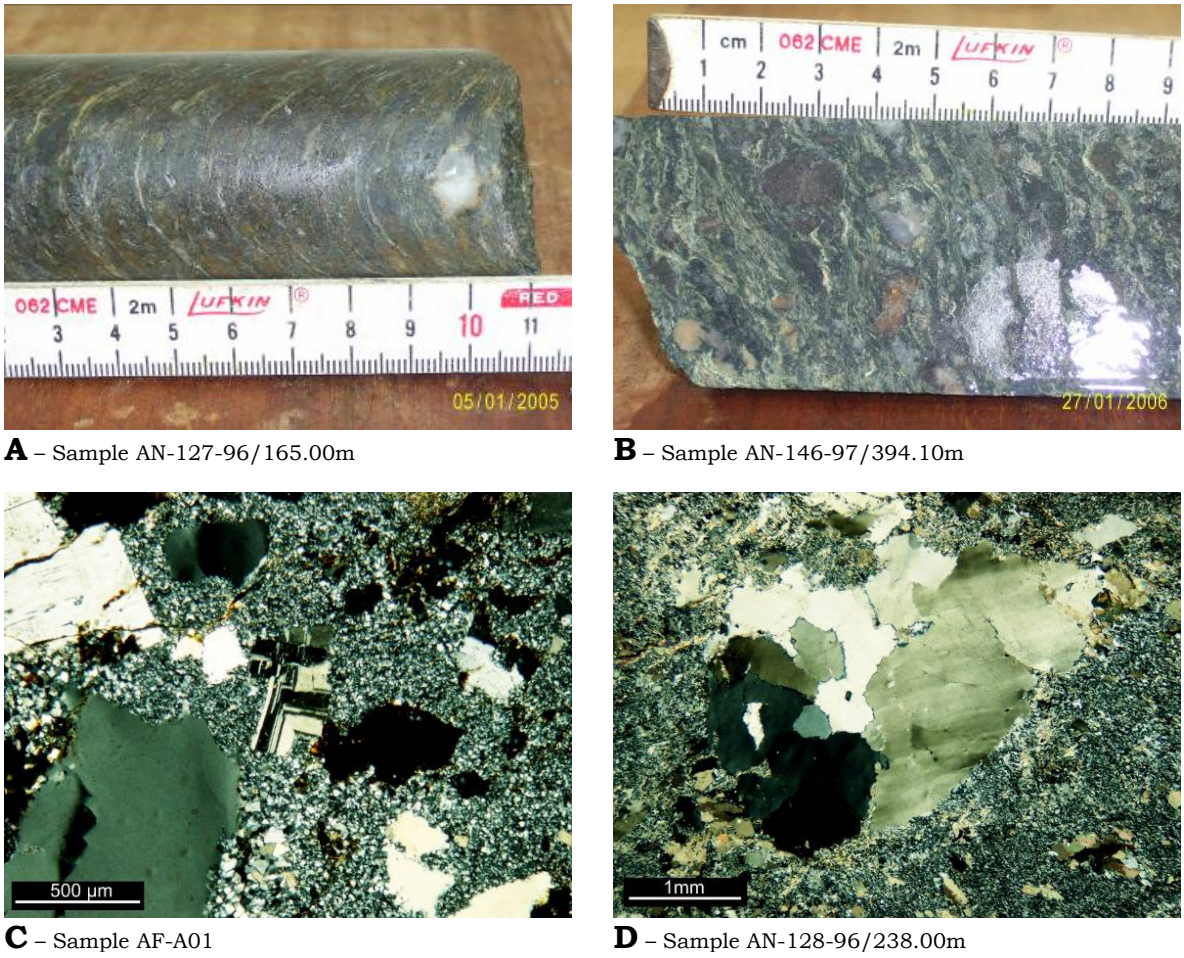

A – Sample AN-127-96/165.00m

B – Sample AN-146-97/394.10m

C – Sample AF-A01

D – Sample AN-128-96/238.00m

Figure 17. Small-pebble metaconglomerate in the footwall of Aniuri. A) and B) Quartz, chert pebbles showing smaller sizes compared to the previous case. C) Albite with "checkerboard texture", in the center of the image (transmitted light, crossed nicols). D) Polycrystalline quartz showing indented grain boundaries and undulose extinction (transmitted light, crossed nicols).

The footwall metaconglomerate is characterized by the small size of its pebbles which are much smaller than those of the hanging wall metaconglomerate (Figure 17). We therefore term this type of metaconglomerate as "small-pebble metaconglomerate". It shows a kind of polarity distinguished by an increase in size and in diversity of the pebbles from SE to NW, i.e. from the metaarenite contact toward the metabasalt (Figure 10). In fact, in the vicinity of the contact with the metaarenite, this rock is characterized by fragments mostly made up of quartz inferior to 1 cm in size. While moving away from the contact with the metaarenite, one notes a gradual appearance of other types of fragments (e.g. red chert, volcanic rocks, etc.) and an increase in their size which can reach 3 cm of diameter. The pebbles are generally lenticular and oriented according to

the direction of the main regional schistosity. The matrix of the small-pebble metaconglomerate consists of chlorite, sericite, quartz and feldspar. Carbonate crystals are disseminated in the whole rock with various sizes. The feldspar consists generally of secondary albite distinguished by its "checkerboard texture" (Figure 17C) as described by Thompson and Thompson (1996). The presence of some polycrystalline quartz pebbles with indented grain boundaries evokes their metamorphic origin (Figure 17D).

** Metagabbro*

Metagabbro occurs as sills in the metagraywacke-metaargilite sequence at Jonction. It presents two types of structures according to its thickness (from a few meters to several tens of meters). Samples taken in sills of reduced thickness or from the peripheries of the sills present an important schistosity and a small grain size, with no easily identifiable minerals with naked eye. But, samples taken in the central parts of thicker sills show a coarser texture and no visible signs of schistosity (Figure 18).

A – Sample 1A6-63-97/341.50m

B – Sample 1A6-63-97/78.50m

Figure 18. Drill cores of the metagabbro from Jonction. A) Fine-grained sample. B) Coarse-grained sample.

These observations suggest a chill phenomenon for the smaller-thickness sills and the peripheral parts of the higher-thickness sills due to rapid cooling. Due to metamorphism and particularly water-rock interaction (e.g. hydrothermal

alteration), the mineralogical identity of this rock of igneous origin is almost completely obliterated. The primary igneous mineral assemblage is largely destroyed by a pervasive chloritic and carbonate alteration. The rock consists of feldspar, chlorite, carbonate, quartz, leucoxene, tremolite (?), epidote (pistachite) and zoisite. Its intrusive character (granular structure) is only observed in the central parts of sills of relatively strong thickness (Figure 19).

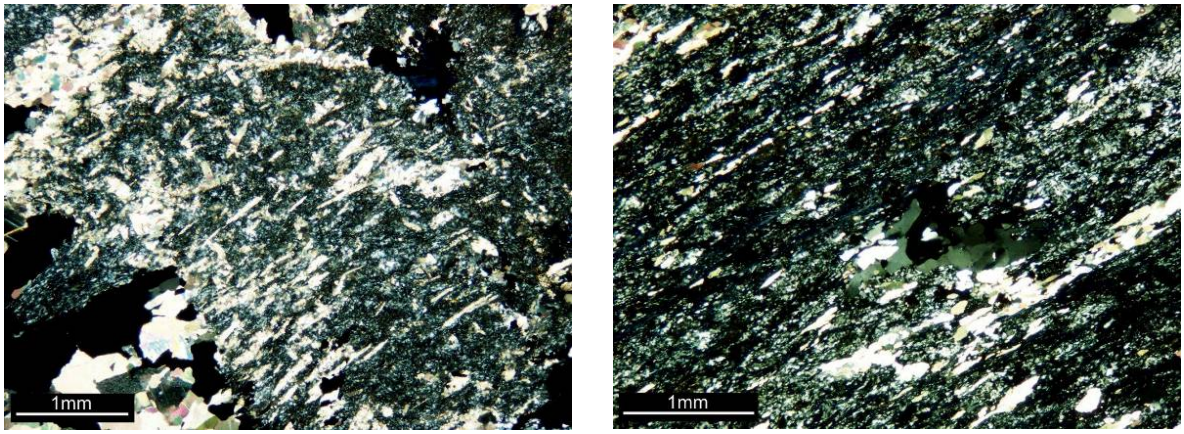

A – Sample 1A6-63-97/341.50m

B – Sample 1A6-72-97/165.95m

C – Sample 1A6-63-97/78.50m

D – Sample 1A6-74-98/105.10m

Figure 19. Microscopic view of the metagabbro from Jonction (transmitted light, crossed nicols). A) Fine-grained metagabbro showing plagioclase laths replaced by carbonate; chlorite is distinguished by its bluish abnormal interference color. B) Fine grained metagabbro with oriented texture and secondary quartz crystals; C) Coarse-grained metagabbro showing a granular structure and characterized by the presence of chlorite, carbonate and plagioclase. D) Coarse-grained metagabbro made up of feldspar, tremolite (high interference color), zoisite (blue granular aggregates) and leucoxene (brown).

** Metabasalt*

At Aniuri, this rock is located in the northwestern most part of the zone explored by drilling. Its contact with the "small-pebble metaconglomerate" is in places made by a transitional zone distinguished by the presence of rounded rock fragments in a volcanic matrix. The metabasalt is generally crossed by calcite (± quartz ± epidote) veinlets with non-preferential orientation (Figure 20A) and contains magnetite (in places). This rock consists mainly of chlorite, epidote, plagioclase and carbonate. This mineral assemblage is characteristic of propylitic alteration of mafic volcanic rocks. The structure is fine-grained with plagioclase phenocrysts (Figure 20B).

A – Sample AN-88-95/315m

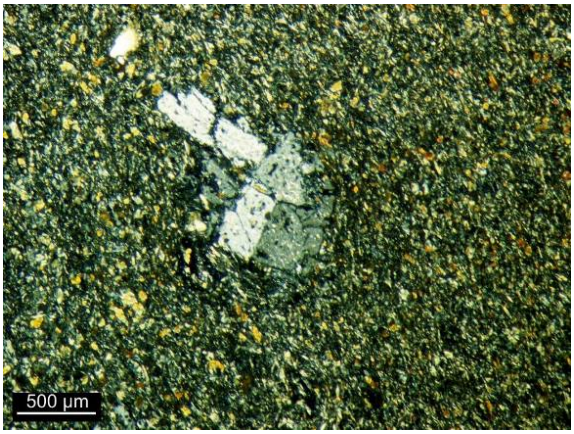

B – Sample AN-100-95/270.10m

Figure 20. Metabasalt of Aniuri. A) Drill core of metabasalt crossed by veinlets of calcite + quartz + epidote (green olive color). B) Thin section image of metabasalt showing a propylitic alteration. Phenocrysts of feldspar (plagioclase) in a groundmass made up of chlorite, epidote, feldspar and carbonate (transmitted light, crossed nicols).

At Jonction, the metabasalt was not reached by drill holes, but it is exposed to the northwest of the metaarenite facies. Except some rare silicified zones, this rock is barren.

3-2. Alteration

3-2-1. Alteration facies

Several major alteration facies are recognized according to the mineralization zones and the different rock types of the Aniuri and Jonction deposits. The alteration facies are defined by detailed petrographic studies at hand specimen and thin section scale. The different alteration facies are summarized in Table 3.

Table 3. Summary of alteration facies with mineralogical assemblages according to host rocks.

Alteration facies	Typical assemblage	Host rock
Sulfides-sericite-quartz-carbonate (Silicic, phyllic alteration)	Quartz veins + sericite + carbonate + sulfides ± free gold ± chlorite ± rutile-anatase ± graphite	Metaarenite (ore zones)
Chlorite-sericite-carbonate	Chlorite + sericite + carbonate + plagioclase ± rutile-anatase ± tourmaline ± epidote	- Metaarenite (out of ore zones) - Small-pebble metaconglomerate - Coarse-pebble metaconglomerate
Chlorite-epidote (Propylitic alteration)	Chlorite + epidote + plagioclase ± carbonate ± quartz (fine grained) ± magnetite	Metabasalt
Chlorite-carbonate	Chlorite + carbonate + feldspar ± leucoxene ± tremolite ± epidote ± zoisite ± quartz (fine grained)	Metagabbro
Chlorite-carbonate-sericite	Chlorite + carbonate + sericite + feldspar ± graphite ± tourmaline	Metagraywacke-metaargilite

Gold mineralization occurs principally in the metaarenite affected by sulfide-quartz-sericite-carbonate alteration. The metaarenite is originally composed of quartz and feldspar clasts. In the ore zones, however, one notes in addition the presence of quartz veins, dolomite-ankerite, sericite, sulfides (mainly pyrite and

arsenopyrite), and in places “free gold” (native gold) and/or graphite. In those zones, feldspar is completely absent and chlorite appears in low proportion. In fact, in the ore zones, feldspar and chlorite are largely decomposed to sericite and dolomite by the ore-forming solutions. The chemical equations of these reactions can be expressed by:

$$\underset{\text{albite}}{3NaAlSi_3O_8} + \underset{\text{fluid}}{K^+ + 2H^+} \rightarrow \underset{\text{sericite}}{KAl_3Si_3O_{10}(OH)_2} + \underset{\text{quartz}}{6SiO_2} + 3Na^+ \quad [1]$$

$$\underset{\text{chlorite}}{3(Mg,Fe)_5Al_2Si_3O_{10}(OH)_8} + \underset{\text{calcite}}{15CaCO_3} + \underset{\text{fluid}}{2K^+} + 15CO_2 \rightarrow \underset{\text{sericite}}{2KAl_3Si_3O_{10}(OH)_2} + \underset{\text{ferroan dolomite}}{15Ca(Mg,Fe)(CO_3)_2} + \underset{\text{quartz}}{SiO_2} + \underset{\text{fluid}}{9H_2O + 2H^+} \quad [2]$$

Feldspar and chlorite appear gradually when moving away from the mineralization zones. Therefore, contrary to the sulfide-quartz-sericite-carbonate alteration having affected the metaarenite, the chlorite-sericite-carbonate alteration is defined by a significant presence of chlorite and feldspar. The rocks affected by this latter alteration-type appear generally greenish in hand specimen. But, when chlorite is depleted and the proportion of feldspar (albite) remains relatively high, the rocks are generally bleached and take a pink color. Considering the fact that the composition of the metaarenite is notably alteration-type dependent, we term “feldspar depleted metaarenite” the proximal metaarenite relative to the ore zones, and “arkosic metaarenite” the distal ones. Sericite appears ubiquitous in all types of metaarenite, and it shows generally a yellow hue in hand samples.

The mafic igneous rocks are all pervasively altered. Their primary ferromagnesian minerals are completely transformed to chlorite, iron and titanium oxides, the feldspar to carbonate and epidote. Propylitic alteration affects particularly the metabasalt. It comprises mainly chlorite and epidote, together with lesser quantities of zoisite, carbonate, and feldspar (albite).

Metamorphic and hydrothermal alteration facies can be distinguished on the basis of texture, mineralogy, intensity, and distribution. The metamorphic alteration facies is regionally distributed and generally weak, with plagioclase crystals remaining well preserved. The hydrothermal alteration facies, however, is characterized by its local distribution and the important modification of the primary rock texture. It is also distinguished by its high intensity that destroys feldspar minerals. Minerals such as sericite, carbonate and chlorite (?) are not suitable for distinguishing metamorphic facies from hydrothermal facies, because they appear in both types of alteration. The association of quartz veins and sulfides, however, is exclusively related to the hydrothermal alteration facies. In addition, in the study area, the hydrothermal alteration facies are commonly associated with highly-deformed zones (e.g. faults, shear zones). Nevertheless, it is generally difficult to distinguish the weak hydrothermal alteration from regional metamorphism.

Graphite is occasionally observed in the hydrothermal alteration zones and suggests a process of reduction of CO_2 (Ridley and Diamond, 2000). The reaction can be expressed by the following equation:

$$CO_2 + CH_4 \rightarrow 2C + 2H_2O \qquad [3]$$

In summary, alteration in term of sulfidation, silicification, sericitization, and carbonatization occur particularly in the mineralization zones. The outer ore zones are, however, chloritized, sericitized and carbonatized. On the basis of this alteration facies distribution, it appears that the entire study area is chloritized, sericitized and carbonatized. In the mineralization zones, however, chlorite content is relatively low. Hence, we consider as of hydrothermal origin: sulfides, quartz veins/veinlets, partly sericite, partly carbonate; and as of metamorphic origin: chlorite, partly sericite, and also partly carbonate. The hydrothermal alteration (occurring in the mineralization zones) is clearly superimposed on the regional metamorphic alteration. This interpretation is emphasized by the lower amount of chlorite in the ore zone compared to the outer zones, even in the same rock type. In fact, chlorite tends to become

decomposed to other minerals (see equation [2] above) in the hydrothermal alteration zones (ore zones). This simple but important observation allows us to advance that the hydrothermal event postdated metamorphic alteration, which is of greenschist facies.

3-2-2. Alteration mineral chemistry

3-2-2-1. Carbonate mineral chemistry

Carbonate appears ubiquitous in all types of rocks of Aniuri and Jonction. It occurs both in quartz veins and wall rocks as anhedral to euhedral grains in various sizes. All carbonate analyzed by electron microprobe is from mineralization zones and has dolomite-ankerite series composition (Table 4 and Figure 21)

The use of the Mg-Mn-Fe triangular classification diagram of Trdlicka and Hoffman (1976) shows that the chemical composition ranges essentially between dolomite and magnesian ankerite with a predominance of ferroan dolomite (Figure 21). Deer *et al* (1992), consider as ferroan dolomite, carbonate of dolomite-ankerite series which has up to 20 percent of the Mg position filled by Fe^{2+} or Mn, and ankerite if ferrous iron and manganese is >20 percent. With this classification, the analyzed carbonate would be termed ferroan dolomite and ankerite.

Backscattered electron images and electron microprobe analyses permitted to observe zoning within single grains of carbonate (Figure 22 and Table 4). The central parts of crystals are magnesium-rich, whereas the peripheral parts are rich in iron. It is important to note that this zoning does not have an oscillatory character, which would be interpreted as a continuous variation of the carbonate composition. The zoning suggests several growth stages (temperature variation?) and/or variable fluid composition.

Table 4. Representative electron microprobe analyses of carbonate from the mineralization zones. Ideal formulas – dolomite: $CaMg(CO_3)_2$; ankerite: $Ca(Fe^{2+},Mg,Mn)(CO_3)_2$

Sample	1A6-53b-97/151.70m			1A6-72-97/199.64m			1A6-54-97/149.50m			
Analysis N°	CB-1	CB-2	CB-3	CB-4	CB-5	CB-6	CB-7	CB-8	CB-9	CB-10
MnO (wt. %)	0.34	0.44	0.30	0.41	0.50	0.44	0.27	0.26	0.29	0.27
FeO (wt. %)	8.68	11.54	6.69	12.41	12.06	11.52	5.31	5.26	8.61	7.58
MgO (wt. %)	14.86	13.14	16.29	12.64	12.50	12.84	16.84	16.92	14.97	15.45
CaO (wt. %)	28.42	28.22	28.93	27.56	28.13	28.25	27.88	27.57	27.42	27.48
SrO (wt. %)	0.09	0.10	0.14	0.05	0.15	0.14	0.24	0.34	0.18	0.26
BaO (wt. %)	0.00	0.00	0.07	0.00	0.00	0.00	0.00	0.00	0.03	0.02
Total (wt. %)	52.39	53.43	52.41	53.08	53.35	53.20	50.54	50.35	51.49	51.05
$MnCO_3$	0.55	0.70	0.49	0.67	0.81	0.72	0.44	0.42	0.46	0.43
$FeCO_3$	14.00	18.61	10.78	20.01	19.45	18.57	8.56	8.48	13.88	12.21
$CaCO_3$	50.72	50.36	51.62	49.19	50.21	50.42	49.75	49.20	48.94	49.04
$MgCO_3$	31.09	27.48	34.08	26.44	26.16	26.87	35.23	35.40	31.32	32.33
$SrCO_3$	0.13	0.14	0.20	0.08	0.22	0.21	0.35	0.48	0.26	0.37
Number of cations calculated on the basis of $Mn^{2+} + Fe^{2+} + Mg^{2+} + Ca^{2+} + Sr^{2+} = 2$										
Mn	0.01	0.01	0.01	0.01	0.01	0.01	0.01	0.01	0.01	0.01
Fe	0.24	0.32	0.18	0.35	0.34	0.32	0.15	0.15	0.24	0.21
Mg	0.74	0.65	0.79	0.64	0.63	0.64	0.84	0.85	0.75	0.78
Ca	1.01	1.01	1.01	1.00	1.02	1.02	1.00	0.99	0.99	0.99
Sr	0.00	0.00	0.00	0.00	0.00	0.00	0.00	0.01	0.00	0.01
Total	2.00	2.00	2.00	2.00	2.00	2.00	2.00	2.00	2.00	2.00

Table 4 continued

Sample	AN-125-97/162.10m			AN-72-97/116.70m			AN-84-95/125.60m			
Analysis N°	CB-11	CB-12	CB-13	CB-14	CB-15	CB-16	CB-17	CB-18	CB-19	CB-20
MnO (wt. %)	0.40	0.51	0.25	0.70	0.63	0.70	0.98	0.80	0.67	0.67
FeO (wt. %)	9.88	13.11	8.68	17.04	17.15	19.42	8.84	8.96	17.58	15.84
MgO (wt. %)	14.73	12.18	15.32	9.96	9.90	8.12	14.21	14.36	9.50	10.46
CaO (wt. %)	28.56	27.73	28.43	27.38	27.06	26.56	28.43	28.00	27.24	27.40
SrO (wt. %)	0.16	0.12	0.19	0.16	0.11	0.03	0.28	0.35	0.28	0.16
BaO (wt. %)	0.00	0.00	0.01	0.00	0.00	0.06	0.00	0.00	0.04	0.00
Total (wt. %)	53.73	53.65	52.87	55.24	54.85	54.89	52.74	52.47	55.31	54.52
$MnCO_3$	0.65	0.83	0.41	1.13	1.03	1.14	1.58	1.29	1.09	1.08
$FeCO_3$	15.94	21.14	13.99	27.48	27.66	31.32	14.26	14.45	28.35	25.54
$CaCO_3$	50.97	49.48	50.75	48.87	48.29	47.40	50.74	49.97	48.61	48.89
$MgCO_3$	30.82	25.49	32.05	20.85	20.71	16.98	29.73	30.04	19.87	21.89
$SrCO_3$	0.23	0.17	0.26	0.23	0.15	0.04	0.40	0.50	0.40	0.22
Number of cations calculated on the basis of $Mn^{2+} + Fe^{2+} + Mg^{2+} + Ca^{2+} + Sr^{2+} = 2$										
Mn	0.01	0.01	0.01	0.02	0.02	0.02	0.03	0.02	0.02	0.02
Fe	0.27	0.37	0.24	0.48	0.49	0.57	0.25	0.25	0.50	0.45
Mg	0.72	0.61	0.75	0.50	0.50	0.42	0.71	0.72	0.48	0.53
Ca	1.00	1.00	1.00	0.99	0.99	0.99	1.01	1.00	0.99	1.00
Sr	0.00	0.00	0.00	0.00	0.00	0.00	0.01	0.01	0.01	0.00
Total	2.00	2.00	2.00	2.00	2.00	2.00	2.00	2.00	2.00	2.00

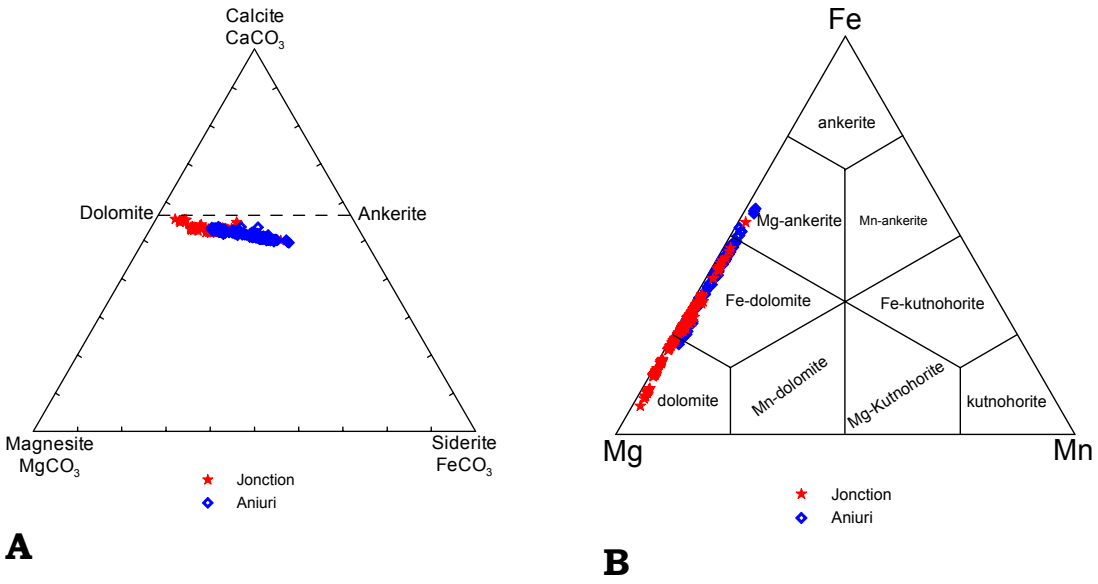

Figure 21. Ternary plots of carbonate composition calculated from electron microprobe analyses. A) $FeCO_3$-$CaCO_3$-$MgCO_3$ plot in mole percent; B) Mn-Fe-Mg classification diagram for dolomite group (fields after Trdlicka and Hoffman, 1976)

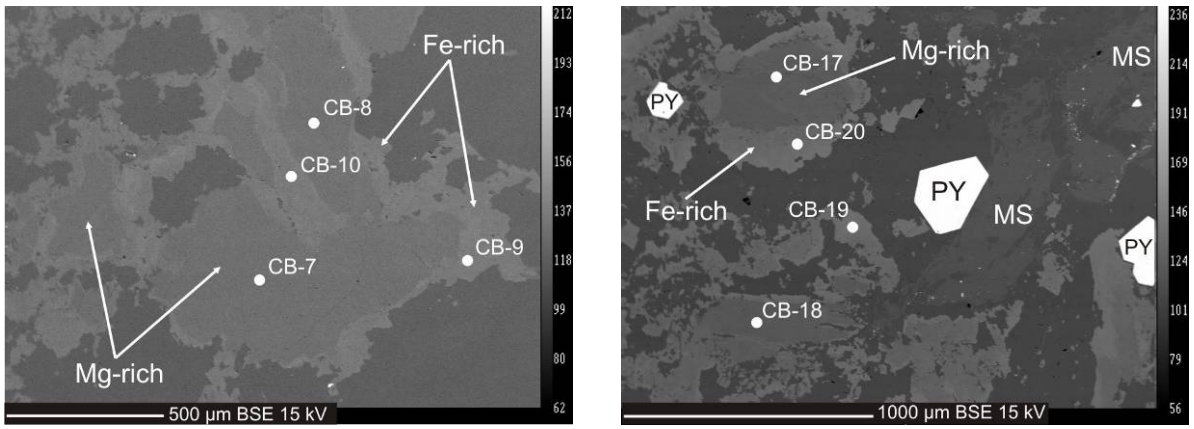

A – Sample 1A6-54-97/149.50m

B – Sample AN-84-95/125.50m

Figure 22. Backscattered electron images of zoning in carbonates of dolomite-ankerite series from the mineralization zones. A) Sample from Jonction; B) Sample from Aniuri. The numbers (e.g. CB-7, CB-8) represent electron microprobe points listed in Table 4. MS: muscovite; PY: pyrite.

3-2-2-2. Sericite chemistry

Sericite occurs in different proportions over the entire lithological spectrum of the study area. But it is significantly present in the mineralization zones. Electron microprobe analyses of sericite (Table 5) from the ore zones of Aniuri and Jonction display a muscovite composition according to the classification of micas established by Deer *et al.* (1992) shown in Figure 23. The micas analyzed show some compositional variation, but are within the field of muscovite. The formulas calculated on the basis of 22 oxygen atoms show Si content ranges from 5.9 to 6.2 atoms per formula unit (a.p.f.u.). The (Mg,Fe) and Na contents are all low (generally bellow 0.5 a.p.f.u.). The sum of atoms in the octahedral position is close to 4, which is characteristic for di-octahedral micas like muscovite.

Table 5. Representative electron microprobe analyses of sericite from the mineralization zones of Jonction and Aniuri. Note that the general formula of micas is $X_2Y_{4-6}Z_8(OH,F)_4$, where X (interlayer) is mainly K, Na or Ca but also Ba, Rb, Cs, etc.; Y (octahedral) is mainly Al, Mg or Fe but also Mn, Cr, Ti, Li, etc.; Z (tetrahedral) is mainly Si or Al but perhaps also Fe^{3+} and Ti.

Sample		1A6-74-98/372.70m		1A6-50-97/274m		1A6-53b-97/151.70m		1A6-72-97/199.64m	
Analysis N°		MS-1	MS-2	MS-3	MS-4	MS-5	MS-6	MS-7	MS-8
SiO_2 (wt. %)		46.84	46.58	47.24	47.70	47.14	48.51	47.06	46.35
Al_2O_3 (wt. %)		39.05	39.80	38.80	37.55	38.28	35.64	39.46	39.40
TiO_2 (wt. %)		0.14	0.08	0.17	0.16	0.09	0.10	0.11	0.27
FeO (wt. %)		0.76	0.71	0.76	0.76	1.07	1.65	0.67	0.65
MnO (wt. %)		0.00	0.00	0.00	0.00	0.00	0.00	0.00	0.00
MgO (wt. %)		0.46	0.39	0.89	1.04	0.67	0.76	0.59	0.49
K_2O (wt. %)		8.48	7.86	9.53	9.35	9.00	8.12	9.15	8.86
Na_2O (wt. %)		1.34	1.40	0.36	0.34	0.63	1.04	0.65	0.67
CaO (wt. %)		0.03	0.01	0.00	0.00	0.05	0.05	0.02	0.01
Total (wt. %)		97.10	96.82	97.75	96.89	96.94	95.87	97.71	96.69
Number of cations calculated on the basis of 22 oxygen atoms									
Z	**Si**	6.03	5.99	6.05	6.16	6.09	6.32	6.02	5.99
	Al^{IV}	1.97	2.01	1.95	1.84	1.91	1.68	1.98	2.01
	SUM (Z)	8.00	8.00	8.00	8.00	8.00	8.00	8.00	8.00
Y	**Al^{VI}**	3.95	4.01	3.91	3.87	3.91	3.79	3.97	3.98
	Ti	0.01	0.01	0.02	0.02	0.01	0.01	0.01	0.03
	Fe	0.08	0.08	0.08	0.08	0.12	0.18	0.07	0.07
	Mn	0.00	0.00	0.00	0.00	0.00	0.00	0.00	0.00
	Mg	0.09	0.07	0.17	0.20	0.13	0.15	0.11	0.09
	SUM (Y)	4.13	4.17	4.18	4.16	4.17	4.13	4.16	4.17
X	**K**	1.39	1.29	1.56	1.54	1.48	1.35	1.49	1.46
	Na	0.33	0.35	0.09	0.08	0.16	0.26	0.16	0.17
	Ca	0.00	0.00	0.00	0.00	0.01	0.01	0.00	0.00
	SUM (X)	1.73	1.64	1.65	1.62	1.65	1.62	1.66	1.63
Al_{tot}		5.92	6.03	5.86	5.71	5.82	5.47	5.95	6.00
Mg+Fe		0.17	0.15	0.25	0.28	0.25	0.33	0.18	0.16

Table 5 continued

Sample		AN-125-96/162.10m		AN-72-94/116.70m		AN-122-96/184.50m		AN-84-95/125.60m	
Analysis N°		MS-9	MS-10	MS-11	MS-12	MS-13	MS-14	MS-15	MS-16
SiO_2 (wt. %)		46.54	46.77	46.86	44.95	46.89	46.47	47.52	46.28
Al_2O_3 (wt. %)		39.62	39.59	39.59	38.19	39.55	39.58	40.20	37.03
TiO_2 (wt. %)		0.08	0.07	0.04	0.16	0.05	0.08	0.09	0.07
FeO (wt. %)		0.34	0.29	0.45	2.15	0.47	0.58	0.45	0.42
MnO (wt. %)		0.00	0.00	0.01	0.01	0.00	0.00	0.01	0.01
MgO (wt. %)		0.40	0.42	0.31	0.96	0.35	0.37	0.35	0.39
K_2O (wt. %)		8.33	9.02	8.71	5.50	7.27	8.44	8.40	9.21
Na_2O (wt. %)		1.34	0.84	0.83	2.23	2.03	1.27	1.38	1.12
CaO (wt. %)		0.01	0.00	0.00	0.04	0.00	0.00	0.01	0.00
Total (wt. %)		96.66	97.01	96.79	94.18	96.60	96.79	98.40	94.53
Number of cations calculated on the basis of 22 oxygen atoms									
Z	Si	6.00	6.01	6.03	5.94	6.02	5.99	6.01	6.13
	Al^{IV}	2.00	1.99	1.97	2.06	1.98	2.01	1.99	1.87
	SUM (Z)	8.00	8.00	8.00	8.00	8.00	8.00	8.00	8.00
Y	Al^{VI}	4.01	4.02	4.03	3.88	4.01	4.00	4.01	3.91
	Ti	0.01	0.01	0.00	0.02	0.00	0.01	0.01	0.01
	Fe	0.04	0.03	0.05	0.24	0.05	0.06	0.05	0.05
	Mn	0.00	0.00	0.00	0.00	0.00	0.00	0.00	0.00
	Mg	0.08	0.08	0.06	0.19	0.07	0.07	0.07	0.08
	SUM (Y)	4.13	4.13	4.15	4.32	4.13	4.14	4.13	4.05
X	K	1.37	1.48	1.43	0.93	1.19	1.39	1.36	1.56
	Na	0.33	0.21	0.21	0.57	0.50	0.32	0.34	0.29
	Ca	0.00	0.00	0.00	0.01	0.00	0.00	0.00	0.00
	SUM (X)	1.71	1.69	1.64	1.50	1.70	1.70	1.70	1.84
Al_{tot}		6.02	6.00	6.00	5.94	5.99	6.01	6.00	5.78
Mg+Fe		0.11	0.11	0.11	0.43	0.12	0.13	0.11	0.12

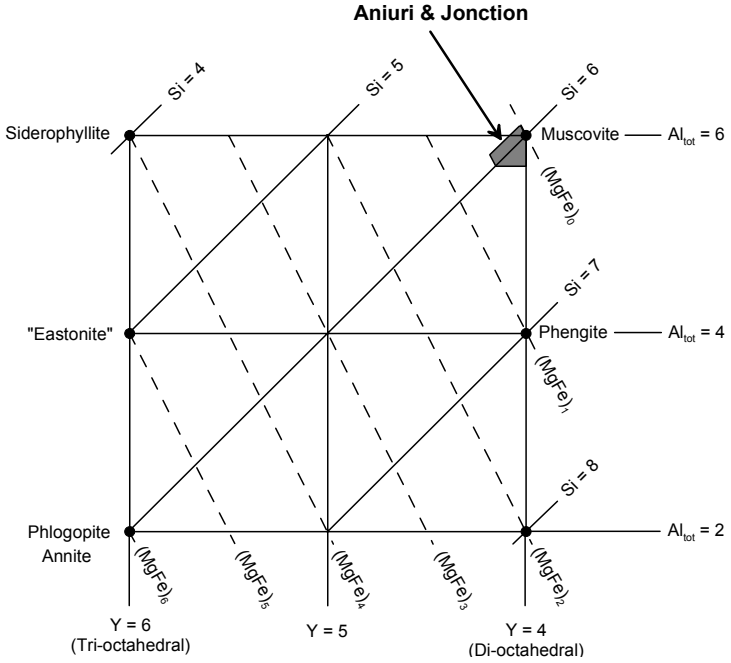

Figure 23. Composition of mica from the mineralization zones of Aniuri and Jonction. Diagram after Deer *et al.* (1992).

3-2-2-3. Chlorite chemistry

Chlorite is found in all lithological units of the studied deposits. But its abundance decreases significantly in the ore zones. This observation suggests a metamorphic origin rather than hydrothermal, because of the overprinting of hydrothermal events on metamorphic rocks.

Considering the nomenclature of Hey (1954), the chlorites analyzed fall in majority in the ripidolite compositional field (Figure 24). Only a few points fall in the pycnochlorite and diabantite fields.

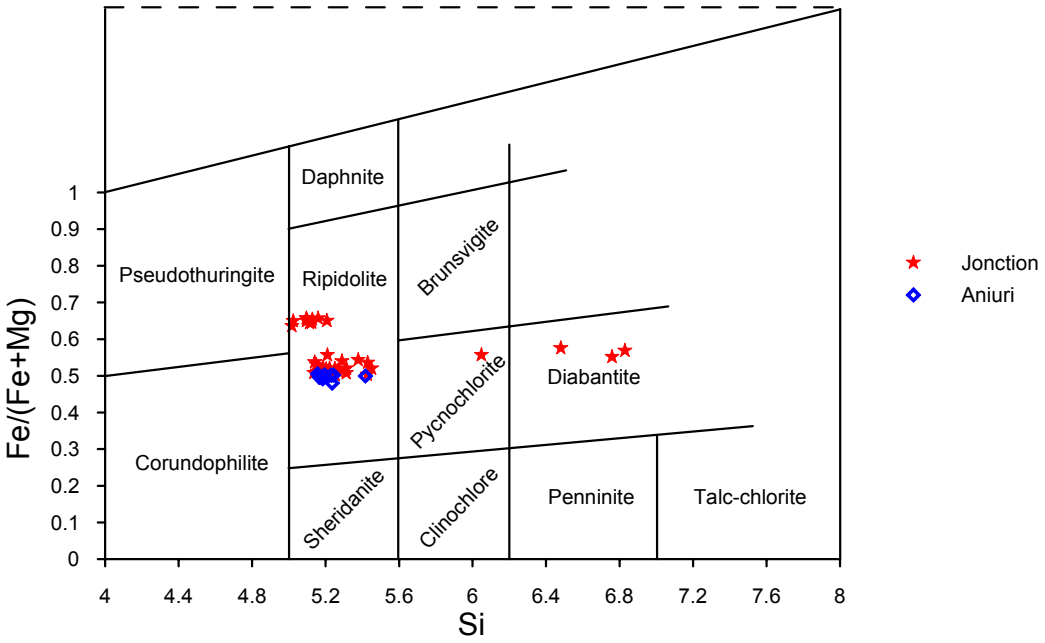

Figure 24. Composition of ore zone chlorite (fields after Hey, 1954). By using the nomenclature of Bayliss (1975), all the plotted chlorites belong to the clinochlore-chamosite solid solution series.

However, a number of years ago, some authors (Bayliss, 1975; Bailey, 1980) proposed a new nomenclature of trioctahedral chlorites which is recommended by the nomenclature committee of AIPEA (Association Internationale Pour l'Étude des Argiles) for its simplicity. In this new nomenclature, trioctahedral chlorites should be named according to the dominant divalent octahedral cation present. Thus, the recommended species names are: clinochlore for Mg-dominant [end member = $(Mg_5Al)(Si_3Al)O_{10}(OH)_8$], chamosite for Fe^{2+}-dominant

[end member = $(Fe_5^{2+}Al)O_{10}(OH)_8$], nimite for Ni-dominant [end member = $(Ni_5Al)(Si_3Al)O_{10}(OH)_8$], and pennantite for Mn-dominant [end member = $(Mn_5Al)(Si_3Al)O_{10}(OH)_8$]. By using this nomenclature, the chlorites plotted in the above diagram (Figure 24) should be redefined as iron-aluminian clinochlore and magnesium-aluminian chamosite for ripidolite, iron clinochlore for pycnochlorite, and magnesian siliconian chamosite for diabantite. In others words, all analyzed chlorites are members of the clinochlore-chamosite solid solution series with a predominance of chamosite due to the relatively high content of iron (Table 6).

The chlorites analyzed present very low contents of MnO (less than 0.05 wt.%). The structural formulae (Table 6) were calculated on the basis of 28 oxygen atoms, which implies the non-consideration of H_2O; in addition, all Fe was treated as Fe^{2+}. The sum of octahedral cations is very close to 12 in all analyzed chlorites, confirming their tri-octahedral type (Deer *et al.*, 1992).

The chemical composition of chlorite varies with the physico-chemical conditions (e.g. temperature) prevailing during its formation. Therefore, chlorite solid solution has been used by several authors as geothermometer. Cathelineau and Nieva (1985) used that possibility during the study of the geothermal system of Los Azufres (Mexico), where chlorite constitutes a major hydrothermal alteration product of the andesitic host rock. By combining microthermometric data on fluid inclusions found in coexisting minerals with chlorite (e.g. quartz), they noted a positive correlation between Al^{IV} and formation temperature, which can be described as a regression equation. In others words, they observed that Al^{IV} increases and Al^{VI} decreases with chlorite formation temperature. Using additional data from Los Azufres and Salton Sea (California), Cathelineau (1988) redefined the following relationship between Al^{IV} and temperature:

$$T\ [°C] = -61.92 + 321.98Al^{IV} \qquad [4]$$

Still on the base of empirical calibration, Kranidiotis and MacLean (1987)

suggested a different equation by taking into account the variation in Fe/(Fe+Mg) in chlorite. They proposed a corrected Al^{IV} value (Al_c^{IV}) as follows:

$$Al_c^{IV} = Al^{IV} + 0.7(Fe/[Fe + Mg]), \quad [5]$$

from which the temperature is calculated according to:

$$T\ [°C] = 106Al_c^{IV} + 18 \quad [6]$$

Table 6. Representative electron microprobe analyses (in wt.%) of chlorite from the host rock of the mineralization zones, calculated structural formulas and chlorite geothermometry

Sample		AN-125-96/162.10m					1A6-74-98/372.70m			
Analysis N°		CL-1	CL-2	CL-3	CL-4	CL-5	CL-6	CL-7	CL-8	CL-9
SiO_2 (wt. %)		24.19	25.99	24.64	24.31	24.16	23.46	24.07	23.44	22.84
TiO_2 (wt. %)		0.01	0.04	0.03	0.04	0.05	0.04	0.05	0.02	0.05
Al_2O_3 (wt. %)		24.41	24.98	24.12	23.99	23.98	23.85	24.09	23.63	23.99
Cr_2O_3 (wt. %)		0.07	0.06	0.06	0.08	0.07	0.07	0.05	0.01	0.05
FeO (wt. %)		23.37	22.47	22.79	23.92	24.32	30.20	29.88	31.10	30.25
MnO (wt. %)		0.01	0.03	0.05	0.04	0.04	0.04	0.04	0.05	0.06
MgO (wt. %)		13.31	12.63	13.84	13.27	13.36	9.35	9.01	9.34	9.16
CaO (wt. %)		0.02	0.00	0.00	0.00	0.01	0.00	0.00	0.01	0.02
Na_2O (wt. %)		0.01	0.05	0.00	0.00	0.02	0.05	0.01	0.00	0.04
K_2O (wt. %)		0.08	0.63	0.01	0.02	0.03	0.01	0.19	0.02	0.02
Total (wt. %)		85.47	86.87	85.53	85.67	86.03	87.07	87.38	87.62	86.47
Numbers of ions on the basis of 28 oxygen atom equivalents ignoring H_2O										
Tetra.	**Si**	5.17	5.42	5.24	5.19	5.16	5.11	5.21	5.10	5.02
	Al^{IV}	2.83	2.58	2.76	2.81	2.84	2.89	2.79	2.90	2.98
	SUM (IV)	8.00	8.00	8.00	8.00	8.00	8.00	8.00	8.00	8.00
Octa.	**Al^{VI}**	3.31	3.55	3.28	3.24	3.19	3.24	3.35	3.16	3.24
	Ti	0.00	0.01	0.00	0.01	0.01	0.01	0.01	0.00	0.01
	Cr	0.01	0.01	0.01	0.01	0.01	0.01	0.01	0.00	0.01
	Fe	4.17	3.92	4.05	4.27	4.34	5.50	5.40	5.66	5.57
	Mn	0.00	0.00	0.01	0.01	0.01	0.01	0.01	0.01	0.01
	Mg	4.24	3.92	4.38	4.23	4.25	3.04	2.91	3.03	3.00
	Ca	0.00	0.00	0.00	0.00	0.00	0.00	0.00	0.00	0.00
	Na	0.00	0.02	0.00	0.00	0.01	0.02	0.01	0.00	0.01
	K	0.02	0.17	0.00	0.01	0.01	0.00	0.05	0.00	0.01
	SUM (VI)	11.77	11.60	11.74	11.77	11.82	11.83	11.74	11.87	11.86
Fe/(Fe+Mg)		0.50	0.50	0.48	0.50	0.51	0.64	0.65	0.65	0.65
Chlorite compositional geothermometry										
T1 (°C)		851	770	828	841	853	868	837	872	896
T2 (°C)		355	329	347	353	357	372	362	374	382

Table 6 continued

Sample		1A6-72-97/199.64m					1A6-53b-97/151.70m			
Analysis N°		CL-10	CL-11	CL-12	CL-13	CL-14	CL-15	CL-16	CL-17	CL-18
SiO_2 (wt. %)		23.71	36.42	33.03	24.02	23.82	24.95	23.91	24.29	24.78
TiO_2 (wt. %)		0.07	0.14	0.16	0.01	0.12	0.02	0.04	0.04	0.03
Al_2O_3 (wt. %)		24.13	31.44	29.14	23.91	24.05	23.82	24.23	23.87	23.87
Cr_2O_3 (wt. %)		0.01	0.02	0.01	0.02	0.03	0.07	0.12	0.12	0.19
FeO (wt. %)		24.92	11.61	15.18	25.77	24.75	23.83	23.92	23.02	21.61
MnO (wt. %)		0.04	0.03	0.02	0.03	0.03	0.06	0.08	0.06	0.05
MgO (wt. %)		12.04	4.94	6.27	11.52	12.31	12.97	12.99	12.80	11.19
CaO (wt. %)		0.00	0.03	0.00	0.00	0.00	0.02	0.04	0.10	0.11
Na_2O (wt. %)		0.02	0.37	0.22	0.02	0.01	0.02	0.00	0.02	0.17
K_2O (wt. %)		0.19	5.04	4.11	0.02	0.05	0.00	0.01	0.03	0.35
Total (wt. %)		85.13	90.02	88.15	85.31	85.16	85.77	85.34	84.35	82.35
Numbers of ions on the basis of 28 oxygen atom equivalents ignoring H_2O										
Tetra.	Si	5.14	6.83	6.48	5.21	5.15	5.31	5.14	5.25	5.45
	Al^{IV}	2.86	1.17	1.52	2.79	2.85	2.69	2.86	2.75	2.55
	SUM (IV)	8.00	8.00	8.00	8.00	8.00	8.00	8.00	8.00	8.00
Octa.	Al^{VI}	3.31	5.78	5.22	3.32	3.28	3.29	3.27	3.33	3.64
	Ti	0.01	0.02	0.02	0.00	0.02	0.00	0.01	0.01	0.01
	Cr	0.00	0.00	0.00	0.00	0.00	0.01	0.02	0.02	0.03
	Fe	4.52	1.82	2.49	4.67	4.48	4.24	4.30	4.16	3.97
	Mn	0.01	0.00	0.00	0.00	0.01	0.01	0.01	0.01	0.01
	Mg	3.89	1.38	1.83	3.72	3.97	4.12	4.16	4.12	3.67
	Ca	0.00	0.01	0.00	0.00	0.00	0.01	0.01	0.02	0.03
	Na	0.01	0.13	0.08	0.01	0.00	0.01	0.00	0.01	0.07
	K	0.05	1.20	1.03	0.01	0.01	0.00	0.00	0.01	0.10
	SUM (VI)	11.80	10.35	10.68	11.74	11.77	11.69	11.78	11.70	11.52
Fe/(Fe+Mg)		0.54	0.57	0.58	0.56	0.53	0.51	0.51	0.50	0.52
Chlorite compositional geothermometry										
T1 (°C)		859	315	427	837	856	803	860	823	759
T2 (°C)		361	184	222	355	359	341	359	347	327

Note:

- The general formula of chlorite is $[R^{2+},R^{3+}]_{12}^{VI}[Si_{8-x}R_x^{3+}]^{IV}O_{20}(OH)_{16}$ where R^{2+} = Mg, Fe, Mn, Ni, Zn ; R^{3+} = Al, Fe,Cr ; and x (generally) ~1-3
- FeO represents the total iron content
- SUM (IV) and SUM (VI) represent, the sum of tetrahedral and octahedral cations, respectively
- T1 is the temperature calculated after the method of Catelineau (1988) and T2, that after the method of Kranidiotis and MacLean (1987)
- The sample AN-125-96/162.10m is from Aniuri and all others are from Jonction

The temperatures derived from the ore zone chlorite compositions using the equation of Cathelineau (1988) for chlorite geothermometry are in the interval of 315 to 896°C (Table 6). However, with the method of Kranidiotis and Maclean (1987) the temperatures are in the range of 184 - 382°C. De Caritat *et al.* (1993) noted that empirical chlorite geothermometers are not universally

applicable, as the composition of chlorite is sensitive to parameters other than temperature (e.g. coexisting mineral assemblage). Nevertheless, the temperatures obtained by the equation of Kranidiotis and Maclean (1987), seem to be much more reasonable for a hydroxyled mineral like chlorite.

3-2-3. Downhole alteration variations

In this section, vertical and lateral variations in the alteration trends are examined through two inclined diamond drill holes (DDH), namely AN-138-97 on the transversal section 10+00 SW for the Aniuri deposit, and 1A6-72-97 on the transversal section 13+75 SW for the Jonction deposit. Drill locations are shown in Figures 10 and 11. The selected DDH cross the representative lithological sequences of the studied deposits. Along each drill hole, K_2O, Na_2O, arsenic and gold contents have been plotted in order to illustrate alteration and mineralization variations along the lithological sequences (Figure 25). In both deposits, one notes a depletion of Na_2O coupled by a relative increase in K_2O in the gold-bearing zones, which is much more perceptible by the increase in K_2O/Na_2O ratio in the ore zones. Microscopic observations permit to identify albite as the most important sodium-bearing mineral in rock samples. Therefore, the depletion of Na_2O would mean depletion of sodic feldspar. This fact is confirmed by the absence of feldspar in the gold-bearing samples (Figure 15). Figure 26 shows that the phenomenon of sodic plagioclase breakdown affects almost all gold-bearing samples of both the Jonction as well as the Aniuri deposit. The mineralization zones are in addition distinguished by enrichment in arsenic, expressed mineralogically by the presence of arsenopyrite. Arsenic generally appears as halo of several tens of meters around the main gold ore zones. At Jonction, in some rare cases, native gold has been found in samples out of the main mineralization zone, but without any arsenic content. This exceptional type of gold mineralization is interpreted as genetically different from the main one described here.

Figure 25 also shows the distribution of the alteration minerals in the lithological sequence crossed by the selected drill holes. One notes the depletion of feldspar (albite) in the mineralization zones as mentioned above, but, in addition, a relative decrease of chlorite. Carbonate is observed in the ore zones and in all types of lithology of the studied deposits. Sericite also is ubiquitous, but seems to be absent in the mafic igneous rocks. Quartz veins and sulfides are generally found in the mineralization zones.

In summary, the main gold mineralization zone at Aniuri, as well as at Jonction, is distinguished by quartz veins, feldspar-destructive, sericite and carbonate alteration, accompanied by the presence of sulfides and an extensive halo of arsenic.

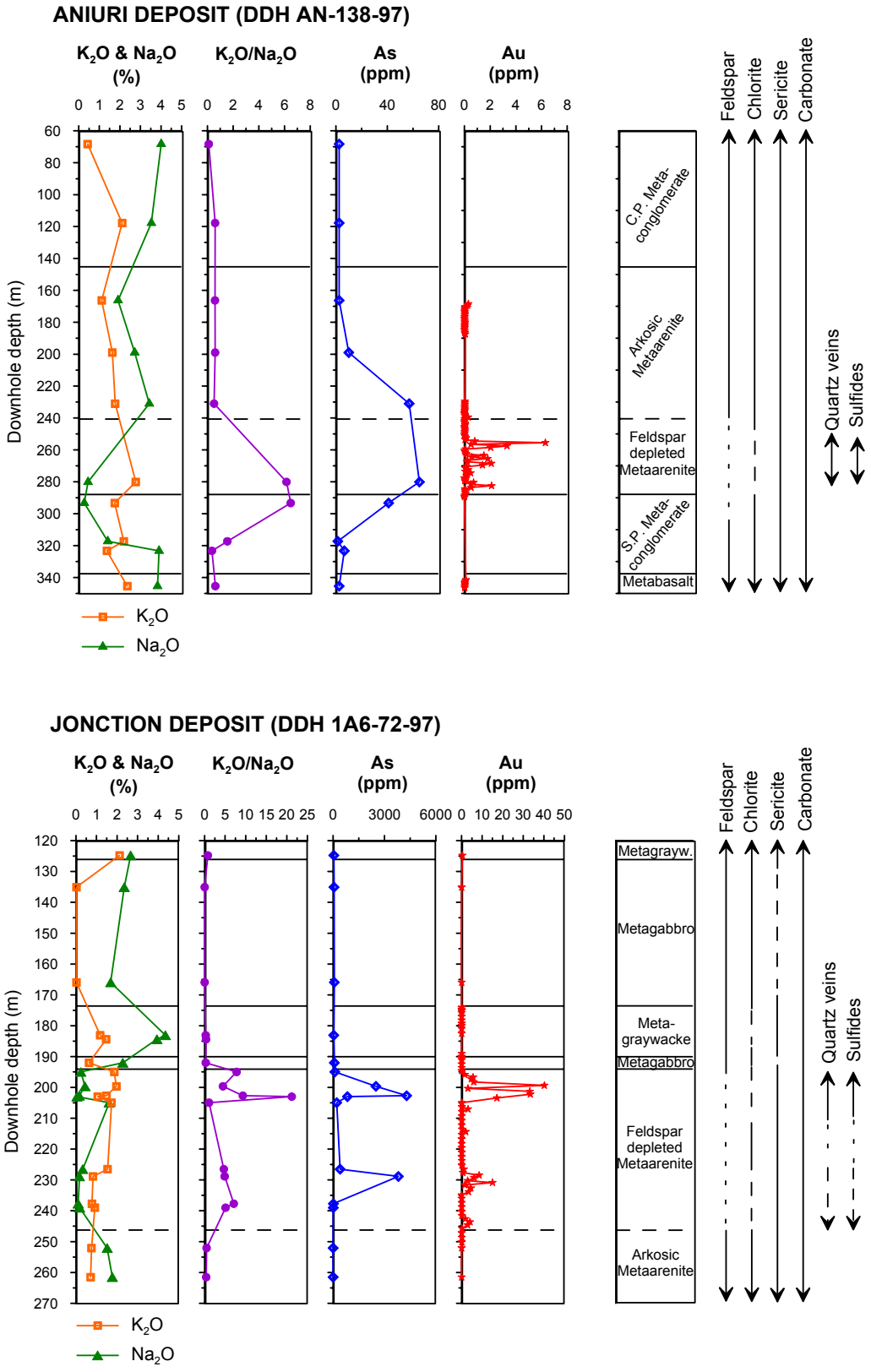

Figure 25. Downhole alteration variation along representative drill holes of Aniuri (DDH AN-138-97) and Jonction (DDH 1A6-72-97). Note the similar features of the mineralization zones of both gold deposits.

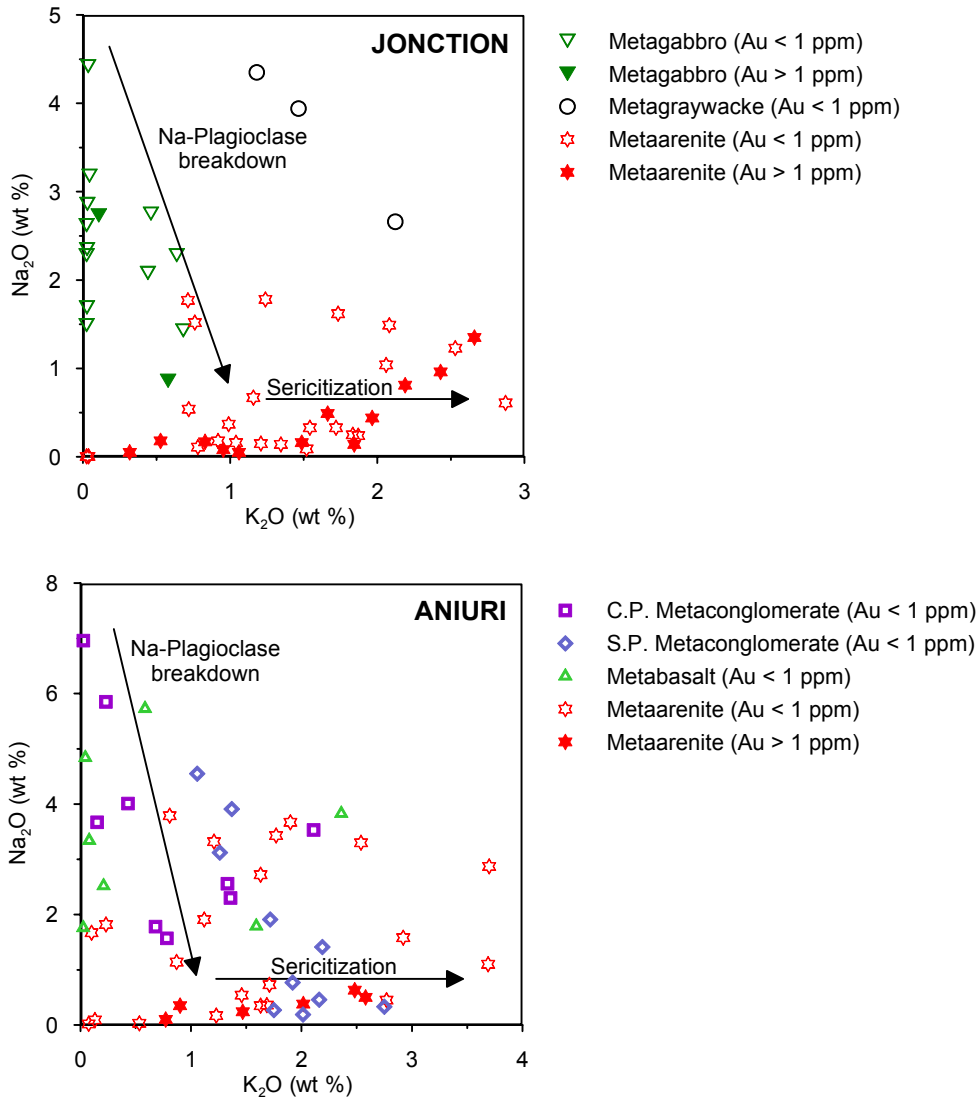

Figure 26. Na_2O versus K_2O plot, indicating that almost all gold-bearing samples are strongly depleted in sodium. This fact is mineralogically expressed by the disappearance of sodic feldspar (e.g. albite) in the mineralization zones.

3-2-4. Quantitative evaluation of alteration intensity

In this section, the intensity of the alteration is estimated by using alteration indexes. In addition, an assessment of element gains or losses is made by comparing the concentration of some elements in the altered rocks with a reference.

3-2-4-1. Alteration box

Alteration index, such as the Ishikawa alteration (AI) has been plotted versus the chlorite-carbonate-pyrite index (CCPI) to evaluate the quantitative importance of some alteration minerals in some altered rocks. The Ishikawa alteration index was originally defined to measure the intensity of sericite and chlorite alteration associated with the Kuroko-VHMS deposits (Ishikawa *et al.*, 1976). It is expressed by the following formula:

$$AI = 100\,\frac{(K_2O + MgO)}{(K_2O + MgO + Na_2O + CaO)} \qquad [7]$$

The Ishakawa AI does not take into account carbonate alteration that can be important in some VHMS alteration systems as well as in hydrothermal systems in general. For that reason, Large *et al.* (2001) introduced a complementary alteration index, called chlorite-carbonate-pyrite index (CCPI) which evaluates the enrichment of Mg-Fe chlorite, Mg-Fe carbonate and pyrite in altered rocks. The chlorite-carbonate-pyrite index is defined by the formula

$$CCPI = 100\,\frac{(MgO + FeO)}{(MgO + FeO + Na_2O + K_2O)} \qquad [8]$$

where FeO represents the total iron content of the rock.

Thus, the combination of the Ishikawa alteration index and the chlorite-carbonate-pyrite index makes it possible to appreciate in one diagram (alteration box), the intensity of enrichment of alteration minerals such as epidote, ankerite, dolomite, Mg-Fe chlorite, sericite.

A series of samples from the hosted-rock of gold mineralization (e.g. metaarenite) of Aniuri and Jonction have been plotted distinctly in an IA-CCPI alteration box (Figure 27). In both cases, samples plotted in the center of the diagram and toward albite position are considered to be least hydrothermally altered, whereas those more affected by hydrothermal alteration plot in the ankerite-sericite-chlorite triangle, at varying position dependent on the principal alteration minerals present. This interpretation is confirmed by

petrographic and geochemical studies already performed above. All samples from gold mineralization zones plot in the ankerite-sericite-chlorite triangle and are strongly feldspar-depleted, whereas samples which plot out of this triangle are all barren and feldspathic. These latter sample types represent the arkosic metaarenite, and those which plot in the ankerite-sericite-chlorite triangle, correspond to feldspar-depleted metaarenite. In fact, the samples which plot in the alteration triangle can be interpreted to have been much more affected by hydrothermal alteration than greenschist-facies metamorphic samples.

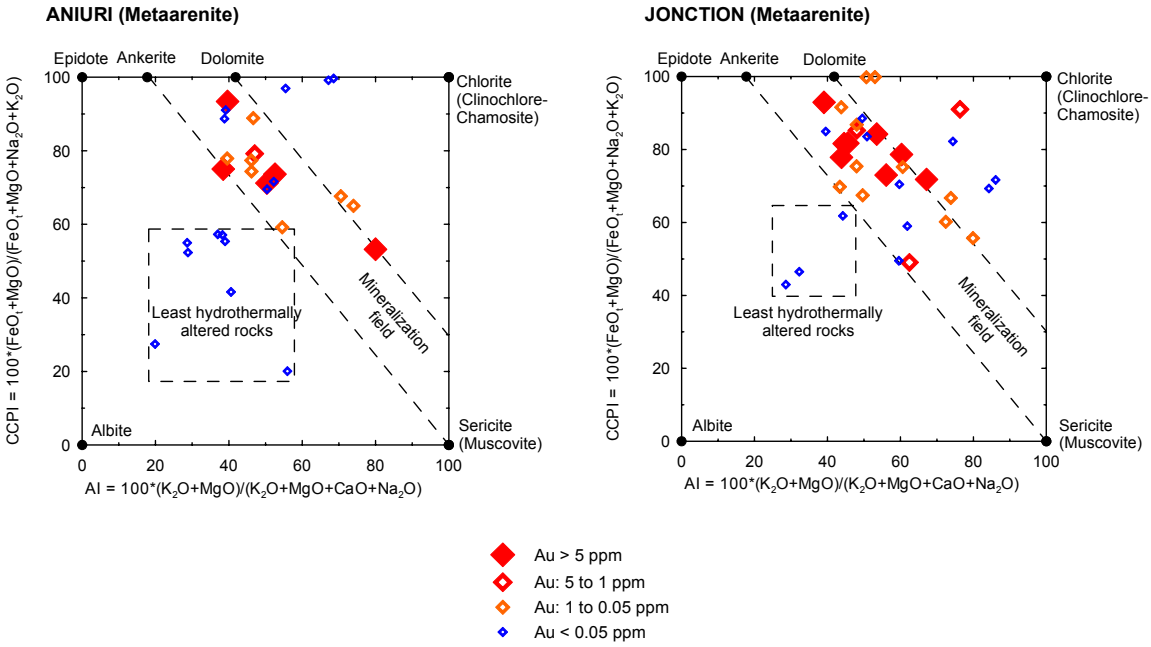

Figure 27. AI-CCPI alteration box plot for metaarenite samples from Aniuri and Jonction. The data (classified by gold content) show the relationship between gold-bearing samples and alteration minerals.

In the alteration boxes, the array of gold-bearing samples is very similar for both gold deposits. It shows a mineralization field which extents from ankerite-dolomite position toward sericite (muscovite) position. Therefore, Fe-Mg carbonate and sericite appear to be the most important hydrothermal alteration minerals in the gold mineralization zones of Aniuri and Jonction. In the alteration boxes, the location of some gold-bearing samples toward the chlorite position shows that although chlorite does not represent a main alteration mineral in the ore zones, it can be present in those zones. This is

confirmed by microscopic studies where, contrary to feldspar, the presence of chlorite in the samples from the mineralization zones is noted, but in a lesser amount compared to the outer ore zones.

3-2-4-2. Multi-element and bivariate diagrams

An assessment of element gains or losses in altered rock requires an estimate of the element concentration prior to alteration, i.e. availability of unaltered samples of the same rock type. However, all rocks in the study area have been affected to different extent by metamorphism and hydrothermal alteration. Therefore, average upper continental crust (UCC) has been used as reference for the multi-element diagram plots. In these plots, selected element abundances of the altered rocks are normalized to upper continental crust abundances. For those elements below the detection limit, we used the half of that detection limit value for the plots.

The rock samples studied for each deposit are classified in two groups according to their gold content (i.e. gold-bearing samples and barren samples). The multi-element diagrams show an enrichment of As, Sb, W and Bi in gold-bearing samples (1.36 – 22.7 ppm Au) in comparison to the upper continental crust composition (Figure 28). In the samples considered as barren (<0.002 – 0.041 ppm Au), one notes also an enrichment of As, Sb and Bi (Figure 29), but to a lesser extent in comparison to the gold-bearing rock samples. Note, however, that the relative enrichment in Bi appears similar in both gold-bearing and barren rock samples. Spatially, the analyzed barren samples are adjacent to the mineralization zones, i.e. in the hanging wall (HW) for Aniuri, and in the footwall (FW) for Jonction. The enrichment of As and Sb in the barren zones adjacent to the gold ore zones, even at relatively low values, shows the large extent of these element halos.

On bivariate plots (Figure 30), one notes that, the enrichment of gold content in the rock samples is coupled with a gain of arsenic, antimony and tungsten. The

plot Au-Sb shows however a greater scatter. In the case of Bi, the increase of gold content does not imply necessary Bi enrichment.

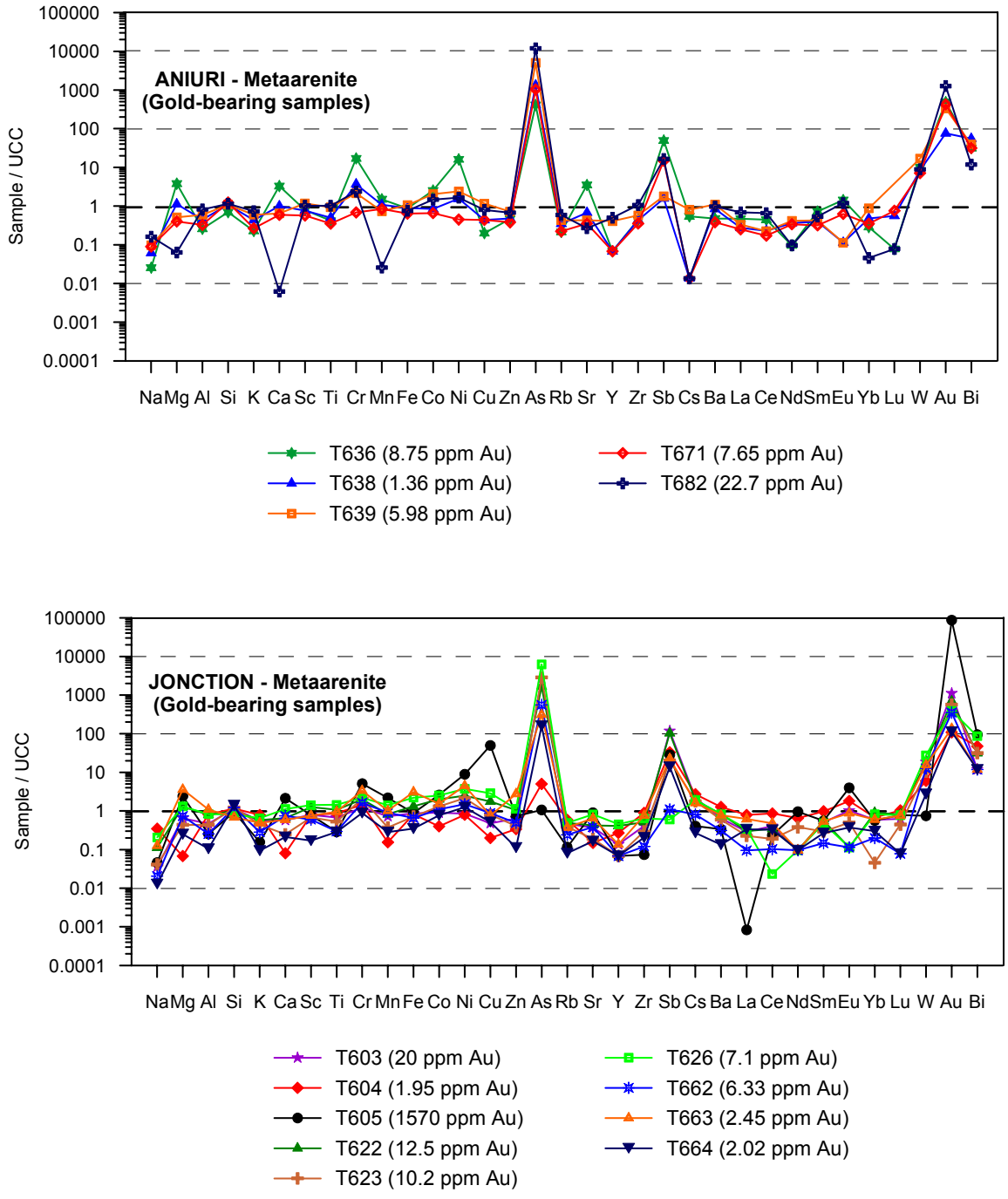

Figure 28. Upper-continental-crust normalized element abundance patterns for gold mineralization zones (normalization factors from Taylor and McLennan, 1985).

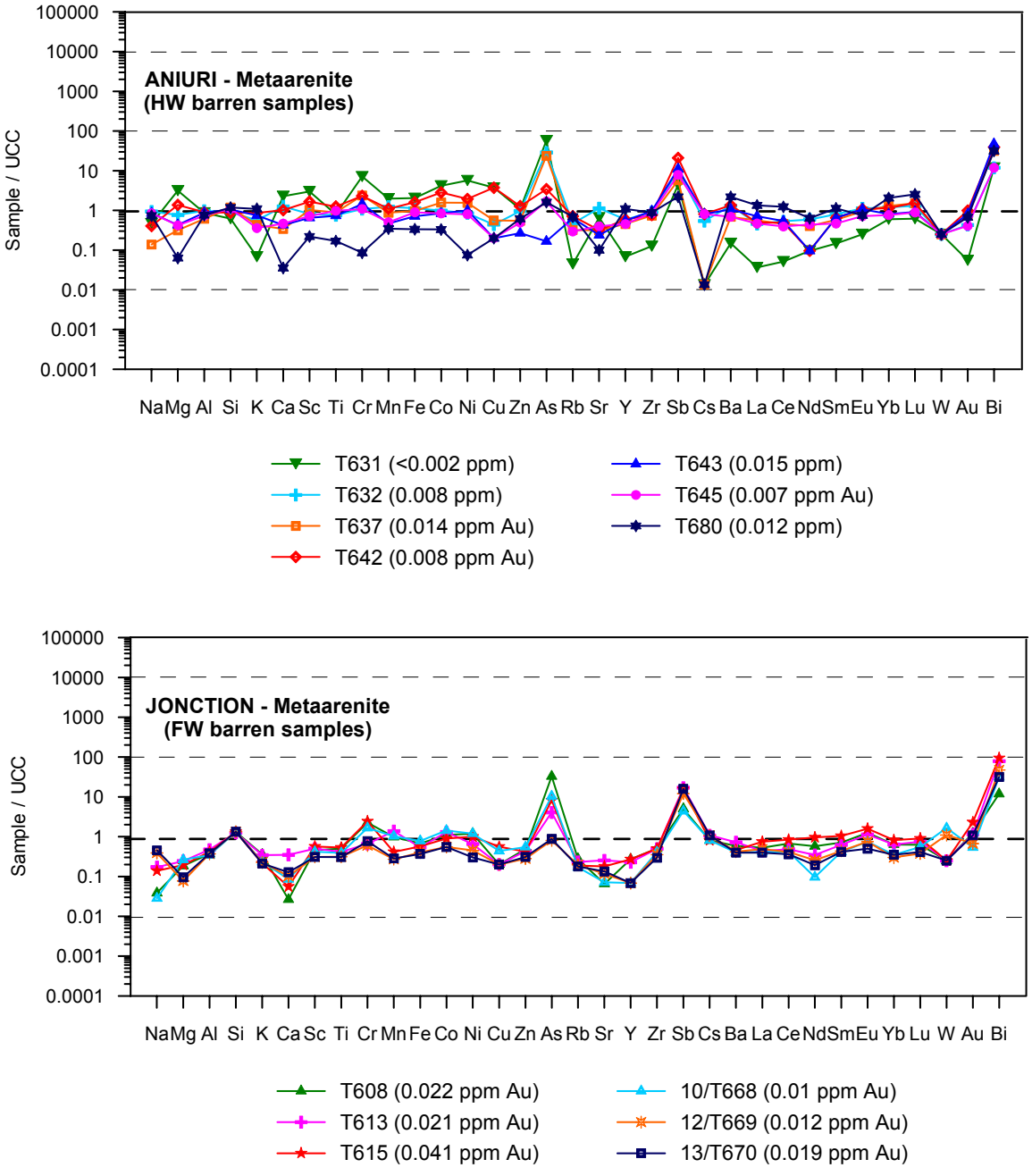

Figure 29. Upper-continental-crust normalized element abundance patterns for barren zones adjacent to ore zones (normalization factors from Taylor and McLennan, 1985). HW: hanging wall; FW: footwall

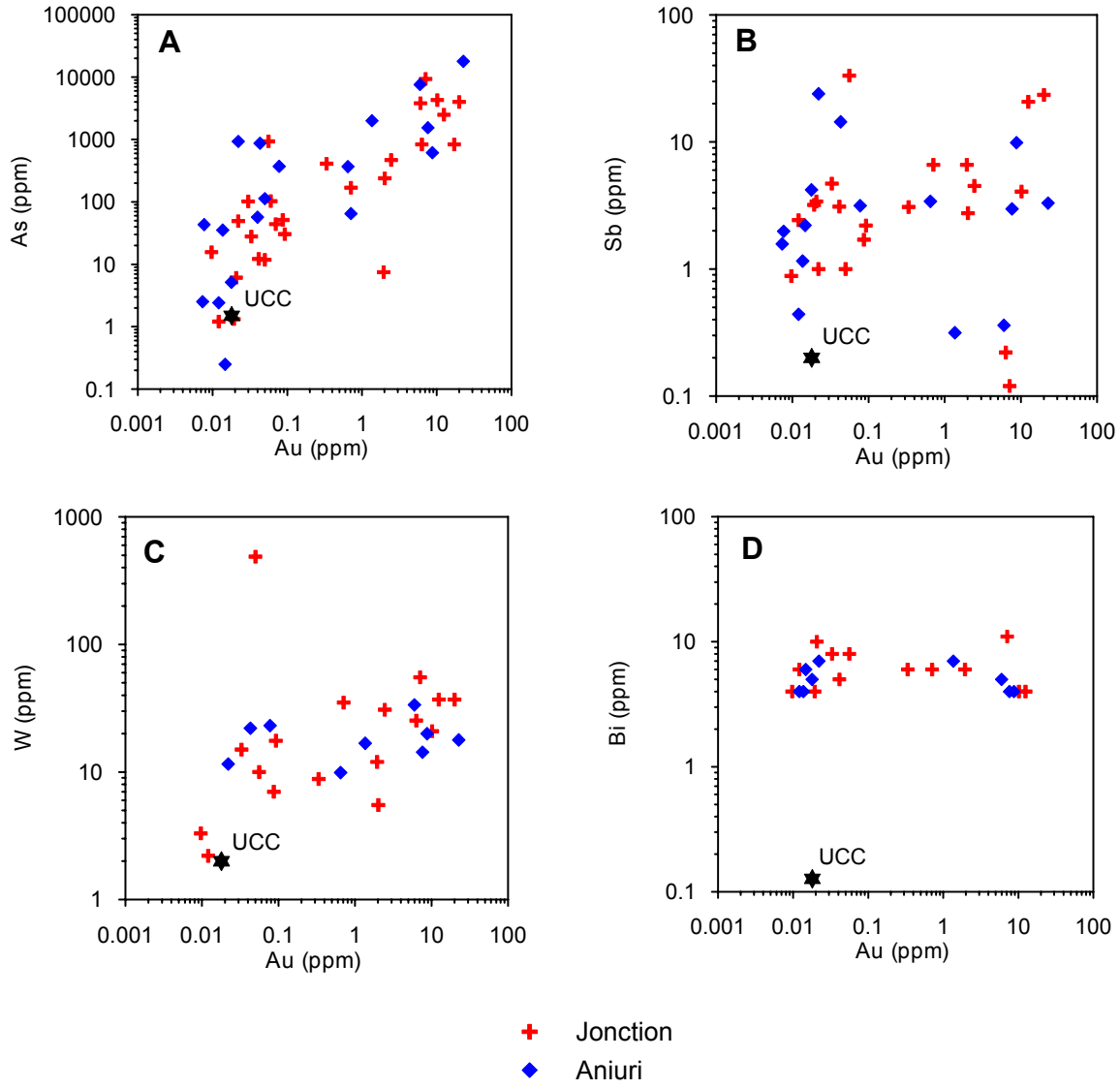

Figure 30. Correlation of arsenic, antimony, tungsten, and bismuth with gold content in whole rock samples (metaarenite) from Jonction and Aniuri. UCC represents the upper continental crust composition determined by Taylor and McLennan (1985).

In summary, among the different elements of the diagrams, arsenic has the best positive correlation with gold content. Furthermore, its halo is extensive, as even in the barren rock samples the arsenic content remains relatively high.

The normalization of element abundance in both gold-bearing and barren rock samples with upper continental crust composition has emphasized the geochemical signature of gold mineralization in the Afema gold district. This signature is characterized by Au-As-W-Sb-Bi, where the couple Au-As, and to a

lesser extent W and Sb, represents the principal metal association of the gold mineralization.

3-2-5. Relationship between hydrothermal alteration and deformation

Hydrothermal alteration is closely associated in space with highly deformed zones. The inner zones of hydrothermal alteration, characterized by the presence of quartz-carbonate veins, the destruction of feldspar minerals, and the presence of gold-bearing sulfides, are mainly restricted to narrow mylonitic zones, while a wide pervasive alteration envelope with muscovite, disseminated carbonate and chlorite is characterized by less important mineralogical and chemical modification in the moderately deformed zones. The degree of deformation varies across the gold deposits. It increases from the margins toward the main mineralization zones. The superimposition of highly deformed zones with hydrothermally altered zones evokes a genetic relationship between deformation and hydrothermal activity.

3-3. Geodynamic setting

3-3-1 Relationship between the composition of clastic sedimentary rocks and that of their source rocks

The chemical composition of terrigenous clastic sedimentary rocks depends particularly on provenance or source rocks. The clastic sedimentary rocks are derived from magmatic rocks, metamorphic rocks, or other exogenous rocks by weathering, erosion, transportation, deposition, lithification. The most important agent in this process is undoubtedly water. According to one hypothesis quoted by Whitfield and Turner (1979), the composition of seawater can be understood by the following global reaction:

Igneous rocks + Acid volatiles + Water $\rightarrow$ Seawater + Sediment + Atmosphere.

Therefore, some authors (e.g. Whitfield and Turner, 1979; Taylor and McLennan, 1985) defined the notion of "water-rock partition coefficients". Through that notion, they examined the partitioning of elements between upper crustal rocks and natural waters during the weathering and erosion of superficial rocks to form sediments, and used the following formula:

$$K_y = X_y^w / X_y^{UC} \quad [9]$$

where K_y is the partition coefficient for some element y between some natural water (w) and the upper crust (UC); X_y^w, the concentration of element y in some natural water, and X_y^{UC}, the concentration of element y in the upper crust.

As seawater constitutes the largest reservoir of dissolved material, the relationship between the residence time (τ) of various elements and the seawater-upper crust partition coefficients (K_y^{sw}) has been determined (Figure 31). Residence time τ is defined as the total amount of an element in seawater, divided by the rate at which it is added to the oceans.

According to Taylor and McLennan (1985), elements with very high K_y^{sw} and τ ($\log K_y^{sw} \geq -3$; $\log \tau \geq 5$), notably most alkali and alkaline earth elements, B and U, are strongly partitioned into natural waters and remain for long periods of time. In the oceans however, elements with the lowest residence times and seawater-upper crust partition coefficients ($\log K_y^{sw} \leq -6$; $\log \tau \leq 3$), namely Ti-group (Ti, Zr, Hf), Al-group (Al, Ga), REE (including Y, Sc), Th, Nb, Sn, Be are least soluble in natural waters; consequently they have the greatest potential for being preserved in the clastic sedimentary record. Therefore, these so-called immobile elements become a potential tool for the characterization of the geotectonic setting. However, caution should be taken in this attempt; because these elements are not perfectly immobile, particularly in high-temperature hydrothermal environments.

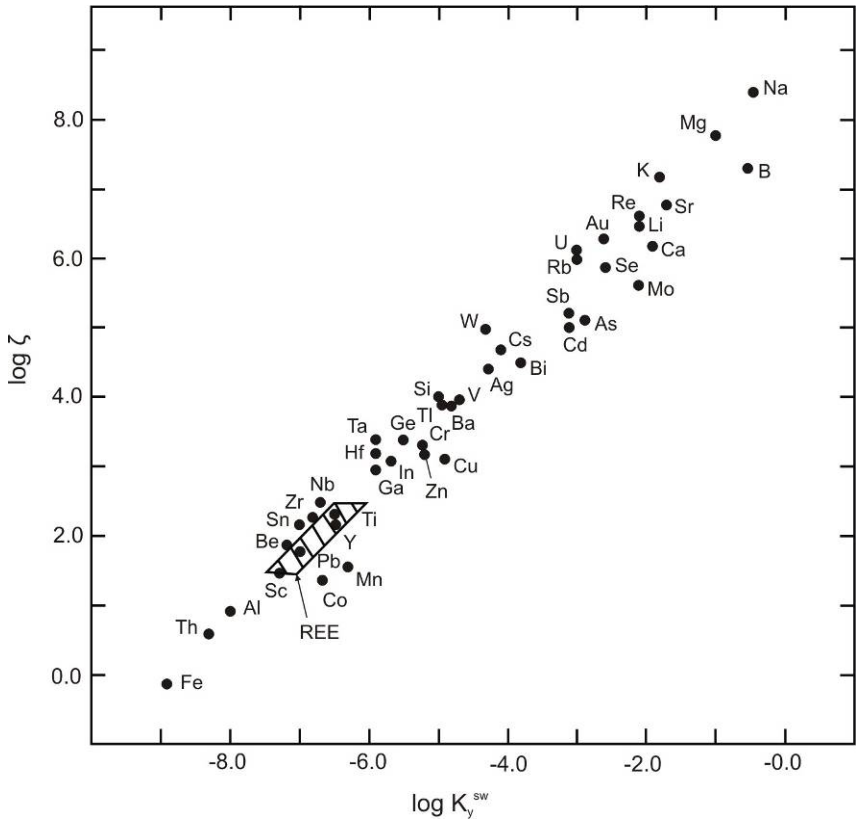

Figure 31. Plot of residence time (expressed as log τ) against seawater-upper crust partition coefficient (expressed as log K_y^{sw}). Elements with the lowest residence times and seawater-upper crust partition coefficients are the least soluble and have the greatest potential for remaining in the clastic sedimentary record, thus preserving the best record of their source (Taylor and McLennan, 1985).

3-3-2. Geotectonic setting of the metasedimentary rocks

In this section, the elements used for the discrimination of the geotectonic setting are those considered to be least mobile and better preserved in clastic sedimentary record, such as La and Th. The data of these elements of metaarenite from the studied deposits have been plotted in the (La versus Th) plot suggested by Bhatia and Crook (1986) to discriminate tectonic setting of sedimentary basins in eastern Australia. On this diagram (Figure 32), the samples plot distinctly, in the field of oceanic island arcs. This result means that the metaarenite of Aniuri and Jonction (and by extension the metasedimentary rocks of the studied area) derive from oceanic island arc. This

tectonic setting is also recorded by Hirdes *et al.* (2007) who investigated on metabasalt from the studied area (i.e. Sefwi belt).

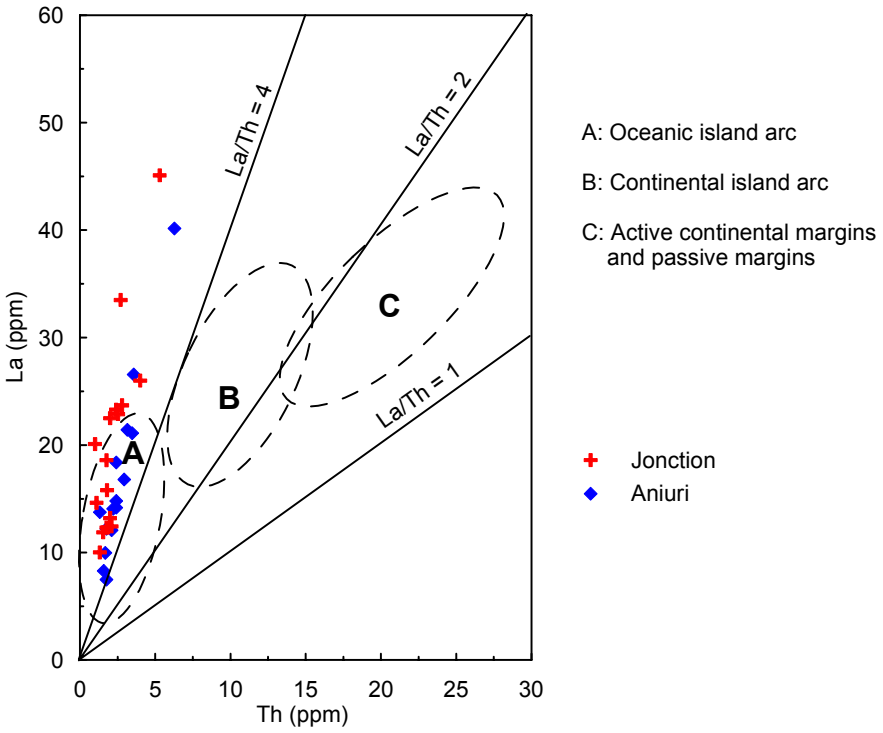

Figure 32. La-Th plot of metaarenite from Aniuri and Jonction for discrimination of tectonic setting. Dashed lines represent the dominant fields for various tectonic settings studied by Bhatia and Crook (1986).

The oceanic island arc setting is in agreement with a model presented by some authors (e.g. Ledru *et al.*, 1994) for the Birimian crust formation. According to that model, the Birimian crust formed through closure of an oceanic basin between two Archean cratons, with progressive accretion of island arcs and oceanic plateaus against a growing continental mass. This process involved a continental collision, which would correspond to the Eburnean tectonothermal event. Furthermore, based on the presence of lavas with frequent pillow structures and sediments virtually free of older recycled components, Abouchami *et al.* (1990) suggested that Birimian terranes formed in ocean basins far from continental influence.

3-4. Mineralogical and physico-chemical studies of gold mineralization

3-4-1. Mineralogical description of gold ores

The gold mineralization characteristics of the studied deposits of the Afema gold district (e.g. Aniuri and Jonction) are very similar. At the macroscopic scale, the main mineralization zones of both deposits are distinguished by a significant amount of sulfides (especially pyrite and arsenopyrite in variable proportions on the order of 1-10%) which are generally associated with quartz-carbonate veins parallel to the main regional schistosity (Figures 33A and 33B). This type of mineralization is also, characterized by rarity of “free gold” (i.e. native visible gold); therefore, it is considered as refractory ore. A second type of gold mineralization consists of native gold (± chalcopyrite) in quartz-carbonate veins. Both types of mineralization are hosted by the metaarenite and occur locally together. The second gold mineralization type has been observed at the Jonction deposit outside of the main mineralization zone. Contrary to the gold-bearing rock samples of the main mineralization zones, the rock samples from this latter type of mineralization are devoid of pyrite and arsenopyrite. The gold is “free” and appears in association with chalcopyrite directly in the quartz-carbonate veins. A typical example is presented in the Figure 33C with sample 1A6-53-97/151.70m. Note that the first type of mineralization as represented by pyrite- and arsenopyrite-rich ores is the main style of gold mineralization of Aniuri and Jonction. The second type of gold mineralization, i.e. native gold in quartz veins (without pyrite and arsenopyrite) is rarely found, and is generally associated with the sulfide rich ores in the main mineralization zones. Anyway, hand specimens (drill cores) of gold-bearing samples are generally silicified, carbonatized, sulfides-rich, and in cases with native gold (Figure 33). In the main mineralization zone, they contain locally graphite and/or chlorite. The particularity of the graphite is its cryptocrystalline nature, i.e. no visible crystallinity. This type of graphite is commonly called “amorphous graphite”. When present, it gives a smoky aspect to the quartz veins.

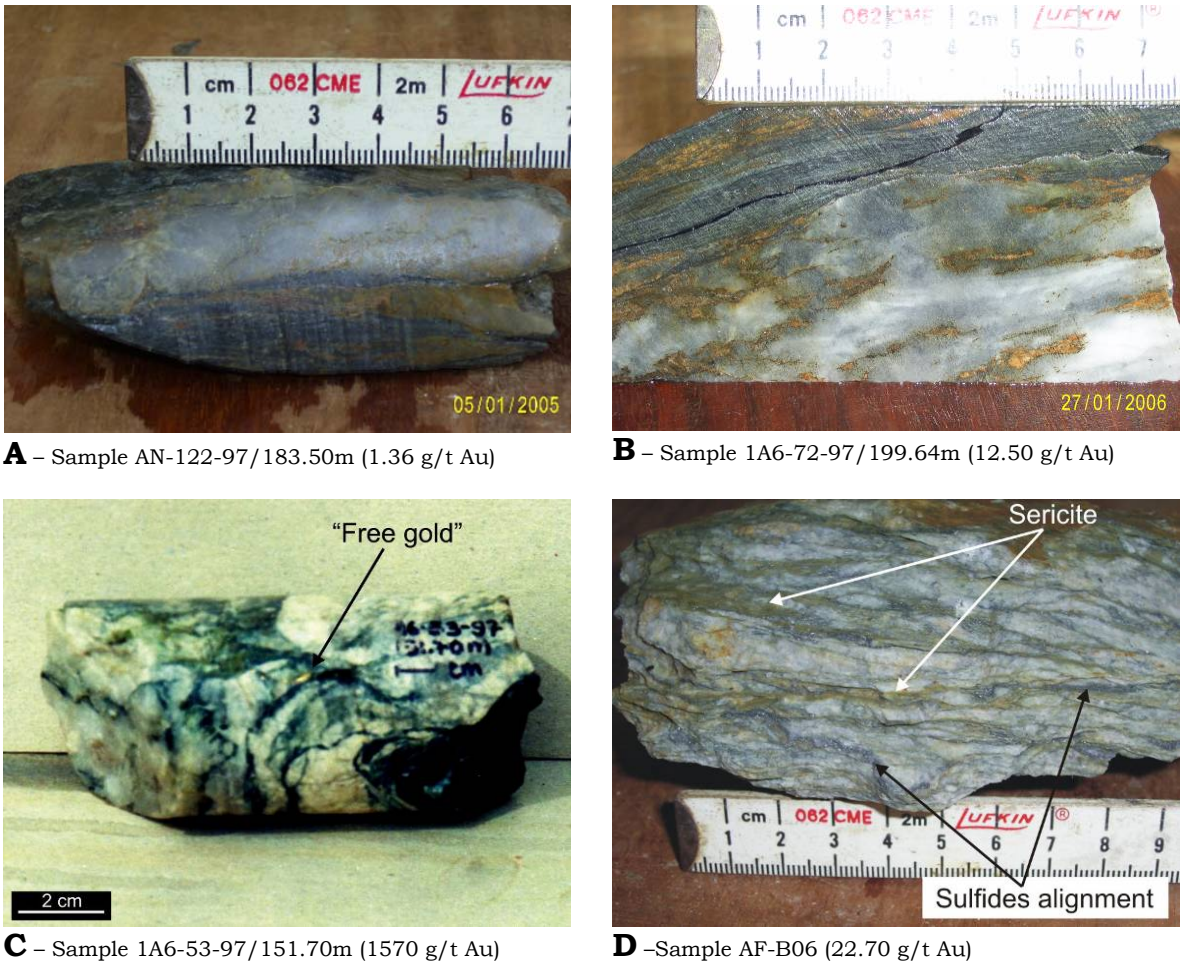

A – Sample AN-122-97/183.50m (1.36 g/t Au)

B – Sample 1A6-72-97/199.64m (12.50 g/t Au)

C – Sample 1A6-53-97/151.70m (1570 g/t Au)

D –Sample AF-B06 (22.70 g/t Au)

Figure 33. Typical hand specimens of gold-bearing ores. A) Gold-bearing drill core from the Aniuri deposit. B) Gold-bearing drill core from the Jonction deposit. In both cases, note the presence of quartz-carbonate veins and the deformed character of the rock. The carbonates (Fe-rich) show brownish color due to their oxidation. The sulfides (not visible on these images) are located in the walls of the quartz-carbonate veins (i.e. in the dark parts of the samples). C) Drill core from Jonction deposit, showing a speck "free gold" in a quartz-carbonate vein. D) Isolated gold-bearing sample, showing an alignment of sulfides (grey) following the schistosity orientation, which is expressed by sericitic levels (yellowish).

The quartz veins are deformed and alternate with sheet silicates and graphite, which give a foliated aspect of the hand specimen. The presence of iron carbonates in the mineralization zones is highlighted by a brownish color from oxidation on exposure of the drill cores for a certain time into air (Figures 33A and 33B).

The principal sulfides observed in the gold ores of Aniuri and Jonction are pyrite and arsenopyrite. Arsenopyrite seems to be the best indicator for the presence of gold. All rock samples with arsenopyrite are gold-bearing, while

pyrite occurs both in mineralized and barren samples. The amount of arsenopyrite is a good measure of gold grade. In drill core, arsenopyrite appears as fine needles generally with sizes <1 mm. Pyrite however, shows two variants: one with "large" size (millimeter-length), and the second with smaller size (generally <0.5 mm). Rock samples containing exclusively coarse-grained pyrite are generally barren with respect to gold content. Gold-bearing rock samples are furthermore distinguished by the alignment of sulfides following that of sericite and chlorite, which define the main regional schistosity (S_2) (Figure 33D).

In thin section, ore samples are distinguished by mylonitic textures resulting from ductile deformation. These textures are particularly characterized by the dynamic recrystallization of quartz grains and the orientation of sheet silicates (sericite, chlorite) and graphite. The quartz veins are also deformed, which gives them a ribbon-like aspect, commonly termed "quartz ribbons", with undulose extinction, elongated subgrains, and serrate grain boundaries (Figure 34).

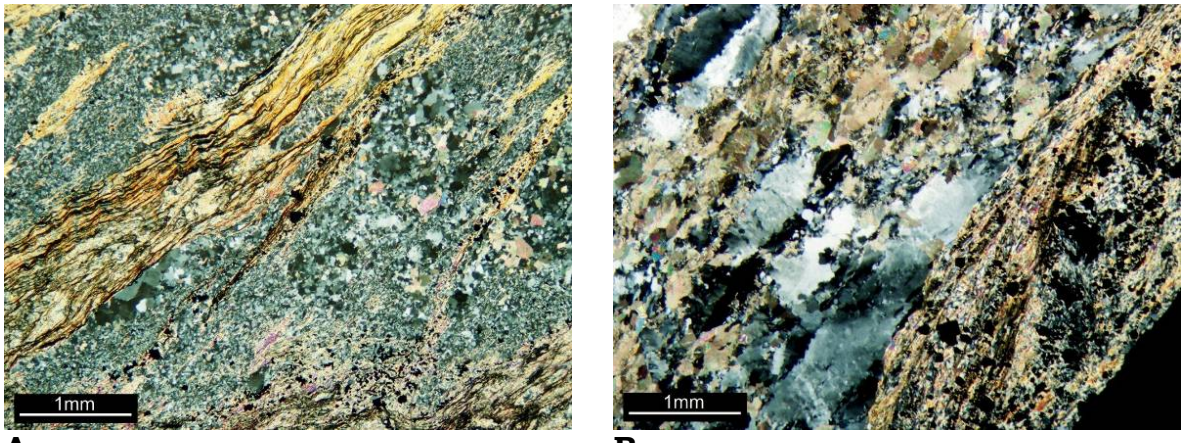

A – Sample 1A6-50-97/274m

B – Sample AN-72-94/116.70m

Figure 34. Gold-bearing samples showing a mylonitic texture (transmitted light, crossed nicols). A) Dynamic recrystallization of quartz in association with oriented aggregates of sericite, graphite and aligned sulfides. B) "Quartz ribbons" alternating with sericite, chlorite, graphite, and recrystallized quartz. Sulfides are observed in the inter-ribbon levels and carbonate is disseminated in the whole rock.

The main foliation (S_2) is expressed by the "quartz ribbons" and the alignment of minerals such as sericite, chlorite and graphite. These latter minerals represent with fine-grained quartz (recrystallized quartz) and sulfides the inter-ribbon material. Disseminated carbonate is abundant. By using the twinning pattern, these carbonate crystals can be identified as of dolomite-ankerite series composition (Figure 35). In fact, many rhombohedral carbonate minerals present rhombohedral cleavage and lamellar twins which are usually parallel to the edges or along the long diagonal axes of the rhombs. But, only dolomite-ankerite series may show lamellar twins parallel either to the long or the short diagonal axes of the rhombs (Nesse, 1991; MacKenzie and Guilford, 1992). This observation is in agreement with the data obtained from electron microprobe analysis on carbonates of the mineralization zones, which show compositions varying between those of dolomite and magnesian ankerite. The zones with very high content of carbonate are usually depleted in sulfides, and hence show relatively low content of gold.

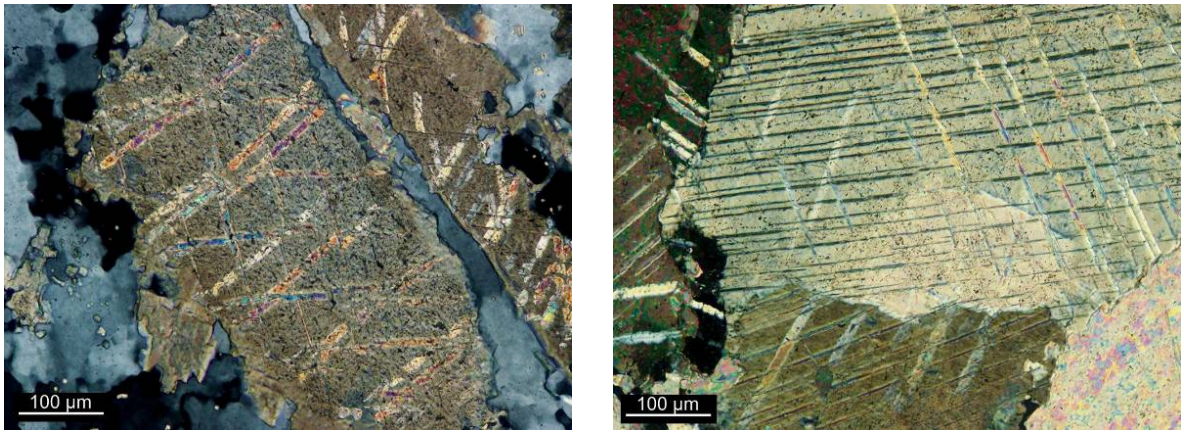

A – Sample AN-84-95/125.50m

B – Sample 1A6-50-97/278.40m

Figure 35. Carbonate crystals of gold-bearing samples with specific twinning characteristic of dolomite (transmitted light, crossed nicols). A) Aniuri deposit. B) Jonction deposit.

Microscopic observation of polished sections and electron microprobe analysis permitted to identify the ore minerals in the gold mineralization zones. The main ore minerals are pyrite [FeS_2], arsenopyrite [FeAsS] and rutile [TiO_2], accompanied by minor chalcopyrite [$CuFeS_2$], sphalerite [ZnS], tetrahedrite [$(Cu,Fe,Ag,Zn)_{12}Sb_4S_{13}$], tennantite [$(Cu,Ag,Zn,Fe)_{12}As_4S_{13}$], gold, and trace

amounts of pyrrhotite [$Fe_{1-x}S$] and galena [PbS]. Fluorapatite [$Ca_5(PO_4)_3F$], monazite [$(Ce,La,Nd,Th)PO_4$] and yttrium oxide [Y_2O_3] were identified as accessory minerals by electron microprobe. Pyrite and arsenopyrite are generally associated. Occasionally, pyrite hosts inclusions of arsenopyrite, chalcopyrite, sphalerite, and pyrrhotite (Figure 36). Pyrrhotite, in particular, has always been found as inclusion in pyrite.

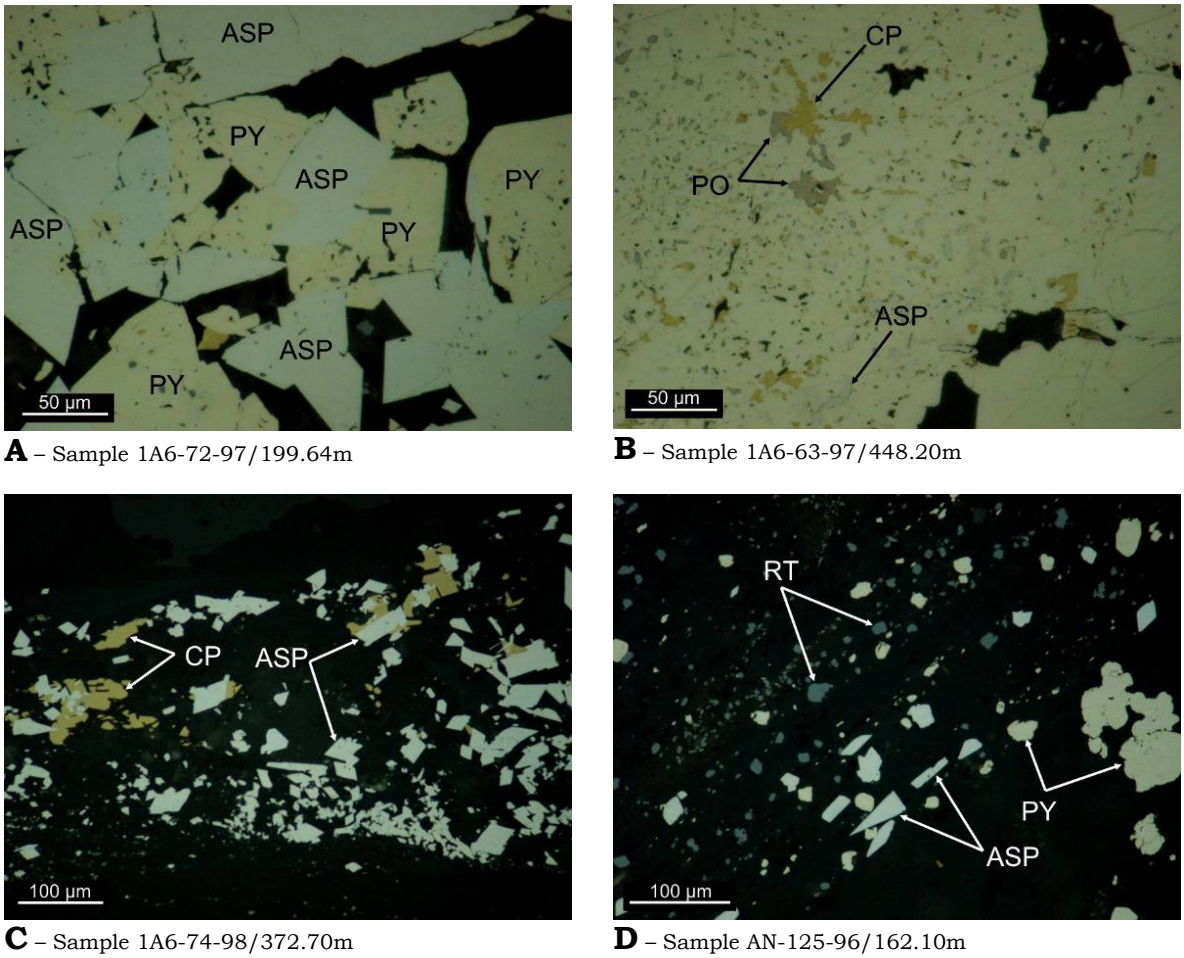

A – Sample 1A6-72-97/199.64m

B – Sample 1A6-63-97/448.20m

C – Sample 1A6-74-98/372.70m

D – Sample AN-125-96/162.10m

Figure 36. Ore minerals in the mineralization zones of Jonction and Aniuri (reflected light, in air). A) Association of pyrite and arsenopyrite representing the main sulfides of gold-bearing samples. B) Inclusions of chalcopyrite, pyrrhotite and arsenopyrite in a pyrite crystal. C) Fine-grained arsenopyrite associated with chalcopyrite in quartz. D) Alignment of pyrite, arsenopyrite and rutile following the direction of the schistosity. PY: pyrite; ASP: arsenopyrite; PO: pyrrhotite; CP: chalcopyrite; RT: rutile.

Pyrite occurs in two distinct crystal habits: (1) fine-grained pyrite (generally <500 µm in diameter) which is hypidiomorphic or xenomophic; (2) coarse-grained pyrite (from a few hundred micrometers to nearly 3 millimeters) which

is idiomorphic (Figure 37). Fine-grained pyrite is mostly observed in gold-bearing samples, whereas coarse-grained pyrite is ubiquitous. The fine-grained pyrite crystals are generally aligned following the direction of the schistosity. Coarse-grained pyrite crystals however are randomly distributed in the rock.

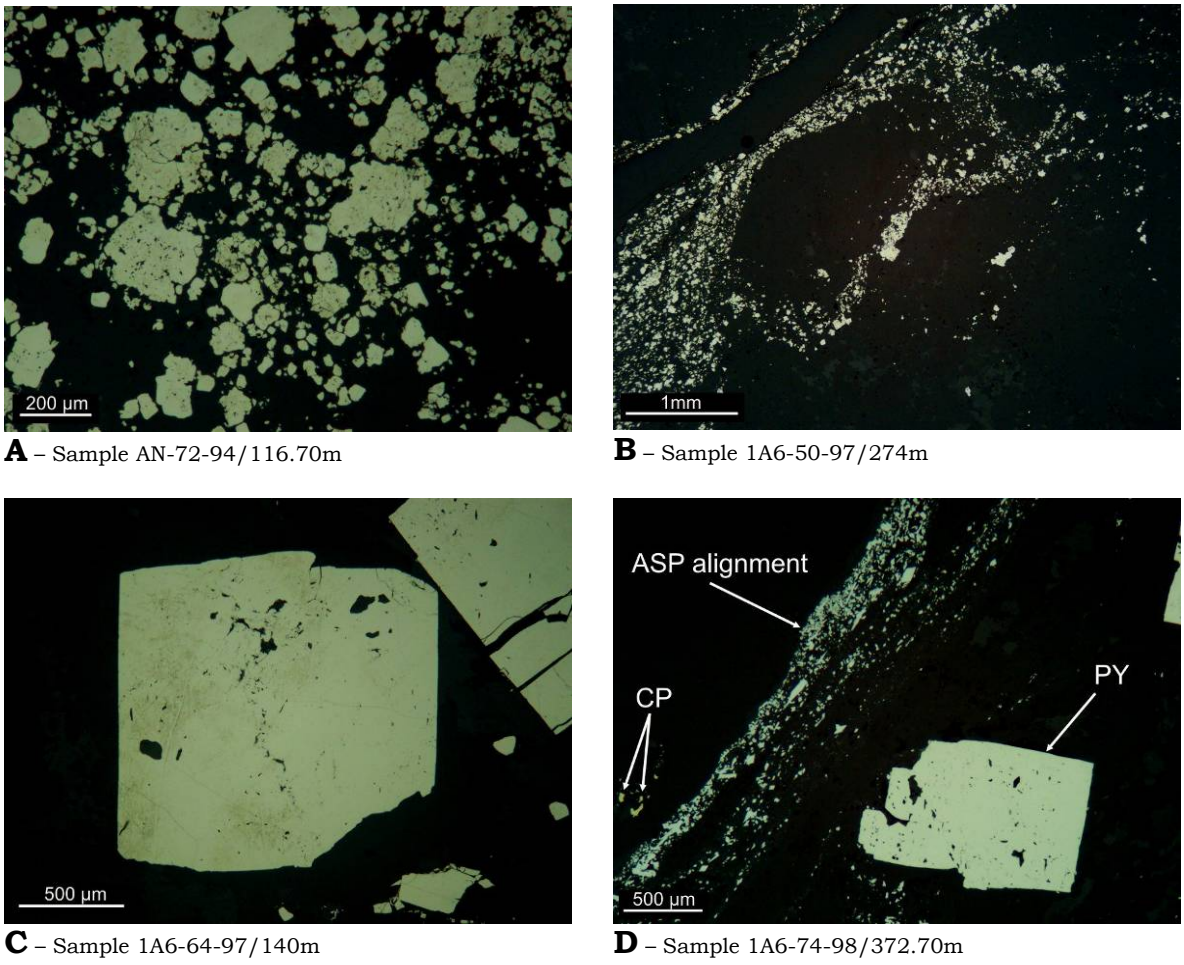

A – Sample AN-72-94/116.70m

B – Sample 1A6-50-97/274m

C – Sample 1A6-64-97/140m

D – Sample 1A6-74-98/372.70m

Figure 37. Different types of pyrite occurring in the studied deposits (reflected light, in air). A) Granular aggregates of fine-grained pyrite. B) Alignment of fine-grained pyrite. C) Coarse-grained pyrite. D) Coarse-grained pyrite occurring with arsenopyrite and chalcopyrite.

Arsenopyrite occurs idiomorphic and with small sizes (up to 300 µm). The crystals show a preferential orientation, which is parallel to the main regional schistosity. Arsenopyrite is generally found in gold-bearing samples having more than 3 ppm Au. It is completely absent in barren rock samples (e.g. Au <0.5 ppm), which is not the case for pyrite.

Chalcopyrite and sphalerite occur in small amounts in many samples. Most commonly, they are found as inclusions in pyrite crystals. In a few cases, they are observed as individual crystals in the gangue minerals. Both occur as xenomorphic crystals and measure up to some tens of micrometers. They are mostly associated.

Pyrrhotite is rare. It is essentially observed as xenomorphic inclusions in some pyrite crystals from Jonction deposit. It measures only a few tens of micrometers.

Rutile is very common. In fact, it is omnipresent in both ores and non-mineralized host rocks. Rutile is fine-grained (generally <50 μm), showing irregular shapes and generally aligned parallel to the direction of the schistosity. Locally, some grains reach 200 μm in size. Rutile is furthermore observed as inclusions in pyrite and arsenopyrite crystals, by filling cavities or fractures in those minerals.

Tetrahedrite and tennantite are xenomorphic and generally fill fractures in pyrite. They are in places associated with chalcopyrite.

Galena is rare. It occurs as small crystal (up to 50 μm) in the gangue minerals.

In a few cases, fluorapatite is observed in the mineralization zone samples. It presents various sizes (up to 200 μm) and appears in association with gangue minerals.

Monazite is rarely found as very small inclusions (only a few micrometers) in some pyrite crystals.

Yttrium oxide (recognized by microprobe analysis) occurs as xenomorphic fine crystals (<50 μm) associated with rutile trails. It has been observed in only one sample of the Aniuri deposit.

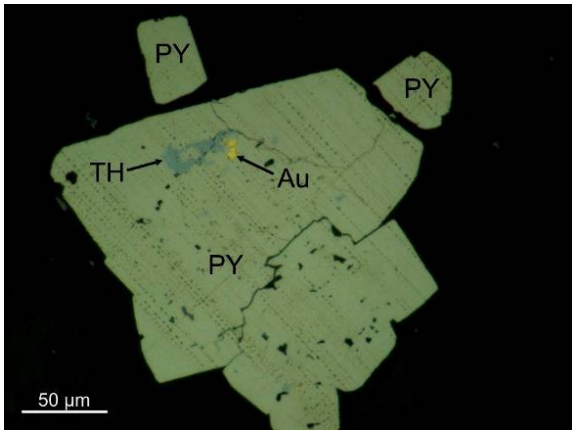

A – Sample 1A6-63-97/469m

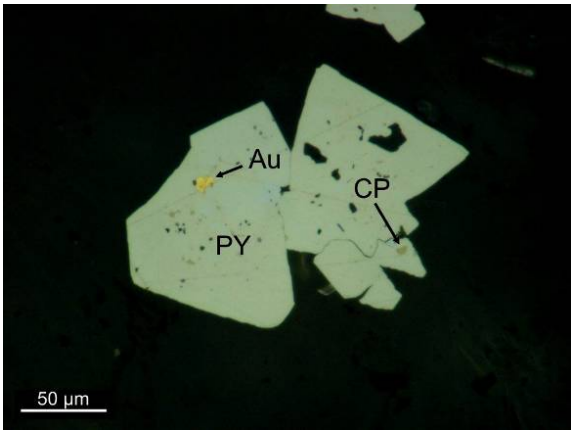

B – Sample 1A6-72-97/199.64m

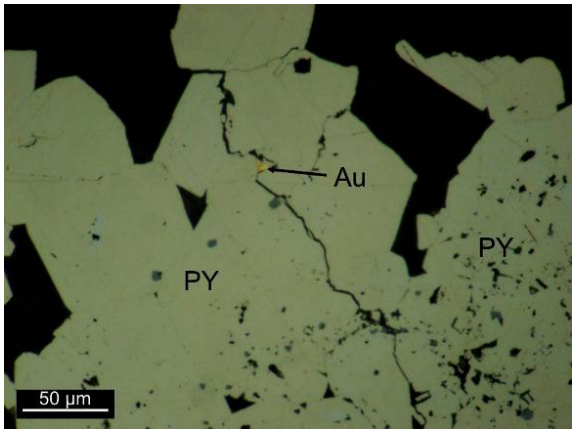

C – Sample AN-125-96/167.30m

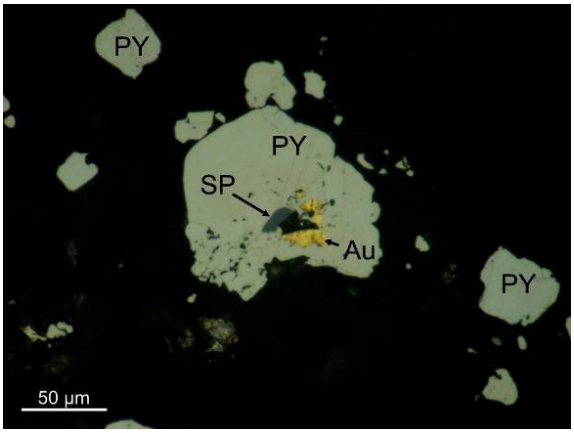

D – Sample AN-72-94/116.70m

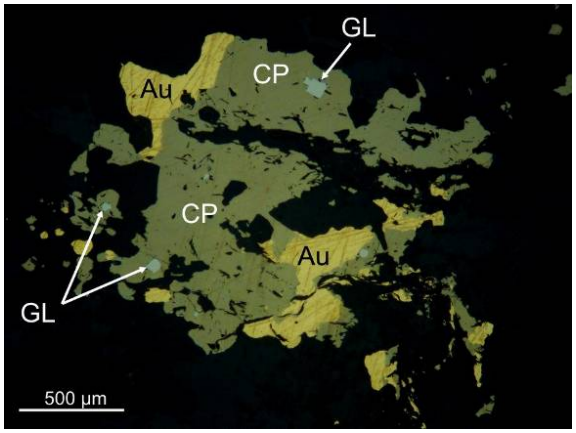

E – Sample 1A6-53-97/151.70m

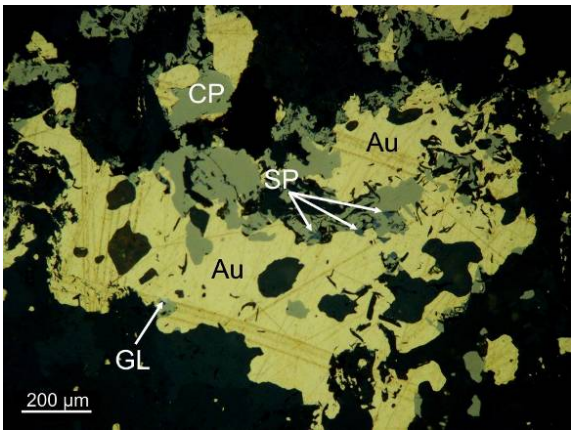

F – Sample 1A6-53-97/151.70m

Figure 38. Microscopic observation of gold. A) Tetahedrite and gold occurring in a fracture of pyrite. B) Gold as inclusions in a pyrite crystal. C) Gold in a fracture in pyrite crystals. D) Gold and sphalerite in a cavity of a pyrite crystal. E) and F) Native gold in quartz-carbonate gangue (free gold) associated with chalcopyrite, galena and sphalerite. Reflected light, in air.

Usually, gold is easily observed in polished sections of rock samples with grades above 10 ppm Au, and it occurs essentially as micrometric inclusions or as interstitial fillings in pyrite crystals (Figures 38A to 38D). Although, the

amount of arsenopyrite seems to positively correlate with gold content in the different samples, gold is rarely observed in arsenopyrite crystals. In pyrite, gold inclusions occur generally in fractures and cavities.

The above microscopic description of gold distribution is characteristic of the main mineralization zones of the Aniuri and Jonction deposits. A second type of gold mineralization occurs as individual gold aggregates in gangue minerals without association with pyrite and arsenopyrite. The ore minerals observed in this latter type of gold mineralization are principally chalcopyrite and a minor amount of sphalerite and galena (Figures 38E and 38F). This type of gold mineralization was recognized in only one sample from the Jonction deposit.

Graphite was identified in some gold-bearing hand specimen samples but occurs only relictically in polished sections. This is probably due to the removal of graphite during the polishing process (figure 39).

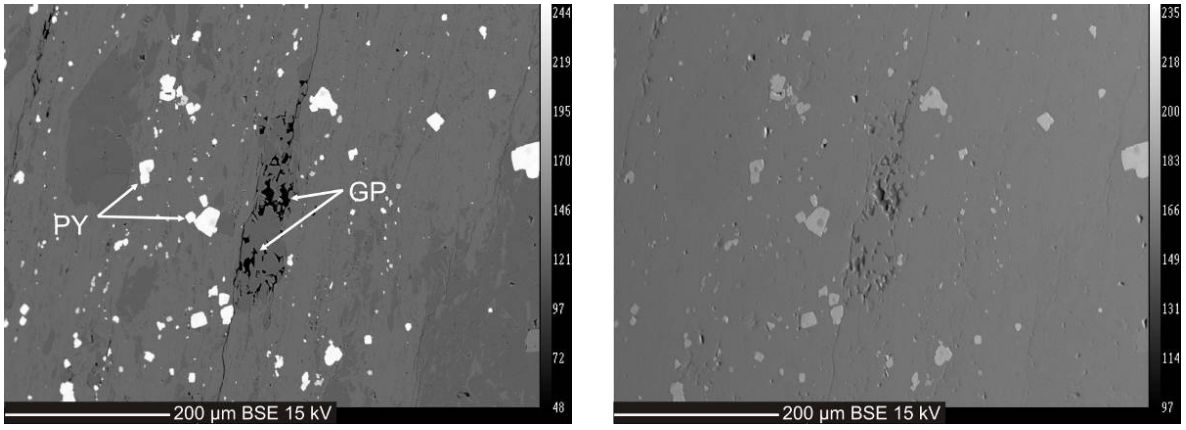

A – Sample 1A6-50-97/274m

B – Sample 1A6-50-97/274m (Topography)

Figure 39. Backscattered electron (BSE) images of graphite in a gold-bearing sample. A) Polished section showing graphite retained in the fractures of the sample after polishing. B) The same BSE image, but with a topographic view, which highlights the cavities in which graphite is retained.

3-4-2. Time relation between deformation and ore minerals

This section aims to establish the relative chronology between sulfides and deformation events, as well as between the different types of sulfides.

Ore minerals (e.g. sulfides, rutile-anatase) are aligned and oriented parallel to the direction of the main regional schistosity (Figures 36D and 40A). They are generally molded by oriented sheet silicates (e.g. sericite, chlorite) and graphite, which define this schistosity (Figure 40B). In addition, most sulfide crystals develop on their faces strain fringes (also called pressure fringes), represented by quartz fibers. Generally, strain fringes occurring around sulfide crystals are characterized by face-controlled and non-deformed fibers (Figure 40C). A few crystals, however, present strain fringes distinguished by face controlled and displacement fibers, which suggests simple shear (Figure 40D). The above observations indicate the synkinematic nature of the sulfides. The mineralization occurred, therefore, during development of the schistosity (e.g. deformation). Coarse-grained pyrite crystals, contrary to fine-grained pyrite and arsenopyrite, present locally two distinct generations of quartz fibers (strain fringes) on their faces (Figure 40E). This fact would mean that coarse-grained pyrite has undergone at least two successive episodes of deformation. In addition, coarse-grained pyrite seems to be much more affected by brittle deformation than fine-grained pyrite (Figure 40F). Considering these latter elements, coarse-grained pyrite seems to have formed earlier in comparison to fine-grained pyrite and arsenopyrite. In short, the sulfides (ore minerals in general) can be considered to be deposited during the deformation events, with coarse-grained pyrite earlier-formed compared to fine-grained pyrite and arsenopyrite.

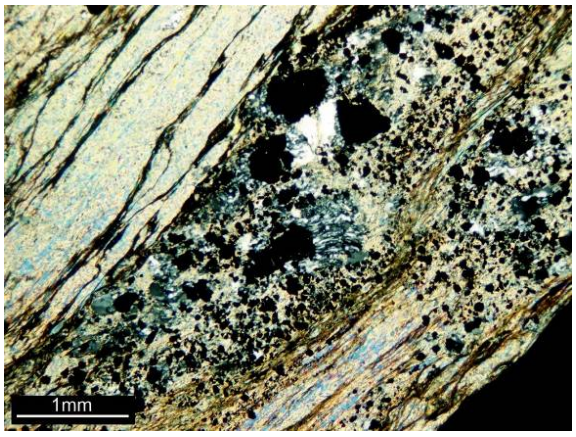

A – Sample AN-72-94/116.70m

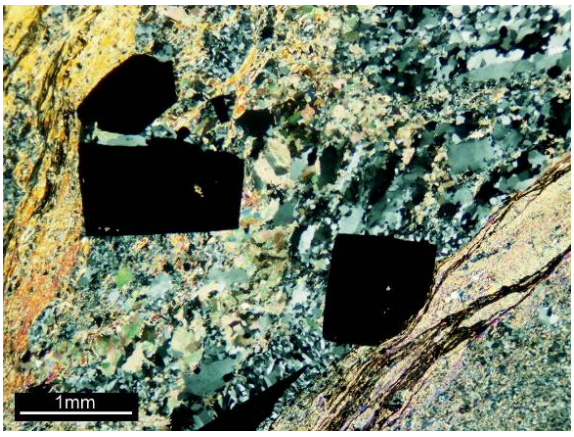

B – Sample 1A6-74-98/372.70m

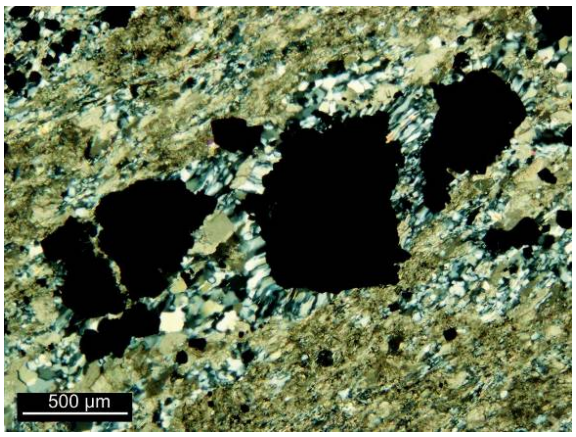

C – Sample 1A6-72-97/199.64m

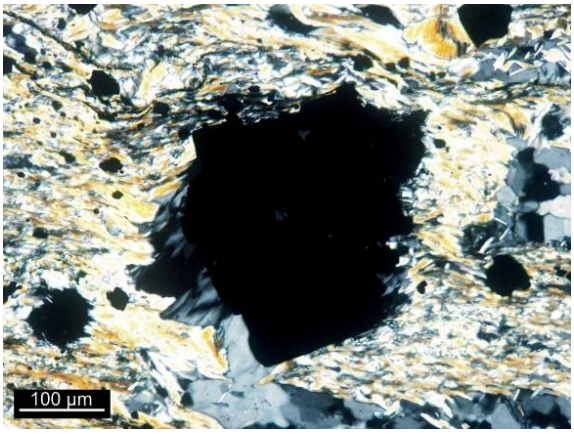

D – Sample 1A6-50-97/274m

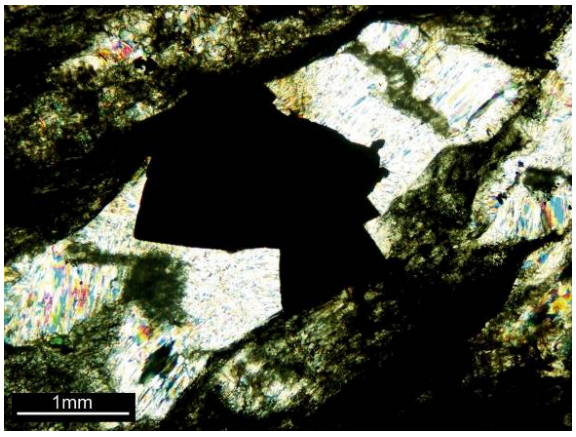

E – Sample 1A6-64-97/140m

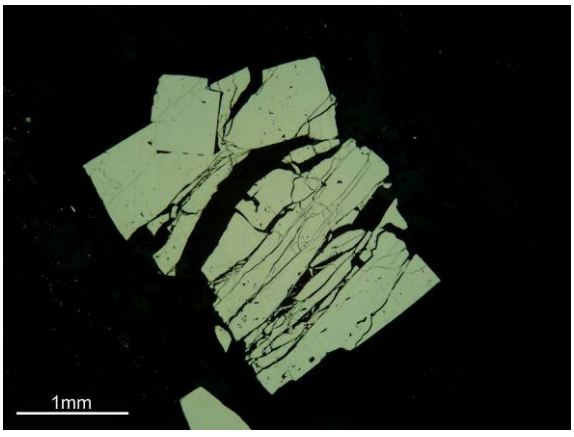

F – Sample 1A6-64-97/140m

Figure 40. Sulfide deformation textures. A) Alignment of sulfides (fine-grained pyrite and arsenopyrite) following the direction of the schistosity (transmitted light, crossed nicols). B) Sulfides (coarse-grained pyrite crystals) molded by oriented sericite and graphite (transmitted light, crossed nicols). C) Aligned sulfides showing strain fringes with face-controlled and non-deforming fibers. D) Sulfides with dextral antiaxial strain fringes indicating simple shear (transmitted light, crossed nicols). E) Thick section showing two distinct generations of quartz fibers representing strain fringes around a coarse-grained pyrite crystal. Note that the high interference colors of the quartz fibers are due to the thickness of this section (transmitted light, crossed nicols). F) Polished section showing a coarse-grained highly fractured pyrite crystal (reflected light, in air).

3-4-3. Chemical and textural studies of ore minerals

In the previous sections, a positive correlation between gold content of rock samples and the presence of some sulfides (e.g. arsenopyrite and pyrite) was pointed out. Furthermore, the existence of two types of pyrite (e.g. fine-grained and coarse-grained pyrite), and the occurrence of gold as microscopic grains in some pyrite crystals was observed, where the location of gold is in micro-fractures and cavities. This section aims to shed light on the compositional and textural variations of ore minerals (pyrite and arsenopyrite in particular), based on electron microprobe analysis and complemented by reconnaissance laser ablation ICP-MS analysis.

Pyrite and arsenopyrite are the major ore minerals of the studied deposits, and their compositional trend can be appreciated in a ternary diagram Fe-As-S. All analyzed arsenopyrite crystals are arsenic-deficient and enriched in sulfur relative to stoichiometric arsenopyrite, which is characterized by As = 33.33 at.%, S = 33.33 at.% and Fe = 33.33 at.% (Figure 41). All data are along the line representing the stoichiometric composition $FeAs_{1-x}S_{1+x}$, where the ratio Fe:(As+S) is 1:2. With regard to pyrite, one notes a trend toward arsenopyrite composition. This trend is along the stoichiometric line of arsenopyrite. The trend of arsenic-deficient arsenopyrite is in accordance with the fact that, löllingite is observed in none of the studied polished sections from the mineralization zones.

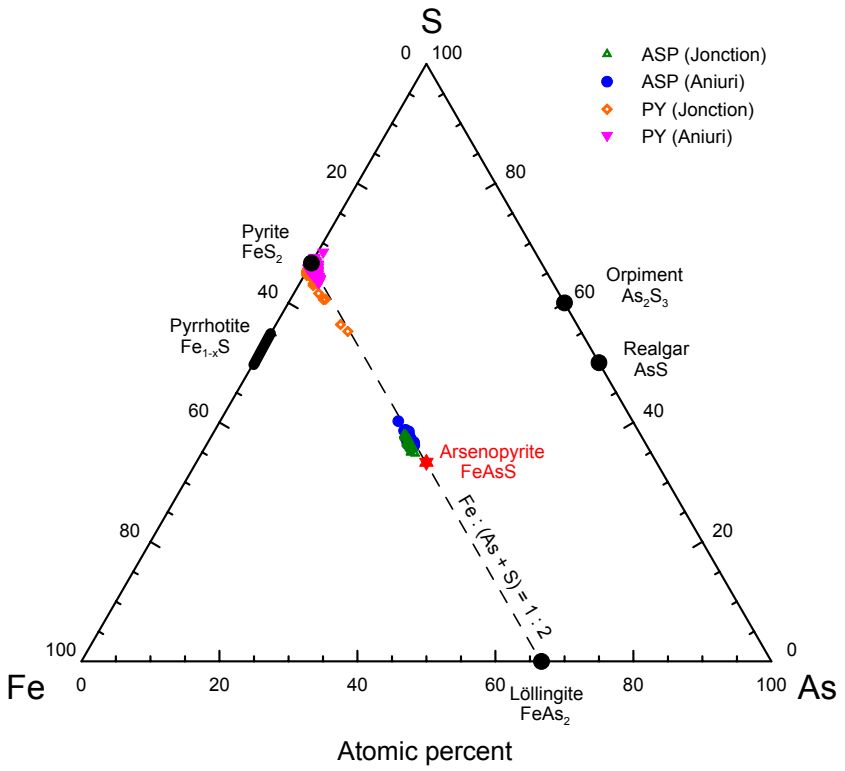

Figure 41. Arsenopyrite and pyrite compositions of the mineralization zones of Jonction and Aniuri in the ternary system Fe-As-S.

The compositional trend of pyrite, presented on the ternary diagram of Figure 41, indicates a slight enrichment in arsenic. Note that the arsenic-rich pyrite corresponds very often to fine-grained pyrite. The enrichment in arsenic of this type of pyrite is always coupled with sulfur deficiency (i.e. strong negative correlation between As and S) (Figure 42), suggesting a substitution mechanism between As and S. In consequence, the formula of the arsenian pyrite can be written as: $Fe(As_xS_{1-x})_2$, where x commonly ranges between 0.016 and 0.045, corresponding approximately to 2 to 5 wt.% of arsenic in the case of the Jonction and Aniuri deposits (Table 7). In very rare cases, arsenian pyrite containing more than 15 wt.% of arsenic has been observed.

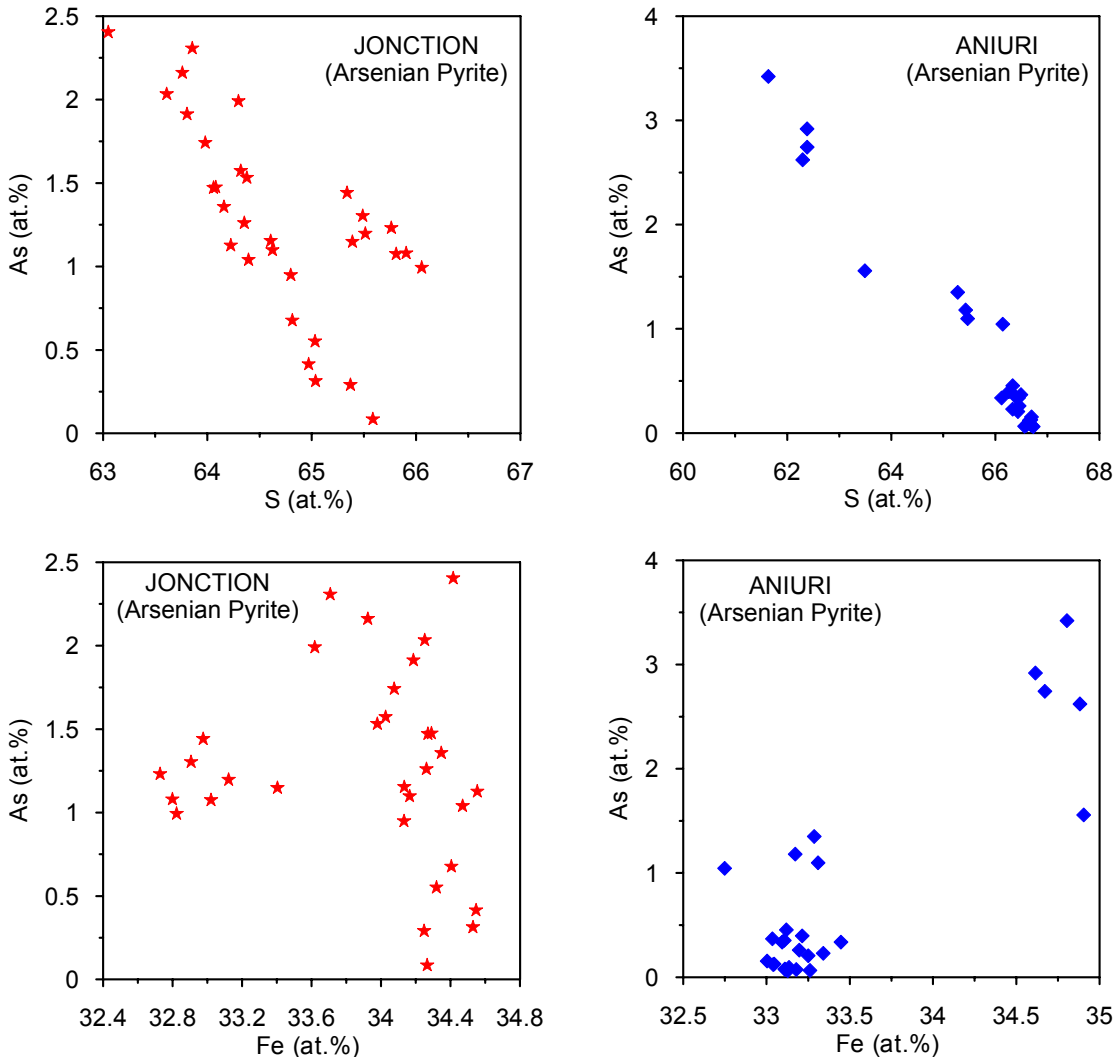

Figure 42. Distribution of As versus S and versus Fe of arsenian pyrite from Jonction and from Aniuri.

Backscattered electron (BSE) images and electron microprobe analysis permitted to highlight zonal textures and compositions occurring in some sulfide crystals. Fine-grained arsenian pyrite represents the main zoned sulfide. The zoning is expressed by zonal arrangement of cavities (partial dissolution by corrosion) and zonal arrangement of inclusions of some minerals (e.g. chalcopyrite, arsenopyrite, and pyrrhotite), which gives a poikilitic texture of arsenian pyrite crystals. The zoning in arsenian pyrite is furthermore expressed by variation in the sulfur and arsenic content. Arsenic-rich zones of arsenian pyrite crystals appear lighter grey than non-arsenic or arsenic-poor zones (Figure 43 and Table 7).

Table 7. Electron microprobe analyses of pyrite, arsenopyrite and gold from Jonction and Aniuri. The spot positions are shown on Figures 43, 45, 47 and 50 below. The last five data in italic (spot numbers 86 to 90) were obtained with different analytical settings, in which the detection limit of gold was significantly decreased to about 40 ppm instead of 600 ppm for the rest of data. F-PY: fine-grained pyrite; C-PY: coarse-grained pyrite; ASP: arsenopyrite.

Rock sample	Spot N°	Mineral type	Composition (wt. %)												Formula (a.p.f.u.)					As/S
			S (0.03)	Fe (0.04)	Co (0.03)	Ni (0.02)	Zn (0.06)	As (0.03)	Ag (0.05)	Sb (0.04)	Au (0.06)	Cu (0.05)	Pb (0.4)	Total	Co	Ni	Fe	As	S	
1A6-63-97/	1	F-PY	53.17	45.50	0.00	0.09	0.02	0.26	0.02	0.00	0.00	0.02	0.00	99.07	0.000	0.002	0.986	0.004	2.007	0.002
448.20m	2	F-PY	53.18	45.56	0.00	0.05	0.02	0.24	0.02	0.00	0.01	0.00	0.00	99.08	0.000	0.001	0.987	0.004	2.007	0.002
	3	F-PY	53.09	45.42	0.00	0.05	0.05	0.18	0.01	0.00	0.00	0.02	0.00	98.83	0.000	0.001	0.987	0.003	2.008	0.001
(6.33 g/t Au)	4	F-PY	53.26	45.40	0.00	0.01	0.03	0.08	0.01	0.00	0.00	0.03	0.04	98.86	0.000	0.000	0.985	0.001	2.013	0.001
	5	F-PY	52.09	45.36	0.00	0.00	0.02	2.58	0.03	0.00	0.05	0.04	0.00	100.16	0.000	0.000	0.986	0.042	1.972	0.021
	6	F-PY	51.61	44.68	0.00	0.01	0.04	2.16	0.02	0.00	0.03	0.06	0.03	98.63	0.000	0.000	0.984	0.035	1.980	0.018
	7	ASP	20.39	32.85	0.00	1.30	0.02	41.52	0.00	0.01	0.00	0.02	0.00	96.11	0.000	0.037	0.980	0.923	1.059	0.871
	8	ASP	19.83	32.70	0.69	0.35	0.00	42.61	0.01	0.03	0.00	0.04	0.00	96.25	0.020	0.010	0.981	0.953	1.036	0.920
1A6-72-97/	9	ASP	21.23	35.68	0.02	0.08	0.03	41.12	0.02	0.00	0.13	0.03	0.00	98.34	0.000	0.002	1.035	0.889	1.072	0.829
199.64m	10	ASP	21.47	35.79	0.00	0.02	0.00	40.81	0.00	0.01	0.00	0.02	0.00	98.12	0.000	0.001	1.036	0.881	1.082	0.814
	11	F-PY	52.07	46.50	0.00	0.07	0.02	1.10	0.03	0.00	0.03	0.06	0.00	99.88	0.000	0.001	1.010	0.018	1.970	0.009
(12.50 g/t Au)	12	F-PY	49.70	46.40	0.00	0.02	0.02	3.15	0.04	0.00	0.05	0.05	0.00	99.41	0.000	0.000	1.029	0.052	1.919	0.027
	13	F-PY	50.30	46.29	0.00	0.01	0.03	2.73	0.02	0.00	0.06	0.03	0.17	99.64	0.000	0.000	1.021	0.045	1.933	0.023
	14	F-PY	52.36	46.29	0.00	0.07	0.02	0.32	0.03	0.00	0.00	0.02	0.00	99.11	0.000	0.001	1.008	0.005	1.985	0.003
1A6-63-97/	15	F-PY	53.70	46.39	0.00	0.03	0.02	0.13	0.02	0.00	0.02	0.02	0.00	100.31	0.000	0.001	0.994	0.002	2.004	0.001
448.20m	16	F-PY	52.18	45.75	0.00	0.01	0.03	2.16	0.01	0.01	0.05	0.04	0.00	100.25	0.000	0.000	0.993	0.035	1.972	0.018
	17	F-PY	52.36	45.38	0.00	0.24	0.02	2.00	0.01	0.01	0.07	0.03	0.00	100.11	0.000	0.005	0.984	0.032	1.978	0.016
(6.33 g/t Au)	18	F-PY	52.71	45.84	0.00	0.01	0.03	1.74	0.00	0.01	0.05	0.04	0.00	100.42	0.000	0.000	0.990	0.028	1.982	0.014
	19	F-PY	53.52	46.22	0.00	0.00	0.03	0.91	0.00	0.02	0.04	0.03	0.00	100.76	0.000	0.000	0.989	0.014	1.996	0.007
	20	F-PY	51.92	45.72	0.00	0.00	0.03	2.22	0.01	0.01	0.12	0.18	0.00	100.20	0.000	0.000	0.995	0.036	1.968	0.018
	21	F-PY	52.15	45.20	0.00	0.05	0.05	2.28	0.03	0.02	0.14	0.20	0.24	100.35	0.000	0.001	0.984	0.037	1.977	0.019
	22	F-PY	51.80	45.33	0.00	0.01	0.04	2.41	0.02	0.05	0.14	0.31	0.10	100.21	0.000	0.000	0.990	0.039	1.970	0.020
	23	F-PY	52.52	45.91	0.00	0.00	0.05	1.70	0.02	0.00	0.05	0.04	0.00	100.29	0.000	0.000	0.993	0.027	1.979	0.014
	24	F-PY	52.19	45.89	0.00	0.02	0.03	2.07	0.00	0.01	0.05	0.04	0.00	100.29	0.000	0.000	0.995	0.033	1.971	0.017
AN-125-96/	25	F-PY	53.82	45.62	0.00	0.01	0.00	0.18	0.02	0.00	0.00	0.04	0.00	99.70	0.000	0.000	0.981	0.003	2.016	0.001
167.30m	26	F-PY	53.75	45.61	0.00	0.04	0.00	0.25	0.01	0.00	0.00	0.02	0.00	99.67	0.000	0.001	0.981	0.004	2.014	0.002
	27	F-PY	53.47	45.58	0.00	0.00	0.01	0.83	0.02	0.00	0.02	0.02	0.00	99.94	0.000	0.000	0.981	0.013	2.005	0.007
(8.28 g/t Au)	28	F-PY	53.61	45.81	0.00	0.01	0.01	0.73	0.04	0.00	0.03	0.00	0.01	100.24	0.000	0.000	0.984	0.012	2.004	0.006
	29	F-PY	54.04	45.64	0.00	0.01	0.01	0.11	0.01	0.01	0.01	0.02	0.03	99.89	0.000	0.000	0.979	0.002	2.019	0.001
	30	F-PY	53.31	45.55	0.00	0.00	0.00	0.99	0.03	0.00	0.01	0.03	0.02	99.93	0.000	0.000	0.982	0.016	2.002	0.008
	31	F-PY	51.81	45.08	0.00	0.00	0.03	2.76	0.00	0.03	0.01	0.04	0.00	99.76	0.000	0.000	0.984	0.045	1.970	0.023
	32	F-PY	52.54	45.31	0.00	0.00	0.03	1.94	0.02	0.00	0.07	0.03	0.01	99.96	0.000	0.000	0.983	0.031	1.985	0.016
	33	F-PY	52.06	45.02	0.00	0.00	0.03	2.42	0.00	0.00	0.03	0.01	0.00	99.57	0.000	0.000	0.982	0.039	1.978	0.020
	34	ASP	22.25	35.10	0.00	0.01	0.01	40.84	0.02	0.01	0.06	0.05	0.00	98.35	0.000	0.000	1.010	0.875	1.114	0.786
	35	ASP	23.28	35.08	0.00	0.01	0.02	39.89	0.00	0.01	0.15	0.04	0.00	98.48	0.000	0.000	0.999	0.847	1.154	0.734
	36	F-PY	52.30	44.75	0.00	0.01	0.01	2.26	0.00	0.00	0.01	0.03	0.00	99.37	0.000	0.000	0.976	0.037	1.987	0.019
	37	F-PY	53.32	45.40	0.00	0.00	0.03	1.06	0.00	0.00	0.01	0.02	0.00	99.84	0.000	0.000	0.979	0.017	2.003	0.009
	38	F-PY	52.23	45.53	0.00	0.00	0.04	2.26	0.00	0.00	0.01	0.02	0.00	100.09	0.000	0.000	0.988	0.037	1.974	0.019
	39	F-PY	52.46	45.23	0.00	0.09	0.00	1.88	0.03	0.00	0.06	0.03	0.08	99.86	0.000	0.002	0.983	0.030	1.985	0.015
	40	F-PY	53.19	45.54	0.00	0.00	0.03	0.97	0.00	0.01	0.00	0.02	0.08	99.85	0.000	0.000	0.983	0.016	2.000	0.008
	41	F-PY	52.11	45.00	0.00	0.00	0.00	2.26	0.02	0.00	0.02	0.04	0.00	99.45	0.000	0.000	0.982	0.037	1.981	0.019
	42	ASP	22.09	35.37	0.00	0.08	0.01	41.35	0.00	0.01	0.04	0.01	0.00	98.97	0.000	0.002	1.013	0.883	1.102	0.801
	43	ASP	22.63	35.88	0.00	0.01	0.01	40.58	0.03	0.03	0.00	0.03	0.00	99.18	0.000	0.000	1.020	0.860	1.120	0.768
	44	ASP	22.02	35.51	0.00	0.10	0.01	41.37	0.01	0.00	0.12	0.03	0.00	99.15	0.000	0.003	1.017	0.883	1.098	0.804
	45	ASP	21.96	35.72	0.00	0.04	0.03	41.41	0.01	0.00	0.26	0.04	0.01	99.47	0.000	0.001	1.022	0.883	1.094	0.807
	46	ASP	22.77	36.54	0.00	0.00	0.03	40.52	0.03	0.03	0.00	0.02	0.00	99.94	0.000	0.000	1.030	0.851	1.118	0.762
	47	ASP	23.02	36.02	0.00	0.01	0.02	39.97	0.00	0.02	0.01	0.01	0.00	99.07	0.000	0.000	1.020	0.844	1.136	0.743
	48	ASP	21.92	35.53	0.00	0.04	0.02	41.34	0.00	0.00	0.30	0.05	0.00	99.20	0.000	0.001	1.019	0.884	1.095	0.807
	49	ASP	21.75	35.19	0.00	0.01	0.03	41.52	0.02	0.01	0.14	0.02	0.00	98.69	0.000	0.000	1.015	0.892	1.092	0.817

Table 7 continued

Rock sample	Spot N°	Mineral type	Composition (wt. %)												Formula (a.p.f.u.)					As/S
			S (0.03)	Fe (0.04)	Co (0.03)	Ni (0.02)	Zn (0.06)	As (0.03)	Ag (0.05)	Sb (0.04)	Au (0.06)	Cu (0.05)	Pb (0.4)	Total	Co	Ni	Fe	As	S	
AN-122-96/	50	F-PY	51.58	46.86	0.00	0.00	0.03	0.96	0.03	0.00	0.00	0.03	0.06	99.54	0.000	0.000	1.023	0.016	1.961	0.008
184.50m	51	F-PY	48.81	45.72	0.00	0.00	0.03	4.80	0.03	0.01	0.06	0.04	0.23	99.71	0.000	0.000	1.021	0.080	1.898	0.042
	52	F-PY	48.44	45.43	0.00	0.00	0.04	5.12	0.02	0.01	0.06	0.06	0.29	99.47	0.000	0.000	1.020	0.086	1.894	0.045
(5.98 g/t Au)	53	F-PY	51.89	46.41	0.00	0.00	0.03	0.81	0.01	0.00	0.02	0.05	0.00	99.23	0.000	0.000	1.013	0.013	1.973	0.007
	54	F-PY	52.27	46.84	0.00	0.00	0.02	0.05	0.02	0.01	0.01	0.06	0.07	99.34	0.000	0.000	1.019	0.001	1.980	0.000
	55	F-PY	52.19	46.38	0.00	0.02	0.04	0.14	0.01	0.01	0.00	0.02	0.00	98.82	0.000	0.000	1.012	0.002	1.984	0.001
	56	F-PY	50.22	45.91	0.00	0.00	0.05	2.76	0.02	0.03	0.01	0.03	0.15	99.18	0.000	0.000	1.017	0.046	1.937	0.024
	57	F-PY	51.47	46.85	0.00	0.03	0.03	0.91	0.03	0.00	0.02	0.03	0.06	99.44	0.000	0.001	1.024	0.015	1.960	0.008
AN-84-95/	58	F-PY	51.66	46.80	0.00	0.01	0.02	2.26	0.01	0.01	0.05	0.02	0.00	100.81	0.000	0.000	1.014	0.036	1.949	0.019
125.50m	59	F-PY	50.87	46.54	0.00	0.00	0.01	3.37	0.02	0.00	0.03	0.03	0.00	100.87	0.000	0.000	1.014	0.055	1.931	0.028
	60	F-PY	53.52	47.40	0.00	0.00	0.02	0.22	0.00	0.00	0.01	0.03	0.01	101.23	0.000	0.000	1.010	0.004	1.986	0.002
(12.57 g/t Au)	61	F-PY	53.06	47.29	0.00	0.03	0.00	0.48	0.02	0.00	0.01	0.03	0.04	100.97	0.000	0.001	1.013	0.008	1.979	0.004
	62	F-PY	50.37	46.39	0.00	0.00	0.04	4.01	0.00	0.01	0.01	0.04	0.00	100.88	0.000	0.000	1.015	0.065	1.919	0.034
	63	F-PY	51.14	46.60	0.00	0.03	0.04	2.92	0.02	0.00	0.00	0.03	0.00	100.79	0.000	0.001	1.014	0.047	1.938	0.024
	64	F-PY	52.75	47.18	0.00	0.11	0.03	0.90	0.01	0.00	0.00	0.04	0.00	101.02	0.000	0.002	1.012	0.014	1.971	0.007
	65	F-PY	52.55	47.00	0.00	0.23	0.05	0.90	0.00	0.01	0.00	0.04	0.00	100.78	0.000	0.005	1.011	0.014	1.969	0.007
	66	Gold	0.04	0.36	0.00	0.00	0.04	0.00	4.52	0.00	89.13	0.07	0.00	94.16						
AN-72-94/	67	Gold	2.88	3.57	0.00	0.00	0.05	0.19	5.36	0.02	84.54	0.22	4.67	101.50						
116.70m	68	Gold	4.88	3.08	0.00	0.03	0.06	0.31	5.88	0.00	81.83	0.31	0.00	96.37						
	69	Gold	1.20	1.07	0.02	0.01	0.04	0.02	5.38	0.03	79.27	0.24	0.00	87.27						
(25.50 g/t Au)	70	F-PY	53.65	46.35	0.00	0.49	0.01	0.14	0.00	0.00	0.05	0.01	0.00	100.71	0.000	0.010	0.991	0.002	1.997	0.001
	71	F-PY	52.07	45.98	0.00	0.17	0.02	2.20	0.03	0.01	0.14	0.03	0.14	100.78	0.000	0.003	0.996	0.035	1.965	0.018
	72	F-PY	52.42	46.45	0.00	0.06	0.03	2.05	0.03	0.01	0.10	0.04	0.00	101.20	0.000	0.001	1.000	0.033	1.965	0.017
1A6-64-97/	73	C-PY	52.88	46.75	0.00	0.00	0.01	0.04	0.02	0.00	0.02	0.00	0.00	99.72	0.000	0.000	1.010	0.001	1.989	0.000
140m	74	C-PY	52.87	46.44	0.00	0.00	0.01	0.12	0.01	0.00	0.00	0.01	0.00	99.47	0.000	0.000	1.005	0.002	1.993	0.001
	75	C-PY	52.48	47.32	0.00	0.01	0.03	0.22	0.02	0.00	0.02	0.01	0.00	100.10	0.000	0.000	1.022	0.003	1.974	0.002
(0.02 g/t Au)	76	C-PY	52.20	47.41	0.00	0.01	0.02	0.30	0.01	0.00	0.01	0.01	0.00	99.96	0.000	0.000	1.026	0.005	1.968	0.002
	77	C-PY	52.18	47.08	0.00	0.02	0.02	0.32	0.00	0.00	0.00	0.00	0.04	99.64	0.000	0.000	1.022	0.005	1.973	0.003
	78	C-PY	52.21	47.21	0.00	0.00	0.00	0.19	0.02	0.00	0.00	0.00	0.00	99.63	0.000	0.000	1.024	0.003	1.973	0.002
	79	C-PY	51.92	47.44	0.00	0.01	0.01	0.37	0.01	0.00	0.00	0.00	0.00	99.76	0.000	0.000	1.030	0.006	1.964	0.003
	80	C-PY	51.74	46.96	0.00	0.00	0.01	0.24	0.03	0.00	0.00	0.00	0.01	99.01	0.000	0.000	1.026	0.004	1.969	0.002
	81	C-PY	51.77	46.97	0.00	0.02	0.01	0.35	0.02	0.00	0.00	0.01	0.05	99.19	0.000	0.000	1.025	0.006	1.968	0.003
	82	C-PY	51.98	47.46	0.00	0.00	0.00	0.15	0.01	0.00	0.01	0.00	0.00	99.62	0.000	0.000	1.031	0.002	1.967	0.001
	83	C-PY	51.98	47.69	0.00	0.00	0.02	0.10	0.02	0.00	0.00	0.00	0.02	99.84	0.000	0.000	1.034	0.002	1.964	0.001
	84	C-PY	51.75	47.55	0.00	0.00	0.00	0.24	0.01	0.01	0.00	0.01	0.00	99.57	0.000	0.000	1.035	0.004	1.961	0.002
	85	C-PY	51.70	47.66	0.00	0.00	0.01	0.26	0.01	0.00	0.00	0.01	0.00	99.65	0.000	0.000	1.037	0.004	1.959	0.002
			S (0.06)	Fe (0.07)	Co (0.002)			As (0.005)	Ag (0.006)		Au (0.004)	Cu (0.05)		Total	Co		Fe	As	S	
1A6-74-98/	*86*	*C-PY*	*54.495*	*47.738*	*0.002*			*0.603*	*0.000*		*0.001*	*0.002*		*102.841*	*0.000*		*1.001*	*0.009*	*1.990*	*0.005*
372.70m	*87*	*C-PY*	*54.186*	*47.902*	*0.003*			*0.345*	*0.003*		*0.004*	*0.000*		*102.443*	*0.000*		*1.008*	*0.005*	*1.986*	*0.003*
	88	*C-PY*	*54.909*	*47.602*	*0.003*			*0.575*	*0.004*		*0.000*	*0.000*		*103.094*	*0.000*		*0.994*	*0.009*	*1.997*	*0.004*
(7.10 g/t Au)	*89*	*C-PY*	*53.911*	*47.552*	*0.002*			*0.401*	*0.000*		*0.001*	*0.000*		*101.866*	*0.000*		*1.006*	*0.006*	*1.987*	*0.003*
	90	*C-PY*	*53.418*	*47.038*	*0.002*			*0.542*	*0.004*		*0.003*	*0.006*		*101.013*	*0.000*		*1.005*	*0.009*	*1.987*	*0.004*

Figure 44 presents analytical profiles across a zoned arsenian pyrite crystal shown on Figure 43C. Gold occurs exclusively in the arsenic-rich part of the pyrite crystal. Furthermore, the content of gold correlates positively with that of arsenic. Cu also occurs in the arsenic-rich parts of the crystal, but without correlation with any element mentioned on the diagrams (e.g. S, Fe, Au and Ni). The presence of Cu is principally due to inclusions of chalcopyrite in this part of the pyrite crystal. Ni however, seems to occur randomly in the pyrite.

Coarse-grained pyrite, contrary to fine-grained pyrite, is totally unzoned, arsenic-poor and barren with respect to gold content (Figure 45 and Table 7). A profile across a crystal of this type of pyrite (Figures 45B and 46) shows its compositional homogeneity. Its gold content is below the detection limit (about 600 ppm), which is nevertheless considered to be too high. So, additional analyses were performed on the same crystals with a significantly improved gold detection limit of 40 ppm. Again the gold content is below this improved detection limit (Table 7). To come to a solid conclusion concerning the abundance of gold in this type of pyrite particularly, we then used laser ablation - inductively coupled plasma - mass spectrometry (LA-ICP-MS), which has a gold detection limit 0.01 - 0.02 ppm. The results are presented in Table 8. Coarse-grained pyrite is indeed barren; its gold content does not exceed 0.5 ppm, while gold in fine-grained pyrite (e.g. arsenian pyrite) reaches up to about 140 ppm (Figure 49). We conclude that, coarse-grained pyrite (e.g. arsenic-poor pyrite) is very low in gold (<0.5 ppm Au), while fine-grained pyrite (e.g. arsenian pyrite) is gold-bearing (up to ca. 2000 ppm Au, see Table 7).

Arsenopyrite appears in acicular crystals and is often intergrown with corroded pyrite (Figure 47A). Arsenopyrite, compared to arsenian pyrite, is relatively homogeneous, although weak variations in the arsenic and sulfur content have been observed in some crystals. This is also expressed by a kind of slight variation in the grey color of the BSE images, where lighter grey zones correspond to higher As/S mole ratio (Figures 47 and 48). Most of the arsenopyrite crystals are devoid of inclusions and signs of corrosion. At Aniuri as well as at Jonction, arsenopyrite is generally gold-bearing, with a rough

positive correlation between its gold content and the As/S mole ratio (Figure 48).

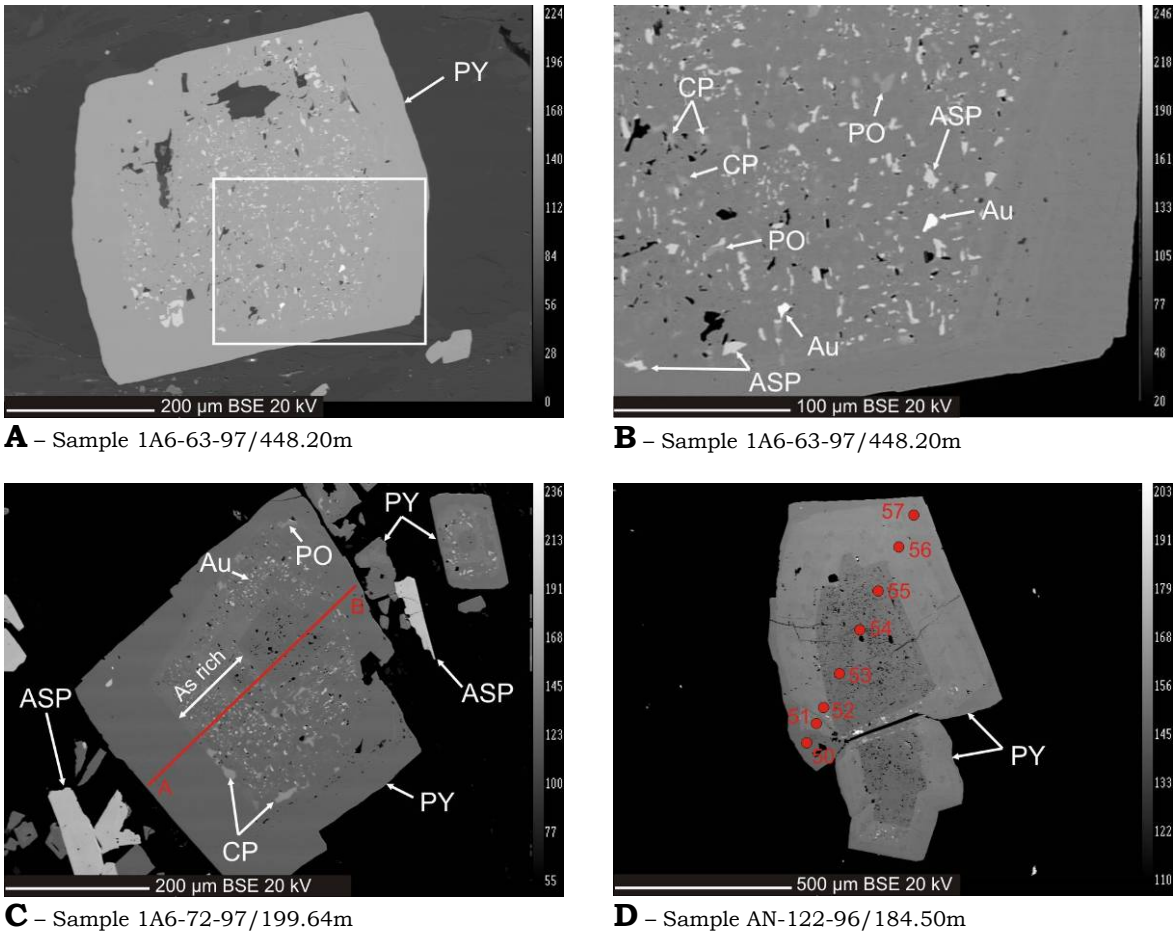

A – Sample 1A6-63-97/448.20m

B – Sample 1A6-63-97/448.20m

C – Sample 1A6-72-97/199.64m

D – Sample AN-122-96/184.50m

Figure 43. BSE images of fine-grained pyrite from gold-bearing samples of Jonction and Aniuri showing zonal textures. The numbers correspond to the analytical positions of EMPA presented in Table 7. A) Pyrite crystal showing partial dissolution and poikilitic texture in its central part. B) Close up view of part of the pyrite crystal of the previous image showing inclusions of gold, arsenopyrite, chalcopyrite and pyrrhotite in its central part. C) Pyrite crystal with three distinct zones from the core to the rim: arsenic-poor and partially dissolved zone - arsenic-rich, poikilitic and partially dissolved zone - arsenic-poor and non dissolved zone. The line A-B marks the EPMA profile shown in Figure 44. D) Zoned crystal of pyrite with overgrowth of arsenic-rich periphery around arsenic-poor and partially dissolved core. Note the well-preserved outline of early-formed crystal.

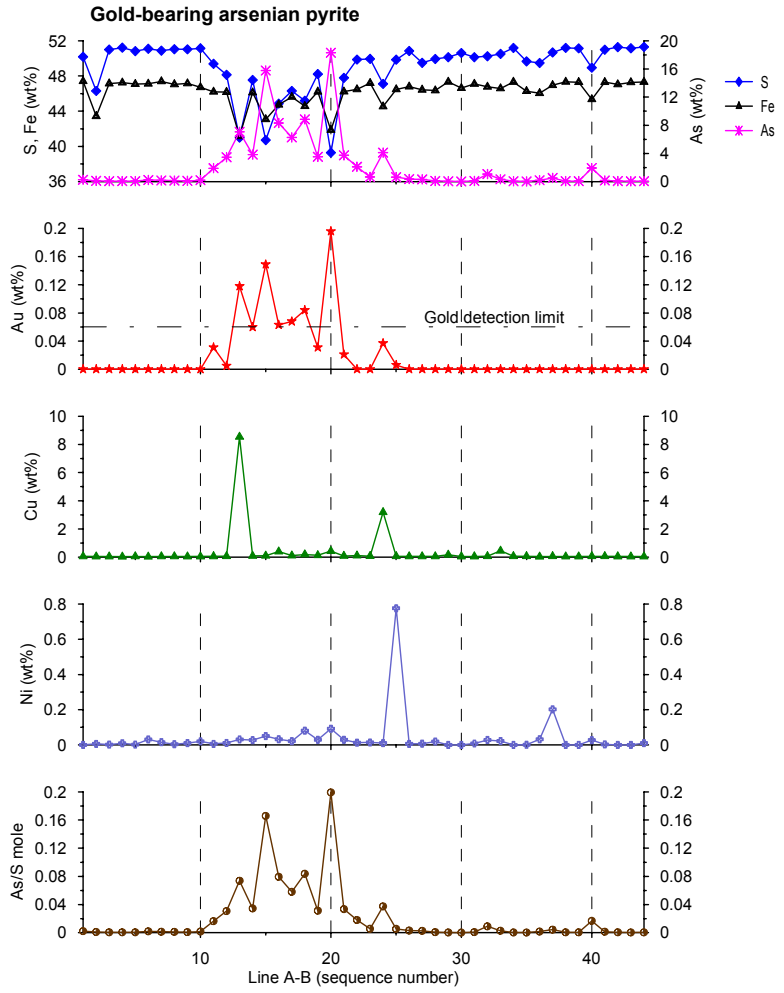

Figure 44. Analytical profile across a zoned fine-grained arsenian pyrite crystal (see Figure 43C for crystal image) – Sample 1A6-72-97/199.64m.

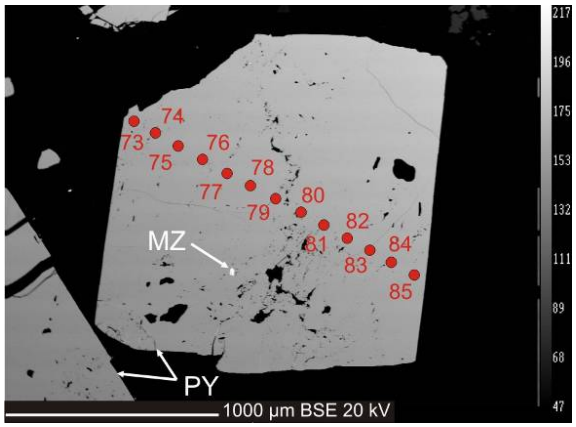

A – Sample 1A6-64-97/140m

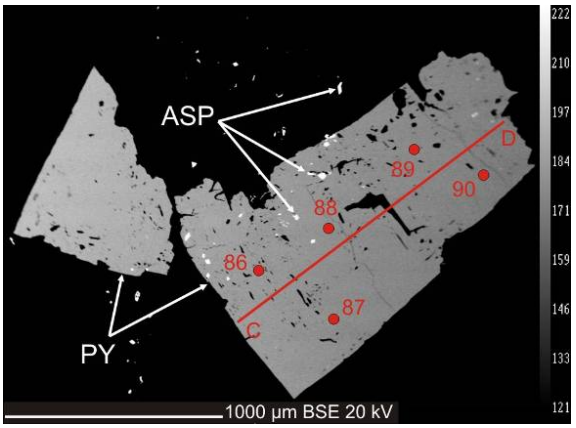

B – Sample 1A6-74-98/372.70m

Figure 45. BSE images of coarse-grained pyrite devoid of zoning and arsenic-poor. A) Coarse-grained pyrite with inclusion of monazite. B) Crystals of coarse-grained pyrite incorporating tiny crystals of arsenopyrite in cavities. The line C-D marks the EMPA profile shown in Figure 46.

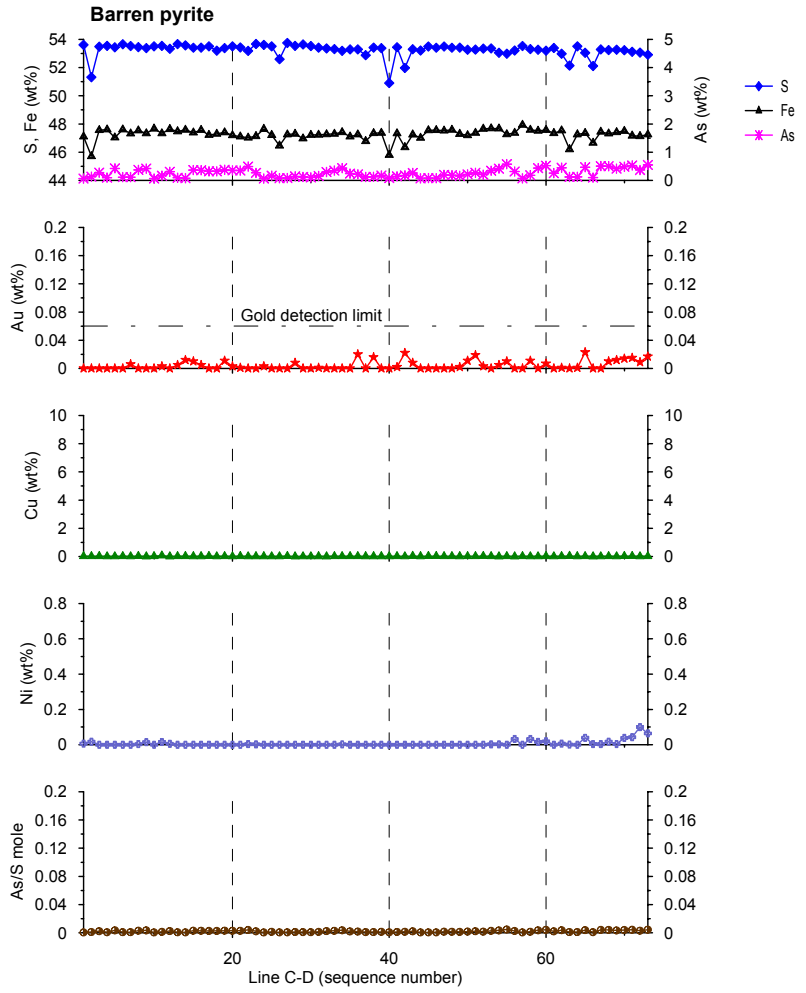

Figure 46. Analytical profile across a non-zoned coarse-grained pyrite crystal (see Figure 45B for crystal image) – Sample 1A6-74-98/372.70m

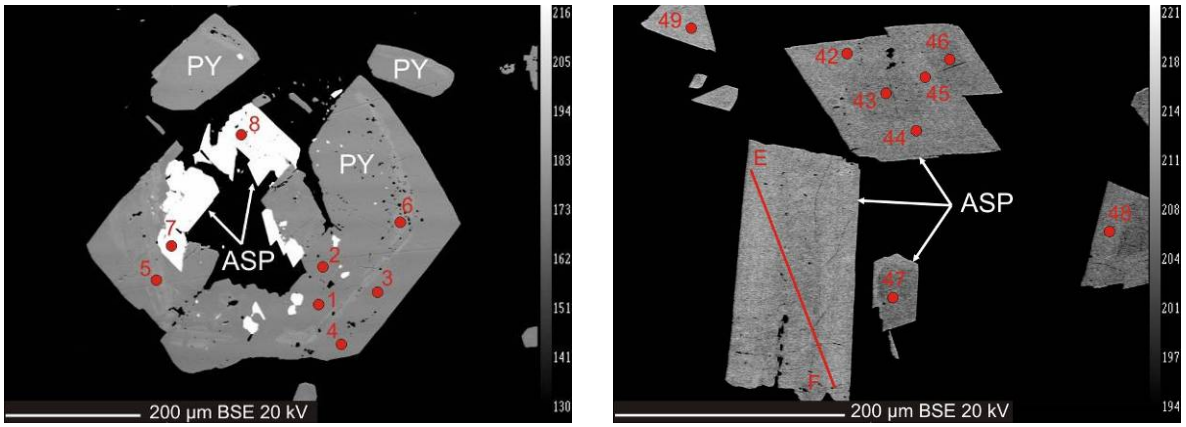

A – Sample 1A6-63-97/448.20m

B – Sample AN-125-96/167.30m

Figure 47. BSE images of arsenopyrite. A) Arsenopyrite located in corroded arsenian pyrite crystal. B) Gold-bearing arsenopyrite weakly zoned. The line E-F marks the EMPA profile shown in Figure 48.

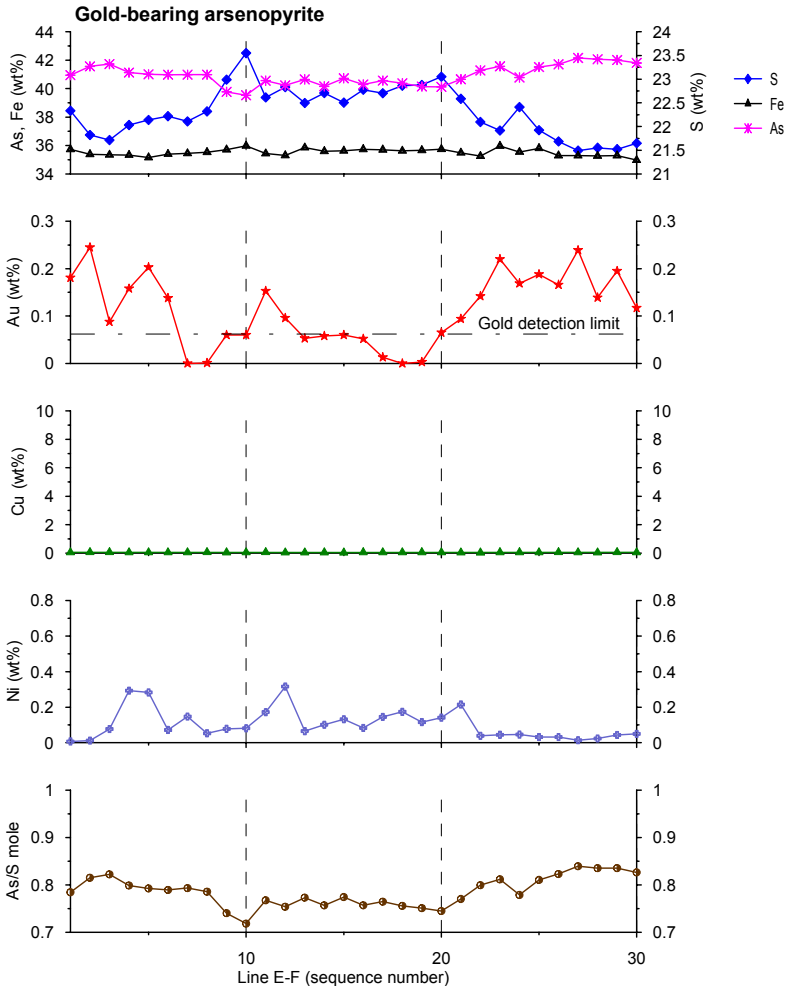

Figure 48. Analytical profile across a slightly zoned arsenopyrite crystal (see Figure 47B for crystal image) – Sample AN-125-96/167.30m

In fact, the gold content seems to positively correlate with the arsenic content of arsenopyrite. Contrary to arsenian pyrite, arsenopyrite does not show microscopic inclusions of gold; but electron microprobe analysis reveals up to 3000 ppm Au. LA-ICP-MS analyses confirmed the regular presence of gold in arsenopyrite crystals (Table 8). Thus, gold is essentially present in arsenopyrite in submicroscopic form, whereas in pyrite, it mostly occurs as microscopic inclusions. The arsenopyrite composition in both studied deposits is similar. It shows arsenic contents ranging from 37.0 to 42.7 wt.% and occasionally elevated contents of cobalt (up to 2.3 wt.%) and nickel (up to 2.5 wt.%). Antimony is quite absent in the arsenopyrite (<0.1 wt.%).

Table 8. Laser ablation – inductively coupled plasma – mass spectrometry (LA-ICP-MS) analyses of fine-grained pyrite (F-PY), coarse-grained pyrite (C-PY), and arsenopyrite (ASP). The rock sample 1A6-74-98/372.70m with 7.10 g/t Au is from Jonction and the rock sample AN-122-96/184.50m with 5.98 g/t Au is from Aniuri. All spots in coarse-grained pyrite have less than 0.5 ppm Au, except spot J-23. This latter analysis point is attributed to an inclusion of gold-bearing arsenopyrite inside the coarse-grained pyrite crystal.

Rock sample 1A6-74-98/372.70m (7.10 g/t Au)					
Spot No.	Mineral type	Au (ppm)	Spot No.	Mineral type	Au (ppm)
J-1	ASP	391	J-19	C-PY	0.08
J-2	ASP	313	J-20	C-PY	0.04
J-3	ASP	98	J-21	C-PY	<0.02
J-5	ASP	152	J-22	C-PY	0.05
J-6	ASP	223	J-22a	C-PY	0.10
			J-23	C-PY	5.23
J-7	ASP	173	J-24	C-PY	0.04
J-8	ASP	145	J-25	C-PY	0.04
J-9	ASP	197	J-26	C-PY	0.08
J-10	ASP	109	J-27	C-PY	0.46
			J-28	C-PY	0.04
J-11	C-PY	0.37			
J-12	C-PY	0.11	J-29	C-PY	0.02
J-13	C-PY	<0.01	J-30	C-PY	0.05
J-14	C-PY	0.05	J-31	C-PY	0.06
J-15	C-PY	0.04	J-32	C-PY	<0.01
J-16	C-PY	<0.01	J-33	C-PY	0.19
J-17	C-PY	0.04	J-34	C-PY	0.10
J-18	C-PY	0.15	J-35	C-PY	0.04

Rock sample AN-122-96/184.50m (5.98 g/t Au)					
Spot No.	Mineral type	Au (ppm)	Spot No.	Mineral type	Au (ppm)
A-1	ASP	42.10	A-16	F-PY	74.50
A-2	ASP	53.50	A-17	F-PY	45.90
A-3	ASP	40.20	A-18	F-PY	1.59
A-4	ASP	31.00	A-19	F-PY	4.75
			A-20	F-PY	6.54
A-5	ASP	18.50	A-21	F-PY	22.20
A-6	ASP	686.0	A-22	F-PY	5.00
A-7	ASP	9.02	A-23	F-PY	45.90
A-8	ASP	30.50	A-24	F-PY	5.68
			A-25	F-PY	3.80
A-9	ASP	7.23	A-26	F-PY	6.06
A-10	ASP	15.40	A-27	F-PY	62.70
A-11	ASP	26.20			
			A-28	ASP	0.11
A-12	F-PY	27.70	A-29	ASP	55.20
A-13	F-PY	1.63	A-30	F-PY	96.30
A-14	F-PY	1.84	A-31	ASP	1.46
A-15	F-PY	141.00	A-32	ASP	3.55

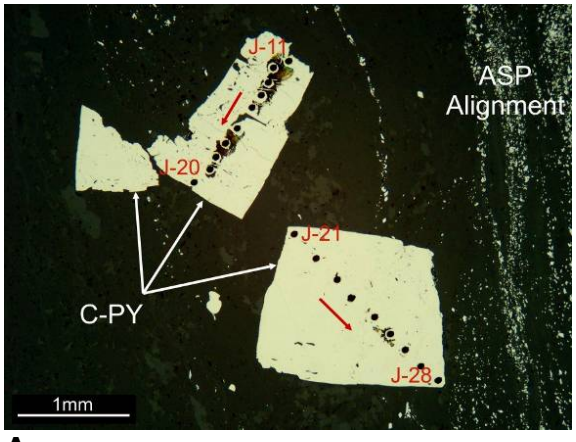

A – Sample 1A6-74-98/372.70m

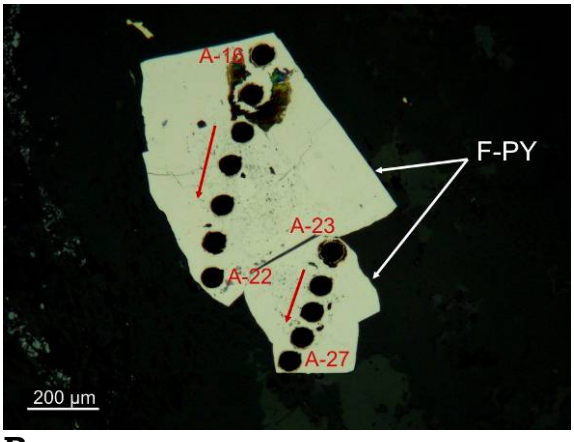

B – Sample AN-122-96/184.50m

Figure 49. Coarse-grained pyrite (C-PY) and fine-grained pyrite (F-PY) analyzed by LA-ICP-MS. The same crystals were also analyzed by electron microprobe (Figures 43D and 45B). The gold contents corresponding to the different analytical spots are presented in Table 8.

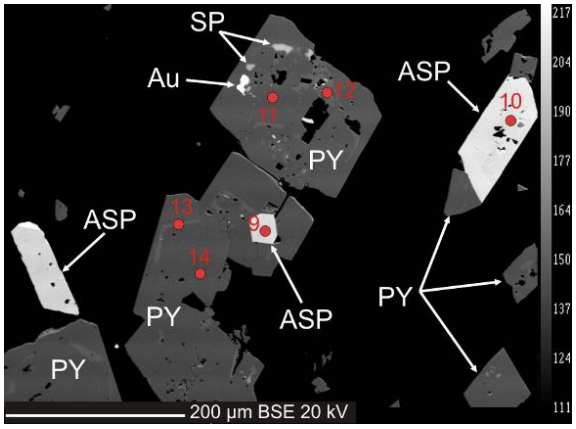

A – Sample 1A6-72-97/166.64m

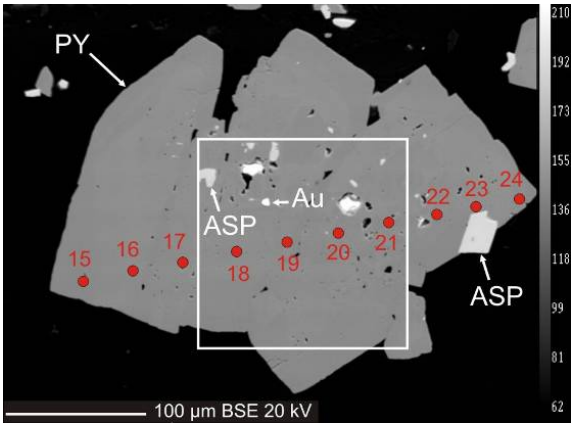

B – Sample 1A6-63-97/448.20m

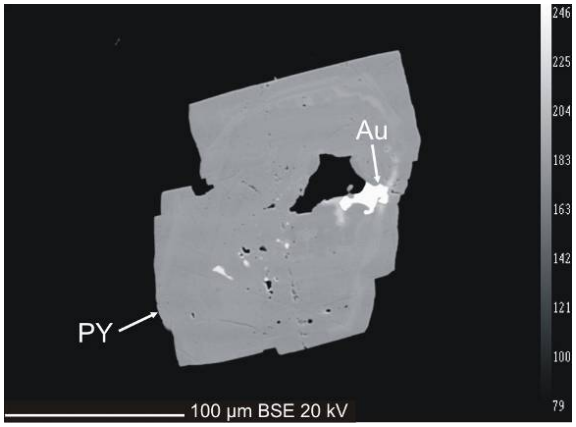

C – Sample 1A6-63-97/448.20m

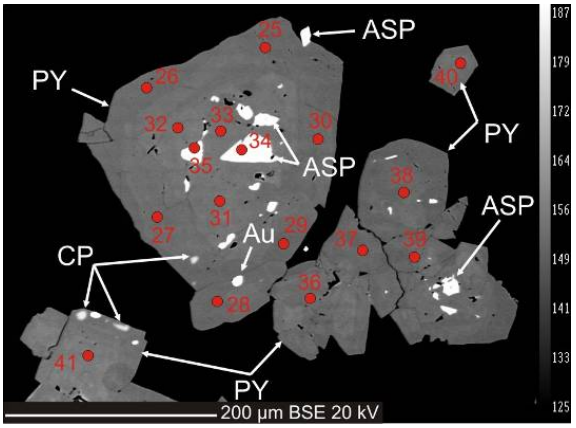

D – Sample AN-125-96/167.30m

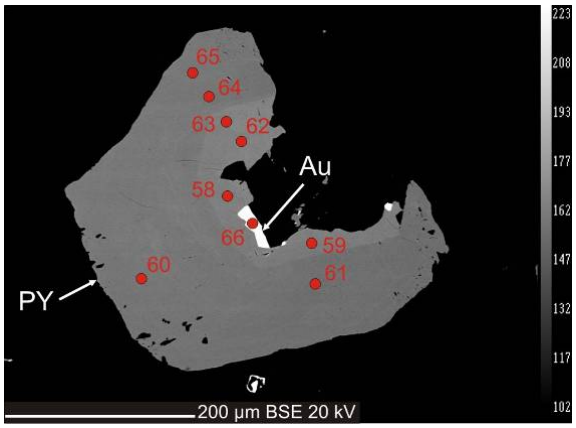

E – Sample AN-84-95/125.50m

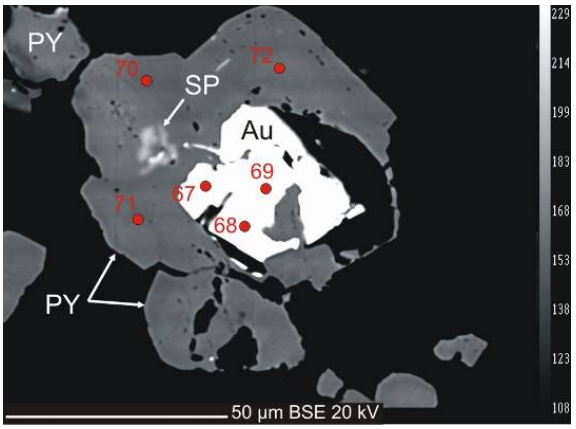

F – Sample AN-72-94/116.70m

Figure 50. BSE images of microscopic gold associated with pyrite. A) Pyrite associated with arsenopyrite, and containing gold and sphalerite inclusions. B) Gold and arsenopyrite included in pyrite crystal. For the framed zone, see Figure 51. The framed area corresponds to the zone scanned for the presence of Au, Ag, Cu and As, discussed in a later section. C) Incorporation of gold in a cavity of a pyrite crystal. D) Arsenopyrite, chalcopyrite and gold included in pyrite crystals. Note the particular location of gold in a micro-fracture. E) Gold located in an arsenic-rich and corroded part of a pyrite crystal. F) Gold grain located in a corroded pyrite crystal.

In the sulfide ore, gold usually occupies micro-fissures and figures of corrosion in pyrite crystals (Figures 38A, 38D and 50). An elemental scan (electron microprobe) for the presence of some specific elements (e.g. Au, Ag, Cu and As) in a single arsenian pyrite crystal reveals that gold inclusions are made up of Au-Ag-Cu alloys. However, silver and copper are low, e.g. <8 wt.% Ag and <0.5 wt.% Cu (Table 7).

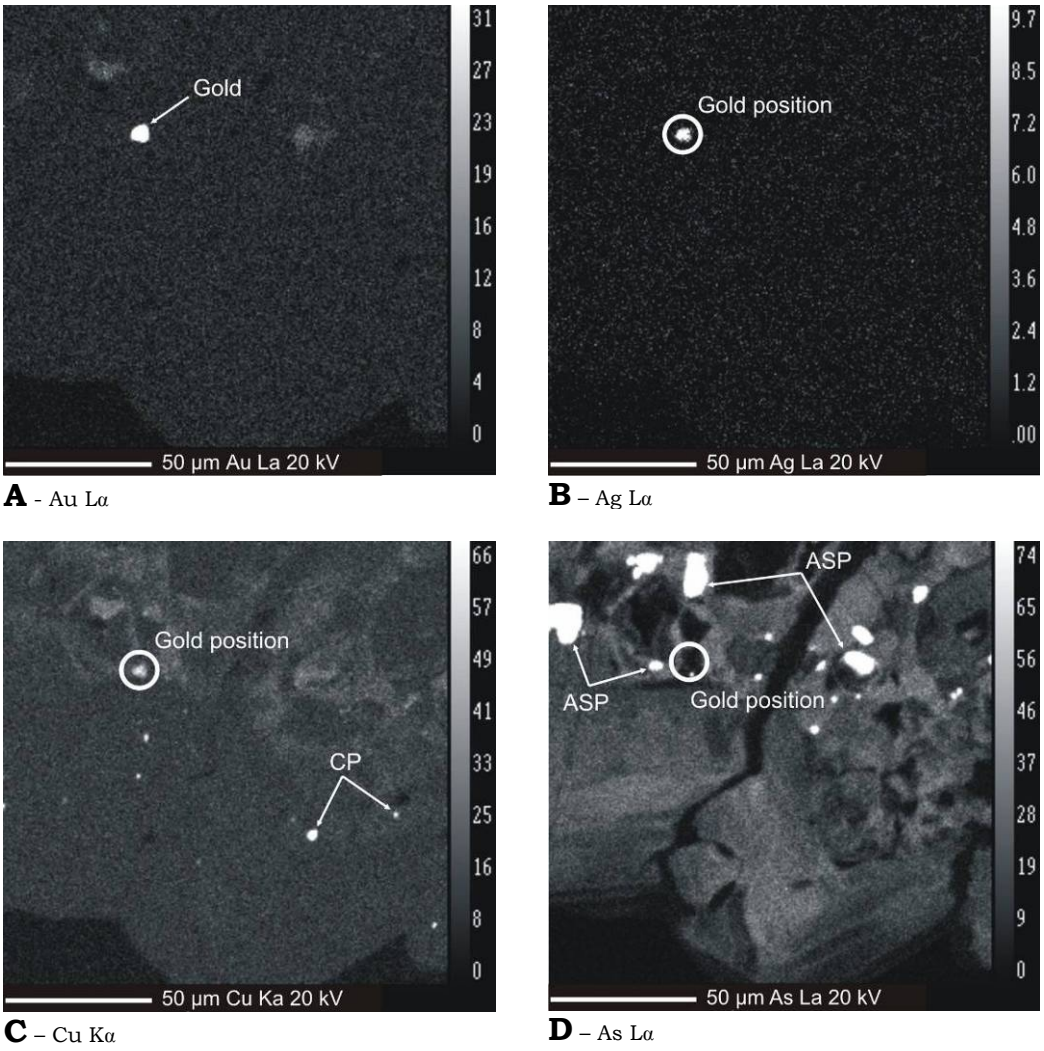

A - Au Lα **B** – Ag Lα

C – Cu Kα **D** – As Lα

Figure 51. Elemental concentration mapping of gold-bearing arsenian pyrite crystal by electron microprobe. See Figure 50B for crystal image. A) Distribution pattern of gold. The white dot corresponds to gold inclusion. B) Distribution pattern of silver. C) Distribution pattern of copper. Presence of chalcopyrite inclusions D) Distribution pattern of arsenic. One notes many inclusions of arsenopyrite and heterogeneous distribution of arsenic in arsenian pyrite. Ag and Cu occur exactly in the position of the gold inclusion, i.e. gold is alloyed with silver and copper.

The microanalytical data show that gold is positively correlated with the arsenic-rich sulfides. Laser ablation (LA-ICP-MS) data indicate additionally that tellurium, bismuth and copper are coupled with gold content in both pyrite and arsenopyrite as well, as seen in the successive bivariate plots of tellurium, bismuth, and copper signals versus gold abundance (Figures 52 and 53). Te, As, Bi and Cu can not be quantified due to the absence of an appropriate standard.

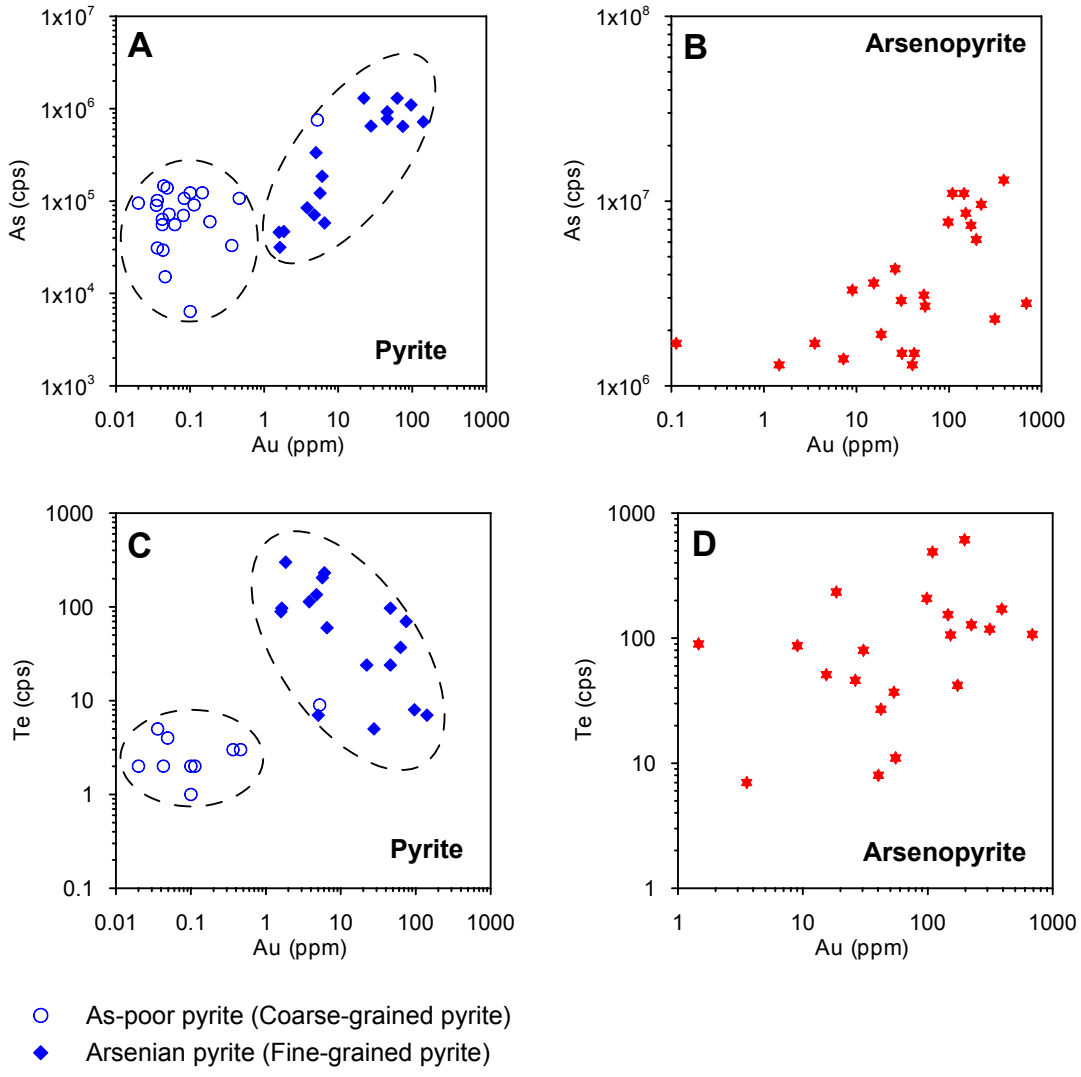

Figure 52. Correlation of arsenic and tellurium with gold content in pyrite and arsenopyrite. The data are from LA-ICP-MS and the values of As and Te are expressed in count per second (cps).

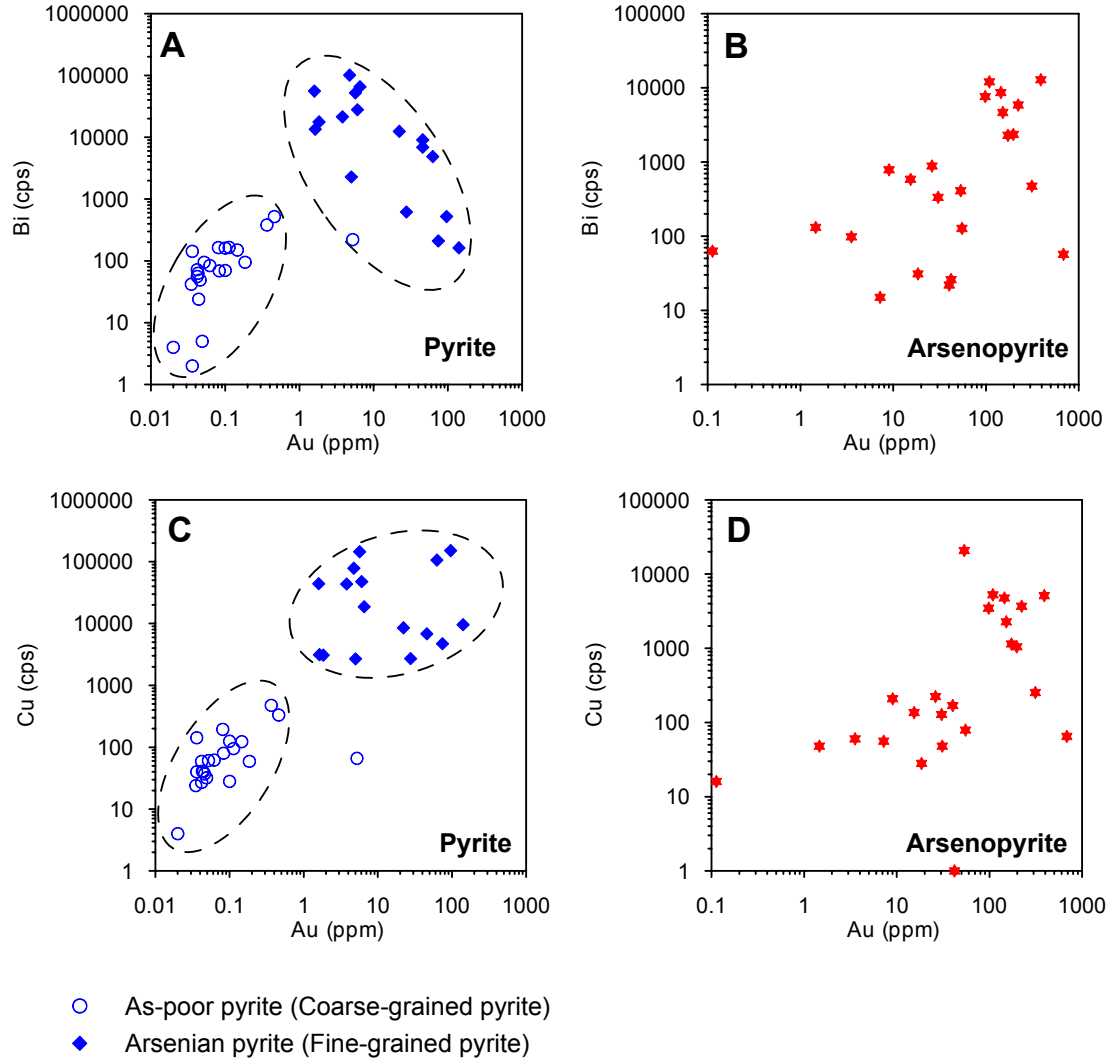

Figure 53. Correlation of bismuth and copper with gold content in pyrite and arsenopyrite. The data are from LA-ICP-MS and the values of Bi and Cu are expressed in count per second (cps).

The arsenian pyrite (classified as fine-grained pyrite) is enriched in Au, Te, Bi and Cu; whereas the arsenic-poor pyrite (classified as coarse-grained pyrite) is poor in Au, Te, Bi and Cu. Arsenopyrite, which is always gold-bearing, has Te, Bi and Cu abundances nearly proportional to its gold content. These observations suggest that, the gold mineralizing fluids were enriched in As, Te, Bi, and Cu.

3-4-4. Paragenetic evolution of ore minerals

On the basis of micro-tectonic analysis, compositional, structural and textural features, three distinct stages of mineralization can be distinguished (Figure 54).

Stage I is characterized by the deposition of coarse-grained pyrite (arsenic-poor pyrite). This stage is devoid of gold, as rock samples containing essentially coarse-grained pyrite always are barren with respect to gold content. This fact has been confirmed by electron microprobe and laser ablation analyses.

Stage II corresponds to the crystallization of fine-grained arsenian pyrite and arsenopyrite. This stage, contrary to the previous one, is arsenic-rich and is accompanied by gold deposition.

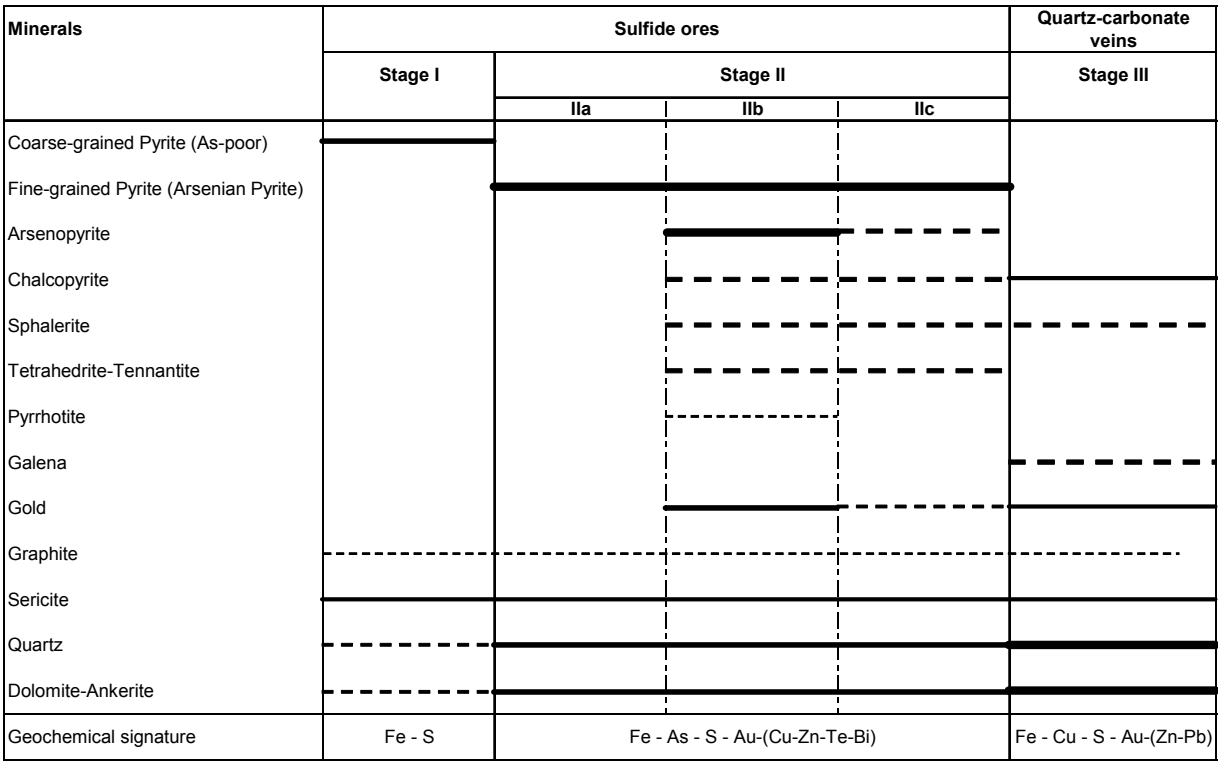

Figure 54. Paragenetic sequence of hypogene ore and gangue minerals of the studied deposits. Line thicknesses correspond to the relative abundances of minerals deposited.

Stage II can be subdivided into three sub-stages (e.g. IIa, IIb and IIc), which took place successively in a relatively short time. The pyrite crystal presented in Figure 43C summarizes all three sub-stages, during fine-grained pyrite growth, with three distinct textural and compositional zones. The central zone is arsenic-poor and corroded. The intermediate zone is arsenic-rich, corroded, and presents a poikilitic texture, which is characterized by many inclusions (e.g. chalcopyrite, pyrrhotite, arsenopyrite and gold). The outer zone, as the central zone, is arsenic-poor, but is devoid of signs of corrosion. The zoning pattern observed in this single crystal indicates a successive variation in the hydrothermal fluid composition. After the deposition of the first sub-stage pyrite, occurred the infiltration of an ore fluid, rich in arsenic and enriched in Au, Te, Bi, Cu, and Zn. This metal signature can be derived from the inclusion minerals in arsenian pyrite, and from the trace-metal composition of arsenian pyrite.

Stage III corresponds to the second type of gold mineralization, i.e. quartz-carbonate veins. This stage during which the second type of gold mineralization formed (e.g. quartz-carbonate veins with “free gold”) is characterized by the deposition of native gold, and base metals sulfides like chalcopyrite, sphalerite and galena. It is furthermore distinguished by the notable absence of arsenopyrite and all other arsenic-bearing minerals.

3-4-5. Physical and chemical conditions of mineralization estimated from arsenopyrite composition

Compositional changes in arsenopyrite, a major sulfide of the Afema deposit, record changes in the hydrothermal fluid system. The variation in As/S ratio, depends on temperature, sulfur fugacity and, to a very minor extent on pressure (Kretschmar and Scott, 1976; Sharp *et al.*, 1985). Because of its refractory behavior, arsenopyrite usually preserves, its original textures and composition (Choi and Youm, 2000), and is frequently used as geothermometer for hydrothermal systems.

The Fe-As-S system along the pseudobinary pyrite-löllingite join (see Figure 41) was calibrated experimentally by Kretschmar and Scott (1976), later modified by Sharp *et al.* (1985), which allows the determination of formation temperature and sulfur fugacity from arsenopyrite compositions.

The "arsenopyrite geothermometer" requires that arsenopyrite is in equilibrium with either pyrite or pyrrhotite which buffer the sulfur fugacity (Kretschmar and Scott, 1976). In the gold deposits of Afema district, arsenopyrite is observed in almost all gold-bearing rock samples in association with pyrite. Pyrite (fine-grained type, in particular) coexists with arsenopyrite in various ways: individual crystals, intergrown crystals, and host crystals for arsenopyrite inclusions. Pyrrhotite, on the contrary, is rarely found and occurs exclusively as inclusions in only a few pyrite crystals. Therefore, equilibrium between arsenopyrite and pyrite can be assumed. The arsenopyrite contains less than 1 wt.% combined Co, Ni and Sb, as recommended by Kretschmar and Scott (1976).

The compositional ranges of the selected arsenopyrite samples are 27.8 to 31.0 at.% As for the Jonction deposit (APPENDIX 5) and 25.8 to 30.2 at.% As for the Aniuri deposit (APPENDIX 6). The compositional range of arsenopyrite from the Jonction deposit then corresponds to less than 253°C to 360°C as formation temperature, and less than $10^{-12.7}$ to $10^{-7.8}$ as sulfur fugacity $f(S_2)$. The compositional range of arsenopyrite from the Aniuri deposit corresponds to less than 253°C to 308°C as formation temperature, and less than $10^{-12.7}$ to $10^{-9.6}$ as sulfur fugacity (Figure 55).

The wide range of arsenopyrite composition from both deposits, which involve large intervals of temperatures (at least 117°C for Jonction and 55°C for Aniuri) and $f(S_2)$, may reflect variation in formation temperature and/or fluctuation in sulfur fugacity in the hydrothermal system (Lowell and Gasparrini, 1982). In such a case, can we really say that arsenopyrite remained in equilibrium with the surrounded mineral assemblages? Any way, Sharp *et al.* (1985)

recommended the use of the arsenopyrite geothermometer with caution and preferably in conjunction with other thermometers.

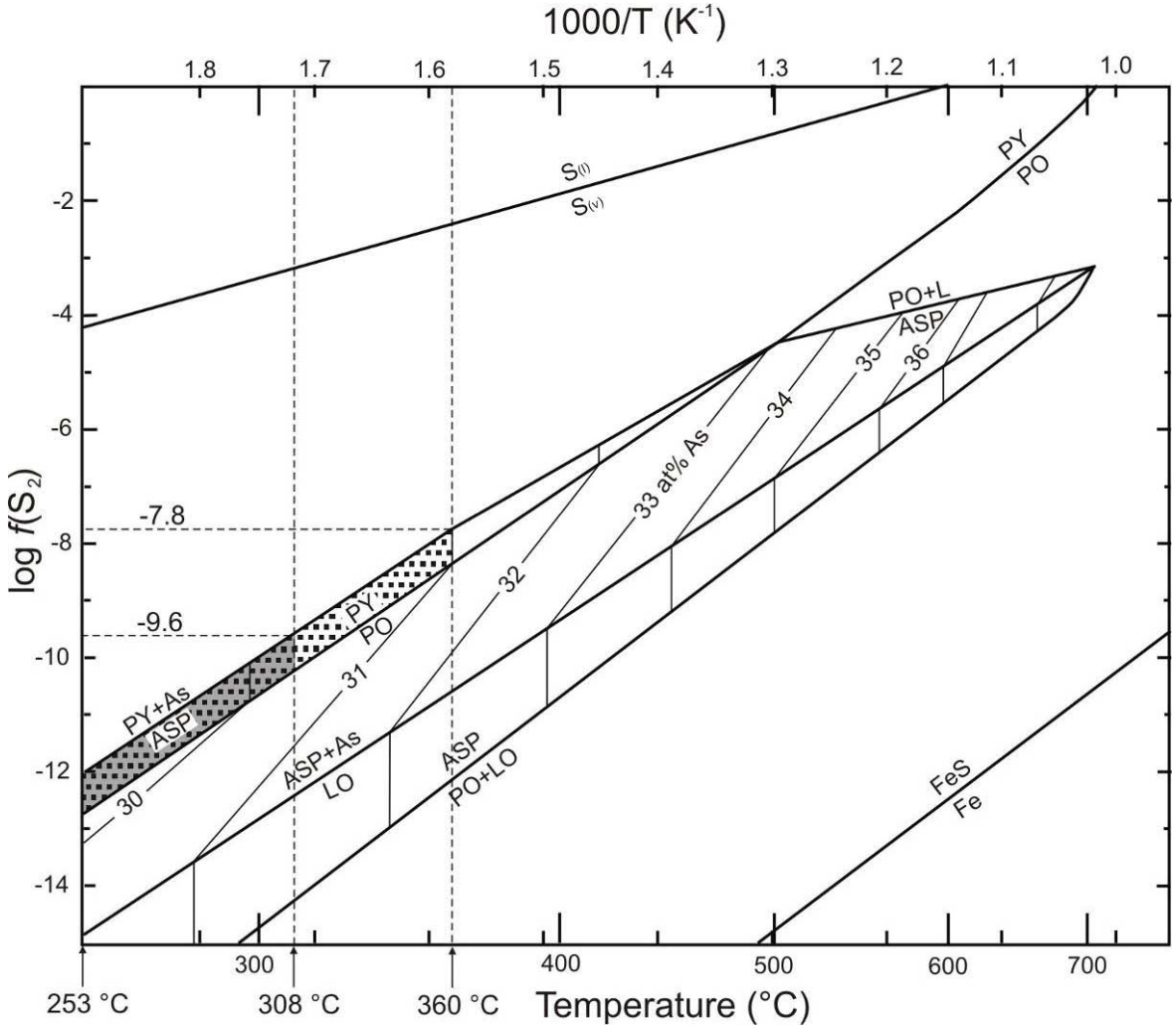

Figure 55. Temperature and sulfur fugacity $f(S_2)$ estimation from arsenopyrite composition. The compositional range of arsenopyrite from the Jonction deposit is represented by the dotted area and that of arsenopyrite from the Aniuri deposit, by the shaded area. Diagram fields after Kretschmar and Scott (1976), later modified by Sharp *et al.* (1985).

3-4-6. Characteristics of the gold-mineralizing fluids

A widely used method for the determination of ore fluid characteristics, from which the physico-chemical environment of ore deposition can be elucidated, is the study of fluid inclusions. In the case of the Afema deposits, quartz is the most suitable mineral for such investigations.

Detailed petrography carried out on the ore-related quartz veins revealed two different modes of occurrence of fluid inclusions: (1) irregular three-dimensional clusters within non-recrystalized grains, and (2) along sub-grain boundaries (Figure 56). Owing to the deformed feature of the mineralization zones, the quartz veins are mostly recrystallized and the fluid inclusions, where have not been destroyed, they have moved from the cores of sub-grains to sub-grain boundaries. The non-recrystallized quartz grains however, are mostly characterized by scattering of small two-phase aqueous (liquid + vapor) inclusions at room temperature. The genetic classification of the inclusions recommended by Roedder (1984) was difficult to carry out, as the criteria established by this author were not easily applicable in the studied samples, but it is unlikely that primary fluid inclusions have survived the long post-depositional history.

Attempts to determine the physico-chemical conditions of quartz deposition through microthermometry of fluid inclusions were thwarted by the absence or paucity of suitable inclusions in the selected samples. In fact, the inclusions were found to be too small (generally <10 μm) for accurate freezing experiments, where changes of phases were not readily visible. The heating experiments on a few two-phase aqueous inclusions permitted to obtain, however, homogenization into the liquid phase, with temperatures (T_h) ranging from 138.7 to 315.1°C for both deposits. Note that during this experiment, some inclusions decrepitated at 204.6 to 319.7°C before homogenization. The fluid inclusion homogenization temperature (T_h) values are an estimate of the minimum temperature of formation (e.g. trapping temperature: T_t) of a given fluid and, therefore require a pressure correction ($T_t - T_h$) to convert the measured T_h value into a T_t (Sherpherd *et al.*, 1985). Assuming 1 kbar for fluid-trapping pressure (P_t) and ignoring the salinities, the trapping temperature would give about 205 – 412°C (Figure 57).

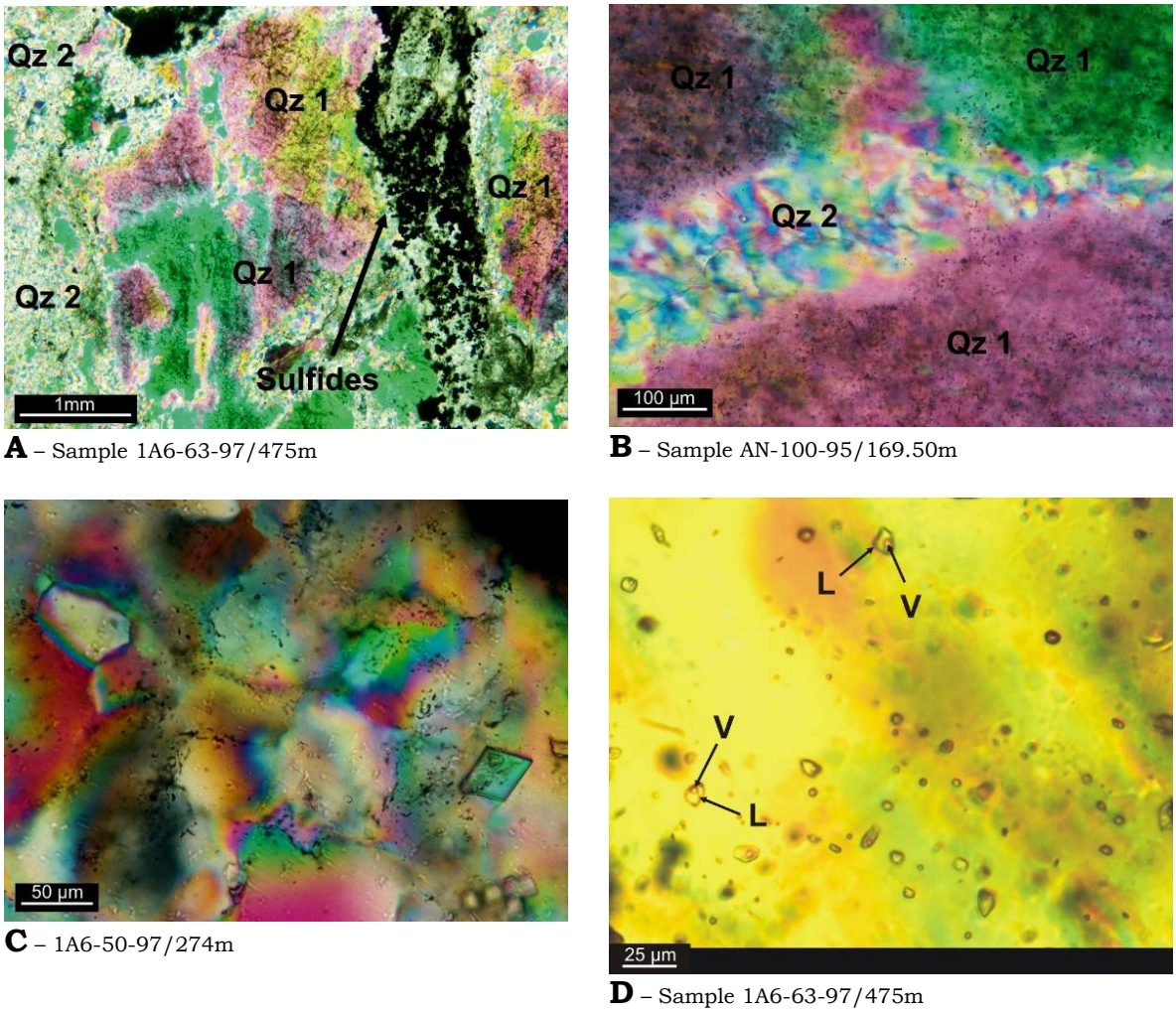

A – Sample 1A6-63-97/475m

B – Sample AN-100-95/169.50m

C – 1A6-50-97/274m

D – Sample 1A6-63-97/475m

Figure 56. Fluid inclusions in quartz – Very small black dots are fluid inclusions (thick sections, transmitted light, crossed nicols). A) Irregular three dimensional cloud-like clusters in non-recrystallized quartz grains indicated by Qz 1. B) Irregular three dimensional clusters in non-recrystallized quartz grains (Qz 1). Note the absence of fluid inclusions in the sub-grains (i.e. recrystallized grains) indicated by Qz 2. C) Sub-grains showing fluid inclusions along their boundaries. D) Small two-phase aqueous (liquid + vapor) inclusions scattered in a non-recrystallized quartz grain at room temperature (24°C). L = liquid; V = vapor.

The mineral assemblage gives some information on ore fluid composition. The stability of graphite shows the reducing nature of the fluids. The high proportion of carbonate (dolomite-ankerite series) implies that CO_2 was significantly present in the fluids. The fact that ore minerals are mainly represented by sulfides (pyrite and arsenopyrite) suggests the presence of H_2S in the fluids from which they crystallized. In summary, the mineralization fluids were reducing, and enriched in CO_2 and H_2S.

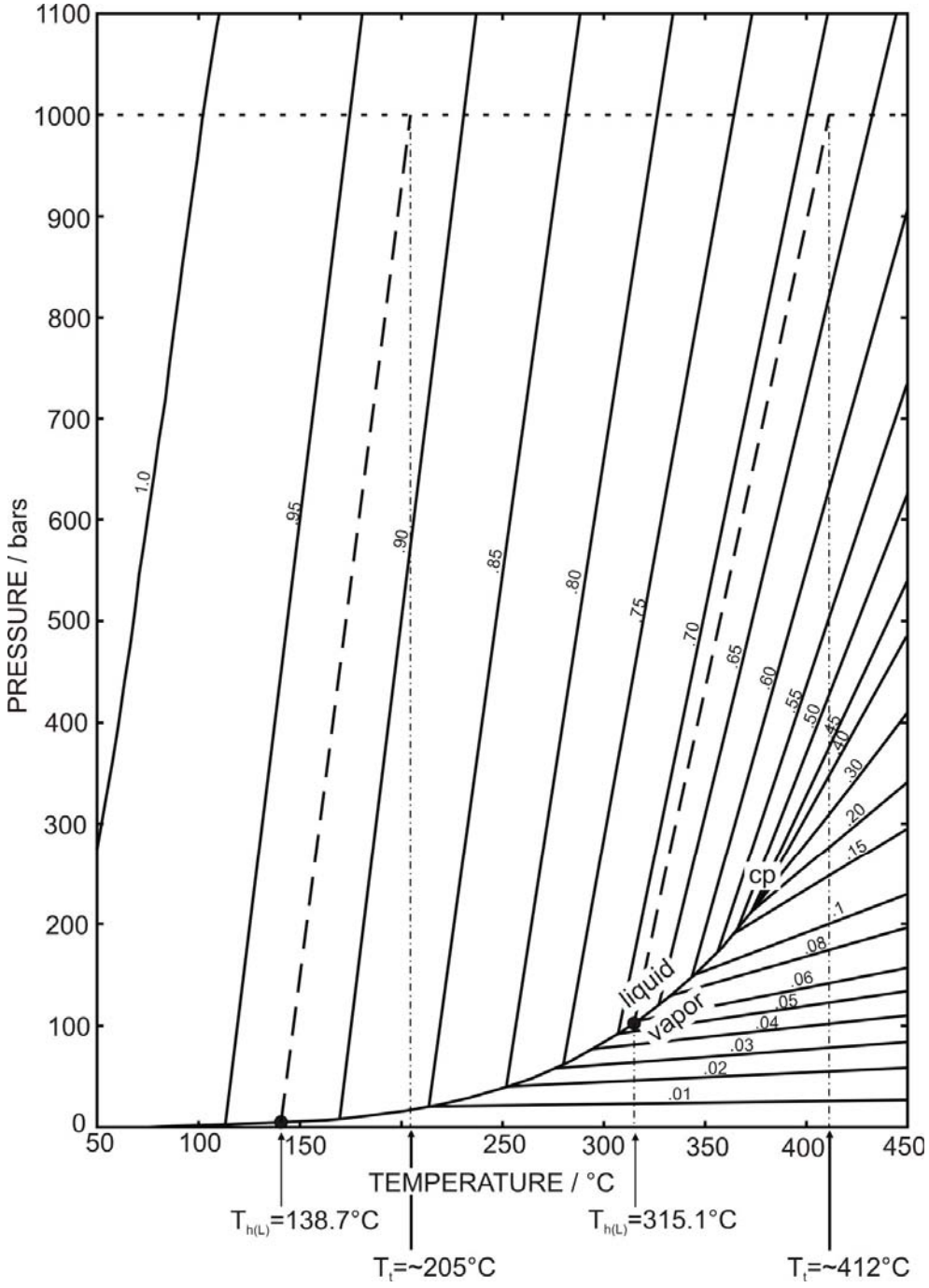

Figure 57. Estimate of trapping temperatures of fluid inclusions from ore-related quartz veins at 1 kbar using the P-T diagram for pure water. The H_2O isochors have been redrawn from Crawford (1981), who modified the initial version (from Fisher, 1976). $T_{h(L)}$: homogenization temperature into liquid; T_t: trapping temperature; cp: critical point.

In hydrothermal solutions, ore metals (particularly gold) are transported by two main classes of complexes: sulfide (HS^- and H_2S) and chloride (Cl^-). Concerning the Afema gold deposits, the reducing nature of the ore fluid, the low abundance of base metals (e.g. Cu, Zn, Pb), i.e. high gold/base metal ratios,

and the association of gold with Fe-sulfides suggests gold transport as reduced sulfur complexes. This hypothesis is supported by the studies of Barnes (1979), which indicates that sulfide complexes are more stable at lower temperature (below ~350°C) than chloride complexes.

3-4-7. Precipitation and concentration of gold

Arsenian pyrite and arsenopyrite are the major host minerals of gold. Gold occurs in arsenian pyrite microscopically (up to about 5 μm of diameter) and submicroscopically, whereas in arsenopyrite, it occurs essentially "invisible", i.e. submicroscopically. In both minerals, gold correlates positively with arsenic (Figures 52 and 58), which suggests that the presence of arsenic in these minerals has played an important role in gold fixation. In addition, micro-analytical profiles across gold-bearing arsenian pyrite and arsenopyrite crystals show a superimposition of highly auriferous zones with relative higher As/S molar ratios zones (Figures 44 and 48). This relationship between gold and As-rich, Fe sulfide minerals is not specific to the Afema gold district. It has been observed in many other gold deposits over the world, namely: Bogosu, Prestea and Ashanti in Ghana (Mumin *et al.*, 1994; Oberthür *et al.*, 1994; Oberthür *et al.*, 1997), Nando-Pinkun and Royal Family in Zimbabwe (Lotz, 1994; Lotz and Puchelt, 1994), Geita in Tanzania (Borg, 1994), Twin Creeks and Carlin-trend gold deposits in USA (Simon *et al.*, 1999; Palenik *et al.*, 2004), Roudny in Czech Republic (Zacharias *et al.*, 2004), Emperor in Fiji (Pals *et al.*, 2003).

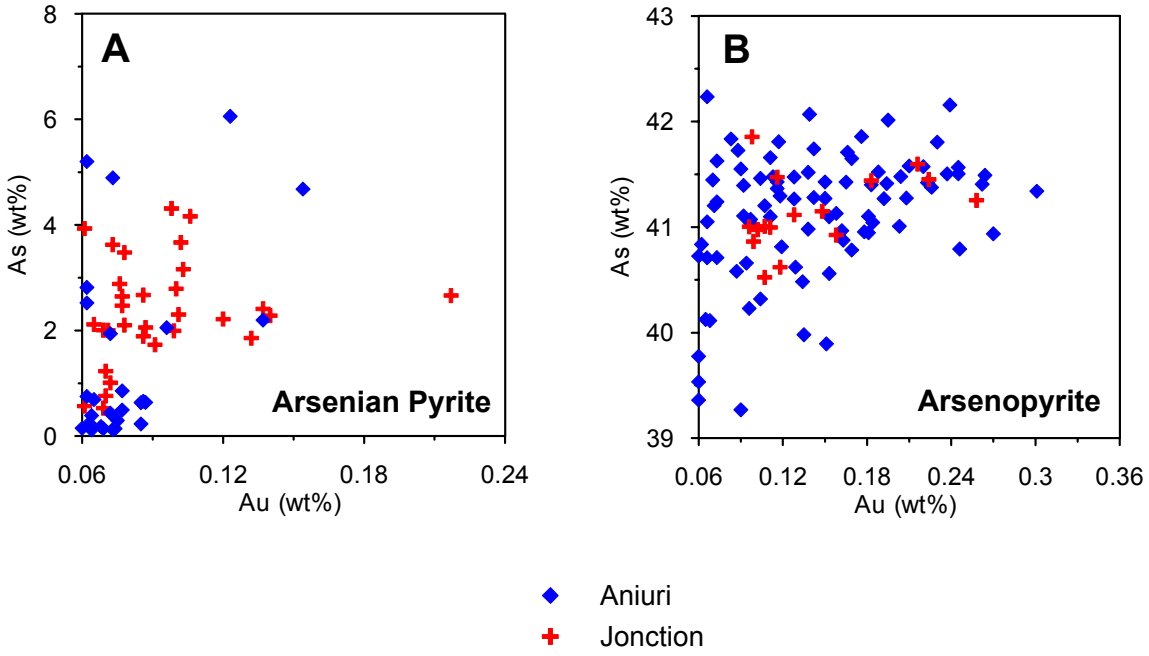

Figure 58. Correlation of arsenic with gold content in arsenian pyrite (A) and in arsenopyrite (B). Electron microprobe data were 600 ppm Au detection limit.

How can the selective association of gold with As-rich, Fe sulfide minerals be explained? The answer to this question seems to lie in a kind of electrochemical "attraction" exerted by these sulfides on gold in hydrothermal fluids (Möller, 1994; Möller and Kersten, 1994). Möller and Kersten (1994) mounted natural pyrite, arsenopyrite and chalcopyrite crystals as electrodes in galvanic cells (also called voltaic or electrochemical cells) with 1 M KCl, aerated as well as H_2S-saturated solutions in which they dissolved gold foils. In the experiment, linked sulfides of variable composition were used to simulate crystals with inhomogeneous chemical composition (e.g. zoned crystals). Depending on their chemical composition, the sulfide minerals behaved as P-type or N-type semiconductors.

A P-type semiconductor is a semiconductor in which electrical conduction is due mainly to the movement of positive "holes", by adding a certain type of atoms (i.e. "doping"). For example, a semiconductor from the group 14 of the periodic table, such as silicon (four valences), in which one introduces an impurity from group 13 (e.g. Boron or aluminum, trivalent atoms) becomes a P-type semiconductor. In this P-type semiconductor, one electron is missing from

one of the four covalent bonds normal for the silicon lattice. Thus, the atom of group 13 (dopant) generates a positive carrier (hole) in the silicon crystal by the acceptance of an electron valence bond. An N-type semiconductor, however, is a semiconductor in which electrical conduction is due chiefly to movement of electrons. This latter type of semiconductor results from doping silicon with phosphor, arsenic or antimony (group 15) for instance.

With regard to arsenopyrite and pyrite, the substitution of S by As acts as electron acceptor and leads to P-type conductivity, characterized by As/S molar ratios >1 for arsenopyrite and >0 for pyrite. However, the substitution of As by S in arsenopyrite involves an N-type conductivity, with As/S molar ratios <1. Möller (1994) explained this process by a schematic diagram (Figure 59), in which the replacement of S by As creates an electron "hole" in the valence band (e.g. electron acceptor: equation [10]), whereas the substitution of As by S involves an excess of electrons (e.g. electron donor: equation [11]).

Electron acceptor: $As + e^- \Rightarrow As^-$ [10]

Electron donor: $S \Rightarrow S^+ + e^-$ [11]

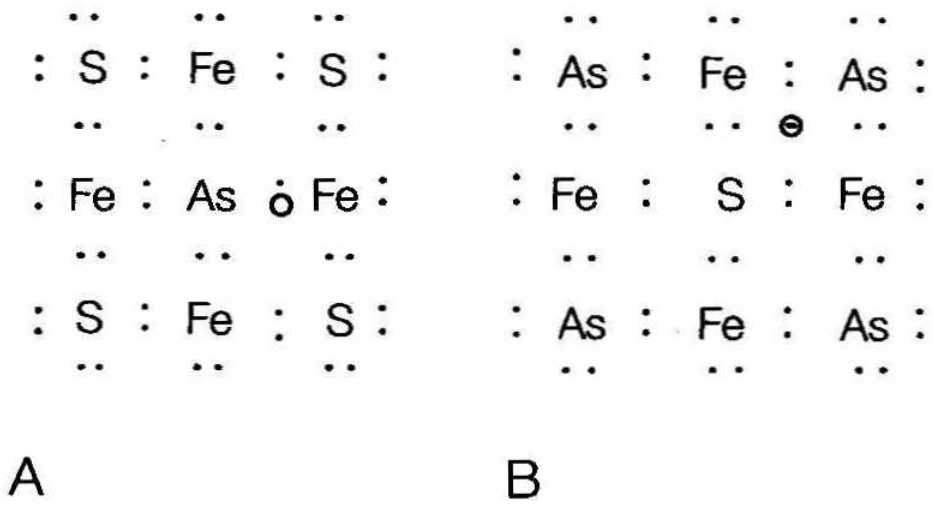

Figure 59. Schematic diagram of electron distribution in semiconductors. A) P-type: As substituting S. B) N-type: S substituting As (Möller, 1994)

The process of substitution of S by As in pyrite which involved the crystallization of arsenian pyrite, occurred probably at elevated temperature and/or rapid cooling of the mineralization fluid, where the structure of pyrite might be more tolerant for incorporation of "impurities" (e.g. arsenic).

In the experiment of Möller and Kersten (1994) described above, the amount of Au deposited at the cathodes (P-type conductivity) by the reaction of equation [12], exceeded that accumulated at the anodes (N-type conductivity). And, the negatively charged Au-complexes were concentrated by adsorption processes at the anode surface, particularly at places with high field strength, namely corners and edges of the sulfide crystals (Figure 60).

$$Au^{+} + e^{-} \Leftrightarrow Au^{0} \qquad [12]$$

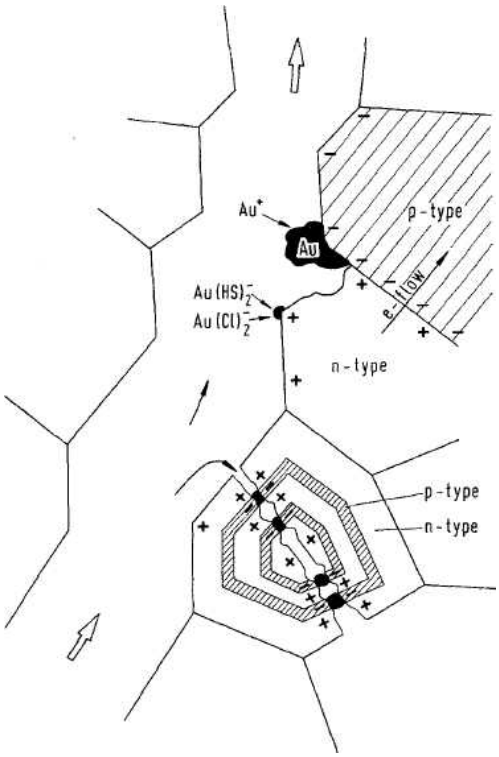

Figure 60. Electrochemical reactions of a gold-bearing fluid moving along a pore made up of P-type (cathode) and N-type (anode) sulfides as well as fractured N- and P-type zoned crystals (Möller and Kersten, 1994). Gold will be preferentially fixed on P-type semiconductor domains.

At the anode, gold would be released by the decomposition of gold complexes (e.g. bisulfide complexes) according to the reaction of equation [13].

$$Au(HS)_2^- \Leftrightarrow Au^0 + 2S + 2H^+ + 3e^- \qquad [13]$$

In the Afema gold district, As/S molar ratios range between 0.64 and 0.89 for arsenopyrite, and up to 0.2 for arsenian pyrite. As a consequence, arsenian pyrite behaved as P-type sulfide, and arsenopyrite as N-type. The P-type conductivity feature of arsenian pyrite, permitted to this sulfide to act as cathode for gold accumulation from the ore fluids. This hypothesis is corroborated by the fact that the quasi totality of microscopic gold inclusions observed, is associated with arsenian pyrite crystals (Figures 38A to 38D, and 50). In this sulfide, gold is observed particularly in defect zones such as fractures or corroded zones, where field strength is supposed to be relatively higher. Arsenopyrite also contains gold - but in submicroscopic form essentially. The accumulation of gold in arsenopyrite would have been favored by its slightly compositional inhomogeneity (alternation of P- and N-type zones), which is not always perceptible.

The form under which gold is incorporated in arsenian pyrite and arsenopyrite has been a matter of great debate. Recently, Bennett and Benning (2004) showed that at elevated temperature (e.g. 250°C), gold is incorporated into the structure of arsenian pyrite as Au^+, whereas at low temperature (e.g. 25°C), it is adsorbed on the surface of this sulfide. Furthermore, Reich *et al.* (2005) suggested that gold is present as Au^+ in the lattice of arsenian pyrite until its concentration in this sulfide reaches a saturation level, from which point it accumulates as neutral nanoparticles (Au^0).

3-5. Geochronological study

3-5-1. Rb-Sr and Sm-Nd geochronology of whole rocks

Rb-Sr and Sm-Nd isotope analysis has been performed on four metaarenite (gold-ore host rock) samples from the Jonction deposit and on five metabasalt samples from the Aniuri deposit. All samples are from drill core, except the sample AF-A05 which is from outcrop. The analytical data are given in Table 9 and isochron diagrams are presented in Figure 61.

The Rb-Sr and Sm-Nd data do not yield acceptable isochrons. With the regression model 3 fit (Ludwig, 2001), which assumes variations in the daughter isotopic ratio independently to the parent isotopic ratio, the data of Rb-Sr obtained on metaarenite from Jonction scatter around an errorchron of 1921 ± 71 Ma, with an initial $^{87}Sr/^{86}Sr$ ratio of 0.70308 ± 0.00045 and an MSWD (Mean Square of Weighted Deviates) of 17. The Sm-Nd data for the same rock samples from Jonction, give an errorchron at 2068 ± 670 Ma, with an initial $^{143}Nd/^{144}Nd$ ratio of 0.51007 ± 0.00059 and an MSWD = 191 (Figure 61).

The mean square of weighted deviates (MSWD) represents an instrument of testing for excess scatter beyond analytical uncertainty in the isochron calculation. Thus, it expresses the goodness of fit and by extension, tests for open system behavior or non-uniform initial ratios. The MSWD is defined as the sum of the squares of deviations of data from the isochron divided by the number of degrees of freedom of the population samples, i.e. number of data points minus two (Richards and Noble, 1998). The decay constant for ^{87}Rb in the isochron calculations was 1.42×10^{-11} $year^{-1}$ (Steiger and Jager, 1977), and that for ^{147}Sm was 6.54×10^{-12} $year^{-1}$ (Lugmair and Marti, 1978).

Table 9. Rb-Sr and Sm-Nd isotopic data for metaarenite from Jonction and metabasalt from Aniuri. The age of 2190 Ma is assumed for initial ratio and ε_{Nd} calculations.

Sample ID	Drill core No.	Rb (ppm)	Sr (ppm)	$^{87}Rb/^{86}Sr$	± 2σ (%)	$^{87}Sr/^{86}Sr$	± 2σ	Sm (ppm)	Nd (ppm)	$^{147}Sm/^{144}Nd$	± 2σ (%)	$^{143}Nd/^{144}Nd$	± 2σ	$(^{87}Sr/^{86}Sr)t$	$(^{143}Nd/^{144}Nd)t$	$\varepsilon^{t}_{Nd,CHUR}$	$T_{Nd,DM}$ (Ma)
Jonction deposit (Metaarenite)																	
T 607	1A6-57-97/311.20m	3.159	1461.500	0.0063	0.609	0.703224	0.000005	4.9003	20.5495	0.1441	0.3	0.511994	0.000006	0.703027	0.509915	2.24	2520
T 662	1A6-63-97/447.30m	29.620	140.720	0.6097	0.464	0.719872	0.000005	0.7280	3.2772	0.1343	0.3	0.511937	0.000003	0.700613	0.510000	3.92	2317
T 664	1A6-63-97/449m	9.429	63.150	0.4323	0.396	0.715169	0.000006	1.2871	7.9006	0.0985	0.3	0.511399	0.000004	0.701513	0.509979	3.49	2306
T 667	1A6-72-97/204.95m	58.080	338.370	0.4971	0.497	0.716793	0.000005	1.6799	6.9925	0.1452	0.3	0.512047	0.000003	0.701091	0.509952	2.98	2443
Aniuri deposit (Metabasalt)																	
T 633	AN-100-95/270.10m	2.753	9.013	0.0883	0.405	0.703040	0.000013	3.9099	14.2609	0.1657	0.3	0.512307	0.000003	0.700250	0.509916	2.27	2663
T 634	AN-107-95/27.10m	1.765	296.120	0.0172	0.425	0.703348	0.000006	2.3268	7.5103	0.1873	0.3	0.512555	0.000007	0.702803	0.509854	1.04	3404
T 646	AN-140-97/169m	59.290	368.760	0.4655	0.509	0.715054	0.000005	2.4371	9.3112	0.1582	0.3	0.512167	0.000005	0.700349	0.509885	1.65	2685
T 679	AF-A05	15.300	297.990	0.1485	0.402	0.705814	0.000004	4.0998	19.4823	0.1272	0.3	0.511719	0.000003	0.701122	0.509884	1.64	2509
References																	
Bulk Earth (CHUR)				0.0827		0.705200				0.1967		0.512638		0.702588	0.509800	0.00	
Depleted Mantle (DM)				0.0460		0.702600				0.2137		0.513150		0.701147	0.510067	5.23	

The parameters used in the calculations are the following:

Bulk Earth (CHUR) – Present day

$^{87}Rb/^{86}Sr$ = 0.0827 (DePaolo, 1988)

$^{87}Sr/^{86}Sr$ = 0.7052 (Zindler *et al.*, 1982)

$^{147}Sm/^{144}Nd$ = 0.1967 (Jacobsen and Wasserburg, 1980)

$^{143}Nd/^{144}Nd$ = 0.512638 (Goldstein *et al.*, 1984)

Depleted Mantle (DM) – Present day

$^{87}Rb/^{86}Sr$ = 0.046 (Taylor and McLennan, 1985)

$^{87}Sr/^{86}Sr$ = 0.7026 (Taylor and McLennan, 1985)

$^{147}Sm/^{144}Nd$ = 0.2137 (Peucat *et al.*, 1988)

$^{143}Nd/^{144}Nd$ = 0.51315 (Peucat *et al.*, 1988)

Initial ratio calculation at (t) age:

$$\left(^{87}Sr/^{86}Sr\right) = \left(^{87}Sr/^{86}Sr\right)_0 + \left(^{87}Rb/^{86}Sr\right)\left(\exp(\lambda t) - 1\right) \qquad [14]$$

($^{87}Sr/^{86}Sr$) and ($^{87}Rb/^{86}Sr$) represent the present ratios; $(^{87}Sr/^{86}Sr)_0$ corresponds to the initial ratio; λ is the decay constant and t, i.e. the age. The calculation of $(^{143}Nd/^{144}Nd)_0$ is similar to that Rb-Sr. For ε calculation, refer to text.

Depleted mantle (DM) model age calculation:

$$T_{Nd,DM} = \frac{1}{\lambda}\ln\left[\frac{\left(\left(^{143}Nd/^{144}Nd\right)^{today}_{sample} - \left(^{143}Nd/^{144}Nd\right)^{today}_{DM}\right)}{\left(\left(^{147}Sm/^{144}Nd\right)^{today}_{sample} - \left(^{147}Sm/^{144}Nd\right)^{today}_{DM}\right)} + 1\right] \qquad [15]$$

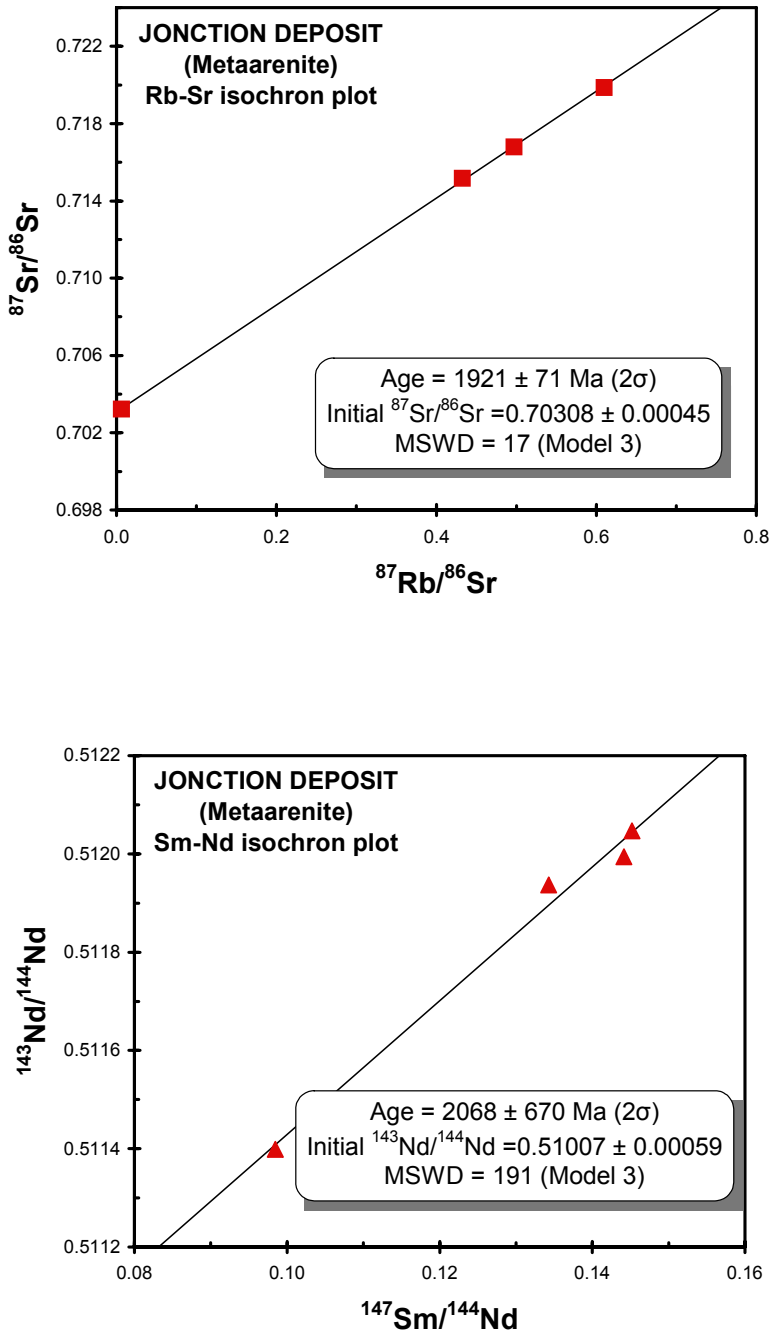

Figure 61. Rb-Sr and Sm-Nd isochron diagrams for metaarenite from the Jonction deposit. Analytical uncertainty is much smaller than symbol size.

At Aniuri, the whole rock dating has been performed on metabasalt samples from outside of the mineralization zone. As in the case of metaarenite from the Jonction deposit, the Rb-Sr and Sm-Nd systems are disturbed. The Rb-Sr data

give an errorchron of 1658 ± 1900 Ma, with an initial ratio $^{87}Sr/^{86}Sr$ of 0.7015 ± 0.0070 and an MSWD = 130000. The Sm-Nd data, however, are characterized by an errorchron of 2191 ± 360 Ma, with an initial ratio $^{143}Nd/^{144}Nd$ of 0.50989 ± 0.00039 and an MSWD = 77 (Figure 62).

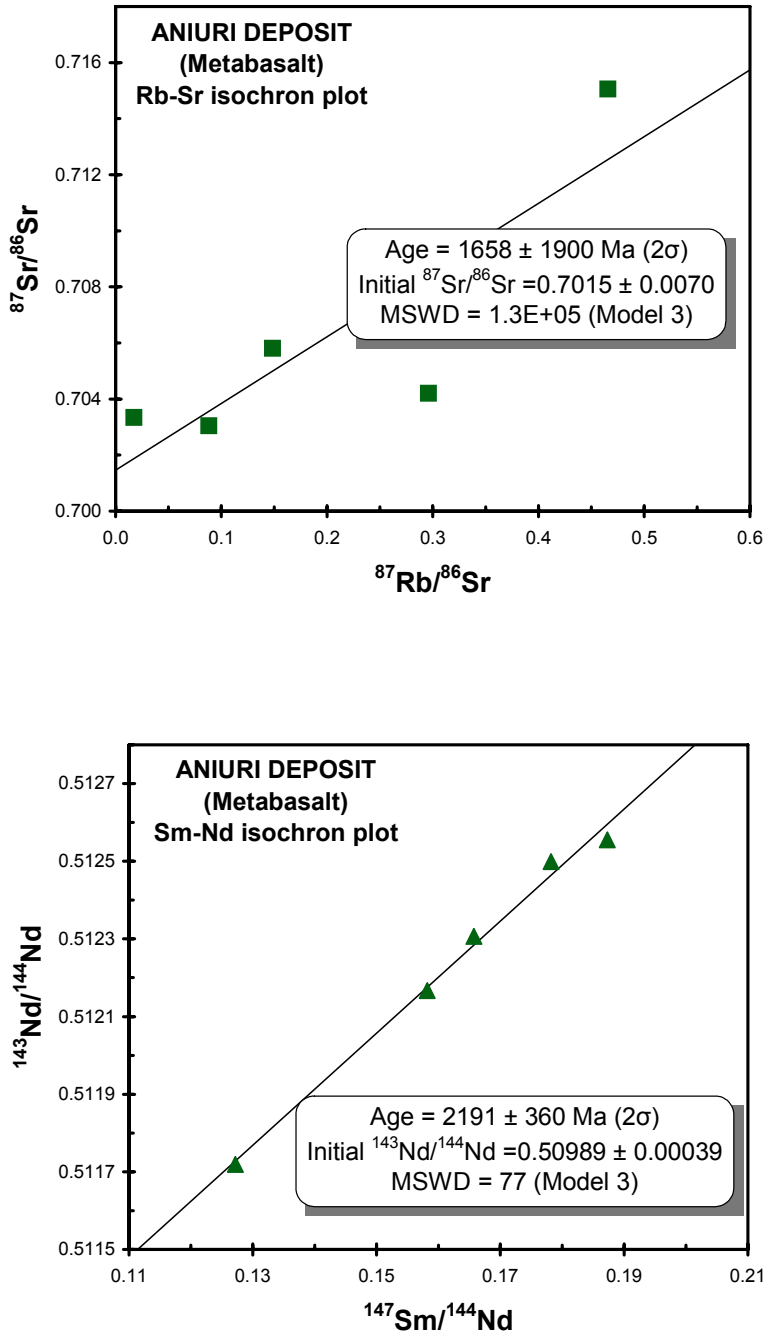

Figure 62. Rb-Sr and sm-Nd isochron diagrams for metabasalt from the Aniuri deposit. Analytical uncertainty is much smaller than symbol size.

The fact that the isotopic data define errorchrons, i.e. MSWD >2.5 (Brooks *et al.*, 1972), instead of isochrons indicates that the isotopic ratios of the rocks reflect not one closed system, but a mixture of several geological processes. The age of metavolcanic assemblage (Sefwi belt) and the metasedimentary assemblage (Kumasi basin) of the studied area was defined by Hirdes *et al.* (2007) using more robust U-Pb dating of zircons. They obtained that the metavolcanic assemblage formed between 2189 Ma and 2166 Ma, whereas the ages of the metasedimentary assemblage falls into the interval of ca. 2190 Ma to 2129 Ma. Based on these data, we can calculate the Sr and Nd isotopic compositions of our metaarenite and metabasalt samples, relative to those of the depleted mantle and bulk Earth (Table 9 and Figure 63). The results indicate that both rock types are in between depleted mantle and bulk Earth (represented by the CHUR) with $\varepsilon_{Nd(2190)}$ = +1.0 to +3.9 and $^{87}Sr/^{86}Sr_{(2190)}$ = 0.700 to 0.703. Given the fact that the samples have a disturbed Sr and Nd isotope information, these data nevertheless indicate the isotopically little evolved nature of the rocks studied.

Note that the parameter $\varepsilon_{Nd(t)}$ represents the measured Nd isotopic ratio of a sample at some time (t) in the past, normalized to the present-day isotopic composition of the CHUR (Chondritic Uniform Reservoir) or the DM (Depleted Mantle). Concerning CHUR, it is defined as:

$$\mathcal{E}^{t}_{\mathrm{CHUR}} = \left[\frac{\left(^{143}Nd/^{144}Nd\right)^{t}_{\mathrm{sample}}}{\left(^{143}Nd/^{144}Nd\right)^{t}_{\mathrm{CHUR}}} - 1 \right] \times 10^{4} \qquad [16]$$

where:

$$\left(^{143}Nd/^{144}Nd\right)^{t}_{\mathrm{CHUR}} = \left(^{143}Nd/^{144}Nd\right)^{\mathrm{today}}_{\mathrm{CHUR}} - \left(^{147}Sm/^{144}Nd\right)^{\mathrm{today}}_{\mathrm{CHUR}} \times (\exp(\lambda t) - 1) \qquad [17]$$

and:

$$\left(^{143}Nd/^{144}Nd\right)^{t}_{\mathrm{sample}} = \left(^{143}Nd/^{144}Nd\right)^{\mathrm{today}}_{\mathrm{sample}} - \left(^{147}Sm/^{144}Nd\right)^{\mathrm{today}}_{\mathrm{sample}} \times (\exp(\lambda t) - 1) \qquad [18]$$

In these equations, t represents the time of crystallization and λ represents the ^{147}Sm decay constant. $\varepsilon_{Nd(t)}$ for the depleted mantle (DM) is calculated by

substituting the appropriate DM values in place of $(^{143}Nd/^{144}Nd)_{CHUR}$ and $(^{147}Sm/^{144}Nd)_{CHUR}$ in the equations [16] and [17].

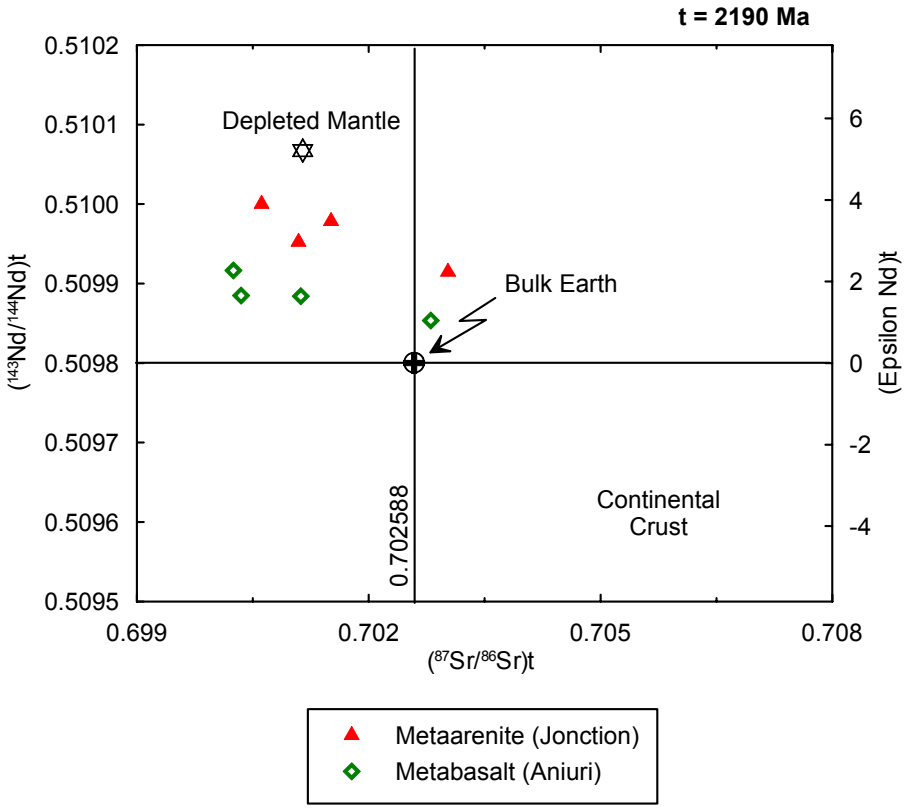

Figure 63. $^{143}Nd/^{144}Nd$ versus $^{87}Sr/^{86}Sr$ isotope correlation diagram showing the position of the samples studied relative to that of depleted and enriched mantle sources at 2190 Ma.

In the Nd-Sr diagram (Figure 63), at 2190 Ma (i.e. igneous age), the samples plot between depleted mantle and bulk Earth. None of the rock samples plots in the continental crust domain. This situation excludes any major recycling of preexisting old crustal material, such as Archean crust. In others words, this result indicates that the metavolcanic rocks and the precursors of the metasedimentary rocks of the studied area were extracted either directly from the mantle to form "new" crust, or are from continental crust formed not so long before 2.19 Ga. The mean crustal residence ages are mainly in between 2.7 – 2.3 Ga (when calculated for depleted mantle – see Table 9), but will be shorter if a chondritic component is mixed in, as possible for mantle plumes. This interpretation is in agreement with the study carried out by Boher *et al.* (1992), which concluded that the major part of the West African protolith

(Birimian formations included) formed directly by crustal accretion through a mantle plume mechanism at about 2.1 Ga, remote from an Archean crust environment. As a consequence, the lower crust and supracrustal rocks of the study area may have similar age (e.g. Paleoproterozoic).

3-5-2. Ar-Ar geochronology of hydrothermal muscovite

The mineralization zones of the Afema district are characterized by sulfide-sericite-quartz-carbonate alteration. The sericite is essentially composed of muscovite (Table 5 and Figure 23). This mineral was formed directly with the quartz-carbonate veins and gold-bearing sulfides from the hydrothermal system. The muscovite Ar-Ar age can, therefore, provide age information of vein formation and gold mineralization.

Two muscovite-rich samples of metaarenite from the ore zones were selected for Ar-Ar isotope analysis. The results are presented in Table 10 and as conventional age spectra in Figure 64. Sample 1A6-71-97/A is from the Jonction deposit, whereas sample AF-B06 comes from a non-identified location (hand specimen sampled at the mine dump of the “Brahima Nord” mine). The age spectra exhibit plateau ages of 1833 ± 16 Ma for 51 percent of gas released in the case of sample 1A6-71-97/A (Jonction deposit), and 1840 ± 17 Ma for 42 percent of gas released in the case of sample AF-B06. Both spectra are partially disturbed, where the depletion for the first heating increments suggests partial loss of $^{40}Ar^*$ during young thermal overprint. 500 Ma corresponds to the upper limit of this thermal disturbance for sample 1A6-71-97/A and about 850 Ma for sample AF-B06. In the interpretation of muscovite $^{40}Ar/^{39}Ar$ ages, it is important to note that the argon closure temperature for muscovite is 350 ± 50°C (Hanes, 1991). The plateau age indicates the time of closure for argon loss, which corresponds to the cooling age below 350 ± 50°C, i.e. the minimum age of the thermal reset or the crystallization of muscovite.

Table 10. Ar-Ar data on muscovite from ore zones of Afema gold district.

Temp. ºC	^{36}Ar (× 10^{15} moles)	$Cl^{(1)}$ (× 10^{9} moles)	$Ca^{(2)}$ (× 10^{9} moles)	$K^{(3)}$ (× 10^{9} moles)	^{40}Ar (× 10^{15} moles)	$^{40}Ar^{*(4)}$ (%)	$^{40}Ar^{*}/^{39}Ar$	Cum. ^{39}Ar (%)	$Age^{(5)}$ (Ma)
Sample 1A6-71-97/A muscovite	*mass = 0.00904 g*								
500	0.31 ± 0.07	0.2 ± 0.07	9.7 ± 2.1	22.4 ± 0.4	147 ± 1	37.5	21.5 ± 7.8	0.2	331.4 ± 109.8
600	0.12 ± 0.10	0.37 ± 0.05	9.1 ± 3.6	95.2 ± 1.4	1194 ± 3	97.0	105.9 ± 2.7	0.9	1244.7 ± 22.5
675	0.20 ± 0.13	0.38 ± 0.07	31.9 ± 10.2	367.3 ± 6.4	6103 ± 16	99.0	143.4 ± 1.7	3.6	1537.5 ± 12.2
725	0.43 ± 0.11	0.91 ± 0.28	91.2 ± 15.9	792.4 ± 12.2	14788 ± 26	99.1	161.2 ± 1.0	9.5	1661.9 ± 6.6
750	0.45 ± 0.10	1.23 ± 0.22	99.7 ± 14.7	725.4 ± 10.7	14213 ± 30	99.1	169.1 ± 0.7	15.0	1714.3 ± 4.9
775	0.91 ± 0.20	0.00 ± 0.49	100.7 ± 12.0	1120.1 ± 17.3	23054 ± 58	98.8	177.3 ± 1.1	23.3	1766.9 ± 7.3
800	0.24 ± 0.27	nd		1408.8 ± 20.4	29938 ± 73	99.8	184.7 ± 0.7	33.9	1813.7 ± 4.2
825	0.30 ± 0.13	nd	6.7 ± 34.9	1562.8 ± 25.2	33688 ± 65	99.7	187.4 ± 1.4	45.6	1829.8 ± 8.6
850	0.39 ± 0.21	nd	48.6 ± 27.4	1579.9 ± 22.9	34043 ± 97	99.7	187.1 ± 0.7	57.4	1828.5 ± 4.0
875	0.30 ± 0.21	nd	39.8 ± 10.0	1599.0 ± 23.2	34459 ± 70	99.7	187.3 ± 0.6	69.3	1829.6 ± 3.4
900	0.15 ± 0.17	nd	45.1 ± 18.2	996.8 ± 14.5	21779 ± 41	99.8	190.0 ± 0.7	76.8	1846.1 ± 4.1
975	0.11 ± 0.19	0.09 ± 0.26	9.0 ± 24.2	1022.1 ± 15.3	22125 ± 53	99.9	188.4 ± 1.0	84.4	1836.0 ± 5.9
1050	0.08 ± 0.19	nd	22.6 ± 23.6	1267.3 ± 18.9	28272 ± 60	99.9	194.3 ± 0.9	93.9	1871.6 ± 5.5
1150	0.12 ± 0.20	nd	58.1 ± 29.9	780.8 ± 12.8	17954 ± 72	99.8	200.0 ± 1.9	99.7	1905.7 ± 11.0
1400	0.51 ± 0.11	0.09 ± 0.06	56.3 ± 7.0	36.4 ± 1.2	944 ± 3	84.1	190.0 ± 9.5	100.0	1846.1 ± 57.8
Total	*4.62 ± 0.65*	*3.3 ± 0.67*	*628.4 ± 72.2*	*13376.9 ± 60.7*	*282703 ± 206*		*183.3 ± 0.3*		*1804.5 ± 8.6*
Sample AF-B06 muscovite	*mass = 0.00924 g*								
500	0.73 ± 0.10	0.3 ± 0.05	5.6 ± 2.0	55.5 ± 0.8	656 ± 1	67.1	69.2 ± 4.7	0.6	902 ± 48
600	0.38 ± 0.10	0.54 ± 0.15	19.7 ± 3.3	246.4 ± 3.8	3190 ± 9	96.5	108.7 ± 1.2	3.1	1268 ± 10
675	0.52 ± 0.09	0.83 ± 0.21	63.7 ± 6.8	791.4 ± 14.1	13205 ± 38	98.8	143.7 ± 1.6	11.1	1540 ± 12
730	0.57 ± 0.21	nd	65.5 ± 16.7	1432.0 ± 20.9	28155 ± 50	99.4	170.3 ± 0.6	25.6	1722 ± 4
780	0.62 ± 0.23	nd	81.2 ± 18.9	1781.5 ± 26.8	37684 ± 55	99.5	183.4 ± 0.9	43.7	1805 ± 6
820	0.52 ± 0.20	nd	15.8 ± 21.2	1481.2 ± 24.5	32062 ± 79	99.5	187.7 ± 1.7	58.7	1832 ± 10
900	0.54 ± 0.21	nd	19.4 ± 9.1	1639.2 ± 24.4	35860 ± 77	99.6	189.8 ± 0.9	75.3	1845 ± 6
975	0.31 ± 0.17	0.16 ± 0.19	20.6 ± 12.3	986.3 ± 14.5	21597 ± 31	99.6	190.0 ± 0.8	85.3	1846 ± 5
1025	0.53 ± 0.13	0.91 ± 0.15	61.0 ± 10.9	546.6 ± 8.0	11542 ± 12	98.7	181.5 ± 0.8	90.9	1793 ± 5
1100	0.42 ± 0.23	nd	39.8 ± 13.4	630.2 ± 9.5	14199 ± 24	99.1	194.6 ± 1.3	97.2	1874 ± 8
1140	0.23 ± 0.11	0.39 ± 0.06	57.7 ± 7.6	205.2 ± 3.1	4562 ± 7	98.5	190.8 ± 1.8	99.3	1851 ± 11
1200	0.20 ± 0.08	0.19 ± 0.05	40.0 ± 6.5	55.4 ± 0.9	1223 ± 1	95.0	182.7 ± 3.8	99.9	1801 ± 23
1400	0.34 ± 0.10	nd	23.7 ± 4.1	11.2 ± 0.7	428 ± 1	76.3	252.4 ± 28.2	100.0	2190 ± 142
Total	*5.91 ± 0.58*	*3.3 ± 0.36*	*513.7 ± 42.4*	*9861.8 ± 54.2*	*204364 ± 145*		*177.3 ± 0.4*		*1778 ± 8*

(1) Determined from $^{37}Cl(n,\gamma,\beta)^{38}Ar$:

$$Cl = 9.0149\times10^{4}\cdot\frac{(^{38}Ar)}{\beta\,.\,J}(mole/mole)$$

$$\beta = \left[\frac{K}{Cl}\cdot\frac{(^{38}Ar)}{(^{39}Ar)}\right]_{Hb3gr}$$

$(K/Cl)_{Hb3gr}$ = 5.242; β = 7.37 ± 0.12; J = 0.00938 ± 0.000134

(2) Determined from $^{40}Ca(n,\alpha)^{37}Ar$:

$$Ca = 7.975\times10^{4}\cdot\frac{(^{37}Ar)}{\alpha\,.\,J}(mole/mole)$$

$$\alpha = \left[\frac{K}{Ca}\cdot\frac{(^{37}Ar)}{(^{39}Ar)}\right]_{Hb3gr}$$

$(K/Ca)_{Hb3gr}$ = 0.1674; α = 0.49 ± 0.02

(3) Determination from $^{39}K(n,p)^{39}Ar$:

$$K = \frac{(^{39}Ar)}{J}\cdot\frac{K}{(^{40}K)}\cdot\frac{\lambda}{(\lambda_e)}(mole/mole)$$

λ/λ_e = 9.54; $^{40}K/K = 1.167\times10^{-4}$

(4) $^{40}Ar^{*} = {}^{40}Ar_{total} - 295.5\times{}^{36}Ar$

(5) Total age includes uncertainties on the J value

Note: 2 standard deviation errors; nd = not determined. The reaction expressed as $^{39}K(n,p)^{39}Ar$ for example, signifies that a fast neutron is incorporated within the ^{39}K atom with the resultant ejection of a proton causing the formation of ^{39}Ar.

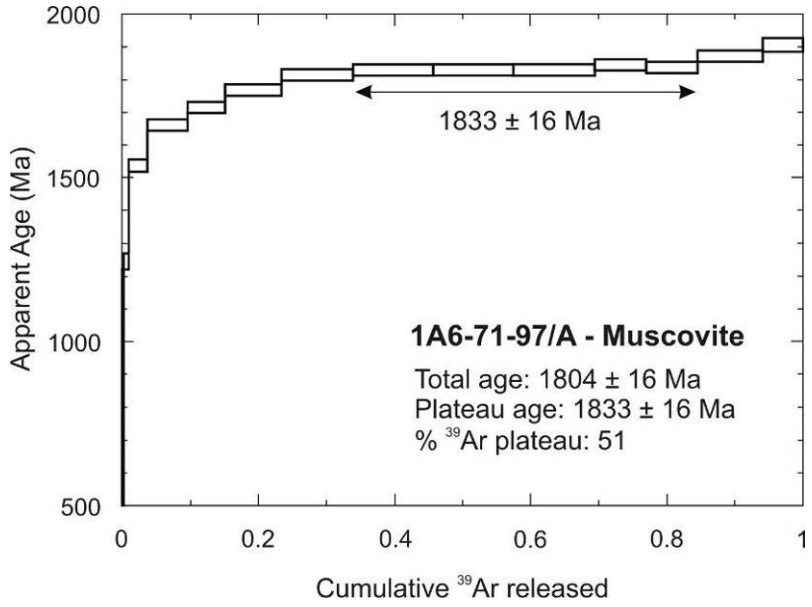

A

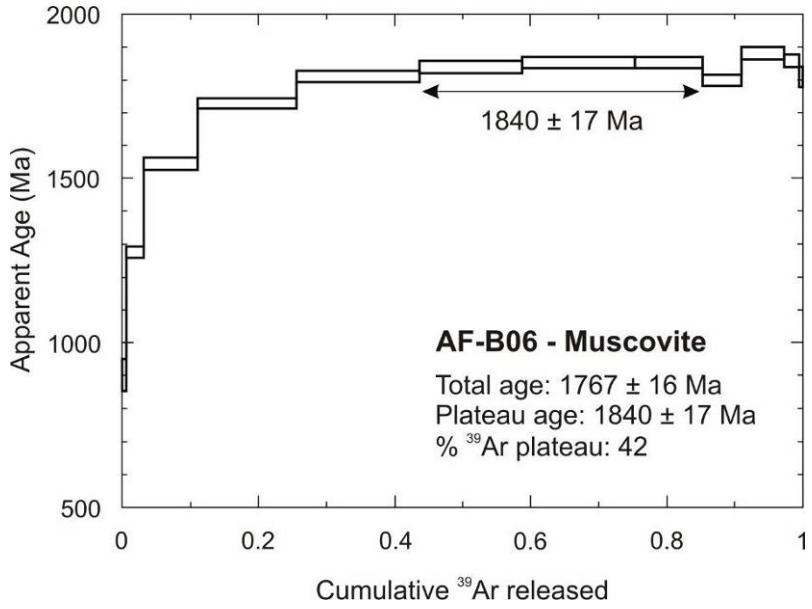

B

Figure 64. $^{40}Ar/^{39}Ar$ apparent age spectra for muscovite from mineralization zones of Afema gold deposits. A) Drill core sample from Jonction. B) Isolated sample (hand specimen from mine dump) from Afema gold district. The width of rectangles represents the analytical error in the apparent age of the individual temperature step at ± 2σ.

3-5-3. Re-Os geochronology of pyrite and arsenopyrite

The best approach to determine the age of gold mineralization is to date ore minerals with which it is closely associated. In the case of the Afema gold deposits, this means dating sulfides, particularly pyrite and arsenopyrite. With regard to these sulfides, Re-Os geochronology is a suitable dating method. The Re-Os isotopic system is based on the beta decay of ^{187}Re to ^{187}Os. Re-Os differs from other isotopic systems (e.g. Rb-Sr, Sm-Nd) because rhenium and osmium (i.e. parent and daughter) have the particularity to be both chalcophile and siderophile in character (rather than lithophile). Consequently, they are easily incorporated into the lattices of sulfide and oxide minerals (Richards and Noble, 1998). Thus, they can be used as chronometer to directly date ore minerals. Usually, Re-Os dating is applied on molybdenite, because this mineral contains abundant rhenium, but negligible osmium. Recently, however, with improvement of the analytical precision, other sulfides (notably pyrite and arsenopyrite) with low Re-content have been successfully used (Stein *et al.*, 2000; Arne *et al.*, 2001; Barra *et al.*, 2003; Morelli *et al.*, 2005).

The following equation is historically used for the age calculation in Re-Os dating:

$$\left(^{187}Os/^{186}Os\right) = \left(^{187}Os/^{186}Os\right)_0 + \left(^{187}Re/^{186}Os\right)(\exp(\lambda t) - 1) \qquad [19]$$

where λ is the decay constant, t is the age, $(^{187}Os/^{186}Os)_0$ is the initial ratio, $(^{187}Os/^{186}Os)$ and $(^{187}Re/^{186}Os)$ correspond to the present ratios (measured). However, this equation does not take into account that ^{186}Os is a radiogenic daughter of the decay $^{190}Pt \rightarrow {}^{186}Os$, which is a significant problem for Pt-rich rocks or minerals. To avoid the possible perturbation by radiogenic ^{186}Os, ^{188}Os is nowadays substituted to ^{186}Os for the normalization (Dickin, 1997). Thus, the above equation becomes:

$$\left(^{187}Os/^{188}Os\right) = \left(^{187}Os/^{188}Os\right)_0 + \left(^{187}Re/^{188}Os\right)(\exp(\lambda t) - 1) \qquad [20]$$

The currently best decay constant (λ) for ^{187}Re is 1.666 x 10^{-11} $year^{-1}$ (Smoliar *et al.*, 1996).

Six samples of gold-bearing metaarenite containing pyrite and arsenopyrite (as main sulfides) were collected from the Jonction deposit for rhenium-osmium isotope analysis. The Re-Os abundance and isotopic data of the selected samples are displayed in the Table 11.

The sulfide concentrates (pyrite + arsenopyrite) have been analyzed two or three times to increase the analytical reliability because of low concentrations of osmium and rhenium. The common Os contents range between 4.5 – 68.2 ppt. The $^{187}Re/^{188}Os$ isotopic ratios give a very large range from 24.13 to about 5000, and low to highly radiogenic Os compositions (0.54 – 112.95). With the regression model 3 fit (Ludwig, 2001), no meaningful isochron results, but an errochron age of 1943 ± 100 Ma with an initial $^{187}Os/^{188}Os$ of -0.8 ± 3.4 (2σ) and MSWD = 798 (Figure 65). The high MSWD indicates considerable scatter. This excess scatter is likely of geologic nature and may be due to the heterogeneous hydrothermal system, due to the successive infiltrations of hydrothermal fluids, as expressed by the sulfide zoning (see sections 3-4-3 and 3-4-4). The closure temperature of osmium in arsenopyrite is ≥ ~500°C (Morelli, 2005), and the geothermometry carried out on arsenopyrite yields not more than 360°C, which makes a postdepositional disturbance unlikely. The closure temperature of osmium in pyrite however remains unknown. For the most Re-rich samples a model age can be calculated, assuming that all ^{187}Os is from ^{187}Re. The data give single-point model ages of 2.1 – 1.8 Ga for samples T622, T690 and T697, in which the rhenium content is greater than 2 ppb.

Table 11. Re-Os isotopic data for gold-bearing pyrite and arsenopyrite from the Jonction deposit.

Sample		Au	Weight	Re (ppb)		^{187}Re (ppb)		Common Os (ppb)		^{187}Os (ppb)		^{187}Re/^{188}Os		^{187}Os/^{188}Os		Model age
ID	Drill core No.	(ppm)	(g)	conc.	± 2σ	conc.	±2σ	conc.	± 2σ	conc.	± 2σ	conc.	± 2σ	conc.	± 2σ	(Ga)
T622	1A6-72-97/199.64m	12.5	1.201	4.7628	0.0493	2.9815	0.0309	0.0065	0.0002	0.0964	0.0009	3492.29	89.05	112.95	2.57	1.91
T622	1A6-72-97/199.64m	12.5	0.400	4.6815	0.0438	2.9306	0.0274	0.0045	0.0003	0.1008	0.0012	4986.76	390.73	172.00	13.43	2.03
T622	1A6-72-97/199.64m	12.5	1.201	4.7564	0.0783	2.9775	0.0490	0.0062	0.0001	0.0910	0.0008	3662.09	106.62	112.32	2.64	1.81
T690	1A6-44-97/av.90m	> 30	1.201	4.9185	0.0437	3.0790	0.0274	0.0073	0.0001	0.0952	0.0010	3196.67	63.23	98.85	1.76	1.83
T690	1A6-44-97/av.90m	> 30	0.401	4.3395	0.0428	2.7165	0.0268	0.0075	0.0004	0.0969	0.0015	2759.58	155.15	98.76	5.60	2.10
T690	1A6-44-97/av.90m	> 30	1.200	3.7725	0.0755	2.3616	0.0473	0.0066	0.0003	0.0821	0.0010	2720.81	120.37	95.05	3.81	2.05
T691	JON-03	3.29	0.498	0.4172	0.0081	0.2612	0.0051	0.0682	0.0019	0.0048	0.0005	24.13	0.82	0.54	0.06	
T691	JON-03	3.29	1.200	0.3951	0.0066	0.2473	0.0042	0.0129	0.0002	0.0036	0.0001	133.06	3.17	2.14	0.08	
T695	JON-07	5.06	0.401	0.1056	0.0091	0.0661	0.0057	0.0105	0.0006	0.0017	0.0002	33.72	3.55	1.24	0.16	
T695	JON-07	5.06	0.612	0.1081	0.0069	0.0677	0.0043	0.0134	0.0005	0.0021	0.0002	26.05	1.92	1.18	0.10	
T696	JON-09	2.44	0.908	1.1421	0.0124	0.7150	0.0078	0.0407	0.0006	0.0048	0.0002	131.29	2.38	0.90	0.03	
T696	JON-09	2.44	1.206	1.1750	0.0154	0.7356	0.0097	0.0275	0.0003	0.0046	0.0001	198.47	3.43	1.28	0.03	
T697	JON-10	21.8	0.268	6.4064	0.0649	4.0104	0.0406	0.0496	0.0006	0.1429	0.0012	604.73	9.89	21.93	0.25	2.10
T697	JON-10	21.8	1.200	6.7829	0.0890	4.2461	0.0557	0.0249	0.0002	0.1473	0.0015	1293.94	19.78	44.93	0.36	2.05

The gold contents were determined with neutron activation method by Actlabs.

The ^{187}Re concentration was calculated using the proportion ^{187}Re = 62.6 % [total Re].

The model age was calculated for samples, in which the rhenium content is greater than 2 ppb, using the following formula:

$$t = \frac{1}{\lambda}\left[\ln\left(1 + \frac{\left(^{187}Os\right)}{\left(^{187}\mathrm{Re}\right)}\right)\right] \qquad [21]$$

where λ (^{187}Re decay constant) = 1.666 x 10^{-11}year^{-1}.

Samples defined by “JON” have been taken from Jonction open pit, the other are drill cores.

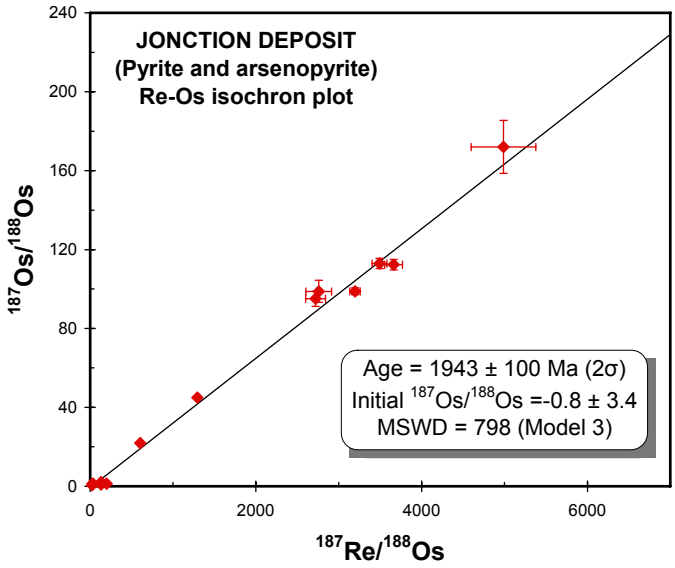

Figure 65. Re-Os isochron diagram for pyrite and arsenopyrite associated with gold mineralization at the Jonction deposit.

4. DISCUSSION AND CONCLUSIONS

4-1. Genetic model for gold mineralization

The proposition of a genetic model for gold mineralization is very important in economic geology, as it can have a great impact on exploration strategies (e.g. what type of deposit to look for, where, and how?). First, it appears necessary to shed light on the major characteristics of the deposits studied, which will serve as basis for the conceptualization of a genetic model for gold mineralization in the Afema gold district.

Gold mineralization, veining, and hydrothermal alteration are integral parts of the hydrothermal system. Textural evidence suggests contemporaneousness of sulfide crystallization and deformation. On a deposit scale, the timing relation between auriferous quartz veins and the deformation elements can be appreciate on a schematic block diagram (Figure 66) performed by Tourigny (1998) in an unpublished mine document.

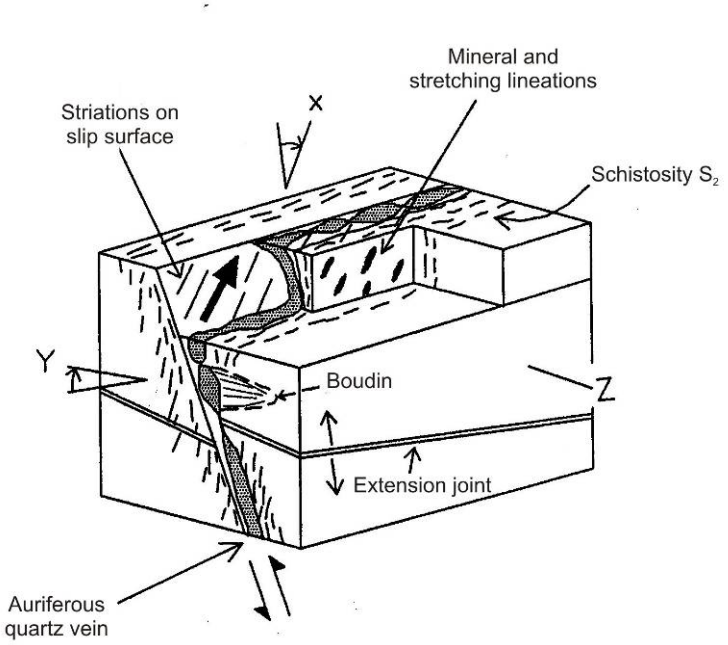

Figure 66. Schematic representation of the geometric relationships between structural elements of shear zones, auriferous quartz veins and corresponding incremental strain axes (after Tourigny, 1998).

On this block diagram, one can see the close relationship between configuration of the auriferous quartz veins and kinematics of the host shear zones. This means that the auriferous quartz veins formed synchronously with penetrative fabrics in their host structure, i.e. the gold mineralization and the hydrothermal alteration took place during the deformation event. Therefore, the gold mineralization is structurally controlled.

The gold deposits of the Afema district are located specifically in a tectonic zone corresponding to the contact between metasedimentary and metavolcanic assemblages. Ore zones are represented by lode systems, which dip in high-angle (nearly vertically) and extend deeply (>400 m below the surface).

Gold mineralization is considered to be post-peak metamorphism and occurs in metasedimentary rocks (metaarenite) affected by epizonal metamorphism and hydrothermal alteration. Sulfidation, silicification, carbonatization, and sericitization characterize the ore zones.

Two primary ore types are recognized: (1) sulfide ore (refractory ore), which is the principal ore, and where pyrite and arsenopyrite represent the main sulfides, and (2) quartz-carbonate veins characterized by the presence of “free gold” and absence of As-rich Fe sulfide minerals. The two types of ore occur together.

In the main ore type (e.g. sulfide ore), two types of pyrite have been identified: (1) fine-grained pyrite, which is generally arsenic-rich (arsenian pyrite) and gold-bearing, (2) coarse-grained pyrite, which is arsenic-poor and barren.

The mineralogical assemblage in the main ore zones suggests reducing ore fluids, enriched in CO_2 and H_2S.

The combined maximum temperatures recorded from fluid inclusion microthermometry and from arsenopyrite geothermometry range at about 205 -

410°C, which can be regarded as the peak temperature of ore deposition. From chlorite geothermometry a range of temperatures up to 380°C were recorded.

The geochemical signature of the gold mineralization is Au-As-S-W-Sb-Cu-Zn-Te-Bi with Au-As-S as the main association.

The geotectonic setting recognized is oceanic island arc, and isotopic evidence indicates that the basement complex overlain by supracrustal rocks is devoid of Archean crust: $\varepsilon_{Nd(2190\ Ma)}$ values of metaarenite and metabasalt are positive, with 2190 Ma corresponding to the maximum age recorded by Hirdes *et al.* (2007) for Birimian formations in the Afema district. In consequence, basement (lower crust) and supracrustal rocks are all of Paleoproterozoic age.

A summary of geochronological data from the present study and from the literature relevant to Paleoproterozoic crustal development and gold mineralization systems in the Afema district and neighboring Ghana is presented in Figure 67.

The summary of the age data for gold mineralization in the Afema district, by taking into account the error intervals, gives an age range between 2.1 – 1.8 Ga. The Ar-Ar ages obtained from hydrothermal muscovite in gold-bearing rocks are at the younger end (1857 – 1817 Ma), the Re-Os errorchron on gold-bearing arsenopyrite and pyrite is 1943 ± 100 Ma, and Re-Os model ages on Re-rich sulfides are up to 2.1 Ga.

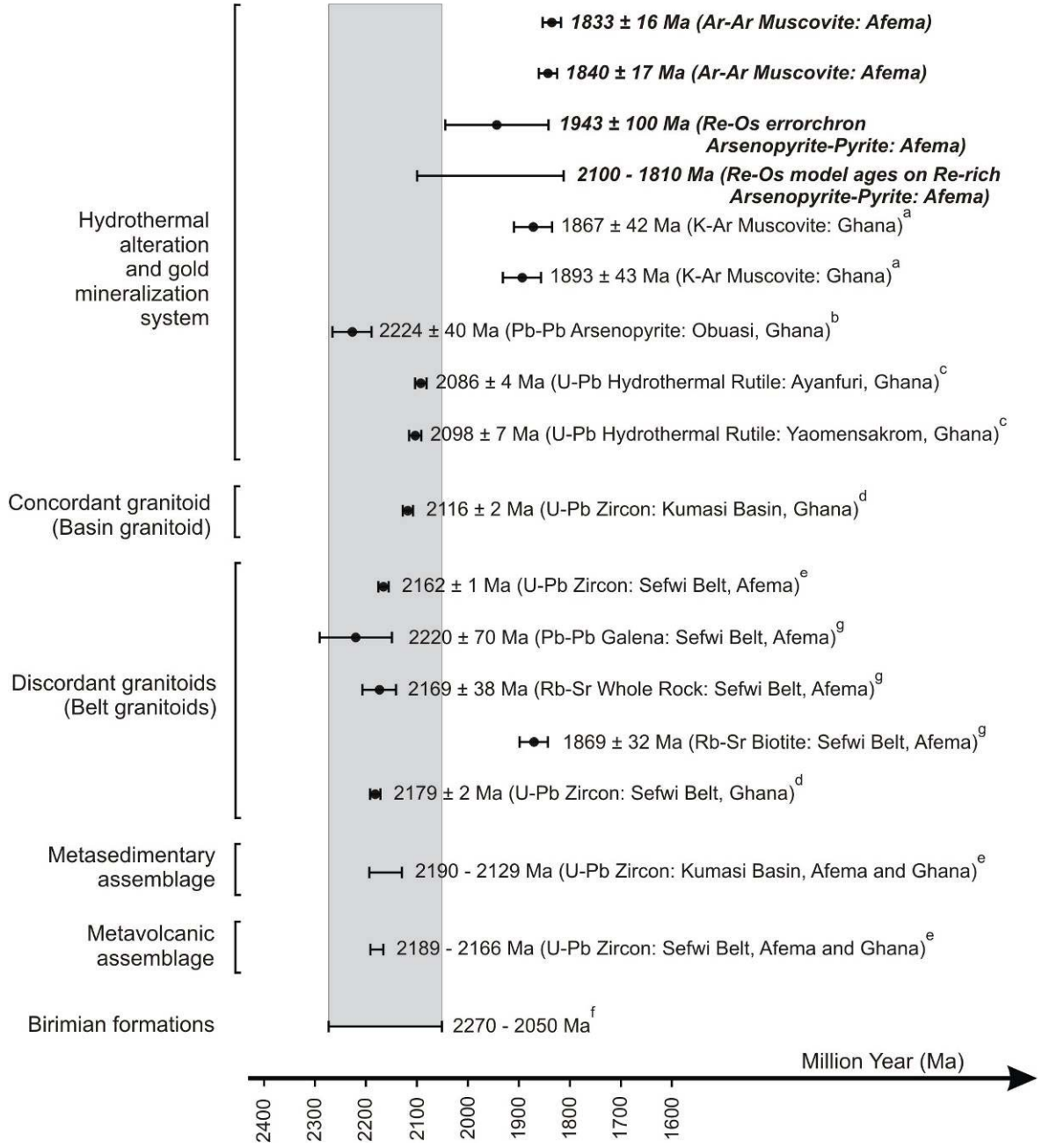

Figure 67 Summary of geochronological data relevant to Paleoproterozoic crustal development and gold mineralization in the Afema district and in neighboring Ghana. Data in bold are from the present study. References: **a)** Ahrendt (1992, cited in Oberthür *et al.*, 1994); **b)** Höhndorf *et al.* (1994); **c)** Oberthür *et al.* (1994); **d)** Hirdes *et al.* (1992); **e)** Hirdes *et al.* (2007); **f)** Abouchami *et al.* (1990), Boher *et al.* (1992), Hirdes *et al.* (1992), Hirdes *et al.* (1996), Oberthür *et al.* (1998), Hirdes and Davis (2002), Pigois *et al.* (2003); **g)** Delor *et al.* (1992).

K-Ar ages on muscovite from neighboring Ghana (1936 – 1825 Ma) overlap with the Ar-Ar age range on muscovite and the Re-Os errorchron on sulfides in the Afema district, while remaining younger than the upper limit of the Re-Os ages. However, the age obtained by Pb-Pb dating on arsenopyrite (2224 ± 40 Ma)

from the Obuasi deposit, is significantly higher than the Ar-Ar, K-Ar and Re-Os ages. This high Pb-Pb age is interpreted by Höhndorf *et al.* (1994) as probable age of detrital components in Birimian sediments and thus have to be compared with the U-Pb ages on zircon which are around 2190 Ma and which define igneous host-rock formation

Also in Ghana, the dating of hydrothermal rutile sampled on basin granitoids (Kumasi basin) transected by gold mineralization yielded U-Pb ages of 2086 ± 4 Ma at Ayanfuri and 2098 ± 7 Ma at Yaomensakrom (Oberthür *et al.*, 1994). It is furthermore mentioned that both granitoids give a U-Pb monazite age of 2105 ± 3 Ma (Davis, 1993 - cited by Oberthür *et al.*, 1994).

By combining the different ages and dating methods, there is a common picture for both the Afema district and Ghana, where the younger Ar-Ar and K-Ar ages obtained on muscovite are identical. These younger ages of 1.9 – 1.8 Ga relate to the blocking temperature for Ar loss in muscovite at 350 ± 50°C, and likely define thermal overprint.

For arsenopyrite, the osmium closure temperature is slightly higher (>500°C) than the supposed temperature of its crystallization (<500°C). Consequently, contrary to argon in muscovite, loss of osmium from arsenopyrite during subsequent thermal overprint is less. Thus, the age obtained from Re-Os on arsenopyrite and pyrite can be regarded as closer to the deposition age of the sulfides.

On a regional scale, the ages of 2098 ± 7 Ma and 2086 ± 4 Ma obtained in Ghana from U-Pb on hydrothermal rutile are among the oldest ages recorded for gold mineralization. These ages are similar to some Re-Os model ages (2100 – 1810 Ma) and close to the errorchron margin for arsenopyrite and pyrite in the Afema district (e.g. 1943 ± 100 Ma). The age around 2.1 Ga fits the Eburnean tectonothermal event (Eburnean Orogeny) which occurred at about 2.1 Ga, and during which Birimian Supergroup as well as plutonic rocks were deformed and metamorphosed (Abouchami *et al.*, 1990; Boher *et al.*, 1992). The

currently available age data for the closest major granitoid intrusion, which is located at about 10 km from the Afema gold deposits (Figure 5 and Table 2), give values of 2220 ± 70 Ma from Pb-Pb on galena, 2169 ± 38 Ma from Rb-Sr on whole rock, and 1869 ± 32 Ma from Rb-Sr on biotite (Delor *et al.*, 1992). The younger age of 1869 ± 32 Ma from biotite corresponds very likely to thermal overprint.

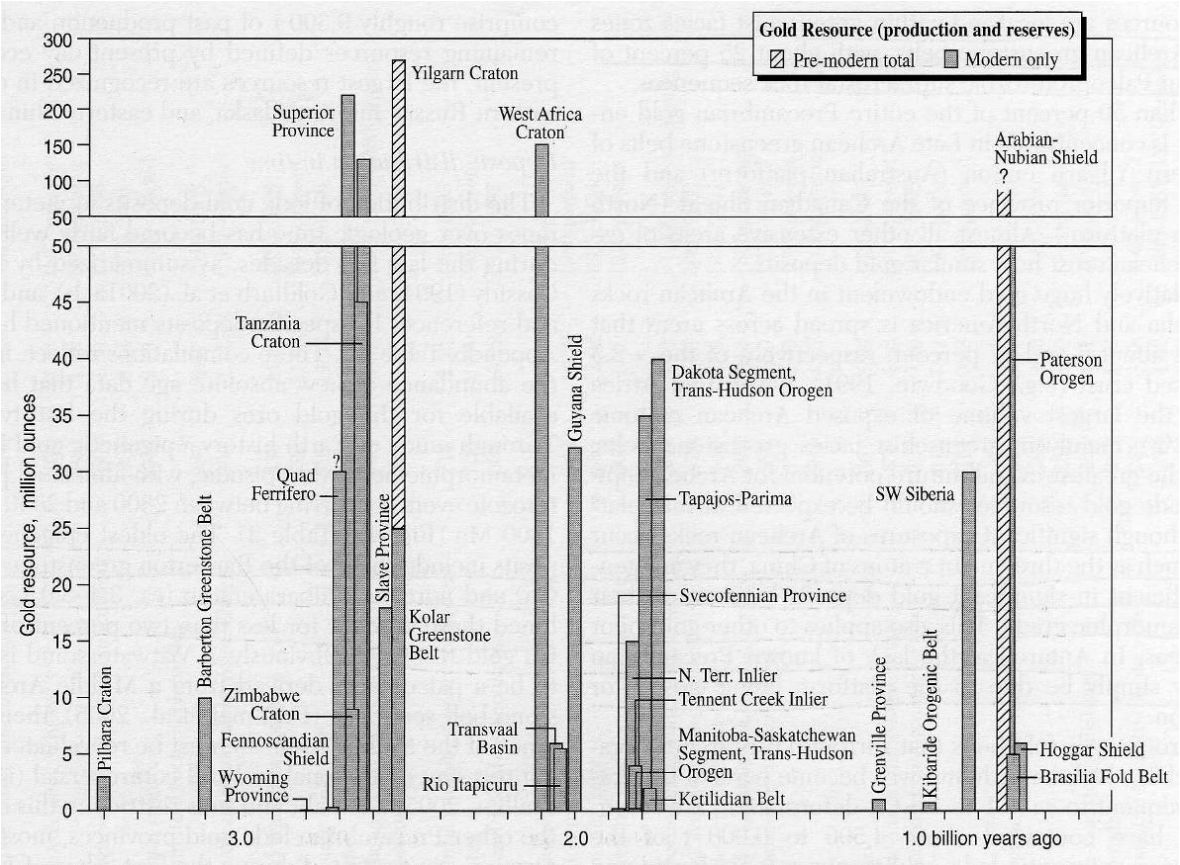

Figure 68. Gold production versus best approximation for the age of gold mineralization of Precambrian orogenic gold deposits (Goldfarb *et al.*, 2001; later modified by Goldfarb *et al.*, 2005).

Comparing cumulative gold production versus the age of gold mineralization for Precambrian orogenic gold deposits worldwide, Goldfarb *et al.* (2001) portray the age of 2.1 Ga is the main event of gold production in the West African craton (Figure 68). In other words, 2.1 Ga is regarded as the metallogenic epoch for gold mineralization in West African craton.

The Afema tectonic zone, which hosts the gold deposits discovered so far, played a significant role in controlling ore-fluid flow. In this major structure, the rocks are highly deformed, which produced fracture permeability for hydrothermal fluids. The ore deposits are notably located in the metaasedimentary assemblage, which can be explained by the higher relative porosity of this rock unit compared to the metavolcanic assemblage (mainly composed of metabasalt). An illustration of the genetic model for gold mineralization in the Afema gold district is presented in Figure 69. The source of the ore fluids (e.g. from metamorphic devolatization, from felsic magma, or from mantle degassing) is not defined.

The various features summarized and discussed above, suggest that the gold mineralization in the Afema district is similar to many other lode gold deposits which are classified as orogenic gold deposits (Kerrich and Cassidy, 1994; McCuaig and Kerrich, 1998; Partington and Williams, 2000; Goldfarb *et al.*, 2001).

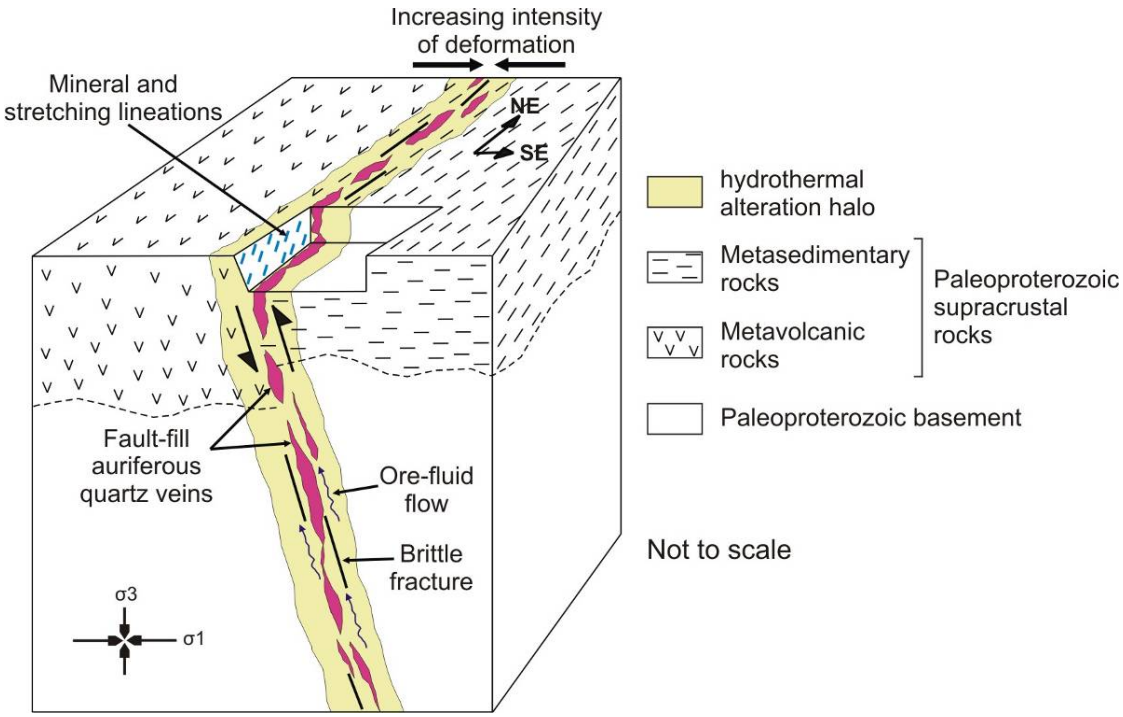

Figure 69. Block diagram illustrating the genetic model of gold mineralization in the Afema gold district. The source of the syn-deformational ore fluids is not defined.

4-2. Recommendations for exploration

Hydrothermal alteration and associated chemical changes can be used effectively in exploration to target gold ore zones. However, the identification of the hydrothermally altered zones in the field is quite difficult, as the hydrothermal assemblages are similar to the low-grade regional metamorphic mineralogy. This difficulty is enhanced due to the significant thickness of lateritic soil cover which can reach several tens of meters, typical for intertropical regions. This problem can, however, be surmounted by the use of some key chemical elements, i.e. As, S, K, and Na. Gold-bearing hydrothermally altered zones in the studied area are generally distinguished by enrichment of As, Sb, S, W, (Te), (Bi) and an increase of the K/Na ratio. Among the quoted elements, arsenic is the best pathfinder for gold mineralization, as it presents a wide primary dispersion halo (>100 m) and a strong positive correlation with gold. Sb and W enrichment are less pronounced, but they also correlate well with Au. The enrichment of other elements in the gold mineralization zones is much less significant in whole rocks analyses. In other words, during geochemical surveys (e.g. soil sampling, stream sediments, trenching), the samples should be analyzed not only for gold but also for As and, (eventually) Sb and W as proximal indicators with wider dispersion than Au.

Besides the hydrothermal alteration, highly deformed zones should also be regarded as metallotect for gold, because the primary control of gold mineralization is structural. Regional structures and contact zones between lithologies with different rheologic features should be particularly targeted.

Mineralogically, silicified zones with presence of sulfides (especially arsenopyrite and fine-grained pyrite) and depletion of feldspar should be regarded with great interest for gold mineralization.

At the end of the present work, it can be noted that several questions on the lode gold mineralization in the Afema gold district have been answered.

However, several outstanding problems remain unresolved. These problems are the precise age of gold mineralization and the origin of the ore fluids. These are problems typical of many other ore deposits as well. Future studies should focus on these gaps in order to propose a more complete metallogenic model for gold mineralization.

REFERENCES

ABOUCHAMI W., BOHER M., MICHARD A. and ALBAREDE F. (1990) - A major 2.1 Ga events of magmatism in West Africa: an early stage of crustal accretion. *Journal of Geophysical Research*, Vol. 95(B11), pp. 17605-17629.

ARNE D. C., BIERLIN F. P., MORGAN J. W. and STEIN H. J. (2001) - Re-Os dating of sulfides associated with gold mineralization in Central Victoria, Australia. *Economic Geology*, Vol. 96(6), pp. 1455-1459.

ARNOULD A.(1959) - Remarques concernant les principes généraux à retenir pour une définition par faciès de la série birrimienne du Mont Goma (Côte d'Ivoire). *Service de Géologie et de Prospection Minière*, Dakar, 12 p. (unpublished)

ARNOULD A.(1961) - Etude géologique des migmatites et des granites précambriens du Nord-Est de la Côte d'Ivoire et de la Haute-Volta méridionale. *Bureau de Recherches Géologiques et Minières (BRGM)*, Paris, Mémoire du BRGM, n° 3, 174 p.

ASSIE K. E. (1998) - Interprétation des sondages miniers dans la région de l'Aféma (Sud-Est de la Côte d'Ivoire): Apport à la compréhension de la stratigraphie et de la minéralisation aurifère du Birimien en Côte d'Ivoire. DEA, *Université de Cocody*, Abidjan, 61 p.

AUBOUIN J. (1961) - Propos sur les géosynclinaux. *Bulletin de la Société Géologique de France*, Vol. 3, pp. 629-702.

BAILEY S. W. (1980) - Summary of recommendations of AIPEA nomenclature committee on clay minerals. *American Mineralogist*, Vol. 65, pp. 1-7.

BARNES H. L. (1979) - Solubilities of ore minerals. *In*: H. L. Barnes (ed) Geochemistry of hydrothermal ore deposits, 2nd ed., *John Wiley & Sons*, New York, pp. 404-460.

BARRA F., RUIZ J., MATHUR R. and TITLEY S. (2003) - A Re–Os study of sulfide minerals from the Bagdad porphyry Cu–Mo deposit, northern Arizona, USA. *Mineralium Deposita*, Vol. 38(5), pp. 585-596.

BATES D. A. (1956) - Gold Coast and Togoland. *In*: Lexique stratigraphique international, vol. 4 Afrique, fascicule 3, *Centre National de la Recherche Scientifique (CNRS)*, Paris, pp. 15-31.

BAYLISS P. (1975) - Nomenclature of the trioctahedral chlorites. *Canadian Mineralogist*, Vol. 13, pp. 178-180.

BENNETT A. J. and BENNING L. G. (2004) - Gold and arsenic interactions with pyrite in hydrothermal solutions. Goldschmidt Conference, Copenhagen, Danemark, *Geochimica et Cosmochimica Acta*, vol. 68 (11S), p. A293.

BESSOLES B.(1977) - Géologie de l'Afrique: le craton ouest africain. *Bureau de Recherches Géologiques et Minières*, Paris, Mémoire du BRGM, n°88, 403 p.

BHATIA M. R. and CROOK K. A. W. (1986) - Trace element characteristics of graywackes and tectonic setting discrimination of sedimentary basins. *Contributions to Mineralogy and Petrology*, Vol. 92(2), pp. 181-193.

BOHER M., ABOUCHAMI W., A. M., ALBAREDE F. and ARNDT N. T. (1992) - Crustal growth in West Africa at 2.1 Ga. *Journal of Geophysical Research*, Vol. 97(B1), pp. 345-369.

BORG G. (1994) - The Geita gold deposit in NW Tanzania - Geology, ore petrology, geochemistry and timing of events. *In*: T. Oberthür (ed) Metallogenesis of selected gold deposits in Africa. Geologisches Jahrbuch, Reihe D, Heft 100, *Bundesanstalt für Geowissenschaften und Rohstoffe*, Hannover, pp. 545-595.

BROOKS C., HART S. R. and WENDT I. (1972) - Realistic use of two-error regression treatments as applied to rubidium-strontium data. *Reviews of Geophysics and Space Physics*, Vol. 10(2), pp. 551-577.

CATHELINEAU M. (1988) - Cation site occupancy in chlorites and illites as a function of temperature. *Clay Minerals*, Vol. 23(4), pp. 471-485.

CATHELINEAU M. and NIEVA D. (1985) - A chlorite solid solution geothermometer the Los Azufres (Mexico) geothermal system. *Contributions to Mineralogy and Petrology*, Vol. 91(3), pp. 235-244.

CHOI S.-G. and YOUM S.-J. (2000) - Compositional variation of arsenopyrite and fluid evolution at the Ulsan deposit, Southeastern Korea: a low-sulfidation porphyry system. *Canadian Mineralogist*, Vol. 38(3), pp. 567-583.

CLIFFORD T. N. (1970) - The structural framework of Africa. *In*: T. N. Clifford and I. G. Gass (eds) African magmatism and tectonics, *Oliver and Boyd*, Edinburgh, pp. 1-26.

CRAWFORD M. L. (1981) - Phase equilibria in aqueous fluid inclusions. *In*: L. S. Hollister and M. L. Crawford (eds) Short course in fluid inclusions: application to petrology, vol. 6, *Mineralogical Association of Canada*, Calgary (Canada), pp. 75-100.

DAVIS D. W., HIRDES W., SCHALTEGGER U. and NUNOO E. A. (1994) - U-Pb age constraints on deposition and provenance of Birimian and gold-bearing Tarkwaian sediments in Ghana, West Africa. *Precambrian Research*, Vol. 67(1-2), pp. 89-107.

DE CARITAT P., HUTCHEON I. and WALSHE J. L. (1993) - Chlorite geothermometry; a review. *Clays and Clay Minerals*, Vol. 41(2), pp. 219-239.

DEER W. A., HOWIE R. A. and ZUSSMAN J. (1992) - An introduction to the rock-forming minerals. 2nd ed., *Pearson Education Limited*, Harlow, 696 p.

DELOR C., DIABY I., SIMEON Y., ADOU M., BI ZAMBLE Z., TASTET J.-P., YAO B., KONAN G., CHIRON J.-C. and DOMMANGET A. (1992) - Carte géologique de la Côte d'Ivoire à 1/200000; Feuille Grand-Bassam. *Direction de la Géologie*, Abidjan.

DEPAOLO D. J. (1988) - Neodymium isotope geochemistry: An introduction. *Springer Verlag*, New York, 181 p.

DICKIN A. P. (1997) - Radiogenic isotope geology. *Cambridge University Press*, Cambridge (United Kingdom), 490 p.

DOTT R. H., JR. (1964) - Wacke, graywacke and matrix - what approach to immature sandstone classification? *Journal of Sedimentary Petrology*, Vol. 34, pp. 625-632.

DU A., WU S., SUN D., WANG S., QU W., MARKEY R., STAIN H., MORGAN J. and MALINOVSKIY D. (2004) - Preparation and certification of Re-Os dating reference materials: Molybdenites HLP and JDC. *Geostandards and Geoanalytical Research*, Vol. 28(1), pp. 41-52.

FAURE G. (1986) - Principles of isotope geology. 2nd ed., *John Wiley & Sons*, New York, 589 p.

FISHER J. R. (1976) - The volumetric properties of H_2O - a graphical portrayal. *Journal of Research of the U.S. Geological Survey*, Vol. 4, pp. 189-193.

GEBRE-MARIAM M., HAGEMANN S. G. and GROVES D. I. (1995) - A classification scheme for epigenetic Archaean lode-gold deposits. *Mineralium Deposita*, Vol. 30, pp. 408-410.

GOLDFARB R. J., BAKER T., DUBÉ B., GROVES D. I., HART C. J. R. and GOSSELIN P. (2005) - Dristribution, character, and genesis of gold deposits in metamorphic terranes. *In*: J. W. Hedenquist, J. F. H. Thompson, R. J. Goldfarb and J. P. Richards (eds) Economic Geology: One hundredth anniversary volume 1905-2005, *Society of Economic Geologists*, Littleton (USA), pp. 407-450.

GOLDFARB R. J., GROVES D. I. and GARDOLL S. (2001) - Orogenic gold and geologic time: a global synthesis. *Ore Geology Reviews*, Vol. 18(1-2), pp. 1-75.

GOLDSTEIN S. L., O'NIONS R. K. and HAMILTON P. J. (1984) - A Sm-Nd isotopic study of atmospheric dusts and particulates from major river systems. *Earth and Planetary Science Letters*, Vol. 70(2), pp. 221-236.

HANES J. A. (1991) - K-Ar and 40Ar/39Ar geochronology: methods and applications. *In*: L. Heaman and L. J. N. (eds) Applications of radiogenic

isotope systems to problems in geology, Short course handbook, vol. 19, *Mineralogical Association of Canada*, Toronto, pp. 27-57.

HEY M. H. (1954) - A new review of the chlorites. *The Mineralogical Magazine*, Vol. 30(224), pp. 277-292.

HIRDES W. and DAVIS D. W. (1998) - First U-Pb zircon age of extrusive volcanism in the Birimian Supergroup of Ghana/West Africa. *Journal of African Earth Sciences*, Vol. 27(2), pp. 291-294.

HIRDES W. and DAVIS D. W. (2002) - U-Pb Geochronology of Paleoproterozoic Rocks in the Southern Part of the Kedougou-Kenieba Inlier, Senegal, West Africa: Evidence for Diachronous Accretionary Development of the Eburnean Province. *Precambrian Research*, Vol. 118(1-2), pp. 83-99.

HIRDES W., DAVIS D. W. and EISENLOHR B. N. (1992) - Reassessment of Proterozoic granitoid ages in Ghana on the basis of U/Pb zircon and monazite dating. *Precambrian Research*, Vol. 56(1-2), pp. 89-96.

HIRDES W., DAVIS D. W., LUDTKE G. and KONAN G. (1996) - Two generations of Birimian (Paleoproterozoic) volcanic belts in northeastern Cote d'Ivoire (West Africa): consequences for the `Birimian controversy'. *Precambrian Research*, Vol. 80(3-4), pp. 173-191.

HIRDES W., KONAN K. G., N'DA D., OKOU A., SEA P., ZAMBLE Z. B. and DAVIS D. W.(2007) - Geologie de la partie nord de la zone d'Aboisso, avec carte géologique 1/100000. *Direction de la Géologie - Projet de coopération géologique ivoiro-allemande (2001-2003)*, Abidjan, Bulletin n° 3, 180 p.

HIRDES W., LEUBE A., MAUER R. and MOORBATH S. (1987) - The evolution of the Birimian Supergroup in Ghana / West Africa. 14th Colloquium of African Geology, Berlin, 18-22 August 1987, pp. 48-49.

HIRDES W., SENGER R., ADJEI J., EFA E., LOH G. and TETTEY A.(1993) - Explanatory notes for the geological map of Southwest Ghana 1:100000. *Bundesanstalt für Geowissenschaften und Rohstoffe (BGR)*, Hannover, Geologisches Jahrbuch, Reihe B, Heft 83, 139 p.

HÖHNDORF A., OBERTHÜR T., GAST L., VETTER U. and SCHMIDT MUMM A. (1994) - Lead isotope systematics of the mineralization at the Ashanti gold mine, Obuasi, Ghana. *In*: T. Oberthür (ed) Metallogenesis of selected gold deposits in Africa. Geologisches Jahrbuch, Reihe D, Heft 100, *Bundesanstalt für Geowissenschaften und Rohstoffe*, Hannover, pp. 155-165.

HUTCHINSON R. W. (1987) - Metallogeny of Precambrian gold deposits; space and time relationships. *Economic Geology*, Vol. 82(8), pp. 1993-2007.

ISHIKAWA Y., SAWAGUCHI T., IWAYA S. and HORIUCHI M. (1976) - Delineation of prospecting targets for Kuroko deposits based on modes of volcanism of

underlying dacite and alteraton haloes. *Mining Geology*, Vol. 26, pp. 105-117.

JACOBSEN S. B. and WASSERBURG G. J. (1980) - Sm-Nd isotopic evolution of chondrites. *Earth and Planetary Science Letters*, Vol. 50(1), pp. 139-155.

JOURDAN F. and RENNE P. R. (2007) - Age calibration of the Fish Canyon sanidine 40Ar/39Ar dating standard using primary K-Ar standards. *Geochimica et Cosmochimica Acta*, Vol. 71(2), pp. 387-402.

JUNNER N. R.(1935) - Gold in the Gold Coast. *Gold Coast Geological Survey*, Accra, Bulletin n° 4, 52 p.

JUNNER N. R.(1940) - Geology of the Gold Coast and western Togoland. *Gold Coast Geological Survey*, Accra, Bulletin n° 11, 40 p.

KERRICH R. and CASSIDY K. F. (1994) - Temporal relationships of lode gold mineralization to accretion, magmatism, metamorphism and deformation -- Archean to present: A review. *Ore Geology Reviews*, Vol. 9(4), pp. 263-310.

KITSON A. E.(1928) - Provisional geological map of the Gold Coast and western Togoland, with brief descriptive notes thereon. *Gold Coast Geological Survey*, Accra, Bulletin n° 2, 13 p.

KRANIDIOTIS P. and MACLEAN W. H. (1987) - Systematics of chlorite alteration at the Phelps Dodge massive sulfide deposit, Matagami, Quebec. *Economic Geology*, Vol. 82(7), pp. 1898-1911.

KRETSCHMAR U. and SCOTT S. D. (1976) - Phase relations involving arsenopyrite in the system Fe-As-S and their application. *Canadian Mineralogist*, Vol. 14(3), pp. 364-386.

LARGE R. R., GEMMELL J. B., PAULICK H. and HUSTON D. L. (2001) - The Alteration Box Plot: A Simple Approach to Understanding the Relationship between Alteration Mineralogy and Lithogeochemistry Associated with Volcanic-Hosted Massive Sulfide Deposits. *Economic Geology*, Vol. 96(5), pp. 957-971.

LEDRU P., JOHAN V., MILÉSI J. P. and TEGYEY M. (1994) - Markers of the last stages of the Palaeoproterozoic collision: evidence for a 2 Ga continent involving circum-South Atlantic provinces. *Precambrian Research*, Vol. 69(1-4), pp. 169-191.

LEMOINE S., TEMPIER P., BASSOT J. P., CAEN-VACHETTE M., Y. V., WENMENGA U. and TOURÉ S.(1985) - The Burkinian, an orogenic cycle, precursor of the Eburnean of West Africa. *Centre International pour la Formation et les Echanges Géologiques (CIFEG)*, Paris, 13th Colloquium of african geology, St-Andrews (Scotland, september 10-13, 1985), Publication occasionnelle n° 3, 27 p.

LEUBE A., HIRDES W., MAUER R. and KESSE G. O. (1990) - The early Proterozoic Birimian Supergroup of Ghana and some aspects of its associated gold mineralization. *Precambrian Research*, Vol. 46, pp. 139-165.

LOTZ U. (1994) - Gold mineralization in carbonaceous metasediments of zimbabwean greenstone belts (Part B): Nando-Pinkun Mine, Kadoma district - Isotopic evidence for epigenetic lode-type gold mineralization. *In*: T. Oberthür (ed) Metallogenesis of selected gold deposits in Africa. Geologisches Jahrbuch, Reihe D, Heft 100, *Bundesanstalt für Geowissenschaften und Rohstoffe*, Hannover, pp. 513-543.

LOTZ U. and PUCHELT H. (1994) - Gold mineralization in carbonaceous metasediments of zimbabwean greenstone belts (Part A): Royal Family mine, Filabusi disdrict - Evidence for metamorphic mobilization of gold from sedimentary protores *In*: T. Oberthür (ed) Metallogenesis of selected gold deposits in Africa. Geologisches Jahrbuch, Reihe D, Heft 100, *Bundesanstalt für Geowissenschaften und Rohstoffe*, Hannover, pp. 447-511.

LOWELL G. R. and GASPARRINI C. (1982) - Composition of arsenopyrite from topaz greisen veins in southeastern Missouri. *Mineralium Deposita*, Vol. 17(2), pp. 229-238.

LUDWIG K. R. (2001) - Users manual for Isoplot/Ex rev. 2.49: A geochronological toolkit for Microsoft Excel. *Berkeley Geochronology Center, Special Publication No. 1a*, Berkeley (USA), 56 p.

LUGMAIR G. W. and MARTI K. (1978) - Lunar initial 143Nd/144Nd: Differential evolution of the lunar crust and mantle. *Earth and Planetary Science Letters*, Vol. 39(3), pp. 349-357.

MACKENZIE W. S. and GUILFORD C. (1992) - Atlas de pétrographie - Minéraux de roches observés en lame mince. *Masson*, Paris, 98 p.

MCCUAIG T. C. and KERRICH R. (1998) - P-T-t-deformation-fluid characteristics of lode gold deposits: evidence from alteration systematics. *Ore Geology Reviews*, Vol. 12(6), pp. 381-453.

MILÉSI J.-P., LEDRU P., FEYBESSE J.-L., DOMMANGET A. and MARCOUX E. (1992) - Early proterozoic ore deposits and tectonics of the Birimian orogenic belt, West Africa. *Precambrian Research*, Vol. 58(1-4), pp. 305-344.

MILESI J. P., FEYBESSE J. L., LEDRU P., DOMMANGET A., OUEDRAOGO M. F., MARCOUX E., PROST A., VINCHON C., SYLVAIN J. P., V. J., TEGYEY M., CALVEZ J. Y. and LAGNY P. (1989) - Les minéralisations aurifères de l'Afrique de l'Ouest: leurs relations avec l'évolution lithostructurale au Protérozoique inférieur. *Chronique de la Recherche Minière*, Vol. 497, pp. 3-98.

MÖLLER P. (1994) - Accumulation of gold on natural sulfides: the electrochemical function of arsenic in nature. *In*: T. Oberthür (ed)

Metallogenesis of selected gold deposits in Africa. Geologisches Jahrbuch, Reihe D, Heft 100, *Bundesanstalt für Geowissenschaften und Rohstoffe*, Hannover, pp. 639-660.

MÖLLER P. and KERSTEN G. (1994) - Electrochemical accumulation of visible gold on pyrite and arsenopyrite surfaces. *Mineralium Deposita*, Vol. 29(5), pp. 404-413.

MORELLI R. M. (2005) - Re-Os arsenopyrite geochronology of the Homestake gold deposit, Black Hills, South Dakota, and implications for chronometer closure temperature. 2005 Salt Lake City Annual Meeting (October 16-19, 2005), Salt Lake City, 19 October 2005, *Geological Society of America*, vol. 37, No. 7, p. 452. (Abstract)

MORELLI R. M., CREASER R. A., SELBY D., KONTAK D. J. and HORNE R. J. (2005) - Rhenium-osmium geochronology of arsenopyrite in Meguma Group gold deposits, Meguma Terrane, Nova Scotia, Canada: evidence for multiple gold-mineralizing events. *Economic Geology*, Vol. 100(6), pp. 1229-1242.

MUMIN A. H., FLEET M. E. and CHRYSSOULIS S. L. (1994) - Gold mineralization in As-rich mesothermal gold ores of the Bogosu-Prestea mining district of the Ashanti Gold Belt, Ghana: remobilization of "invisible" gold. *Mineralium Deposita*, Vol. 29(6), pp. 445-460.

NESSE W. D. (1991) - Introduction to optical mineralogy. 2nd ed., *Oxford University Press*, New York, 335 p.

NEUENDORF K. K. E., MEHL JR. J. P. and JACKSON J. A. (2005) - Glossary of geology. 5th ed., *American Geological Institute*, Alexandria (USA), 779 p.

OBERTHÜR T., VETTER U., DAVIS D. W. and AMANOR J. A. (1998) - Age constraints on gold mineralization and Paleoproterozoic crustal evolution in the Ashanti belt of southern Ghana. *Precambrian Research*, Vol. 89, pp. 129-143.

OBERTHÜR T., VETTER U., MUMM A. S., WEISER T., AMANOR J. A., GYAPONG W. A., KUMI R. and BLENKINSOP T. G. (1994) - The Ashanti gold mine at Obuasi, Ghana: mineralogical, geochemical, stable isotope and fluid inclusion studies on the metallogenesis of the deposit. *In*: T. Oberthür (ed) Metallogenesis of selected gold deposits in Africa. Geologisches Jahrbuch, Reihe D, Heft 100, *Bundesanstalt für Geowissenschaften und Rohstoffe*, Hannover, pp. 31-129.

OBERTHÜR T., WEISER T., AMANOR J. A. and CHRYSSOULIS S. L. (1997) - Mineralogical siting and distribution of gold in quartz veins and sulfide ores of the Ashanti mine and other deposits in the Ashanti belt of Ghana: genetic implications. *Mineralium Deposita*, Vol. 32(1), pp. 2-15.

PALENIK C. S., UTSUNOMIYA S., REICH M., KESLER S. E., WANG L. and EWING R. C. (2004) - "Invisible" gold revealed: Direct imaging of gold nanoparticles in a Carlin-type deposit. *American Mineralogist*, Vol. 89(10), pp. 1359-1366.

PALS D. W., SPRY P. G. and CHRYSSOULIS S. (2003) - Invisible Gold and Tellurium in Arsenic-Rich Pyrite from the Emperor Gold Deposit, Fiji: Implications for Gold Distribution and Deposition. *Economic Geology*, Vol. 98(3), pp. 479-493.

PAPON A.(1973) - Géologie et minéralisation du Sud-Ouest de la Côte d'Ivoire. *Bureau de Recherches Géologiques et Minières*, Paris, Mémoire du BRGM, n° 80, 284 p.

PARTINGTON G. A. and WILLIAMS P. J. (2000) - Proterozoic lode gold and (iron)-copper-gold deposits: a comparison of Australian and global examples. *In*: S. G. Hagemann and P. E. Brown (eds) Gold in 2000, vol. 13, *Reviews in Economic Geology*, pp. 69-101.

PETTIJOHN F. J., POTTER P. E. and SIEVER R. (1987) - Sand and sandstone. 2nd ed., *Springer-Verlag*, New York, 553 p.

PEUCAT J. J., VIDAL P., BERNARD-GRIFFITHS J. and CONDIE K. C. (1988) - Sr, Nd, and Pb isotopic systematics in the Archaean low- to high-grade transition zone of southern India: syn accretion vs. post-accretion granulites. *Journal of Geology*, Vol. 97, pp. 537-550.

PIGOIS J.-P., GROVES D. I., FLETCHER I. R., MCNAUGHTON N. J. and SNEE L. W. (2003) - Age constraints on Tarkwaian palaeoplacer and lode-gold formation in the Tarkwa-Damang district, SW Ghana. *Mineralium Deposita*, Vol. 38(6), pp. 695-714.

REICH M., KESLER S. E., UTSUNOMIYA S., PALENIK C. S., CHRYSSOULIS S. L. and EWING R. C. (2005) - Solubility of gold in arsenian pyrite. *Geochimica et Cosmochimica Acta*, Vol. 69(11), pp. 2781-2796.

RICHARDS J. P. and NOBLE S. R. (1998) - Application of radiogenic isotope systems to the timing and origin of hydrothermal processes. *In*: Techniques in hydrothermal ore deposits geology, Reviews in economic geology, vol. 10, *Society of Economic Geologists*, Littleton (USA), pp. 195-233.

RIDLEY J. R. and DIAMOND L. W. (2000) - Fluid chemistry of orogenic lode gold deposits and implications for genetic models. *In*: S. G. Hagemann and P. E. Brown (eds) Gold in 2000, Reviews in Economic geology, vol. 13, *Society of Economic Geologists, Inc.*, Littleton (USA), pp. 141-162.

ROBERT F. and POULSEN K. H. (2001) - Vein formation and deformation in greenstone gold deposits. *In*: J. P. richards and R. Tosdal (eds) Structural controls one ore genesis, vol. 14, *Reviews in Economic Geology*, pp. 111-155.

ROEDDER E. (1984) - Fluid inclusions. Reviews in Mineralogy, vol. 12, *Mineralogical Society of America*, Washington D. C., 646 p.

SHARP Z. D., ESSENE E. J. and KELLY W. C. (1985) - A re-examination of the arsenopyrite geothermometer; pressure considerations and applications to natural assemblages. *Canadian Mineralogist*, Vol. 23(4), pp. 517-534.

SHERPHERD T. J., RANKIN A. H. and ALDERTON D. H. M. (1985) - A pratical guide to fluid inclusion studies. *Blackie*, Glasgow (UK), 239 p.

SIMON G., KESLER S. E. and CHRYSSOULIS S. (1999) - Geochemistry and textures of gold-bearing arsenian pyrite, Twin Creeks, Nevada; implications for deposition of gold in carlin-type deposits. *Economic Geology*, Vol. 94(3), pp. 405-421.

SMOLIAR M. I., WALKER R. J. and MORGAN J. W. (1996) - Re-Os Ages of Group IIA, IIIA, IVA, and IVB Iron Meteorites. *Science*, Vol. 271(5252), pp. 1099-1102.

SONNENDRUCKER P.(1967) - Etude de synthèse sur l'or en Côte d'Ivoire: la région aurifère du Sanwi. *Société pour le développement minier de la Côte d'Ivoire (SODEMI)*, Abidjan, Rapport n° 192, 87 p. (unpublished)

STEIGER R. H. and JAGER E. (1977) - Subcommission on geochronology: Convention on the use of decay constants in geo- and cosmochronology. *Earth and Planetary Science Letters*, Vol. 36(3), pp. 359-362.

STEIN H. J., MORGAN J. W. and SCHERSTEN A. (2000) - Re-Os dating of low-level highly radiogenic (LLHR) sulfides: the Harnas gold deposit, southwest Sweden, records continental-scale tectonic events. *Economic Geology*, Vol. 95(8), pp. 1657-1671.

TAGINI B. (1971) - Esquisse structurale de la Côte d'Ivoire: Essai de géotectonique régionale. Doctorat, *Université Lausanne*, Société pour le Développement Minier de la Côte d'Ivoire (SODEMI), 302 p.

TAYLOR P. N., MOORBATH S., LEUBE A. and HIRDES W. (1992) - Early Proterozoic crustal evolution in the birimian of Ghana: constraints from geochronology and isotope geochemistry. *Precambrian Research*, Vol. 56(1-2), pp. 97-111.

TAYLOR S. R. and MCLENNAN S. M. (1985) - The continental crust: its composition and evolution - An examination of the geochemical record preserved in sedimentary rocks. *Blackwell Scientific Publications*, Oxford, 312 p.

TEMPIER P. (1969) - Nouvelle chronologie relative des granites de Côte d'Ivoire. *Annale de la faculté des Sciences de l'Université d'Abidjan*, Vol. 5, pp. 93-98.

TEMPIER P.(1986) - Le Burkinien: cycle orogénique majeur du Protérozoique inférieur en Afrique de l'Ouest. *Centre International pour la Formation et les Echanges Géologiques (CIFEG)*, Paris, Publication occasionnelle n° 10, 17-23 p.

THOMPSON A. J. B. and THOMPSON J. F. H. (1996) - Atlas of alteration: a field and petrographic guide to hydrothermal alteration minerals. *Geological association of Canada*, Newfoundland, 119 p.

TOURIGNY G.(1998) - Analyse structurale de la zone tectonique d'Aféma et son application à la recherche des gisements aurifères: Permis d'Exploitation 29, Côte d'Ivoire, Afrique de l'Ouest. *Eden Roc Mineral Corporation document*, 56 p. (unpublished)

TRDLICKA Z. and HOFFMAN V. (1976) - Untersuchungen der chemischen Zusammensetzung der Gangkarbonate von Kutna Hora / CSSR. *Freiberger Forschungshefte*, Vol. C 321, pp. 29-81.

WHITFIELD M. and TURNER D. R. (1979) - Water-rock partition coefficients and the composition of seawater and river water. *Nature*, Vol. 278(5700), pp. 132-137.

WRIGHT J. B., HASTINGS D. A., JONES W. B. and WILLIAMS H. R. (1985) - Geology and mineral resources of West Africa. *Allen & Unwin*, London, 187 p.

YACE I.(1984) - Le Précambrien de l'Afrique de l'Ouest et ses corrélations avec le Brésil oriental. *Centre International pour la Formation et les Echanges Géologiques (CIFEG)*, Paris, Rapport final du projet PICG 108-144, publication occasionnelle, n° 2, 28 p.

YACE I. (2002) - Initiation à la géologie: l'exemple de la Côte d'Ivoire et de l'Afrique de l'Ouest. *CEDA*, Abidjan, 183 p.

ZACHARIAS J., FRYDA J., PATEROVA B. and MIHALJEVIC M. (2004) - Arsenopyrite and As-bearing pyrite from the Roudny deposit, Bohemian Massif. *Mineralogical Magazine*, Vol. 68(1), pp. 31-46.

ZINDLER A., JAGOUTZ E. and GOLDSTEIN S. (1982) - Nd, Sr and Pb isotopic systematics in a three-component mantle: a new perspective. *Nature*, Vol. 298(5874), pp. 519-523.

APPENDIX 1

Major and trace element data of rocks from Jonction. Shading refers to alternative analytical method used. ICP1: Inductively Coupled Plasma with extraction by lithium borate (ITS); ICP2: Inductively Couple Plasma with extraction by Aqua Regia (ITS); XRF1: X-Ray Fluorescence with extraction by pressed pellets (ITS); XRF2: X-Ray Fluorescence spectrometry on lithium metaborate fused disks; INAA: Instrumental Neutron Activation Analysis (Actlabs); FA: Fire Assay (Somiaf).

Sample		Lithology	SiO_2	TiO_2	Al_2O_3	Fe_2O_3t	MnO	MgO	CaO	Na_2O	K_2O	P_2O_5	SO_3	Cl	F	LOI	Total	As	Au	Ba	Bi	Br
ID	Drill core No.		XRF 2	XRF 2	XRF 2	XRF 2	XRF 2	XRF 2	XRF 2	XRF 2	XRF 2	XRF 2	XRF 2	XRF 2	XRF 2	(XRF 2)	XRF 2	INAA	INAA	XRF 2	XRF 2	INAA
			ICP 1	ICP 1	ICP 1	ICP 1	ICP 1	ICP 1	ICP 1	ICP 1	ICP 1	ICP 1	-	-	-	(ICP 1)	ICP 1	ICP 2	FA	ICP 1	-	-
			%	%	%	%	%	%	%	%	%	%	%	%	%	%	%	ppm	ppm	ppm	ppm	ppm
C04	1A6-47-97/180m	Metagabbro	45.97	0.74	13.75	12.62	0.18	6.73	6.96	2.62	<0.05	0.12				10.17	99.89	63		13		
T606	1A6-57-97/193m	Metagabbro	49.52	1.50	12.35	16.74	0.19	5.16	7.35	2.73	0.11	0.15	0.49	0.03	0.09	3.21	99.61	12.9	1.950	33	13	<0.5
T609	1A6-63-97/78.50m	Metagabbro	41.52	0.49	14.26	9.46	0.16	8.00	10.17	3.18	0.05	0.03	0.15	0.03	<0.05	12.01	99.55	85.2	0.067	12	7	<0.5
T610	1A6-63-97/341.50m	Metagabbro	58.73	0.55	11.30	6.59	0.10	2.44	7.90	4.42	0.04	0.08	0.52	0.04	0.10	6.93	99.73	13.4	0.047	12	6	<0.5
T611	1A6-64-97/151.50m	Metagabbro	34.96	0.38	7.49	12.30	0.20	5.86	13.68	0.86	0.58	0.02	5.12	0.03	0.09	17.96	99.52	503	3.190	117	7	<0.5
15/T612	1A6-64-97/174m	Metagabbro	44.04	0.74	13.49	12.53	0.18	4.98	7.45	1.43	0.68	0.07	0.21	0.04	0.07	13.71	99.63	7.8	0.034	201	13	<0.5
B17	1A6-65-97/86m	Metagabbro	49.34	0.96	12.05	14.09	0.19	5.35	6.57	1.49	<0.05	0.15				7.97	98.18	36		11		
C03	1A6-65-97/89m	Metagabbro	42.88	0.54	12.66	9.15	0.16	7.18	12.17	2.28	<0.05	0.07				13.21	100.33	73		<10		
14/T614	1A6-67-97/114.10m	Metagabbro	37.35	0.40	14.96	9.48	0.14	6.56	10.02	2.08	0.44	0.03	0.14	0.04	0.10	17.84	99.58	8.5	0.029	104	12	<0.5
T616	1A6-68-97/160m	Metagabbro	42.09	0.68	12.74	12.17	0.18	6.77	7.79	2.75	0.46	0.07	0.27	0.02	0.05	13.57	99.61	112.0	0.023	92	13	<0.5
02/T619	1A6-72-97/135.10m	Metagabbro	47.63	1.11	12.56	15.36	0.21	5.67	6.40	2.35	0.03	0.12	0.33	0.04	0.08	7.74	99.62	53.3	0.028	16	9	<0.5
03/T620	1A6-72-97/165.95m	Metagabbro	46.10	1.10	11.91	15.07	0.22	5.56	7.85	1.69	0.03	0.11	0.14	0.04	0.10	9.74	99.66	71.3	0.038	13	7	<0.5
05/T666	1A6-72-97/192m	Metagabbro	44.55	1.09	12.60	14.72	0.19	4.98	6.39	2.28	0.64	0.13	0.27	0.04	0.10	11.64	99.60	73.3	0.014	123	4	<0.5
T625	1A6-74-98/105.10m	Metagabbro	47.21	0.35	17.14	9.20	0.15	9.19	10.05	2.86	0.03	0.02	0.09	0.02	0.09	3.19	99.58	1.3	0.010	<5	4	<0.5
01/T618	1A6-72-97/124.80m	Metagraywacke	67.32	0.52	14.22	4.57	0.04	1.70	2.21	2.66	2.12	0.09	0.27	0.04	0.06	3.85	99.68	38.2	0.365	573	6	<0.5
04	1A6-72-97/183.10m	Metaargillite	61.11	0.75	15.80	8.07	0.05	2.39	1.30	4.35	1.18	0.20	0.23	0.00	<0.05	4.17	99.63	37.5	0.010	281	5	<0.5
T621	1A6-72-97/184.40m	Metaargillite	63.48	0.67	15.67	6.63	0.05	2.07	1.24	3.94	1.47	0.15	0.28	0.04	0.07	3.90	99.66	<0,5	0.023	372	<3	<0.5
A07	1A6-33-97/116.50m	Metaarenite	74.51	0.25	7.45	3.21	0.12	1.52	3.90	0.33	1.72	0.03				6.82	99.94	44	0.07	429		
B10	1A6-45-97/173m	Metaarenite	40.84	1.37	14.16	16.27	0.28	4.14	5.67	1.04	2.06	0.22				13.86	100.02	103	0.06	608		
VI/T601	1A6-47-97/252.40m	Metaarenite	80.61	0.29	9.34	3.58	0.04	0.60	0.61	0.25	1.83	0.03	0.08	0.04	0.09	2.33	99.74	51.4	0.087	507	<3	<0.5
VII/T602	1A6-48-97/156.50m	Metaarenite	77.06	0.35	12.56	2.95	0.01	0.55	0.30	1.49	2.08	0.03	0.07	0.04	0.06	2.16	99.71	27.9	0.033	541	8	<0.5
T603	1A6-50-97/274m	Metaarenite	75.76	0.34	7.06	3.93	0.06	1.43	2.42	0.14	1.84	0.01	0.27	0.04	<0.05	5.87	99.21	4000	20.000	356	<3	<0.5
T604	1A6-51-97/129.10m	Metaarenite	76.25	0.44	12.46	3.71	0.01	0.15	0.34	1.35	2.66	0.03	0.06	0.04	0.07	2.17	99.73	7.5	1.950	700	6	<0.5
VIII	1A6-51-97/130.25m	Metaarenite	76.65	0.55	11.31	5.21	0.01	0.20	0.45	1.23	2.53	0.06				2.09	100.39					
T605	1A6-53-97/151.70m	Metaarenite	61.87	0.14	3.86	3.99	0.17	5.32	8.94	0.18	0.53	0.00	0.34	0.04	0.09	14.00	99.48	<3.2	1570.000	185	12	<2.5
IX	1A6-57-97/295m	Metaarenite	45.54	0.91	12.46	12.66	0.17	4.37	6.80	1.78	1.24	0.14				12.03	98.16		0.01			
X	1A6-57-97/302.50m	Metaarenite	52.39	0.56	10.53	8.43	0.16	3.50	6.64	0.96	2.43	0.08				13.47	99.23		20.17			
XI	1A6-57-97/310.50m	Metaarenite	35.74	0.39	7.02	7.76	0.18	14.14	12.55	<0.01	<0.05	0.66				21.07	99.72		0.27			

APPENDIX 1 continued

Sample		Lithology	Cd	Co	Cr	Cs	Cu	Ga	Hf	Hg	Ir	Li	Mo	Nb	Ni	Pb	Rb	Sb	Sc	Se	Sn	Sr
ID	Drill core No.		ICP 2	INAA	XRF 2	INAA	XRF 2	XRF 2	INAA	INAA	INAA	ICP 2	XRF 2	XRF 2	XRF 2	XRF 2	XRF 2	INAA	INAA	INAA	XRF 2	XRF 2
			-	ICP 2	ICP 2	-	ICP 2	-	-	-	-	-	-	ICP 2	ICP 2	ICP 2	XRF 1	-	-	-	-	ICP 1
			ppm	ppm	ppm	ppm	ppm	ppm	ppm	ppm	ppb	ppm	ppm	ppm	ppm	ppm	ppm	ppm	ppm	ppm	ppm	ppm
C04	1A6-47-97/180m	Metagabbro	<0.2	46	65		108					73		8	71	2						125
T606	1A6-57-97/193m	Metagabbro		50	5	17	129	21	3	<1	<5		15	3	36	<4	<2	9.1	50.0	<3	<2	313
T609	1A6-63-97/78.50m	Metagabbro		54	318	<1	113	14	<1	<1	<5		16	<2	182	<4	<2	2.1	34.8	<3	<2	125
T610	1A6-63-97/341.50m	Metagabbro		17	60	<1	22	16	2	<1	<5		5	<2	36	10	4	2.9	15.7	<3	<2	103
T611	1A6-64-97/151.50m	Metagabbro		43	61	2	39	6	<1	<1	<5		15	<2	72	<4	18	5.0	22.6	<3	<2	414
15/T612	1A6-64-97/174m	Metagabbro	<0.2	67	159	4	101	16	<1	<1	<5	33	18	<2	97	<4	21	9.0	37.9	<3	<2	185
B17	1A6-65-97/86m	Metagabbro	<0.2	44	48		81					38		11	38	<2						41
C03	1A6-65-97/89m	Metagabbro	<0.2	36	304		76					50		9	93	3						151
14/T614	1A6-67-97/114.10m	Metagabbro	<0.2	50	224	3	77	10	<1	<1	<5	30	16	<2	193	<4	12	8.2	36.4	<3	<2	357
T616	1A6-68-97/160m	Metagabbro		48	72	<1	107	14	<1	<1	<5		17	13	74	<4	13	2.4	42.5	<3	<2	312
02/T619	1A6-72-97/135.10m	Metagabbro	<0.2	51	23	<1	82	18	2	<1	<5	20	13	<2	58	6	4	3.2	41.9	<3	<2	126
03/T620	1A6-72-97/165.95m	Metagabbro	0.3	50	28	<1	66	16	2	<1	<5	35	15	<2	45	<4	3	2.0	43.4	<3	<2	140
05/T666	1A6-72-97/192m	Metagabbro	<0.2	46	38	2	70	17	<1	<1	<5	40	16	<2	50	<4	16	0.9	37.5	<3	<2	197
T625	1A6-74-98/105.10m	Metagabbro		52	308	<1	101	11	<1	<1	<5		13	<2	240	<4	3	11.4	29.0	<3	<2	239
01/T618	1A6-72-97/124.80m	Metagraywacke	<0.2	12	75	5	15	16	4	<1	<5	17	<2	6	32	6	48	3.0	9.1	<3	<2	61
04	1A6-72-97/183.10m	Metaargillite	<0.2	22	79	3	28	19	4	<1	<5	32	<2	4	37	10	37	1.7	18.4	<3	<2	78
T621	1A6-72-97/184.40m	Metaargillite		3	95	<1	26	22	<1	<1	<5		<2	<2	47	10	38	2.0	4.0	<3	<2	81
A07	1A6-33-97/116.50m	Metaarenite	<0.2	11	139		21					<1		2	21	8						155
B10	1A6-45-97/173m	Metaarenite	<0.2	53	51		23					<1		2	46	3						211
VI/T601	1A6-47-97/252.40m	Metaarenite		14	49	5	19	13	2	<1	<5		<2	13	33	9	47	1.7	6.0	<3	<2	50
VII/T602	1A6-48-97/156.50m	Metaarenite		8	34	7	<10	16	3	<1	<5		<2	3	20	6	49	4.7	7.1	<3	<2	74
T603	1A6-50-97/274m	Metaarenite		9	43	8	12	13	<1	<1	<5		<2	<2	17	16	52	23.5	8.8	<3	<2	130
T604	1A6-51-97/129.10m	Metaarenite		4	51	10	<10	16	4	<1	<5		<2	<2	16	7	66	6.6	8.6	<3	<2	52
VIII	1A6-51-97/130.25m	Metaarenite															70					
T605	1A6-53-97/151.70m	Metaarenite		26	178	<3	1242	6	<1	<15	<40		4	<2	178	222	13	5.7	8.6	<45	<2	315
IX	1A6-57-97/295m	Metaarenite															34					
X	1A6-57-97/302.50m	Metaarenite															73					
XI	1A6-57-97/310.50m	Metaarenite															<2					

APPENDIX 1 continued

Sample		Lithology	Ta	Te	Th	U	V	W	Zn	Zr	Y	La	Ce	Pr	Nd	Sm	Eu	Tb	Yb	Lu
ID	Drill core No.		INAA	ICP 2	INAA	INAA	XRF 2	INAA	XRF 2	XRF 2	XRF 2	INAA	INAA	XRF 2	INAA	INAA	INAA	INAA	INAA	INAA
			-	-	-	-	-	-	ICP 2	XRF 1	XRF 1	ICP 2	-	-	-	-	-	-	-	-
			ppm	ppm	ppm	ppm	ppm	ppm	ppm	ppm	ppm	ppm	ppm	ppm	ppm	ppm	ppm	ppm	ppm	ppm
C04	1A6-47-97/180m	Metagabbro		<10					72			<1								
T606	1A6-57-97/193m	Metagabbro	<0.5		1.5	<0.5	342	<1	138	107	35	8.2	29	<50	12	3.8	1.4	1.6	6.0	1.00
T609	1A6-63-97/78.50m	Metagabbro	<0.5		<0.2	<0.5	148	<1	67	21	4	0.9	5	<50	<5	0.9	0.6	<0.5	2.3	0.37
T610	1A6-63-97/341.50m	Metagabbro	<0.5		2.8	<0.5	106	<1	61	111	11	11.7	29	<50	<5	2.9	<0.2	<0.5	2.4	0.39
T611	1A6-64-97/151.50m	Metagabbro	<0.5		<0.2	<0.5	122	12	51	21	3	1.1	<3	<50	<5	0.9	0.7	<0.5	1.1	0.23
15/T612	1A6-64-97/174m	Metagabbro	<0.5	<10	<0.2	<0.5	190	6	113	36	13	1.3	8	<50	<5	1.7	0.8	<0.5	3.2	0.55
B17	1A6-65-97/86m	Metagabbro		<10					88			3								
C03	1A6-65-97/89m	Metagabbro		<10					52			<1								
14/T614	1A6-67-97/114.10m	Metagabbro	<0.5	<10	<0.2	<0.5	167	<1	77	22	6	0.8	<3	<50	<5	0.7	<0.2	<0.5	1.7	0.26
T616	1A6-68-97/160m	Metagabbro	<0.5		<0.2	<0.5	206	7	97	45	13	2.8	11	<50	8	1.6	<0.2	<0.5	3.0	0.45
02/T619	1A6-72-97/135.10m	Metagabbro	<0.5	<10	1.0	<0.5	286	<1	128	78	25	5.8	20	<50	<5	2.9	1.0	<0.5	4.6	0.77
03/T620	1A6-72-97/165.95m	Metagabbro	<0.5	<10	<0.2	<0.5	261	<1	115	76	24	6.2	24	<50	<5	3.0	1.3	0.7	5.2	0.76
05/T666	1A6-72-97/192m	Metagabbro	<0.5	<10	<0.2	<0.5	282	<1	131	84	25	5.0	10	<50	<5	1.7	0.4	<0.5	3.1	0.55
T625	1A6-74-98/105.10m	Metagabbro	<0.5		<0.2	<0.5	137	<1	57	19	<3	<0.5	<3	<50	<5	0.6	0.2	<0.5	1.1	0.15
01/T618	1A6-72-97/124.80m	Metagraywacke	<0.5	<10	2.2	<0.5	70	<1	66	141	9	16.4	41	<50	14	3.5	1.1	<0.5	2.1	0.39
04	1A6-72-97/183.10m	Metaargillite	<0.5	<10	2.2	<0.5	110	98	102	134	17	18.0	34	<50	11	4.0	1.1	0.5	2.6	0.44
T621	1A6-72-97/184.40m	Metaargillite	<0.5		<0.2	<0.5	97	<1	88	147	9	3.5	41	<50	<5	4.1	1.3	<0.5	<0.2	0.38
A07	1A6-33-97/116.50m	Metaarenite		<10					16			12								
B10	1A6-45-97/173m	Metaarenite		<10					108			2								
VI/T601	1A6-47-97/252.40m	Metaarenite	<0.5		2.4	<0.5	36	7	43	106	6	23.3	54	<50	19	4.7	1.4	<0.5	1.7	0.26
VII/T602	1A6-48-97/156.50m	Metaarenite	<0.5		2.7	<0.5	31	15	34	135	11	33.5	79	<50	28	6.4	1.9	<0.5	2.2	0.30
T603	1A6-50-97/274m	Metaarenite	<0.5		<0.5	<0.5	58	37	45	78	3	8.7	26	<50	<5	2.3	0.9	<0.5	1.3	0.20
T604	1A6-51-97/129.10m	Metaarenite	<0.5		2.8	<0.5	68	12	24	169	6	23.7	55	<50	17	4.4	1.6	<0.5	1.5	0.33
VIII	1A6-51-97/130.25m	Metaarenite								207	24									
T605	1A6-53-97/151.70m	Metaarenite	<1.5		<4.5	<20	48	<3	52	14	<3	<0.5	<30	<50	<50	<5	<7	<5	<2.5	<0.5
IX	1A6-57-97/295m	Metaarenite								86	25									
X	1A6-57-97/302.50m	Metaarenite								84	15									
XI	1A6-57-97/310.50m	Metaarenite								137	13									

APPENDIX 1 continued

Sample		Lithology	SiO_2	TiO_2	Al_2O_3	Fe_2O_3t	MnO	MgO	CaO	Na_2O	K_2O	P_2O_5	SO_3	Cl	F	LOI	Total	As	Au	Ba	Bi	Br
ID	Drill core No.		XRF 2	XRF 2	XRF 2	XRF 2	XRF 2	XRF 2	XRF 2	XRF 2	XRF 2	XRF 2	XRF 2	XRF 2	XRF 2	(XRF 2)	XRF 2	INAA	INAA	XRF 2	XRF 2	INAA
			ICP 1	ICP 1	ICP 1	ICP 1	ICP 1	ICP 1	ICP 1	ICP 1	ICP 1	ICP 1	-	-	-	(ICP 1)	ICP 1	ICP 2	FA	ICP 1	-	-
			%	%	%	%	%	%	%	%	%	%	%	%	%	%	%	ppm	ppm	ppm	ppm	ppm
T607	1A6-57-97/311.20m	Metaarenite	34.00	0.34	5.84	6.60	0.15	14.24	13.91	<0.01	0.04	0.62	0.26	0.03	0.08	23.08	99.16	935	0.056	12	8	<0.5
T608	1A6-62-97/258.40m	Metaarenite	86.94	0.25	5.63	3.03	0.08	0.41	0.11	0.15	1.21	0.04	0.02	0.02	<0.05	1.88	99.79	49.2	0.022	322	<3	<0.5
XII	1A6-62-97/259.70m	Metaarenite	87.47	0.17	5.08	2.36	0.05	0.35	0.10	0.16	1.04	0.05				1.49	98.38					
XIII	1A6-63-97/442m	Metaarenite	40.34	0.52	10.03	10.87	0.23	6.66	10.42	0.09	1.52	0.13				17.37	98.27		0.08			
T662	1A6-63-97/447.75m	Metaarenite	80.64	0.15	3.89	2.96	0.07	1.63	3.14	0.08	0.95	0.01	1.14	0.03	<0.05	4.89	99.59	836	6.330	173	<3	<0.5
XIV	1A6-63-97/458m	Metaarenite	85.84	0.12	4.73	1.70	0.05	1.12	1.77	0.37	0.99	0.06				3.17	99.99		0.45			
T663	1A6-63-97/468m	Metaarenite	45.33	0.48	16.63	13.88	0.08	7.96	2.49	0.49	1.66	0.01	2.27	0.03	0.15	8.14	99.60	469	2.450	426	<3	<0.5
T664	1A6-63-97/469m	Metaarenite	92.43	0.14	1.60	1.57	0.02	0.55	0.89	0.05	0.32	0.01	0.51	0.03	<0.05	1.68	99.73	239	2.020	74	<3	<0.5
T665	1A6-63-97/475m	Metaarenite	77.16	0.27	6.18	2.60	0.12	1.95	3.43	0.14	1.35	0.01	0.50	0.02	0.05	5.92	99.70	30.5	0.092	343	<3	<0.5
T613	1A6-64-97/187m	Metaarenite	82.55	0.21	7.22	2.42	0.11	0.54	1.47	0.67	1.16	0.02	0.15	0.05	0.12	3.13	99.80	6.1	0.021	400	10	<0.5
T615	1A6-67-97/135.80m	Metaarenite	87.11	0.27	6.30	2.57	0.03	0.43	0.23	0.54	0.72	0.05	0.03	0.04	0.07	1.40	99.78	12.2	0.041	253	5	<0.5
T617	1A6-68-97/358.70m	Metaarenite	74.46	0.59	13.52	3.89	0.02	0.49	0.24	0.61	2.87	0.04	0.12	0.02	0.09	2.73	99.69	169.0	0.710	816	6	<0.5
06	1A6-72-97/195m	Metaarenite	43.69	0.59	11.86	9.50	0.14	6.81	8.60	0.24	1.87	0.07				15.85	99.29	102	0.03	287		
T622	1A6-72-97/199.64m	Metaarenite	65.51	0.54	12.08	5.99	0.06	2.86	2.74	0.44	1.97	0.01	0.48	0.03	<0.05	6.51	99.26	2500.0	12.500	457	4	<0.5
T623	1A6-72-97/202.69m	Metaarenite	81.83	0.27	6.64	3.22	0.03	0.97	1.04	0.16	1.49	0.01	0.31	0.03	<0.05	3.35	99.36	4290.0	10.200	329	4	<0.5
07	1A6-72-97/203m	Metaarenite	80.41	0.32	4.24	4.84	0.04	1.09	1.82	0.05	1.06	<0.03				4.72	98.65	835	17.18	215		
08/T667	1A6-72-97/204.95m	Metaarenite	41.66	0.53	15.05	9.55	0.13	7.49	7.30	1.62	1.73	0.07	0.22	0.03	0.05	14.09	99.54	213.4	<0,002	417	<3	<0.5
T624	1A6-72-97/226.50m	Metaarenite	84.29	0.34	7.81	2.47	0.06	0.36	0.39	0.33	1.54	0.04	0.13	0.03	<0.05	1.82	99.65	409.2	0.336	398	6	<0.5
09	1A6-72-97/228.85m	Metaarenite	84.89	0.14	3.60	3.90	0.16	0.57	1.50	0.17	0.83	0.05				3.60	99.49	3811	6.05	216		
10/T668	1A6-72-97/237.70m	Metaarenite	87.14	0.19	5.22	3.54	0.08	0.58	0.36	0.11	0.78	0.03	0.08	0.04	0.06	1.56	99.78	15.6	0.010	219	4	<0.5
11	1A6-72-97/239m	Metaarenite	86.92	0.19	5.13	2.77	0.14	0.56	0.78	0.18	0.92	0.03	<0.01	0.00	<0.05	2.02	99.65	11.8	0.050	259	<3	<0.5
12/T669	1A6-72-97/252.05m	Metaarenite	88.01	0.16	5.63	1.81	0.02	0.17	0.43	1.52	0.76	0.02	0.07	0.04	0.05	1.09	99.78	1.2	0.012	231	6	<0.5
13/T670	1A6-72-97/261.50m	Metaarenite	87.56	0.15	5.83	1.66	0.02	0.21	0.54	1.77	0.71	0.02	0.07	0.04	<0.05	1.19	99.77	1.3	0.019	218	4	<0.5
T626	1A6-74-98/372.70m	Metaarenite	53.59	0.72	12.67	9.94	0.11	2.88	4.73	0.81	2.19	0.11	1.22	0.04	0.13	9.58	98.71	9370.0	7.100	453	11	<0.5

APPENDIX 1 continued

Sample		Lithology	Cd	Co	Cr	Cs	Cu	Ga	Hf	Hg	Ir	Li	Mo	Nb	Ni	Pb	Rb	Sb	Sc	Se	Sn	Sr
ID	Drill core No.		ICP 2 -	INAA ICP 2	XRF 2 ICP 2	INAA -	XRF 2 ICP 2	XRF 2 -	INAA -	INAA -	INAA -	ICP 2 -	XRF 2 -	XRF 2 ICP 2	XRF 2 ICP 2	XRF 2 ICP 2	XRF 2 XRF 1	INAA -	INAA -	INAA -	XRF 2 -	XRF 2 ICP 1
			ppm	ppm	ppm	ppm	ppm	ppm	ppm	ppm	ppb	ppm	ppm	ppm	ppm	ppm	ppm	ppm	ppm	ppm	ppm	ppm
T607	1A6-57-97/311.20m	Metaarenite		44	1078	<1	38	7	3	<1	<5		15	<2	622	16	3	33.3	16.0	<3	<2	1402
T608	1A6-62-97/258.40m	Metaarenite		11	79	3	<10	8	2	<1	<5		<2	3	24	<4	31	1.0	5.0	<3	<2	23
XII	1A6-62-97/259.70m	Metaarenite															32					
XIII	1A6-63-97/442m	Metaarenite															54					
T662	1A6-63-97/447.75m	Metaarenite		11	57	3	22	7	<1	<1	<5		3	<2	30	7	27	0.2	6.6	<3	<2	134
XIV	1A6-63-97/458m	Metaarenite															31					
T663	1A6-63-97/468m	Metaarenite		15	118	6	19	22	2	<1	<5		17	4	90	50	42	4.5	8.4	<3	<2	227
T664	1A6-63-97/469m	Metaarenite		8	31	1	13	4	<1	<1	<5		5	<2	25	24	9	2.8	1.9	<3	<2	58
T665	1A6-63-97/475m	Metaarenite		6	52	5	22	8	1	<1	<5		<2	<2	13	9	32	2.2	8.1	<3	<2	160
T613	1A6-64-97/187m	Metaarenite		13	23	4	<10	11	3	<1	<5		<2	2	13	8	26	3.4	5.5	<3	<2	89
T615	1A6-67-97/135.80m	Metaarenite		9	85	3	14	7	2	<1	<5		<2	3	20	<4	21	3.1	6.2	<3	<2	63
T617	1A6-68-97/358.70m	Metaarenite		18	79	9	10	15	5	<1	<5		<2	5	28	7	67	6.6	10.6	<3	<2	81
06	1A6-72-97/195m	Metaarenite	<0.2	28	121		73					34		<1	57	<2						240
T622	1A6-72-97/199.64m	Metaarenite		20	70	7	44	16	<1	<1	<5		3	<2	50	8	55	20.7	13.9	<3	<2	149
T623	1A6-72-97/202.69m	Metaarenite		13	73	7	20	15	<1	<1	<5		<2	<2	43	9	43	4.1	7.5	<3	<2	67
07	1A6-72-97/203m	Metaarenite	0.5	15	213		22					<1		<1	18	16						84
08/T667	1A6-72-97/204.95m	Metaarenite	0.4	44	203	6	86	13	1	<1	<5	24	18	<2	167	7	44	8.5	27.0	<3	<2	332
T624	1A6-72-97/226.50m	Metaarenite		10	94	7	<10	10	1	<1	<5		<2	2	21	5	37	3.1	6.7	<3	<2	41
09	1A6-72-97/228.85m	Metaarenite	2.5	13	220		11					<1		<1	28	12						61
10/T668	1A6-72-97/237.70m	Metaarenite	<0.2	14	58	3	11	7	2	<1	<5	10	<2	<2	24	23	19	0.9	4.6	<3	<2	25
11	1A6-72-97/239m	Metaarenite	<0.2	48	57	4	39	4	<1	<1	<5	9	<2	<2	20	14	28	1.0	4.5	<3	<2	37
12/T669	1A6-72-97/252.05m	Metaarenite	<0.2	6	21	4	<10	5	<1	<1	<5	1	<2	<2	9	8	22	2.4	3.4	<3	<2	41
13/T670	1A6-72-97/261.50m	Metaarenite	<0.2	6	27	4	<10	7	<1	<1	<5	<1	<2	2	6	6	20	3.2	3.4	<3	<2	47
T626	1A6-74-98/372.70m	Metaarenite		25	77	7	72	17	<1	<1	<5		17	3	75	10	55	0.1	15.6	<3	<2	286

APPENDIX 1 continued

Sample		Lithology	Ta	Te	Th	U	V	W	Zn	Zr	Y	La	Ce	Pr	Nd	Sm	Eu	Tb	Yb	Lu
ID	Drill core No.		INAA	ICP 2	INAA	INAA	XRF 2	INAA	XRF 2	XRF 2	XRF 2	INAA	INAA	XRF 2	INAA	INAA	INAA	INAA	INAA	INAA
			-	-	-	-	-	-	ICP 2	XRF 1	XRF 1	ICP 2	-	-	-	-	-	-	-	-
			ppm	ppm	ppm	ppm	ppm	ppm	ppm	ppm	ppm	ppm	ppm	ppm	ppm	ppm	ppm	ppm	ppm	ppm
T607	1A6-57-97/311.20m	Metaarenite	<0.5		4.0	2.8	105	10	63	132	6	26.0	74	<50	24	7.0	2.8	<0.5	1.0	0.17
T608	1A6-62-97/258.40m	Metaarenite	<0.5		1.8	<0.5	31	<1	35	96	6	15.8	43	<50	15	3.2	1.1	<0.5	1.4	0.20
XII	1A6-62-97/259.70m	Metaarenite								65	16									
XIII	1A6-63-97/442m	Metaarenite								60	15									
T662	1A6-63-97/447.75m	Metaarenite	<0.5		<0.2	<0.5	39	25	35	23	<3	2.9	7	<50	<5	0.7	<0.2	<0.5	0.4	<0.05
XIV	1A6-63-97/458m	Metaarenite								45	10									
T663	1A6-63-97/468m	Metaarenite	<0.5		1.8	<0.5	107	31	197	145	3	18.6	31	<50	<5	2.4	0.8	<0.5	1.3	0.24
T664	1A6-63-97/469m	Metaarenite	<0.5		1.3	<0.5	8	6	8	39	<3	10.0	21	<50	<5	1.2	0.3	<0.5	0.7	<0.05
T665	1A6-63-97/475m	Metaarenite	<0.5		1.8	<0.5	36	18	23	76	<3	12.3	23	<50	8	2.1	0.8	<0.5	1.1	0.25
T613	1A6-64-97/187m	Metaarenite	<0.5		2.0	<0.5	26	<1	31	94	5	13.2	31	<50	9	2.8	1.0	<0.5	1.4	0.24
T615	1A6-67-97/135.80m	Metaarenite	<0.5		2.0	<0.5	32	<1	30	95	6	22.5	54	<50	25	4.7	1.4	<0.5	1.8	0.29
T617	1A6-68-97/358.70m	Metaarenite	<0.5		5.3	<0.5	53	35	48	164	24	45.1	110	<50	34	7.1	2.3	1.1	3.7	0.47
06	1A6-72-97/195m	Metaarenite		<10					65			<1								
T622	1A6-72-97/199.64m	Metaarenite	<0.5		<0.2	<0.5	119	37	75	98	9	9.0	22	<50	<5	2.5	<0.2	<0.5	2.0	0.26
T623	1A6-72-97/202.69m	Metaarenite	<0.5		<0.2	<0.5	36	21	29	56	<3	6.8	12	<50	10	1.3	0.4	<0.5	<0.2	0.14
07	1A6-72-97/203m	Metaarenite		<10					37			<1								
08/T667	1A6-72-97/204.95m	Metaarenite	<0.5	<10	<0.2	<0.5	142	15	74	58	3	4.6	<3.3	<50	<5	1.0	0.4	<0.5	1.4	0.26
T624	1A6-72-97/226.50m	Metaarenite	<0.5		2.5	<0.5	52	9	35	114	8	22.9	50	<50	23	3.9	1.1	<0.5	1.5	0.21
09	1A6-72-97/228.85m	Metaarenite		<10					18			2								
10/T668	1A6-72-97/237.70m	Metaarenite	<0.5	<10	2.1	0.7	31	3	39	78	<3	12.4	26	<50	<5	1.9	0.7	<0.5	0.8	0.18
11	1A6-72-97/239m	Metaarenite	1.1	<10	1.0	<0.5	29	488	31	59	4	20.1	33	<50	12	3.3	0.8	0.6	1.1	0.18
12/T669	1A6-72-97/252.05m	Metaarenite	<0.5	<10	1.1	<0.5	24	2	20	67	<3	14.6	26	<50	7	2.0	0.7	<0.5	0.7	0.12
13/T670	1A6-72-97/261.50m	Metaarenite	<0.5	<10	1.5	<0.5	10	<1	22	56	<3	11.9	23	<50	5	1.9	0.4	<0.5	0.8	0.13
T626	1A6-74-98/372.70m	Metaarenite	<0.5		<0.4	<1.2	116	55	81	122	10	10.3	<3	<50	<5	2.2	<0.2	<0.5	1.8	0.25

APPENDIX 2

Major and trace element data of rocks from Aniuri. Shading refers to alternative analytical method used. ICP1: Inductively Coupled Plasma with extraction by lithium borate (ITS); ICP2: Inductively Couple Plasma with extraction by Aqua Regia (ITS); XRF1: X-Ray Fluorescence with extraction by pressed pellets (ITS); XRF2: X-Ray Fluorescence spectrometry on lithium metaborate fused disks; INAA: Instrumental Neutron Activation Analysis (Actlabs); FA: Fire Assay (Somiaf).

Sample		Lithology	SiO_2	TiO_2	Al_2O_3	Fe_2O_3t	MnO	MgO	CaO	Na_2O	K_2O	P_2O_5	SO_3	Cl	F	LOI	Total	As	Au	Ba	Bi	Br
ID	Drill core No.		XRF 2	XRF 2	XRF 2	XRF 2	XRF 2	XRF 2	XRF 2	XRF 2	XRF 2	XRF 2	XRF 2	XRF 2	XRF 2	(XRF 2)	XRF 2	INAA	INAA	XRF 2	XRF 2	INAA
			ICP 1	ICP 1	ICP 1	ICP 1	ICP 1	ICP 1	ICP 1	ICP 1	ICP 1	ICP 1	-	-	-	(ICP 1)	ICP 1	ICP 2	FA	ICP 1	-	-
			%	%	%	%	%	%	%	%	%	%	%	%	%	%	%	ppm	ppm	ppm	ppm	ppm
T630	AN-100-95/73.85m	C-P Metaconglomerate	56.81	0.59	11.74	9.23	0.32	2.76	7.39	1.57	0.78	0.10	0.15	0.03	0.11	8.06	99.63	6.6	0.032	326	7	<0.5
T640	AN-132-97/71.40m	C-P Metaconglomerate	62.30	0.73	13.69	7.98	0.12	3.01	3.01	2.30	1.36	0.13	0.10	0.02	<0.05	4.82	99.61	4.2	0.033	574	<3	<0.5
16	AN-138-97/68.30m	C-P Metaconglomerate	57.48	0.88	14.81	9.32	0.10	3.14	3.38	4.01	0.43	0.14				5.00	98.75	<5		207		
17	AN-138-97/117.80m	C-P Metaconglomerate	46.98	0.77	16.94	8.44	0.11	3.51	6.34	3.53	2.11	0.27				9.08	98.20	<5		771		
T649	AN-146-97/78.10m	C-P Metaconglomerate	71.56	0.33	7.75	4.77	0.14	1.96	4.56	1.78	0.68	0.05	0.07	0.03	<0.05	5.97	99.66	<0.5	<0.002	255	6	<0.5
A03	AN-146-97/138.40m	C-P Metaconglomerate	62.54	0.57	17.65	5.91	0.10	3.29	1.07	6.96	<0.05	0.14				2.18	100.47	<5		28		
A01	AN-146-97/175.50m	C-P Metaconglomerate	73.75	0.19	12.08	3.29	0.04	0.63	2.30	5.85	0.23	<0.03				2.15	100.55	6		120		
A02	AN-146-97/190.50m	C-P Metaconglomerate	70.78	0.28	9.81	7.79	0.07	1.65	2.48	3.67	0.15	0.04				2.93	99.68	<5		74		
B13	AN-146-97/235m	C-P Metaconglomerate	73.83	0.58	13.40	5.08	0.02	0.81	0.27	2.56	1.33	0.07				2.41	100.45	<5		520		
I	AN-53-94/112.50m	Metaarenite	43.30	0.44	10.03	7.27	0.14	8.81	9.92	1.14	0.87	0.56				16.34	99.01		0.42	310		
II	AN-53-94/162.50m	Metaarenite	73.63	0.32	7.93	4.41	0.08	1.34	3.11	0.35	1.63	0.08				6.32	99.28		0.08	353		
T671	AN-72-94/103.70m	Metaarenite	81.93	0.18	4.96	2.88	0.07	0.88	2.50	0.35	0.90	0.06	0.68	0.04	<0.05	4.07	99.52	1550.0	7.650	211	4	<0.5
T627	AN-84-95/140.50m	Metaarenite	87.63	0.21	5.02	2.22	0.05	0.38	0.40	0.17	1.23	0.04	0.24	0.05	0.06	2.04	99.72	368.5	0.648	335	<3	<0.5
C07	AN-98-95/72.30m	Metaarenite	29.91	0.37	6.23	7.50	0.13	18.75	9.14	0.09	0.13	0.12				25.96	98.62	1281		47		
T631	AN-100-95/100.20m	Metaarenite	40.86	0.40	13.23	9.14	0.15	6.98	9.55	1.82	0.23	0.03	0.16	0.03	0.12	16.89	99.60	85.6	<0.002	82	<3	<0.5
T632	AN-100-95/139m	Metaarenite	59.62	0.38	14.84	5.10	0.10	1.70	5.30	3.67	1.90	0.18	1.03	0.04	0.07	5.64	99.57	43.2	0.008	722	<3	<0.5
A04	AN-107-95/146m	Metaarenite	54.91	0.64	19.83	7.99	0.11	2.01	1.28	1.10	3.69	0.14				8.17	100.00	113	0.05	940		
T637	AN-122-96/av154m	Metaarenite	77.74	0.45	9.32	4.34	0.07	0.70	1.43	0.54	1.46	0.04	0.10	0.03	<0.05	3.47	99.70	35.4	0.014	379	4	<0.5
T638	AN-122-96/183.50m	Metaarenite	71.48	0.25	6.80	4.03	0.08	2.47	4.19	0.24	1.47	0.09	0.36	0.03	0.11	7.78	99.39	2000.0	1.360	467	7	<0.5
T639	AN-122-96/184.50m	Metaarenite	71.71	0.46	9.06	4.80	0.06	1.13	2.72	0.38	2.02	0.07	0.56	0.03	0.05	5.91	98.95	7580.0	5.980	605	5	<0.5
III	AN-125-96/155.50m	Metaarenite	62.64	0.39	8.42	6.12	0.10	2.49	5.70	0.73	1.71	0.07				10.39	98.86		0.75	519		
IV	AN-125-96/162.50m	Metaarenite	59.17	0.43	12.38	5.89	0.07	2.70	4.26	0.50	2.58	0.05				9.84	97.99		17.23	861		
C08	AN-129-96/70.50m	Metaarenite	43.50	0.81	13.29	11.66	0.19	6.35	8.36	1.67	0.10	0.13				14.25	100.33	53		37		
T641	AN-132-97/189.50m	Metaarenite	68.55	0.39	9.08	4.65	0.09	2.35	4.35	0.36	1.69	0.31	0.23	0.03	0.08	7.40	99.55	371.7	0.078	391	<3	<0.5
T642	AN-135-97/176.80m	Metaarenite	57.68	0.63	13.64	7.25	0.09	3.03	4.27	1.58	2.92	0.16	0.31	0.04	0.09	7.93	99.61	5.1	0.018	740	5	<0.5
T643	AN-135-97/176.90m	Metaarenite	69.65	0.37	13.32	3.21	0.04	0.95	1.80	3.30	2.54	0.08	0.69	0.04	0.09	3.63	99.71	<0.5	0.015	588	6	<0.5
18	AN-138-97/166.30m	Metaarenite	79.81	0.28	10.13	3.13	0.03	0.63	0.83	1.91	1.12	0.06				2.36	100.38	<5		446		
19	AN-138-97/199m	Metaarenite	71.05	0.55	11.83	4.62	0.05	1.17	1.80	2.72	1.63	0.09				3.89	99.48	10		499		

APPENDIX 2 continued

Sample		Lithology	Cd	Co	Cr	Cs	Cu	Ga	Hf	Hg	Ir	Li	Mo	Nb	Ni	Pb	Rb	Sb	Sc	Se	Sn	Sr
ID	Drill core No.		ICP 2	INAA	XRF 2	INAA	XRF 2	XRF 2	INAA	INAA	INAA	ICP 2	XRF 2	XRF 2	XRF 2	XRF 2	XRF 2	INAA	INAA	INAA	XRF 2	XRF 2
			-	ICP 2	ICP 2	-	ICP 2	-	-	-	-	-	-	ICP 2	ICP 2	ICP 2	XRF 1	-	-	-	-	ICP 1
			ppm	ppm	ppm	ppm	ppm	ppm	ppm	ppm	ppb	ppm	ppm	ppm	ppm	ppm	ppm	ppm	ppm	ppm	ppm	ppm
T630	AN-100-95/73.85m	C-P Metaconglomerate		35	83	4	137	16	1	<1	<5		15	<2	74	<4	20	3.3	28.2	<3	<2	151
T640	AN-132-97/71.40m	C-P Metaconglomerate		25	107	3	74	16	2	<1	<5		7	<2	58	<4	28	2.1	22.7	<3	<2	100
16	AN-138-97/68.30m	C-P Metaconglomerate	<0.2	23	122		18					31		<1	41	<2						197
17	AN-138-97/117.80m	C-P Metaconglomerate	<0.2	20	81		5					26		<1	23	2						308
T649	AN-146-97/78.10m	C-P Metaconglomerate		16	53	2	52	10	1	<1	<5		<2	<2	32	5	16	2.2	12.8	<3	<2	128
A03	AN-146-97/138.40m	C-P Metaconglomerate	<0.2	28	184		33					35		4	66	2						195
A01	AN-146-97/175.50m	C-P Metaconglomerate	<0.2	7	179		162					7		2	19	5						132
A02	AN-146-97/190.50m	C-P Metaconglomerate	<0.2	18	98		112					19		3	31	4						105
B13	AN-146-97/235m	C-P Metaconglomerate	<0.2	14	208		16					12		2	38	3						161
I	AN-53-94/112.50m	Metaarenite															27					724
II	AN-53-94/162.50m	Metaarenite															50					172
T671	AN-72-94/103.70m	Metaarenite		7	24	<1	11	4	<1	<1	<5		<2	<2	9	23	25	3.0	6.3	<3	<2	124
T627	AN-84-95/140.50m	Metaarenite		10	18	1	32	7	<1	<1	<5		<2	3	10	14	31	3.4	4.0	<3	<2	42
C07	AN-98-95/72.30m	Metaarenite	2.5	62	881		39					49		8	858	18						1225
T631	AN-100-95/100.20m	Metaarenite		42	249	<1	93	13	<1	<1	<5		16	<2	114	6	5	0.9	32.9	<3	<2	231
T632	AN-100-95/139m	Metaarenite		10	38	2	11	20	3	<1	<5		3	<2	17	11	52	2.0	9.0	<3	<2	398
A04	AN-107-95/146m	Metaarenite	<0.2	24	70		41					10		2	52	9						257
T637	AN-122-96/av154m	Metaarenite		16	83	<1	14	11	3	<1	<5		<2	3	31	7	36	1.2	11.3	<3	<2	111
T638	AN-122-96/183.50m	Metaarenite		8	129	<1	11	8	<1	<1	<5		<2	<2	31	11	39	0.3	8.4	<3	<2	238
T639	AN-122-96/184.50m	Metaarenite		20	75	3	29	10	2	<1	<5		<2	<2	48	12	48	0.4	13.0	<3	<2	151
III	AN-125-96/155.50m	Metaarenite															50					306
IV	AN-125-96/162.50m	Metaarenite															78					302
C08	AN-129-96/70.50m	Metaarenite	<0.2	38	79		73					34		8	67	2						81
T641	AN-132-97/189.50m	Metaarenite		20	274	2	<10	11	3	<1	<5		<2	<2	133	23	43	3.2	10.3	<3	<2	254
T642	AN-135-97/176.80m	Metaarenite		28	81	3	93	18	3	<1	<5		15	<2	39	20	80	4.2	18.4	<3	<2	112
T643	AN-135-97/176.90m	Metaarenite		8	51	3	<10	16	3	<1	<5		<2	2	20	8	71	2.2	7.1	<3	<2	84
18	AN-138-97/166.30m	Metaarenite	<0.2	8	203		8					5		<1	18	2						124
19	AN-138-97/199m	Metaarenite	<0.2	7	127		6					9		<1	14	2						145

APPENDIX 2 continued

Sample		Lithology	Ta	Te	Th	U	V	W	Zn	Zr	Y	La	Ce	Pr	Nd	Sm	Eu	Tb	Yb	Lu
ID	Drill core No.		INAA	ICP 2	INAA	INAA	XRF 2	INAA	XRF 2	XRF 2	XRF 2	INAA	INAA	XRF 2	INAA	INAA	INAA	INAA	INAA	INAA
			-	-	-	-	-	-	ICP 2	XRF 1	XRF 1	ICP 2	-	-	-	-	-	-	-	-
			ppm	ppm	ppm	ppm	ppm	ppm	ppm	ppm	ppm	ppm	ppm	ppm	ppm	ppm	ppm	ppm	ppm	ppm
T630	AN-100-95/73.85m	C-P Metaconglomerate	<0.5		1.0	<0.5	131	<1	85	67	6	6.9	15	<50	<5	2.0	0.8	<0.5	1.8	0.30
T640	AN-132-97/71.40m	C-P Metaconglomerate	<0.5		1.2	<0.5	157	<1	72	121	13	11.6	21	<50	11	2.2	0.8	0.5	2.5	0.40
16	AN-138-97/68.30m	C-P Metaconglomerate							66			9								
17	AN-138-97/117.80m	C-P Metaconglomerate							80			2								
T649	AN-146-97/78.10m	C-P Metaconglomerate	<0.5		<0.2	<0.5	85	<1	48	45	6	5.4	11	<50	<5	1.2	0.3	<0.5	1.2	0.23
A03	AN-146-97/138.40m	C-P Metaconglomerate							88			12								
A01	AN-146-97/175.50m	C-P Metaconglomerate							18			18								
A02	AN-146-97/190.50m	C-P Metaconglomerate							38			27								
B13	AN-146-97/235m	C-P Metaconglomerate							42			15								
I	AN-53-94/112.50m	Metaarenite								137	13									
II	AN-53-94/162.50m	Metaarenite								85	17									
T671	AN-72-94/103.70m	Metaarenite	<0.5		1.8	<0.5	42	14	27	67	<3	7.5	11	<50	9	1.4	0.6	<0.5	0.8	0.24
T627	AN-84-95/140.50m	Metaarenite	<0.5		1.8	1.1	20	10	33	90	6	12.2	25	<50	10	2.1	0.7	<0.5	1.8	0.26
C07	AN-98-95/72.30m	Metaarenite							51			8								
T631	AN-100-95/100.20m	Metaarenite	<0.5		<0.2	<0.5	144	<1	77	24	<3	1.1	3	<50	<5	0.7	0.2	<0.5	1.3	0.20
T632	AN-100-95/139m	Metaarenite	<0.5		1.3	<0.5	57	<1	68	172	13	13.8	34	<50	15	3.6	1.0	<0.5	2.6	0.42
A04	AN-107-95/146m	Metaarenite							108			9								
T637	AN-122-96/av154m	Metaarenite	<0.5		2.9	<0.5	67	<1	39	141	10	16.8	29	<50	11	2.6	0.8	<0.5	2.8	0.48
T638	AN-122-96/183.50m	Metaarenite	<0.5		1.6	<0.5	41	17	34	82	<3	8.3	15	<50	9	1.8	<0.2	<0.5	1.1	0.18
T639	AN-122-96/184.50m	Metaarenite	<0.5		1.7	<0.5	90	34	51	109	9	10.0	14	<50	11	1.9	<0.2	<0.5	1.9	<0.06
III	AN-125-96/155.50m	Metaarenite								89	17									
IV	AN-125-96/162.50m	Metaarenite								101	15									
C08	AN-129-96/70.50m	Metaarenite							76			<1								
T641	AN-132-97/189.50m	Metaarenite	<0.5		3.5	<0.5	64	23	59	161	10	21.1	39	<50	17	3.8	1.4	<0.5	2.1	0.35
T642	AN-135-97/176.80m	Metaarenite	<0.5		2.4	<0.5	122	<1	91	146	13	14.8	32	<50	<5	2.9	0.9	<0.5	2.5	0.49
T643	AN-135-97/176.90m	Metaarenite	<0.5		3.2	<0.5	43	<1	19	183	12	21.4	35	<50	<5	2.9	0.9	<0.5	1.8	0.29
18	AN-138-97/166.30m	Metaarenite							35			5								
19	AN-138-97/199m	Metaarenite							43			10								

APPENDIX 2 continued

Sample		Lithology	SiO_2	TiO_2	Al_2O_3	Fe_2O_3t	MnO	MgO	CaO	Na_2O	K_2O	P_2O_5	SO_3	Cl	F	LOI	Total	As	Au	Ba	Bi	Br
ID	Drill core No.		XRF 2	XRF 2	XRF 2	XRF 2	XRF 2	XRF 2	XRF 2	XRF 2	XRF 2	XRF 2	XRF 2	XRF 2	XRF 2	(XRF 2)	XRF 2	INAA	INAA	XRF 2	XRF 2	INAA
			ICP 1	ICP 1	ICP 1	ICP 1	ICP 1	ICP 1	ICP 1	ICP 1	ICP 1	ICP 1	-	-	-	(ICP 1)	ICP 1	ICP 2	FA	ICP 1	-	-
			%	%	%	%	%	%	%	%	%	%	%	%	%	%	%	ppm	ppm	ppm	ppm	ppm
20	AN-138-97/231m	Metaarenite	64.18	0.56	13.47	4.80	0.06	2.17	3.28	3.43	1.77	0.16				6.37	100.34	57	0.04	457		
21	AN-138-97/280.10m	Metaarenite	71.59	0.51	11.67	3.73	0.07	0.94	2.64	0.45	2.77	0.05				5.51	100.04	65	0.71	662		
T645	AN-140-97/161.50m	Metaarenite	73.47	0.49	11.23	4.04	0.04	0.93	1.96	3.32	1.21	0.05	0.13	0.03	<0.05	2.77	99.71	2.5	0.007	381	<3	<0.5
T647	AN-140-97/219m	Metaarenite	81.45	0.20	8.95	1.41	0.02	0.33	0.80	3.79	0.81	0.02	0.32	0.03	0.06	1.62	99.80	2.9	<0.002	162	4	<0.5
T648	AN-140-97/229m	Metaarenite	25.71	0.48	6.89	7.35	0.13	20.84	9.56	0.02	0.07	0.38	0.16	0.01	<0.05	27.39	99.03	872.6	0.043	44	<3	<0.5
T651	AN-153-97/60.80m	Metaarenite	44.36	0.28	4.76	6.07	0.12	11.77	9.85	0.03	0.53	0.55	0.22	0.05	0.10	20.51	99.19	930.3	0.022	213	7	<0.5
T680	AF-A07	Metaarenite	77.82	0.09	11.53	1.51	0.03	0.14	0.15	2.87	3.70	0.01	<0,01	0.03	<0.05	1.78	99.66	2.4	0.012	1206	4	<0.5
T682	AF-B06	Metaarenite	75.30	0.51	12.45	3.40	0.00	0.14	0.03	0.63	2.48	0.01	<0.01	0.04	<0.05	3.97	98.90	17900.0	22.700	535	<3	<1.5
T629	AN-88-95/518.70m	S-P Metaconglomerate	66.58	0.48	8.96	6.83	0.19	1.37	4.71	0.19	2.01	0.04	0.18	0.04	0.09	7.99	99.65	90.8	0.009	500	6	<0.5
A06	AN-107-95/65.80m	S-P Metaconglomerate	75.56	0.43	13.08	4.36	0.02	0.63	0.60	0.33	2.75	0.06				2.67	100.58	24		581		
B14	AN-107-95/126m	S-P Metaconglomerate	71.83	0.52	10.32	7.09	0.09	1.02	0.71	0.77	1.92	0.08				5.74	100.18	129	0.04	516		
T635	AN-107-95/57.40m	S-P Metaconglomerate	68.85	0.59	9.88	7.00	0.13	1.05	3.01	1.91	1.72	0.05	0.13	0.03	0.12	5.22	99.70	<0.5	0.020	422	6	<0.5
V	AN-125-96/187.50m	S-P Metaconglomerate	60.07	0.75	14.35	9.46	0.11	2.28	3.34	0.46	2.16	0.13				7.38	100.59		0.02	556		
22	AN-138-97/293.30m	S-P Metaconglomerate	68.69	0.53	8.71	7.74	0.16	1.35	3.48	0.27	1.75	0.09				6.94	99.80	41		457		
23/T644	AN-138-97/317.30m	S-P Metaconglomerate	62.48	0.91	10.60	9.72	0.15	1.73	3.58	1.41	2.19	0.06	0.06	0.04	0.06	6.59	99.58	1.5	0.003	751	6	<0.5
24	AN-138-97/323.30m	S-P Metaconglomerate	64.80	0.83	13.54	7.99	0.60	1.35	1.30	3.91	1.37	0.10	0.04	0.01	0.05	3.70	99.57	6.5	<0.002	662	8	<0.5
T650	AN-146-97/394.10m	S-P Metaconglomerate	66.87	0.80	11.41	9.46	0.09	1.52	1.12	3.12	1.26	0.07	0.05	0.05	0.11	3.78	99.70	1.8	<0.002	572	<3	<0.5
T678	AF-A01	S-P Metaconglomerate	74.04	0.30	11.27	4.13	0.08	1.67	0.61	4.55	1.06	0.10	0.07	0.03	0.08	1.81	99.79	<0.5	<0.002	358	4	<0.5
T628	AN-88-95/315m	Metabasalte	44.30	1.44	14.42	19.01	0.27	6.45	6.63	2.52	0.21	0.16	0.25	0.04	0.09	3.82	99.61	3.7	<0.002	77	11	<0.5
T633	AN-100-95/270.10	Metabasalte	49.45	1.30	14.06	16.16	0.22	5.79	6.15	3.34	0.08	0.17	0.09	0.03	<0.05	2.70	99.54	14.3	<0.002	76	<3	<0.5
26/T634	AN-107-95/27.10m	Metabasalte	46.73	0.89	10.59	11.19	0.34	2.38	11.83	4.84	0.04	0.11	0.25	0.03	0.11	10.27	99.61	<0.5	<0.002	139	9	<0.5
B11	AN-129-96/68m	Metabasalte	48.51	0.83	13.09	12.04	0.11	6.03	7.94	1.76	<0,05	0.14				10.13	100.60	5		10		
25	AN-138-97/345.40m	Metabasalte	52.92	1.40	17.24	15.55	0.09	1.75	1.40	3.83	2.36	0.18				3.92	100.78	<5	0.02	1182		
T646	AN-140-97/169m	Metabasalte	49.79	0.79	14.16	10.16	0.12	5.71	6.38	1.79	1.59	0.25	0.11	0.02	0.13	8.55	99.54	5.1	<0.002	608	4	<0.5
T679	AF-A05	Metaandesite (?)	62.29	0.78	16.24	7.07	0.13	0.74	4.22	5.73	0.58	0.21	0.03	0.03	0.10	1.36	99.51	<0.5	<0.002	317	<3	<0.5

Note: Sample T682 (AF-B06) represents a hand specimen taken at the mine dump of the “Brahima Nord” mine.

APPENDIX 2 continued

Sample		Lithology	Cd	Co	Cr	Cs	Cu	Ga	Hf	Hg	Ir	Li	Mo	Nb	Ni	Pb	Rb	Sb	Sc	Se	Sn	Sr
ID	Drill core No.		ICP 2	INAA	XRF 2	INAA	XRF 2	XRF 2	INAA	INAA	INAA	ICP 2	XRF 2	XRF 2	XRF 2	XRF 2	XRF 2	INAA	INAA	INAA	XRF 2	XRF 2
			-	ICP 2	ICP 2	-	ICP 2	-	-	-	-	-	-	ICP 2	ICP 2	ICP 2	XRF 1	-	-	-	-	ICP 1
			ppm	ppm	ppm	ppm	ppm	ppm	ppm	ppm	ppb	ppm	ppm	ppm	ppm	ppm	ppm	ppm	ppm	ppm	ppm	ppm
20	AN-138-97/231m	Metaarenite	<0.2	11	112		20					11		<1	35	8						269
21	AN-138-97/280.10m	Metaarenite	<0.2	11	136		19					3		<1	23	4						141
T645	AN-140-97/161.50m	Metaarenite		8	38	3	<10	15	2	<1	<5		<2	<2	16	5	33	1.6	7.9	<3	2	140
T647	AN-140-97/219m	Metaarenite		<1	15	<1	46	10	2	<1	<5		3	<2	5	6	18	1.1	2.7	<3	<2	51
T648	AN-140-97/229m	Metaarenite		57	1439	<1	10	9	<1	<1	<5		14	<2	838	17	<2	14.4	13.9	<3	<2	1604
T651	AN-153-97/60.80m	Metaarenite		47	1062	<1	28	7	2	<1	<5		17	<2	630	23	17	23.9	13.4	<3	<2	1232
T680	AF-A07	Metaarenite		3	3	<1	<10	13	3	<1	<5		<2	10	<3	17	78	0.4	2.4	<3	<2	35
T682	AF-B06	Metaarenite		15	83	<1	20	15	<1	<1	<5		<2	<2	33	14	66	3.3	11.2	<3	<2	94
T629	AN-88-95/518.70m	S-P Metaconglomerate		31	79	1	<10	9	2	<1	<5		14	<2	52	5	50	2.2	15.5	<3	<2	86
A06	AN-107-95/65.80m	S-P Metaconglomerate	<0.2	15	82		22					16		1	27	3						79
B14	AN-107-95/126m	S-P Metaconglomerate	<0.2	34	190		66					2		<1	71	5						135
T635	AN-107-95/57.40m	S-P Metaconglomerate		23	111	3	18	10	2	<1	<5		10	<2	52	6	46	3.0	19.2	<3	<2	106
V	AN-125-96/187.50m	S-P Metaconglomerate															54					196
22	AN-138-97/293.30m	S-P Metaconglomerate	<0.2	23	128		15					10		<1	47	<2						120
23/T644	AN-138-97/317.30m	S-P Metaconglomerate	<0.2	38	125	2	27	13	2	<1	<5	6	17	<2	66	<4	61	4.0	22.9	<3	<2	165
24	AN-138-97/323.30m	S-P Metaconglomerate	<0.2	23	175	4	57	16	3	<1	<5	12	<2	6	61	6	42	3.6	27.7	<3	<2	89
T650	AN-146-97/394.10m	S-P Metaconglomerate		22	151	2	26	12	1	<1	<5		13	<2	74	6	33	2.1	22.7	<3	<2	98
T678	AF-A01	S-P Metaconglomerate		10	18	2	<10	11	2	<1	<5		<2	6	12	11	24	1.0	5.9	<3	<2	28
T628	AN-88-95/315m	Metabasalte		57	57	6	99	19	2	<1	<5		<2	<2	67	<4	5	1.9	46.1	<3	<2	91
T633	AN-100-95/270.10	Metabasalte		47	34	1	62	16	2	2	<5		<2	<2	50	<4	<2	0.7	37.6	<3	<2	82
26/T634	AN-107-95/27.10m	Metabasalte	<0.2	27	27	<1	42	10	<1	<1	<5	13	15	<2	42	5	<2	1.4	20.8	<3	<2	283
B11	AN-129-96/68m	Metabasalte	<0.2	40	148		61					69		12	98	2						58
25	AN-138-97/345.40m	Metabasalte	<0.2	34	75		90					15		<1	45	2						69
T646	AN-140-97/169m	Metabasalte		36	127	<1	61	16	1	<1	<5		14	3	46	6	46	2.9	25.3	<3	<2	368
T679	AF-A05	Metaandesite (?)		6	14	<1	207	20	<1	<1	<5		17	3	9	9	6	0.4	<0,1	<3	<2	296

APPENDIX 2 continued

Sample		Lithology	Ta	Te	Th	U	V	W	Zn	Zr	Y	La	Ce	Pr	Nd	Sm	Eu	Tb	Yb	Lu
ID	Drill core No.		INAA	ICP 2	INAA	INAA	XRF 2	INAA	XRF 2	XRF 2	XRF 2	INAA	INAA	XRF 2	INAA	INAA	INAA	INAA	INAA	INAA
			-	-	-	-	-	-	ICP 2	XRF 1	XRF 1	ICP 2	-	-	-	-	-	-	-	-
			ppm	ppm	ppm	ppm	ppm	ppm	ppm	ppm	ppm	ppm	ppm	ppm	ppm	ppm	ppm	ppm	ppm	ppm
20	AN-138-97/231m	Metaarenite							61			7								
21	AN-138-97/280.10m	Metaarenite							36			7								
T645	AN-140-97/161.50m	Metaarenite	<0.5		2.2	<0.5	50	<1	35	163	10	14.1	25	<50	12	2.1	0.6	<0.5	1.7	0.28
T647	AN-140-97/219m	Metaarenite	<0.5		2.1	1.4	15	<1	15	117	<3	12.1	21	<50	<5	1.8	0.7	<0.5	1.3	0.18
T648	AN-140-97/229m	Metaarenite	<0.5		3.6	2.4	124	22	67	142	7	26.6	50	<50	21	4.7	1.4	<0.5	0.8	0.14
T651	AN-153-97/60.80m	Metaarenite	<0.5		2.4	<0.5	87	12	60	108	<3	18.4	35	<50	20	4.1	1.6	<0.5	<0.2	<0.05
T680	AF-A07	Metaarenite	<0.5		6.3	<0.5	<5	<1	44	168	24	40.2	79	<50	17	5.1	0.7	0.8	4.5	0.81
T682	AF-B06	Metaarenite	<0.5		<0.5	<0.5	80	18	48	202	11	20.8	42	<50	<5	2.4	1.1	<0.5	<0.2	<0.05
T629	AN-88-95/518.70m	S-P Metaconglomerate	<0.5		2.2	1.3	83	6	56	110	13	10.9	24	<50	11	2.4	0.8	0.7	3.0	0.41
A06	AN-107-95/65.80m	S-P Metaconglomerate							33			20								
B14	AN-107-95/126m	S-P Metaconglomerate							45			4								
T635	AN-107-95/57.40m	S-P Metaconglomerate	<0.5		2.2	<0.5	106	<1	53	120	17	10.4	19	<50	<5	2.2	0.7	<0.5	2.9	0.58
V	AN-125-96/187.50m	S-P Metaconglomerate								143	26									
22	AN-138-97/293.30m	S-P Metaconglomerate							58			5								
23/T644	AN-138-97/317.30m	S-P Metaconglomerate	<0.5		1.6	<0.5	184	<1	92	133	26	12.8	24	<50	9	3.0	1.1	0.7	3.7	0.60
24	AN-138-97/323.30m	S-P Metaconglomerate	<0.5		2.7	3.1	155	<1	83	105	28	14.6	25	<50	12	3.0	0.9	0.8	4.0	0.73
T650	AN-146-97/394.10m	S-P Metaconglomerate	<0.5		0.8	<0.5	137	<1	67	119	18	7.9	14	<50	<5	1.6	0.3	<0.5	2.5	0.47
T678	AF-A01	S-P Metaconglomerate	<0.5		2.1	<0.5	32	<1	53	177	12	6.4	11	<50	<5	1.0	<0.2	<0.5	2.0	0.40
T628	AN-88-95/315m	Metabasalte	<0.5		0.8	<0.5	328	<1	157	104	28	7.2	18	<50	8	2.8	1.0	1.0	4.1	0.64
T633	AN-100-95/270.10	Metabasalte	<0.5		1.3	1.1	294	<1	141	115	22	7.2	20	<50	7	2.6	0.7	<0.5	3.6	0.53
26/T634	AN-107-95/27.10m	Metabasalte	<0.5		<0.2	<0.5	176	<1	71	84	10	4.3	7	<50	<5	0.9	<0.2	<0.5	2.3	0.29
B11	AN-129-96/68m	Metabasalte							79			<1								
25	AN-138-97/345.40m	Metabasalte							102			8								
T646	AN-140-97/169m	Metabasalte	<0.5		1.2	1.7	198	5	98	103	10	9.2	20	<50	12	2.2	0.8	<0.5	2.3	0.40
T679	AF-A05	Metaandesite (?)	<0.5		1.0	1.8	37	<1	116	183	<3	14.3	6	<50	<5	0.8	<0.2	<0.5	0.9	0.14

APPENDIX 3

Additional whole rock analysis for samples from Jonction and Aniuri. For each element, unit, detection limit and analytical method are given below. Hg-FIMS: Cold vapor – Flow Injection Mercury System; AR-MS: Aqua Regia Digestion – Mass Spectrometry; AR-ICP: Aqua Regia Digestion – Inductively Coupled Plasma. All the analyses were performed by Actlabs.

Sample		Lithology	Hg	Li	Be	B	Na	Mg	Al	P	S	K	Ca	V	Cr	Ti	Mn	Fe	Co	Ni	Cu	Zn	Ga
ID	Drill core No.		ppb	ppm	ppm	ppm	%	%	%	%	%	%	%	ppm	ppm	%	ppm	%	ppm	ppm	ppm	ppm	ppm
			5	0.1	0.1	1	0.001	0.01	0.01	0.001	0.001	0.01	0.01	1	0.5	0.01	1	0.01	0.1	0.1	0.01	0.1	0.02
			Hg-FIMS	AR-MS	AR-MS	AR-MS	AR-MS	AR-MS	AR-MS	AR-ICP	AR-ICP	AR-MS	AR-MS	AR-MS	AR-MS	AR-ICP	AR-MS	AR-MS	AR-MS	AR-MS	AR-MS	AR-MS	AR-MS
Jonction																							
T603	1A6-50-97/274m	Metaarenite	75	< 0.1	0.1	6	0.033	0.67	0.53	0.003	1.201	0.28	1.73	7	5.2	< 0.01	418	2.84	8.7	19.0	17.30	43.4	1.82
T605	1A6-53-97/151.70m	Metaarenite	1030	4.5	< 0.1	3	0.025	2.65	0.29	< 0.001	0.083	0.02	6.34	9	30.8	< 0.01	1300	2.91	21.8	139.0	1270.00	46.6	0.70
T662	1A6-63-97/447.75m	Metaarenite	13	< 0.1	< 0.1	< 1	0.021	0.78	0.13	0.002	0.705	0.07	2.05	3	4.1	< 0.01	485	2.06	9.9	31.8	27.70	31.4	0.34
T663	1A6-63-97/468m	Metaarenite	29	63.6	0.2	1	0.026	3.74	4.22	0.002	1.527	0.06	1.57	38	48.4	< 0.01	525	9.37	14.7	82.8	16.30	167.0	11.50
T664	1A6-63-97/469m	Metaarenite	8	< 0.1	< 0.1	2	0.023	0.26	0.07	< 0.001	0.559	0.03	0.58	1	2.7	< 0.01	151	1.07	7.3	23.1	18.60	5.8	0.15
T622	1A6-72-97/199.64m	Metaarenite	32	12.1	0.1	4	0.021	1.11	0.87	0.005	0.900	0.06	1.83	10	11.5	< 0.01	454	3.85	24.9	45.1	55.10	61.3	2.40
T623	1A6-72-97/202.69m	Metaarenite	22	2.6	< 0.1	1	0.021	0.39	0.27	0.002	0.914	0.07	0.69	3	7.9	< 0.01	201	2.21	15.1	43.5	23.80	25.5	0.93
T626	1A6-74-98/372.70m	Metaarenite	27	14.1	0.1	2	0.039	1.32	1.16	0.035	1.426	0.10	3.14	20	15.6	< 0.01	783	6.96	30.8	70.3	76.90	67.8	3.05
T611	1A6-64-97/151.50m	Metagabbro	37	2.1	< 0.1	4	0.078	2.79	0.27	0.007	1.484	0.06	9.35	16	5.5	< 0.01	1510	8.98	49.3	51.9	40.00	36.8	0.40
Aniuri																							
T671	AN-72-94/103.70m	Metaarenite	5	0.6	< 0.1	2	0.051	0.46	0.23	0.020	0.466	0.08	1.68	3	3.3	< 0.01	478	2.03	5.7	12.4	14.20	20.4	0.43
T627	AN-84-95/140.50m	Metaarenite	7	< 0.1	< 0.1	< 1	0.032	0.19	0.19	0.013	0.226	0.09	0.26	2	4.3	< 0.01	347	1.60	10.0	12.7	41.70	31.7	0.39
T632	AN-100-95/139m	Metaarenite	< 5	13.3	0.2	2	0.048	0.77	1.48	0.065	0.674	0.13	3.61	17	15.7	< 0.01	694	3.62	10.4	16.6	14.80	64.1	5.93
T636	AN-109-95/61m	Metaarenite	< 5	0.6	0.1	4	0.036	4.09	0.20	0.004	0.021	0.09	9.35	9	53.7	< 0.01	832	2.83	22.9	307.0	9.08	25.0	0.28
T638	AN-122-97/183.50m	Metaarenite	7	2.0	0.1	1	0.034	1.17	0.24	0.032	0.454	0.06	2.77	3	8.6	< 0.01	602	2.72	8.5	32.0	13.30	28.2	0.47
T639	AN-122-97/184.50m	Metaarenite	12	< 0.1	< 0.1	3	0.042	0.53	0.24	0.020	1.096	0.11	1.85	4	5.5	< 0.01	406	3.39	23.8	48.3	35.70	47.3	0.41
T682	AF-B06	Metaarenite	8	1.1	< 0.1	< 1	0.045	0.04	0.32	< 0.001	0.637	0.09	< 0.01	3	4.9	< 0.01	11	2.16	12.9	30.5	26.30	43.8	0.65

APPENDIX 3 continued

Sample ID	Drill core No.	Lithology	Ge ppm 0.1 AR-MS	As ppm 0.1 AR-MS	Se ppm 0.1 AR-MS	Rb ppm 0.1 AR-MS	Sr ppm 0.5 AR-MS	Y ppm 0.01 AR-MS	Zr ppm 0.1 AR-MS	Sc ppm 0.1 AR-MS	Pr ppm 0.1 AR-MS	Gd ppm 0.1 AR-MS	Dy ppm 0.001 AR-MS	Ho ppm 0.1 AR-MS	Er ppm 0.1 AR-MS	Tm ppm 0.1 AR-MS	Nb ppm 0.1 AR-MS	Mo ppm 0.01 AR-MS	Ag ppm 0.002 AR-MS	Cd ppm 0.01 AR-MS	In ppm 0.02 AR-MS	Sn ppm 0.05 AR-MS	Sb ppm 0.02 AR-MS
Jonction																							
T603	1A6-50-97/274m	Metaarenite	< 0.1	3480	0.6	10.0	121.0	1.55	9.0	1.5	1.1	0.7	0.376	< 0.1	0.2	< 0.1	< 0.1	0.70	1.280	0.27	< 0.02	0.18	4.79
T605	1A6-53-97/151.70m	Metaarenite	< 0.1	8.1	2.5	0.9	282.0	2.22	0.5	5.0	0.2	0.6	0.471	< 0.1	0.2	< 0.1	< 0.1	0.16	95.400	0.39	0.05	0.06	8.00
T662	1A6-63-97/447.75m	Metaarenite	< 0.1	792	0.6	2.6	118.0	1.15	1.9	1.4	0.3	0.4	0.281	< 0.1	0.1	< 0.1	< 0.1	0.37	0.288	0.13	< 0.02	0.49	1.82
T663	1A6-63-97/468m	Metaarenite	< 0.1	434	0.7	2.4	180.0	1.67	2.2	2.6	0.5	0.6	0.403	< 0.1	0.2	< 0.1	< 0.1	1.51	0.098	< 0.01	< 0.02	0.17	1.54
T664	1A6-63-97/469m	Metaarenite	< 0.1	202	0.5	1.3	50.4	0.67	1.6	0.4	1.0	0.4	0.176	< 0.1	< 0.1	< 0.1	< 0.1	4.58	0.061	0.10	< 0.02	< 0.05	1.31
T622	1A6-72-97/199.64m	Metaarenite	< 0.1	2880	1.5	2.4	89.9	1.26	6.3	2.3	0.6	0.5	0.311	< 0.1	0.1	< 0.1	< 0.1	1.15	0.651	0.25	0.02	< 0.05	10.60
T623	1A6-72-97/202.69m	Metaarenite	< 0.1	4550	1.0	2.5	42.6	0.55	9.1	0.7	0.7	0.4	0.149	< 0.1	< 0.1	< 0.1	< 0.1	0.60	0.448	0.24	< 0.02	< 0.05	9.96
T626	1A6-74-98/372.70m	Metaarenite	< 0.1	> 10000	2.2	3.6	195.0	1.98	26.7	3.9	0.5	1.0	0.567	< 0.1	0.2	< 0.1	< 0.1	1.42	0.432	0.25	0.03	< 0.05	8.86
T611	1A6-64-97/151.50m	Metagabbro	< 0.1	498	1.7	2.5	297.0	3.24	1.3	10.3	0.2	0.8	0.703	0.1	0.4	< 0.1	< 0.1	0.74	0.188	0.35	0.02	0.07	0.92
Aniuri																							
T671	AN-72-94/103.70m	Metaarenite	< 0.1	1370	0.6	2.9	83.5	1.51	5.4	1.3	0.8	0.7	0.384	< 0.1	0.2	< 0.1	< 0.1	0.59	0.164	0.12	< 0.02	0.28	1.11
T627	AN-84-95/140.50m	Metaarenite	< 0.1	344	< 0.1	3.3	25.1	1.09	2.4	0.5	2.3	0.8	0.304	< 0.1	0.1	< 0.1	< 0.1	0.20	0.040	0.24	< 0.02	< 0.05	1.46
T632	AN-100-95/139m	Metaarenite	< 0.1	43.5	< 0.1	5.0	269.0	2.53	1.9	1.6	1.5	1.1	0.600	0.1	0.3	< 0.1	< 0.1	0.42	0.013	0.18	0.02	< 0.05	0.88
T636	AN-109-95/61m	Metaarenite	< 0.1	529	< 0.1	3.7	> 1000	5.59	4.1	5.4	2.4	2.5	1.300	0.2	0.5	< 0.1	< 0.1	0.37	0.174	0.19	0.03	< 0.05	5.56
T638	AN-122-97/183.50m	Metaarenite	< 0.1	1950	< 0.1	2.4	198.0	1.96	6.5	2.3	1.2	1.0	0.488	< 0.1	0.2	< 0.1	< 0.1	0.54	0.021	0.15	< 0.02	< 0.05	1.25
T639	AN-122-97/184.50m	Metaarenite	< 0.1	8880	1.8	3.8	105.0	1.67	23.1	2.0	1.2	0.7	0.384	< 0.1	0.2	< 0.1	< 0.1	0.27	0.179	0.12	0.03	< 0.05	4.00
T682	AF-B06	Metaarenite	< 0.1	> 10000	1.4	3.2	5.0	1.04	38.1	1.3	2.0	0.7	0.270	< 0.1	0.2	< 0.1	< 0.1	0.07	0.054	0.14	0.04	< 0.05	3.91

APPENDIX 3 continued

Sample ID	Drill core No.	Lithology	Te ppm 0.02 AR-MS	Cs ppm 0.02 AR-MS	Ba ppm 0.5 AR-MS	La ppm 0.5 AR-MS	Ce ppm 0.01 AR-MS	Nd ppm 0.02 AR-MS	Sm ppm 0.1 AR-MS	Eu ppm 0.1 AR-MS	Tb ppm 0.1 AR-MS	Yb ppm 0.1 AR-MS	Lu ppm 0.1 AR-MS	Hf ppm 0.1 AR-MS	Ta ppm 0.05 AR-MS	W ppm 0.1 AR-MS	Re ppm 0.001 AR-MS	Au ppb 0.5 AR-MS	Tl ppm 0.02 AR-MS	Pb ppm 0.01 AR-MS	Bi ppm 0.02 AR-MS	Th ppm 0.1 AR-MS	U ppm 0.1 AR-MS
Jonction																							
T603	1A6-50-97/274m	Metaarenite	0.20	1.58	48.1	3.8	8.94	4.59	1.1	0.3	< 0.1	0.2	< 0.1	< 0.1	< 0.05	7.4	< 0.001	> 10000	0.14	10.80	0.13	1.2	< 0.1
T605	1A6-53-97/151.70m	Metaarenite	0.96	0.45	19.0	0.5	1.78	1.02	0.5	0.3	< 0.1	0.2	< 0.1	< 0.1	< 0.05	0.2	0.001	> 10000	0.07	259.00	1.97	0.2	< 0.1
T662	1A6-63-97/447.75m	Metaarenite	0.06	0.48	23.7	0.8	2.27	1.16	0.4	0.2	< 0.1	0.1	< 0.1	< 0.1	< 0.05	13.9	< 0.001	7170	0.05	6.06	0.04	0.5	< 0.1
T663	1A6-63-97/468m	Metaarenite	0.07	1.33	27.7	1.9	4.14	2.09	0.7	0.3	< 0.1	0.2	< 0.1	< 0.1	< 0.05	0.5	0.002	2970	0.04	44.40	0.23	0.5	< 0.1
T664	1A6-63-97/469m	Metaarenite	0.08	0.24	16.9	4.1	8.29	3.52	0.6	0.2	< 0.1	< 0.1	< 0.1	< 0.1	< 0.05	0.4	0.002	1790	0.03	25.70	0.18	0.5	< 0.1
T622	1A6-72-97/199.64m	Metaarenite	0.33	1.56	27.8	2.1	4.94	2.58	0.7	0.2	< 0.1	0.1	< 0.1	< 0.1	< 0.05	1.6	0.002	> 10000	0.06	11.10	0.13	0.4	< 0.1
T623	1A6-72-97/202.69m	Metaarenite	0.16	0.65	25.5	2.5	5.58	2.75	0.6	0.1	< 0.1	< 0.1	< 0.1	< 0.1	< 0.05	0.3	0.001	> 10000	0.06	9.17	0.11	0.4	< 0.1
T626	1A6-74-98/372.70m	Metaarenite	0.28	1.50	35.0	1.7	4.14	2.42	0.9	0.4	0.1	0.2	< 0.1	< 0.1	< 0.05	13.8	0.003	7780	0.07	17.10	0.29	0.5	< 0.1
T611	1A6-64-97/151.50m	Metagabbro	0.17	1.13	28.4	< 0.5	1.37	1.25	0.8	0.4	0.1	0.4	< 0.1	< 0.1	< 0.05	0.3	0.004	9540	0.06	3.60	0.18	0.3	< 0.1
Aniuri																							
T671	AN-72-94/103.70m	Metaarenite	0.08	0.37	34.1	2.7	6.34	3.55	1.0	0.3	< 0.1	0.2	< 0.1	< 0.1	< 0.05	1.0	0.001	3980	0.04	15.00	0.12	0.7	0.2
T627	AN-84-95/140.50m	Metaarenite	0.05	0.29	42.6	8.6	16.30	8.81	1.6	0.3	< 0.1	0.1	< 0.1	< 0.1	< 0.05	< 0.1	0.002	1130	0.05	5.54	0.10	1.2	0.2
T632	AN-100-95/139m	Metaarenite	0.10	0.51	69.7	5.3	11.90	6.28	1.4	0.3	0.1	0.3	< 0.1	< 0.1	< 0.05	< 0.1	0.001	393	0.08	9.00	0.19	0.7	0.1
T636	AN-109-95/61m	Metaarenite	0.05	0.26	50.5	6.4	16.40	10.60	2.9	1.1	0.3	0.4	< 0.1	< 0.1	< 0.05	0.3	< 0.001	932	0.05	8.99	0.10	0.9	0.3
T638	AN-122-97/183.50m	Metaarenite	0.17	0.56	33.6	3.7	8.75	4.97	1.4	0.4	0.1	0.2	< 0.1	< 0.1	< 0.05	< 0.1	0.001	777	0.04	10.00	0.10	0.9	0.2
T639	AN-122-97/184.50m	Metaarenite	0.48	0.62	43.9	4.1	8.58	4.58	1.2	0.3	< 0.1	0.2	< 0.1	0.1	< 0.05	0.3	0.001	6160	0.04	7.55	0.11	1.1	0.2
T682	AF-B06	Metaarenite	0.15	0.60	31.0	7.7	15.40	7.73	1.4	0.3	< 0.1	0.2	< 0.1	0.2	< 0.05	0.1	0.002	> 10000	0.03	8.49	0.30	2.0	0.5

APPENDIX 4

Additional whole rock analysis for samples from Jonction. For each element, unit, detection limit and analytical method are given below. Hg-FIMS: Cold vapor – Flow Injection Mercury System; AR-MS: Aqua Regia Digestion – Mass Spectrometry; AR-ICP: Aqua Regia Digestion – Inductively Coupled Plasma. All the analyses were performed by Actlabs.

Sample		Lithology	Au		Ag		Al	As		B	Ba		Be	Bi	Br	Ca		Co		Cr	
ID	Designation		ppb	ppb	ppm	ppm	%	ppm	ppm	ppm	ppm	ppm	ppm	ppm	ppm	%	%	ppm	ppm	ppm	ppm
			2	0.5	5	0.002	0.01	0.5	0.1	1	50	0.5	0.1	0.02	0.5	1	0.01	1	0.1	5	0.5
			INAA	AR-MS	INAA	AR-MS	AR-MS	INAA	AR-MS	AR-MS	INAA	AR-MS	AR-MS	AR-MS	INAA	INAA	AR-MS	INAA	AR-MS	INAA	AR-MS
T690	1A6-44-97/av. 90m	Metaarenite	> 30000	> 10000	< 5	2.57	0.27	3900	> 10000	2	880	28.2	< 0.1	0.19	< 0.5	< 1	2.88	29	33.6	58	5.4
T691	JON-03	Metaarenite	3290	3350	< 5	0.184	0.26	311	335	2	820	47.1	< 0.1	0.26	< 0.5	< 1	< 0.01	5	6.3	70	3
T692	JON-04	Metaarenite	945	951	< 5	0.196	0.4	223	214	2	510	62.7	0.1	0.1	< 0.5	< 1	< 0.01	3	3.8	47	4.4
T693	JON-05	Metaarenite	376	370	< 5	0.037	0.21	88.9	86.2	2	220	22.4	< 0.1	0.06	< 0.5	< 1	< 0.01	3	2.9	34	3.3
T694	JON-06	Metaarenite	115	145	< 5	0.042	0.29	27.4	22.8	2	610	39.7	< 0.1	0.04	< 0.5	< 1	< 0.01	< 1	0.5	52	3.7
T695	JON-07	Metaarenite	5060	4420	< 5	0.266	0.35	835	830	2	1100	19.2	< 0.1	0.28	< 0.5	< 1	< 0.01	8	9.3	76	7.5
T696	JON-09	Metaarenite	2440	3520	< 5	0.356	0.46	1510	1620	3	620	39.1	< 0.1	0.04	< 0.5	< 1	< 0.01	3	3.2	25	3.6
T697	JON-10	Metaarenite	21800	> 10000	< 5	2.39	0.28	469	530	2	580	28.7	< 0.1	0.1	< 0.5	< 1	< 0.01	8	10.5	84	11.7

Sample		Lithology	Cs		Cu	Fe		Ga	Cd	Ge	Hf		Hg		In	Ir	K	Li	Nb	Mg	Mn	Mo	
ID	Designation		ppm	ppm	ppm	%	%	ppm	ppm	ppm	ppm	ppm	ppm	ppb	ppm	ppb	%	ppm	ppm	%	ppm	ppm	ppm
			1	0.02	0.01	0.01	0.01	0.02	0.01	0.1	1	0.1	1	5	0.02	5	0.01	0.1	0.1	0.01	1	1	0.01
			INAA	AR-MS	AR-MS	INAA	AR-MS	AR-MS	AR-MS	AR-MS	INAA	AR-MS	INAA	Hg-FIMS	AR-MS	INAA	AR-MS	AR-MS	AR-MS	AR-MS	AR-MS	INAA	AR-MS
T690	1A6-44-97/av. 90m	Metaarenite	8	1.2	35.5	5.86	6.33	0.69	0.19	< 0.1	< 1	0.1	< 1	95	0.04	< 5	0.1	2.1	< 0.1	1.5	940	< 1	0.67
T691	JON-03	Metaarenite	12	0.57	3.5	1.46	1.19	0.47	< 0.01	< 0.1	3	< 0.1	< 1	32	< 0.02	< 5	0.14	0.1	< 0.1	< 0.01	3	< 1	0.1
T692	JON-04	Metaarenite	7	0.69	3.92	0.78	0.68	0.92	0.05	< 0.1	2	< 0.1	< 1	59	< 0.02	< 5	0.2	0.1	< 0.1	< 0.01	14	< 1	0.82
T693	JON-05	Metaarenite	4	0.26	0.69	0.84	0.81	0.27	< 0.01	< 0.1	2	< 0.1	< 1	6	< 0.02	< 5	0.06	0.1	< 0.1	< 0.01	59	< 1	0.23
T694	JON-06	Metaarenite	9	0.47	1.26	0.4	0.33	0.5	< 0.01	< 0.1	3	< 0.1	< 1	< 5	< 0.02	< 5	0.12	0.4	< 0.1	< 0.01	8	< 1	0.14
T695	JON-07	Metaarenite	13	0.61	9.37	2.99	2.69	0.61	< 0.01	< 0.1	3	< 0.1	< 1	42	< 0.02	< 5	0.16	0.3	< 0.1	< 0.01	12	< 1	0.14
T696	JON-09	Metaarenite	5	0.49	9.67	0.99	0.96	0.7	< 0.01	< 0.1	2	< 0.1	< 1	11	< 0.02	< 5	0.13	0.4	< 0.1	< 0.01	9	< 1	0.14
T697	JON-10	Metaarenite	7	0.65	24.4	1.82	1.82	0.54	0.02	< 0.1	3	< 0.1	< 1	63	< 0.02	< 5	0.16	0.3	< 0.1	< 0.01	26	< 1	0.69

APPENDIX 4 continued

Sample		Lithology	Na		Ni		P	Pb	Rb		Re	S	Sb		Sc		Se		Sn		Sr	
ID	Designation		%	%	ppm	ppm	%	ppm	ppm	ppm	ppm	%	ppm	ppm	ppm	ppm	ppm	ppm	%	ppm	%	ppm
			0.01	0.001	20	0.1	0.001	0.01	15	0.1	0.001	0.001	0.1	0.02	0.1	0.1	3	0.1	0.02	0.05	0.05	0.5
			INAA	AR-MS	INAA	AR-MS	AR-ICP	AR-MS	INAA	AR-MS	AR-MS	AR-ICP	INAA	AR-MS	INAA	AR-MS	INAA	AR-MS	INAA	AR-MS	INAA	AR-MS
T690	1A6-44-97/av. 90m	Metaarenite	0.15	0.025	420	39.2	0.004	24.7	< 15	3.9	< 0.001	3.943	13	13.1	25.6	3.9	< 3	3.4	< 0.02	0.19	< 0.05	154
T691	JON-03	Metaarenite	0.19	0.026	< 20	11.2	0.001	10.9	80	4.3	0.001	1.293	6.4	1.39	9.6	0.2	< 3	0.8	< 0.02	0.07	< 0.05	2.7
T692	JON-04	Metaarenite	0.14	0.029	< 20	7.4	< 0.001	8.44	< 15	5.8	< 0.001	0.766	4.3	0.76	5.3	0.3	< 3	0.6	< 0.02	0.07	< 0.05	4.4
T693	JON-05	Metaarenite	0.07	0.016	< 20	6.4	0.001	12	33	1.9	< 0.001	0.765	3.2	0.45	3.1	< 0.1	< 3	0.4	< 0.02	0.17	< 0.05	1.2
T694	JON-06	Metaarenite	0.14	0.029	< 20	1.5	0.002	2.78	78	3.6	< 0.001	0.213	3.2	0.64	7.3	< 0.1	< 3	< 0.1	< 0.02	0.1	< 0.05	2.2
T695	JON-07	Metaarenite	0.23	0.036	< 20	21	0.002	8.87	105	5.1	0.002	2.927	11.3	1.63	10.5	0.3	< 3	0.9	< 0.02	0.08	< 0.05	3.4
T696	JON-09	Metaarenite	0.09	0.038	< 20	8.1	0.002	5.15	52	4	< 0.001	0.818	1.9	0.56	4.2	0.4	< 3	0.5	< 0.02	0.12	< 0.05	2.7
T697	JON-10	Metaarenite	0.17	0.039	< 20	28.5	< 0.001	9.44	47	4.6	0.002	2.048	11.5	2.83	9	0.4	< 3	1.8	< 0.02	0.1	< 0.05	3.1

Sample		Lithology	Ta		Te	Th		Ti	Tl	U		V	W		Zn		Zr	Y	La		Ce	
ID	Designation		ppm	ppm	ppm	ppm	ppm	%	ppm	ppm	ppm	ppm	ppm	ppm	ppm	ppm	ppm	ppm	ppm	ppm	ppm	ppm
			0.5	0.05	0.02	0.2	0.1	0.01	0.02	0.5	0.1	1	1	0.1	50	0.1	0.1	0.01	0.5	0.5	3	0.01
			INAA	AR-MS	AR-MS	INAA	AR-MS	AR-ICP	AR-MS	INAA	AR-MS	AR-MS	INAA	AR-MS	INAA	AR-MS	AR-MS	AR-MS	INAA	AR-MS	INAA	AR-MS
T690	1A6-44-97/av. 90m	Metaarenite	< 0.5	< 0.05	0.43	< 0.2	0.3	< 0.01	0.04	< 0.5	< 0.1	7	51	0.6	< 50	88.9	41.9	1.83	6.2	0.7	< 3	2.37
T691	JON-03	Metaarenite	< 0.5	< 0.05	0.1	3.4	1.8	< 0.01	0.03	< 0.5	< 0.1	2	32	0.4	< 50	0.8	2.5	0.63	25.9	13.8	47	28.5
T692	JON-04	Metaarenite	< 0.5	< 0.05	0.03	2.2	0.9	< 0.01	0.05	< 0.5	< 0.1	4	21	0.4	< 50	9.2	1.9	0.65	21	9.3	35	18.7
T693	JON-05	Metaarenite	< 0.5	< 0.05	< 0.02	2.5	1.2	< 0.01	< 0.02	< 0.5	< 0.1	2	14	0.2	< 50	3.8	1.1	0.97	17	8.5	32	17.9
T694	JON-06	Metaarenite	< 0.5	< 0.05	< 0.02	2.3	1.9	< 0.01	0.03	< 0.5	< 0.1	2	21	0.2	< 50	1.4	1.4	1.37	34.8	18.5	57	37.6
T695	JON-07	Metaarenite	< 0.5	< 0.05	0.07	4.6	2.2	< 0.01	0.04	< 0.5	< 0.1	3	37	0.5	< 50	4.9	4.9	0.95	35.2	15	65	31.5
T696	JON-09	Metaarenite	< 0.5	< 0.05	0.09	2.9	1.6	< 0.01	0.03	< 0.5	< 0.1	3	14	0.2	< 50	4.5	4.5	1.25	23.1	15.8	43	32.9
T697	JON-10	Metaarenite	< 0.5	< 0.05	0.03	1.7	0.5	< 0.01	0.03	< 0.5	< 0.1	3	24	0.2	< 50	18.1	2.6	0.34	13.5	2.5	29	5.91

Sample		Lithology	Pr	Nd		Sm		Eu		Gd	Tb		Dy	Ho	Er	Tm	Yb		Lu	
ID	Designation		ppm	ppm	ppm	ppm	ppm	ppm	ppm	ppm	ppm	ppm	ppm	ppm	ppm	ppm	ppm	ppm	ppm	ppm
			0.1	5	0.02	0.1	0.1	0.2	0.1	0.1	0.5	0.1	0.001	0.1	0.1	0.1	0.2	0.1	0.05	0.1
			AR-MS	INAA	AR-MS	INAA	AR-MS	INAA	AR-MS	AR-MS	INAA	AR-MS	AR-MS	AR-MS	AR-MS	AR-MS	INAA	AR-MS	INAA	AR-MS
T690	1A6-44-97/av. 90m	Metaarenite	0.3	13	1.2	1.5	0.5	< 0.2	0.2	0.5	< 0.5	< 0.1	0.411	< 0.1	0.2	< 0.1	< 0.2	0.2	< 0.05	< 0.1
T691	JON-03	Metaarenite	3.7	17	14.2	3.6	2.5	1.1	0.6	1.2	< 0.5	< 0.1	0.24	< 0.1	< 0.1	< 0.1	2	< 0.1	0.28	< 0.1
T692	JON-04	Metaarenite	2.4	< 5	9.21	2.6	1.6	0.7	0.4	0.9	< 0.5	< 0.1	0.213	< 0.1	< 0.1	< 0.1	1.4	< 0.1	0.19	< 0.1
T693	JON-05	Metaarenite	2.2	9	8.21	2.2	1.4	0.6	0.3	0.8	< 0.5	< 0.1	0.217	< 0.1	< 0.1	< 0.1	1	< 0.1	0.15	< 0.1
T694	JON-06	Metaarenite	5	22	19.2	4.5	3.4	1.4	0.8	1.6	0.9	< 0.1	0.381	< 0.1	< 0.1	< 0.1	2	< 0.1	0.32	< 0.1
T695	JON-07	Metaarenite	4.1	18	15.7	4.8	2.8	1.5	0.6	1.3	< 0.5	< 0.1	0.293	< 0.1	< 0.1	< 0.1	2.7	< 0.1	0.36	< 0.1
T696	JON-09	Metaarenite	4.2	< 5	16.3	3.2	2.9	1	0.6	1.5	< 0.5	0.1	0.341	< 0.1	0.1	< 0.1	1.2	< 0.1	0.18	< 0.1
T697	JON-10	Metaarenite	0.7	< 5	2.77	1.6	0.5	0.5	< 0.1	0.2	< 0.5	< 0.1	0.068	< 0.1	< 0.1	< 0.1	1.5	< 0.1	0.19	< 0.1

APPENDIX 5

Electron microprobe data used for arsenopyrite geothermometry (Jonction deposit). Values in brackets below each element represent the detection limits.

Rock sample	Spot	Composition (wt. %)												Composition (at. %)				As/S mole
		S (0.03)	Fe (0.04)	Co (0.03)	Ni (0.02)	Zn (0.06)	As (0.03)	Ag (0.05)	Sb (0.04)	Au (0.06)	Cu (0.02)	Pb (0.4)	Total	S	Fe	As	Total	
1A6-54-97	59 / 1 .	21.65	36.04	0.00	0.01	0.00	40.75	0.01	0.02	0.00	0.03	0.00	98.51	36.22	34.61	29.17	100	0.805
154.50m	60 / 1 .	21.92	36.30	0.00	0.01	0.02	40.68	0.02	0.01	0.00	0.01	0.21	99.17	36.43	34.64	28.93	100	0.794
	61 / 1 .	20.79	36.02	0.00	0.01	0.04	42.00	0.04	0.00	0.00	0.01	0.08	99.00	34.97	34.79	30.24	100	0.865
(1.74 g/t Au)	62 / 1 .	21.54	35.67	0.00	0.01	0.01	39.86	0.01	0.02	0.00	0.03	0.00	97.14	36.45	34.67	28.88	100	0.792
	63 / 1 .	20.88	36.04	0.00	0.02	0.01	41.99	0.04	0.00	0.00	0.01	0.09	99.08	35.07	34.75	30.18	100	0.861
1A6-74-98	56 / 1 .	22.19	35.86	0.00	0.19	0.02	41.09	0.00	0.05	0.01	0.02	0.00	99.43	36.77	34.11	29.13	100	0.792
372.70m	57 / 1 .	22.82	35.84	0.00	0.22	0.03	40.03	0.03	0.02	0.00	0.03	0.00	98.99	37.70	34.00	28.31	100	0.751
	58 / 1 .	21.59	35.41	0.00	0.02	0.03	41.37	0.04	0.00	0.04	0.02	0.00	98.52	36.21	34.10	29.69	100	0.820
(7.10 g/t Au)	66 / 1 .	22.23	35.39	0.00	0.01	0.02	40.38	0.02	0.00	0.02	0.00	0.17	98.24	37.15	33.96	28.89	100	0.778
	66 / 2 .	22.97	36.34	0.00	0.00	0.03	39.66	0.03	0.05	0.00	0.00	0.00	99.07	37.77	34.31	27.92	100	0.739
	66 / 3 .	23.09	36.30	0.00	0.00	0.03	39.43	0.01	0.08	0.00	0.00	0.00	98.93	37.97	34.28	27.75	100	0.731
	66 / 4 .	22.99	36.30	0.00	0.00	0.02	39.55	0.00	0.12	0.00	0.00	0.00	98.98	37.84	34.30	27.86	100	0.736
	66 / 5 .	22.81	36.29	0.00	0.01	0.04	39.62	0.00	0.00	0.00	0.00	0.00	98.78	37.64	34.38	27.98	100	0.743
	66 / 6 .	21.89	35.83	0.00	0.01	0.03	40.91	0.02	0.01	0.05	0.00	0.00	98.75	36.50	34.30	29.19	100	0.800
	67 / 1 .	22.90	35.84	0.00	0.00	0.01	39.55	0.01	0.02	0.00	0.01	0.00	98.33	37.91	34.07	28.02	100	0.739
	69 / 1 .	21.78	35.87	0.00	0.04	0.02	41.40	0.03	0.00	0.05	0.03	0.00	99.20	36.25	34.27	29.48	100	0.813
	70 / 1 .	20.55	35.24	0.00	0.14	0.02	42.76	0.00	0.04	0.00	0.01	0.00	98.75	34.78	34.25	30.98	100	0.891
	71 / 1 .	21.90	35.42	0.00	0.00	0.02	40.61	0.01	0.06	0.00	0.03	0.06	98.12	36.74	34.11	29.15	100	0.794
1A6-72-97	24 / 2 .	21.04	35.14	0.00	0.03	0.03	41.60	0.08	0.07	0.22	0.05	0.48	98.72	35.65	34.18	30.17	100	0.846
199.64m	24 / 3 .	20.95	35.44	0.00	0.05	0.04	41.25	0.06	0.06	0.26	0.03	0.45	98.59	35.54	34.52	29.95	100	0.843
	24 / 4 .	21.94	35.48	0.00	0.03	0.04	40.52	0.06	0.06	0.11	0.03	0.38	98.65	36.78	34.15	29.07	100	0.790
(12.50 g/t Au)	24 / 5 .	21.45	35.58	0.00	0.03	0.05	40.93	0.06	0.07	0.16	0.02	0.52	98.85	36.12	34.39	29.49	100	0.817
	24 / 6 .	21.58	35.32	0.00	0.02	0.03	40.86	0.06	0.06	0.10	0.04	0.37	98.44	36.36	34.17	29.47	100	0.810
	24 / 7 .	21.58	35.66	0.00	0.03	0.04	41.00	0.07	0.07	0.10	0.04	0.35	98.94	36.20	34.35	29.44	100	0.813
	24 / 8 .	21.43	35.11	0.00	0.04	0.02	40.98	0.08	0.08	0.10	0.03	0.41	98.27	36.25	34.09	29.66	100	0.818
	24 / 9 .	21.55	35.71	0.00	0.03	0.04	41.01	0.08	0.07	0.11	0.05	0.40	99.05	36.16	34.39	29.44	100	0.814
	24 / 10 .	21.16	35.08	0.01	0.06	0.05	41.47	0.08	0.06	0.12	0.03	0.40	98.52	35.83	34.11	30.06	100	0.839
	24 / 12 .	21.09	34.84	0.00	0.02	0.04	41.44	0.05	0.05	0.18	0.06	0.50	98.27	35.85	34.00	30.15	100	0.841
	24 / 13 .	21.45	35.46	0.00	0.09	0.02	41.15	0.06	0.07	0.15	0.05	0.39	98.88	36.10	34.26	29.64	100	0.821
	24 / 14 .	21.23	35.35	0.00	0.03	0.03	41.45	0.06	0.06	0.22	0.04	0.43	98.92	35.82	34.24	29.93	100	0.836
	28 / 1 .	21.23	35.68	0.02	0.08	0.03	41.12	0.02	0.00	0.13	0.03	0.00	98.34	35.79	34.54	29.67	100	0.829
	35 / 1 .	22.49	35.86	0.00	0.00	0.00	39.89	0.01	0.04	0.00	0.02	0.02	98.33	37.38	34.23	28.39	100	0.759
	37 / 1 .	22.04	36.00	0.00	0.00	0.02	40.35	0.01	0.08	0.00	0.03	0.00	98.53	36.75	34.46	28.79	100	0.784
	38 / 1 .	21.90	35.52	0.00	0.00	0.03	40.62	0.01	0.04	0.00	0.03	0.13	98.28	36.70	34.17	29.13	100	0.794
	39 / 1 .	22.45	35.93	0.00	0.00	0.04	39.73	0.00	0.05	0.00	0.02	0.00	98.22	37.36	34.33	28.30	100	0.757
	40 / 1 .	22.57	36.07	0.00	0.00	0.01	39.55	0.01	0.07	0.00	0.02	0.00	98.29	37.49	34.40	28.12	100	0.750

APPENDIX 6

Electron microprobe data used for arsenopyrite geothermometry (Aniuri deposit). Values in brackets below each element represent the detection limits.

Rock sample	Spot	Composition (wt. %)												Composition (at. %)				As/S mole
		S (0.03)	Fe (0.04)	Co (0.03)	Ni (0.02)	Zn (0.06)	As (0.03)	Ag (0.05)	Sb (0.04)	Au (0.06)	Cu (0.02)	Pb (0.4)	Total	S	Fe	As	Total	
AN-84-95	3 / 1 .	21.88	36.26	0.00	0.00	0.02	40.96	0.00	0.00	0.18	0.01	0.00	99.31	36.33	34.57	29.10	100	0.801
125.50m	4 / 1 .	21.93	36.08	0.00	0.00	0.03	40.62	0.02	0.00	0.13	0.02	0.06	98.89	36.53	34.51	28.96	100	0.793
	101 / 1 .	21.28	35.72	0.00	0.01	0.05	41.35	0.00	0.02	0.02	0.01	0.00	98.45	35.77	34.47	29.75	100	0.832
(12.57 g/t Au)	102 / 1 .	21.62	35.70	0.00	0.02	0.04	40.94	0.01	0.00	0.01	0.03	0.04	98.40	36.26	34.37	29.38	100	0.810
AN-125-96	5 / 1 .	22.22	35.30	0.00	0.00	0.03	41.03	0.01	0.01	0.06	0.04	0.00	98.70	37.01	33.75	29.24	100	0.790
167.30m	7 / 1 .	22.17	35.33	0.00	0.00	0.02	41.14	0.01	0.00	0.02	0.02	0.00	98.72	36.91	33.77	29.31	100	0.794
	18 / 1 .	22.31	35.56	0.00	0.03	0.05	40.83	0.02	0.00	0.05	0.03	0.00	98.87	37.06	33.91	29.02	100	0.783
(8.28 g/t Au)	28 / 1 .	22.25	35.10	0.00	0.01	0.01	40.84	0.02	0.01	0.06	0.05	0.00	98.35	37.16	33.66	29.19	100	0.786
	30 / 1 .	23.28	35.08	0.00	0.01	0.02	39.89	0.00	0.01	0.15	0.04	0.00	98.48	38.48	33.30	28.23	100	0.734
	44 / 1 .	22.33	35.73	0.00	0.01	0.04	40.95	0.03	0.01	0.18	0.05	0.00	99.33	36.99	33.98	29.03	100	0.785
	44 / 2 .	21.82	35.38	0.00	0.01	0.05	41.57	0.01	0.01	0.25	0.06	0.03	99.17	36.42	33.90	29.69	100	0.815
	44 / 3 .	21.72	35.34	0.00	0.08	0.05	41.73	0.01	0.00	0.09	0.06	0.00	99.06	36.27	33.90	29.83	100	0.822
	44 / 4 .	22.03	35.33	0.00	0.29	0.04	41.13	0.01	0.01	0.16	0.05	0.00	99.06	36.77	33.85	29.38	100	0.799
	44 / 5 .	22.14	35.16	0.00	0.28	0.04	41.01	0.03	0.03	0.20	0.05	0.02	98.95	36.98	33.71	29.31	100	0.793
	44 / 6 .	22.22	35.40	0.00	0.07	0.05	40.98	0.01	0.00	0.14	0.05	0.00	98.92	36.98	33.83	29.19	100	0.789
	44 / 7 .	22.11	35.45	0.00	0.15	0.07	40.99	0.00	0.02	0.00	0.05	0.00	98.82	36.85	33.92	29.23	100	0.793
	44 / 8 .	22.32	35.53	0.00	0.05	0.04	40.98	0.03	0.01	0.00	0.06	0.00	99.01	37.04	33.85	29.11	100	0.786
	44 / 9 .	22.99	35.71	0.00	0.08	0.02	39.78	0.02	0.00	0.06	0.04	0.00	98.70	37.99	33.88	28.13	100	0.740
	44 / 10 .	23.55	35.98	0.00	0.08	0.06	39.53	0.02	0.01	0.06	0.05	0.00	99.34	38.53	33.80	27.68	100	0.718
	44 / 11 .	22.61	35.44	0.00	0.17	0.04	40.56	0.00	0.00	0.15	0.05	0.00	99.03	37.49	33.73	28.78	100	0.768
	44 / 12 .	22.83	35.31	0.00	0.32	0.03	40.23	0.02	0.01	0.10	0.04	0.00	98.87	37.85	33.61	28.54	100	0.754
	44 / 13 .	22.50	35.85	0.00	0.07	0.05	40.65	0.03	0.00	0.05	0.04	0.00	99.23	37.20	34.04	28.76	100	0.773
	44 / 14 .	22.71	35.60	0.00	0.10	0.04	40.16	0.02	0.00	0.06	0.04	0.00	98.73	37.63	33.88	28.49	100	0.757
	44 / 15 .	22.50	35.63	0.00	0.13	0.03	40.73	0.03	0.01	0.06	0.03	0.00	99.16	37.26	33.88	28.86	100	0.775
	44 / 16 .	22.78	35.74	0.00	0.08	0.04	40.29	0.02	0.01	0.05	0.05	0.00	99.05	37.62	33.89	28.48	100	0.757
	44 / 17 .	22.70	35.70	0.00	0.15	0.04	40.57	0.02	0.00	0.01	0.05	0.00	99.24	37.49	33.85	28.67	100	0.765
	44 / 18 .	22.86	35.62	0.00	0.17	0.05	40.38	0.02	0.01	0.00	0.05	0.00	99.17	37.73	33.76	28.52	100	0.756
	44 / 19 .	22.88	35.67	0.00	0.12	0.04	40.15	0.03	0.00	0.00	0.05	0.00	98.93	37.79	33.83	28.38	100	0.751
	44 / 20 .	23.05	35.74	0.00	0.14	0.05	40.13	0.02	0.01	0.07	0.05	0.00	99.24	37.95	33.78	28.27	100	0.745
	44 / 21 .	22.59	35.49	0.00	0.22	0.04	40.66	0.00	0.02	0.09	0.04	0.00	99.14	37.42	33.75	28.83	100	0.770
	44 / 22 .	22.10	35.25	0.00	0.04	0.05	41.28	0.03	0.02	0.14	0.04	0.00	98.94	36.83	33.73	29.44	100	0.800
	44 / 23 .	21.92	35.97	0.00	0.05	0.05	41.57	0.02	0.00	0.22	0.05	0.00	99.84	36.31	34.21	29.48	100	0.812
	44 / 24 .	22.41	35.54	0.00	0.05	0.04	40.78	0.02	0.02	0.17	0.05	0.00	99.08	37.18	33.86	28.96	100	0.779
	44 / 25 .	21.92	35.81	0.00	0.03	0.04	41.52	0.03	0.04	0.19	0.05	0.00	99.63	36.39	34.12	29.49	100	0.811
	44 / 26 .	21.69	35.29	0.00	0.03	0.03	41.71	0.01	0.01	0.17	0.05	0.00	98.98	36.26	33.88	29.85	100	0.823
	44 / 27 .	21.49	35.29	0.00	0.01	0.04	42.16	0.03	0.01	0.24	0.05	0.00	99.31	35.94	33.88	30.17	100	0.839
	44 / 28 .	21.55	35.27	0.00	0.02	0.05	42.07	0.00	0.02	0.14	0.04	0.00	99.17	36.04	33.86	30.10	100	0.835

APPENDIX 6 continued

Rock sample	Spot	Composition (wt. %)												Composition (at. %)				As/S mole
		S (0.03)	Fe (0.04)	Co (0.03)	Ni (0.02)	Zn (0.06)	As (0.03)	Ag (0.05)	Sb (0.04)	Au (0.06)	Cu (0.02)	Pb (0.4)	Total	S	Fe	As	Total	
AN-125-96	44 / 29 .	21.52	35.29	0.00	0.04	0.05	42.01	0.02	0.01	0.20	0.06	0.00	99.20	36.01	33.90	30.09	100	0.836
167.30m	44 / 30 .	21.65	34.97	0.00	0.05	0.04	41.81	0.02	0.01	0.12	0.05	0.03	98.74	36.31	33.68	30.01	100	0.827
	45 / 1 .	22.09	35.37	0.00	0.08	0.01	41.35	0.00	0.01	0.04	0.01	0.00	98.97	36.76	33.79	29.45	100	0.801
(8.28 g/t Au)	45 / 2 .	22.12	35.55	0.00	0.02	0.02	41.05	0.02	0.00	0.07	0.04	0.00	98.87	36.80	33.96	29.23	100	0.794
	45 / 3 .	22.33	36.01	0.00	0.00	0.02	40.95	0.02	0.00	0.00	0.02	0.00	99.35	36.89	34.16	28.96	100	0.785
	45 / 4 .	22.27	35.58	0.00	0.03	0.02	40.96	0.01	0.00	0.01	0.03	0.00	98.92	36.98	33.92	29.11	100	0.787
	45 / 5 .	22.22	35.54	0.00	0.04	0.02	40.88	0.01	0.00	0.02	0.01	0.00	98.73	36.95	33.94	29.11	100	0.788
	45 / 6 .	22.78	35.88	0.00	0.01	0.03	40.35	0.01	0.01	0.00	0.02	0.00	99.10	37.55	33.97	28.48	100	0.758
	45 / 7 .	22.70	36.33	0.00	0.01	0.02	40.41	0.03	0.04	0.00	0.02	0.00	99.55	37.30	34.28	28.42	100	0.762
	45 / 8 .	22.63	35.88	0.00	0.01	0.01	40.58	0.03	0.03	0.00	0.03	0.00	99.18	37.34	33.99	28.66	100	0.768
	45 / 9 .	22.31	36.10	0.00	0.02	0.01	40.91	0.00	0.02	0.00	0.01	0.00	99.38	36.85	34.23	28.92	100	0.785
	45 / 10 .	22.41	35.80	0.00	0.01	0.03	40.80	0.01	0.01	0.00	0.01	0.00	99.07	37.08	34.02	28.90	100	0.779
	45 / 11 .	22.35	35.81	0.00	0.02	0.00	40.63	0.02	0.02	0.00	0.02	0.00	98.88	37.07	34.09	28.84	100	0.778
	45 / 12 .	22.23	35.48	0.00	0.12	0.03	41.07	0.02	0.01	0.10	0.03	0.00	99.09	36.94	33.85	29.21	100	0.791
	45 / 13 .	21.97	35.78	0.00	0.05	0.01	41.48	0.03	0.00	0.13	0.03	0.00	99.47	36.46	34.09	29.46	100	0.808
	45 / 14 .	22.02	35.51	0.00	0.10	0.01	41.37	0.01	0.00	0.12	0.03	0.00	99.15	36.62	33.92	29.45	100	0.804
	45 / 15 .	21.91	35.48	0.00	0.05	0.01	41.40	0.05	0.01	0.09	0.01	0.02	99.03	36.51	33.96	29.53	100	0.809
	45 / 16 .	22.05	35.22	0.00	0.16	0.00	41.03	0.01	0.00	0.01	0.03	0.00	98.51	36.86	33.79	29.35	100	0.796
	46 / 1 .	22.23	35.58	0.00	0.03	0.03	41.10	0.01	0.01	0.11	0.02	0.00	99.13	36.90	33.91	29.19	100	0.791
	46 / 2 .	22.27	35.53	0.00	0.06	0.03	41.04	0.00	0.01	0.10	0.01	0.00	99.04	36.97	33.87	29.16	100	0.789
	46 / 3 .	22.25	35.56	0.00	0.05	0.03	41.11	0.01	0.02	0.09	0.02	0.00	99.12	36.92	33.88	29.20	100	0.791
	46 / 4 .	22.18	35.61	0.00	0.05	0.04	41.20	0.01	0.00	0.11	0.02	0.00	99.21	36.80	33.93	29.27	100	0.795
	46 / 5 .	22.71	35.76	0.00	0.10	0.03	40.48	0.02	0.01	0.13	0.01	0.00	99.26	37.50	33.90	28.60	100	0.763
	46 / 6 .	22.49	35.63	0.00	0.01	0.04	40.47	0.01	0.02	0.00	0.02	0.00	98.68	37.31	33.94	28.74	100	0.770
	46 / 7 .	22.49	36.09	0.00	0.01	0.03	40.90	0.03	0.02	0.00	0.01	0.00	99.56	37.05	34.13	28.83	100	0.778
	46 / 8 .	22.51	35.82	0.00	0.00	0.04	40.56	0.01	0.03	0.00	0.02	0.00	98.99	37.25	34.03	28.72	100	0.771
	46 / 9 .	22.64	35.93	0.00	0.00	0.02	40.45	0.01	0.04	0.00	0.01	0.00	99.10	37.37	34.06	28.58	100	0.765
	46 / 10 .	22.25	35.68	0.00	0.10	0.03	41.10	0.01	0.01	0.18	0.02	0.00	99.39	36.88	33.96	29.16	100	0.791
	46 / 11 .	21.96	35.72	0.00	0.04	0.03	41.41	0.01	0.00	0.26	0.04	0.01	99.47	36.49	34.07	29.44	100	0.807
	46 / 12 .	21.81	35.53	0.00	0.04	0.03	41.40	0.03	0.01	0.18	0.03	0.00	99.06	36.39	34.04	29.57	100	0.813
	46 / 13 .	22.35	36.12	0.00	0.00	0.03	40.90	0.01	0.02	0.00	0.01	0.00	99.45	36.88	34.23	28.89	100	0.783
	46 / 14 .	22.76	36.29	0.00	0.00	0.04	40.56	0.01	0.04	0.00	0.00	0.00	99.70	37.33	34.18	28.48	100	0.763
	46 / 15 .	22.77	36.54	0.00	0.00	0.03	40.52	0.03	0.03	0.00	0.02	0.00	99.94	37.28	34.34	28.39	100	0.762
	46 / 16 .	22.96	36.13	0.00	0.00	0.03	40.28	0.02	0.03	0.00	0.02	0.00	99.47	37.68	34.04	28.28	100	0.751
	46 / 17 .	21.89	35.94	0.00	0.05	0.03	41.48	0.01	0.01	0.11	0.03	0.00	99.54	36.31	34.24	29.45	100	0.811
	46 / 18 .	21.24	34.14	0.00	0.05	0.03	39.53	0.00	0.01	0.00	0.01	0.00	95.01	36.78	33.93	29.29	100	0.796
	47 / 1 .	22.33	35.41	0.00	0.17	0.03	40.71	0.03	0.01	0.07	0.03	0.00	98.78	37.17	33.84	29.00	100	0.780
	48 / 1 .	23.02	36.02	0.00	0.01	0.02	39.97	0.00	0.02	0.01	0.01	0.00	99.07	37.86	34.01	28.13	100	0.743

APPENDIX 6 continued

Rock sample	Spot	Composition (wt. %)												Composition (at. %)				As/S mole
		S (0.03)	Fe (0.04)	Co (0.03)	Ni (0.02)	Zn (0.06)	As (0.03)	Ag (0.05)	Sb (0.04)	Au (0.06)	Cu (0.02)	Pb (0.4)	Total	S	Fe	As	Total	
AN-125-96	49 / 1 .	21.92	35.53	0.00	0.04	0.02	41.34	0.00	0.00	0.30	0.05	0.00	99.20	36.53	33.99	29.48	100	0.807
167.30m	51 / 1 .	21.91	35.21	0.00	0.06	0.02	41.43	0.00	0.01	0.17	0.01	0.00	98.82	36.60	33.78	29.62	100	0.809
	52 / 1 .	21.75	35.19	0.00	0.01	0.03	41.52	0.02	0.01	0.14	0.02	0.00	98.69	36.42	33.83	29.75	100	0.817
(8.28 g/t Au)	53 / 1 .	21.81	34.77	0.00	0.06	0.03	41.64	0.00	0.01	0.00	0.03	0.00	98.36	36.59	33.50	29.91	100	0.817
	54 / 1 .	21.50	34.80	0.00	0.08	0.00	41.82	0.02	0.03	0.00	0.04	0.00	98.29	36.21	33.65	30.14	100	0.833
	54 / 2 .	23.32	35.92	0.00	0.01	0.00	39.79	0.02	0.01	0.02	0.01	0.00	99.10	38.24	33.82	27.93	100	0.730
	54 / 3 .	23.17	35.43	0.00	0.02	0.00	39.46	0.02	0.01	0.00	0.04	0.00	98.16	38.36	33.68	27.96	100	0.729
	54 / 4 .	21.89	34.97	0.00	0.01	0.01	41.38	0.01	0.01	0.23	0.03	0.00	98.52	36.68	33.65	29.68	100	0.809
	54 / 5 .	22.38	35.32	0.00	0.01	0.01	40.97	0.02	0.01	0.16	0.02	0.00	98.88	37.18	33.69	29.13	100	0.783
	54 / 6 .	22.26	35.21	0.00	0.00	0.00	41.04	0.00	0.00	0.18	0.03	0.00	98.73	37.07	33.67	29.26	100	0.789
	54 / 7 .	22.30	35.19	0.00	0.01	0.00	40.88	0.04	0.00	0.16	0.02	0.00	98.58	37.16	33.68	29.16	100	0.785
	54 / 8 .	22.69	35.23	0.00	0.00	0.00	40.24	0.02	0.02	0.04	0.02	0.00	98.26	37.73	33.64	28.64	100	0.759
	54 / 9 .	23.44	35.88	0.00	0.00	0.00	39.47	0.03	0.02	0.00	0.03	0.00	98.87	38.47	33.81	27.72	100	0.720
	54 / 10 .	23.37	35.59	0.00	0.00	0.00	39.61	0.02	0.04	0.00	0.02	0.00	98.64	38.46	33.64	27.90	100	0.726
	54 / 11 .	22.99	35.79	0.00	0.00	0.00	39.98	0.01	0.00	0.14	0.02	0.00	98.93	37.91	33.88	28.21	100	0.744
	54 / 12 .	23.65	36.20	0.00	0.00	0.00	39.27	0.01	0.02	0.09	0.03	0.00	99.27	38.62	33.94	27.44	100	0.711
	54 / 13 .	23.27	35.50	0.00	0.04	0.00	39.90	0.05	0.02	0.00	0.01	0.00	98.78	38.32	33.56	28.12	100	0.734
	54 / 14 .	22.92	35.50	0.00	0.01	0.00	40.27	0.01	0.02	0.00	0.02	0.00	98.74	37.86	33.67	28.47	100	0.752
	54 / 15 .	23.28	35.86	0.00	0.04	0.00	39.96	0.00	0.02	0.00	0.02	0.00	99.19	38.18	33.77	28.05	100	0.735
	54 / 16 .	24.95	36.73	0.00	0.05	0.00	37.43	0.01	0.00	0.00	0.01	0.00	99.18	40.20	33.98	25.82	100	0.642
	54 / 17 .	23.62	35.70	0.00	0.03	0.00	39.27	0.02	0.00	0.00	0.01	0.00	98.65	38.77	33.64	27.59	100	0.712
	54 / 18 .	23.43	35.63	0.00	0.02	0.00	39.36	0.02	0.01	0.06	0.02	0.00	98.55	38.58	33.68	27.74	100	0.719
	54 / 19 .	22.84	35.40	0.00	0.01	0.00	40.32	0.01	0.01	0.10	0.02	0.00	98.71	37.81	33.64	28.56	100	0.755
	54 / 20 .	22.23	35.26	0.00	0.02	0.00	41.27	0.00	0.02	0.13	0.02	0.00	98.95	36.97	33.67	29.37	100	0.794
	54 / 21 .	22.12	35.23	0.00	0.01	0.00	41.27	0.04	0.02	0.15	0.01	0.00	98.84	36.86	33.71	29.43	100	0.799
	54 / 22 .	22.01	35.50	0.00	0.01	0.00	41.27	0.03	0.00	0.19	0.04	0.01	99.06	36.65	33.94	29.41	100	0.802
	54 / 23 .	21.99	35.08	0.00	0.01	0.00	41.28	0.02	0.02	0.21	0.04	0.00	98.64	36.77	33.69	29.55	100	0.804
	54 / 24 .	22.26	35.68	0.00	0.01	0.00	41.10	0.01	0.01	0.15	0.04	0.00	99.25	36.89	33.96	29.15	100	0.790
	54 / 25 .	21.90	34.78	0.00	0.01	0.00	41.58	0.03	0.01	0.21	0.03	0.00	98.54	36.70	33.47	29.83	100	0.813
	65 / 1 .	21.52	35.55	0.00	0.01	0.01	42.22	0.01	0.01	0.01	0.01	0.00	99.37	35.87	34.02	30.12	100	0.840
	66 / 1 .	22.59	35.39	0.00	0.07	0.02	40.86	0.02	0.00	0.03	0.04	0.00	99.02	37.40	33.65	28.96	100	0.774

APPENDIX 7

Laser ablation – inductively coupled plasma – mass spectrometry (LA-ICP-MS) data of arsenopyrite (ASP), coarse-grained pyrite (C-PY) and fine-grained pyrite (F-PY). cps: count per second.

Rock sample 1A6-74-98/372.70m (7.10 g/t Au)						
Mineral type	**Spot**	**Au (ppm)**	**Cu (cps)**	**As (cps)**	**Te (cps)**	**Bi (cps)**
ASP	**J-1**	391	5114	13000000	171	12817
ASP	**J-2**	313	253	2300000	118	473
ASP	**J-3**	98.1	3475	7700000	208	7602
ASP	**J-5**	152	2270	8600000	106	4642
ASP	**J-6**	223	3684	9600000	128	5860
ASP	**J-7**	173	1142	7400000	42	2287
ASP	**J-8**	145	4769	11000000	154	8631
ASP	**J-9**	197	1048	6200000	613	2352
ASP	**J-10**	109	5252	11000000	489	12024
C-PY	**J-11**	0.365	475	33047	3	381
C-PY	**J-12**	0.113	95	90942	2	165
C-PY	**J-13**	<0.01	26	62307	0	3
C-PY	**J-14**	0.049	32	138887	4	5
C-PY	**J-15**	0.044	40	146302	0	24
C-PY	**J-16**	<0.01	40	35303	1	21
C-PY	**J-17**	0.036	40	101677	0	2
C-PY	**J-18**	0.146	123	123264	0	150
C-PY	**J-19**	0.081	194	70049	0	164
C-PY	**J-20**	0.036	142	31104	5	143
C-PY	**J-21**	<0.02	22	21071	3	41
C-PY	**J-22**	0.052	61	72061	0	95
C-PY	**J-22a**	0.100	28	122972	2	70
C-PY	**J-23**	5.23	66	753934	9	221
C-PY	**J-24**	0.042	27	63516	0	72
C-PY	**J-25**	0.035	24	90007	0	42
C-PY	**J-26**	0.083	80	106991	0	69
C-PY	**J-27**	0.461	331	107196	3	520
C-PY	**J-28**	0.042	59	55572	0	56
C-PY	**J-29**	0.020	4	95136	2	4
C-PY	**J-30**	0.046	37	15179	0	49
C-PY	**J-31**	0.062	62	55640	0	84
C-PY	**J-32**	<0.01	3	74937	3	11
C-PY	**J-33**	0.185	59	59788	0	95
C-PY	**J-34**	0.100	125	6389	1	161
C-PY	**J-35**	0.043	41	29474	2	63

Rock sample AN-122-96/184.50m (5.98 g/t Au)						
Mineral type	**Spot**	**Au (ppm)**	**Cu (cps)**	**As (cps)**	**Te (cps)**	**Bi (cps)**
ASP	**A-1**	42.1	1	1500000	27	26
ASP	**A-2**	53.5	20727	3100000	37	410
ASP	**A-3**	40.2	169	1300000	8	22
ASP	**A-4**	31.0	48	1500000	0	0
ASP	**A-5**	18.5	28	1900000	234	31
ASP	**A-6**	686	65	2800000	107	57
ASP	**A-7**	9.02	209	3300000	87	785
ASP	**A-8**	30.5	128	2900000	80	334
ASP	**A-9**	7.23	56	1400000	0	15
ASP	**A-10**	15.4	136	3600000	51	584
ASP	**A-11**	26.2	223	4300000	46	882
ASP	**A-28**	0.113	16	1700000	0	63
ASP	**A-29**	55.2	79	2700000	11	127
ASP	**A-31**	1.46	48	1300000	90	131
ASP	**A-32**	3.55	60	1700000	7	98
F-PY	**A-12**	27.7	2704	647923	5	618
F-PY	**A-13**	1.63	3133	31626	97	13476
F-PY	**A-14**	1.84	3073	46738	300	17696
F-PY	**A-15**	141	9566	720529	7	162
F-PY	**A-16**	74.5	4725	642719	70	211
F-PY	**A-17**	45.9	6825	777632	97	9083
F-PY	**A-18**	1.59	44048	46005	89	55787
F-PY	**A-19**	4.75	78409	71170	135	101130
F-PY	**A-20**	6.54	18676	58044	60	65604
F-PY	**A-21**	22.2	8510	1300000	24	12476
F-PY	**A-22**	5.00	2683	333814	7	2278
F-PY	**A-23**	45.9	1.0*106	924894	24	6899
F-PY	**A-24**	5.68	144894	122093	205	51954
F-PY	**A-25**	3.80	43582	84915	114	21364
F-PY	**A-26**	6.06	47544	185675	231	27885
F-PY	**A-27**	62.7	106128	1300000	37	4874
F-PY	**A-30**	96.3	150900	1100000	8	521